

# The Impact of Stellar Feedback from Massive Stars in the Interstellar Medium

INAUGURAL-DISSERTATION

zur  
Erlangung des Doktorgrades  
der Mathematisch-Naturwissenschaftlichen Fakultät  
der Universität zu Köln



vorgelegt von

**Sebastian Haid**  
aus Graz, Österreich

Köln, 2018

Berichterstatter (Gutachter):  
Prof. Dr. Stefanie Walch-Gassner  
Prof. Dr. Cristiano Porciani

Vorsitzender der Kommission:  
Prof. Dr. Joachim Saur

Tag der mündlichen Prüfung:  
9. April 2018







*Für meine Eltern*



# ABSTRACT

---

The impact of stellar feedback from massive stars is important for the evolution of the interstellar medium and the structures within. Stellar winds, ionizing radiation, and supernovae are considered as the most important processes in shaping molecular clouds, influence rate of star formation, drive turbulences, and even expel gas out of the Galactic disc. Despite understanding the energy contribution from massive stars, the impact of stellar feedback, i.e. the resulting momentum, is still debated and the relative importance of the processes remains unclear. This thesis contains three scientific papers that investigate feedback processes in detail. Three-dimensional, radiation-hydrodynamic simulations are performed to study the relative impact of stellar winds and ionizing radiation from massive stars in homogeneous media. The cold and dense environment is dominated by the radiative feedback. Over the lifetime of the massive star, imparted momentum becomes equally or more important than the impact from a supernova explosion. Stellar wind is the dominant process in warm and rarefied environments. The idea is expanded to a molecular cloud environment that self-consistently evolves from a SN-driven, multiphase interstellar medium in the galactic disc. The first three Myr in the cloud evolution are investigated under the influence of ionizing radiation. Due to the prevailing dense structures, stellar winds can be neglected. The radiative impact is determined by dense, well-shielded structures, which are able to enclose massive stars and their surrounding ionized bubbles. Mutual interactions of feedback and well-shielded regions determine the morphological evolution of molecular clouds. The final type-II supernova impact is investigated by a novel, one-dimensional description including the adiabatic and radiative phases of the evolution. The momentum input from a supernova shock increases with lower densities. Additionally, supersonic turbulence boosts the impact. These three studies indicate that the importance of the individual feedback processes depends on the environmental properties.



## ZUSAMMENFASSUNG

---

Das stellare Feedback von massereichen Sternen ist von essentieller Bedeutung für die Entwicklung des interstellaren Mediums und der darin enthaltenen Strukturen. Hierbei werden stellare Winde, ionisierende Strahlung und Supernovae als die wichtigsten Prozesse benannt. Diese verändern Molekül-Wolken, beeinflussen die Sternentstehungsrate, treiben Turbulenz und schaffen es sogar, Gas aus der galaktischen Scheibe auszustoßen. Obwohl der Energiebeitrag von massereichen Sternen relative gut bekannt ist, wird die Auswirkung, sprich der sich entwickelnde Impuls, noch immer debattiert und die relative Wichtigkeit der Prozesse ist unklar. Diese Arbeit beinhaltet drei Abhandlungen, die die Auswirkung der vorhin genannten Prozesse im Detail untersucht. In drei-dimensionalen, hydrodynamischen Simulation mit Strahlungstransport wird der relative Effekt stellar Winde und ionisierender Strahlung in homogenen Medien untersucht. Dabei zeigt sich, dass kalte und dichte Umgebungen von ionisierender Strahlung dominiert werden. Der sich während des Sternenlebens ergebende Impuls ist zumindest vergleichbar oder sogar größer verglichen mit dem einer Supernova Explosion. Stellar Winde hingegen sind in warmen und dünnen Medien wichtig. Dieses Betrachtung wird erweitert durch Simulationen von selbstkonsistent entwickelten Molekülwolken, die im interstellaren Medium einer galaktischen Scheibe eingebettet sind. Hierbei, wird der Einfluss von ionisierender Strahlung auf die ersten drei Millionen Jahre der Evolution der Wolken untersucht. Auf Grund der vorherrschenden hohen Umgebungsdichten, können stellare Winde vernachlässigt werden. Die Auswirkung der Strahlung wird durch dichte und gut-abgeschirmte Strukturen bestimmt, wobei diese, massereiche Sterne und die dabei entstehenden ionisierenden Blasen einschließen können. Die Entwicklung der Wolken ergibt sich folglich aus dem Vorhandensein gut-abschirmender Regionen. Schlussendlich wird die Auswirkung einer Typ-II Supernova mit Hilfe eines eigens hierfür entwickelten ein-dimensionalen Programms untersucht, dass der Supernova Entwicklung durch die adiabatische bis zum Ende der radiative Phase folgt. Der entstehende Impuls des Schocks nimmt mit abnehmender Dichte zu. Zusätzliche supersonische Turbulenz erhöht nochmals die Wirkung. Diese drei Studien zeigen, dass die Wichtigkeit der einzelnen Prozesse von den Strukturen der Umgebung bestimmt wird.





# CONTENTS

1	INTRODUCTION	1
1.1	Observational evidence	1
1.1.1	The interstellar medium in our Galaxy	2
1.1.2	Molecular clouds	3
1.1.3	Massive star formation and stellar feedback	5
1.2	Physical processes in the interstellar medium	6
1.2.1	Heating processes	6
1.2.2	Cooling processes	7
1.2.3	A multiphase description of the interstellar medium	8
1.3	Stellar feedback processes	9
1.3.1	Stellar wind	9
1.3.2	Ionizing radiation	9
1.3.3	Supernovae	10
1.3.4	Supersonic turbulence	11
2	METHODOLOGY	13
2.1	Magneto-Hydrodynamics	13
2.2	One-dimensional shock description	14
2.3	FLASH 4	15
3	THE RESEARCH	18
4	PAPER I	21
5	PAPER II	39
6	PAPER III	62
7	SUMMARY AND CONCLUSION	80
7.1	Summary	80
7.2	Conclusion	83
7.3	Outlook	83



## INTRODUCTION

---

Our *Sun* is one star among the billions that are located in the *Milky Way*. The space between the stars is called the *interstellar medium* (ISM) and it is not as empty as it might seem. It is filled with gas and small dust grains of varying sizes. It is filled with radiation covering the whole electromagnetic spectrum, high-energetic X-rays to the visible to the faint cosmic microwave background.

The importance of the ISM is reflected in the cycle of star formation. *Molecular clouds* (MC) are able to condense from the reservoir of baryonic matter, which makes up the ISM. Filamentary substructures evolve in these –in an astrophysical context– dense regions. Under the influence of self-gravity, the gas collapses to finally form stars. The most massive stars are more than eight, and up to hundred times more massive than the Sun. Their large mass increases the energy released by nuclear fusion. To stabilize a *massive star* it emits radiation with a peak in the UV regime. Stellar material is ejected as wind, which is driven by line scattering due to the continuum radiation of the star. These processes are known as *stellar feedback*. After millions of years, when the fusion reactions have consumed all the fuel, the star will explode in a single and final, type-II *supernova* (SN). Highly energetic, metal-rich gas and radiation is returned into the ISM. Shocks travel through the surrounding medium and induce turbulent motions. These either disrupt the cycle of star formation or trigger it, hence the cycle closes.

This thesis contains three scientific publications that investigate the importance of stellar feedback on the ISM. On the following pages, I provide the reader with observational evidence and a general introduction to the physics of the ISM. It is structured by spatial scale following the cycle of star formation starting with the ISM on 100 pc-scale down to MCs, star formation, and stellar feedback processes. A more specific background is given in each of the scientific publications.

### 1.1

#### OBSERVATIONAL EVIDENCE

Over the past decades, a variety of ground-based, airborne and space-based telescopes became operational. These include the *Atacama Large Millimeter Array* (ALMA), *Stratospheric Observatory for Infrared Astronomy* (SOFIA), the *Spitzer Space Telescope*, and the *Herschel Space Observatory*. Each of these telescopes reveal small pieces of the puzzle, allowing a better understanding of the ISM. Gas and dust properties are constrained, physical processes investigated, and star formation recorded. This section summarizes some selected observational achievements and derived relations between properties and processes of the ISM.



Figure 1: Observation of 60 degrees of the Galactic plane right to the center of the Galaxy in the infrared wavelength (3-8  $\mu\text{m}$ ) regime as observed by the Spitzer Space Telescope (Churchwell et al. (2009), GLIMPSE survey). The red, extended emission reveals dusty regions of star formation. These are shaped by related stellar feedback processes to form bubbles and inhomogeneous structures. Dark regions are dense regions that shield infrared emission. *Credit: NASA/GLIMPSE consortium*

### 1.1.1

#### THE INTERSTELLAR MEDIUM IN OUR GALAXY

Fig. 1 shows the central part of the Galaxy observed in the infrared regime within the GLIMPSE survey<sup>1</sup>. Inhomogeneous structures, bubbles and tendrils (red, thermal emission from dust) appear around point sources (Churchwell et al. 2009, seen in blue, 4.5  $\mu\text{m}$  emission from dust in ionized and shocked gas). These sources are massive stars or clusters of them. The extended emission around, revealed by dust emission, is the ISM. However, what can be observed by dust is only a small fraction ( $\sim 1$  percent corresponding to the typical dust-to-gas mass ratio) of the mass of the ISM, which totals  $\sim 10^{10} M_{\odot}$  in the Milky Way (Kalberla & Dedes 2008). 99 percent of the mass is gas, which consists to 70 percent of hydrogen, 28 percent helium and 2 percent of heavier elements (metals). In addition to the baryonic matter, the ISM includes the interstellar radiation field (ISRF), a magnetic field and relativistic cosmic rays. These constituents are discussed in more detail below.

Hydrogen is the most abundant chemical species in the ISM. It appears in molecular ( $\text{H}_2$ ), atomic ( $\text{H}$ ) and ionized ( $\text{H}^+$ ) states with volume filling fractions in the ISM of around 0.05, 0.31, and 0.64 (Spitzer 1978; Tielens 2005). Ionized hydrogen occupies the interstellar volume as photoionized gas in HII-regions<sup>2</sup> (temperature  $T \sim 8000$  K, number density  $n \gtrsim 0.1 \text{ cm}^{-3}$ ) or as shock-heated, diffuse gas ( $T \sim 10^6$  K,  $n \sim 10^{-3} \text{ cm}^{-3}$ ) up to scale heights of some kpc above/below the galactic plane (Tielens 2005; Klessen & Glover 2016). Observationally,  $\text{H}^+$  is traced by the emission of the  $\text{H}_{\alpha}$  recombination line (Draine 2011b). The mass of atomic hydrogen has a Gaussian distribution around the galactic plane to scale heights of a few 100 pc. It is found in cold, diffuse clouds ( $T \sim 100$  K,  $n \sim 50 \text{ cm}^{-3}$ ) or in warm, intercloud gas ( $T \sim 8000$  K,  $n \sim 0.5 \text{ cm}^{-3}$ ). Atomic hydrogen can be observed by the 21-cm emission originating from the hydrogen hyperfine splitting (Spitzer 1978; Tielens 2005; Klessen & Glover 2016). Molecular hydrogen is found in discrete clouds which are situated in the central plane ( $T \sim 20$  K,  $n \gtrsim 100 \text{ cm}^{-3}$ ). Molecular hy-

<sup>1</sup><http://www.astro.wisc.edu/glimpse/>

<sup>2</sup>HII and  $\text{H}^+$  express the same ionized state of hydrogen. An entire photoionized bubble is commonly labelled HII-region. In contrary, I use  $\text{H}^+$  for the gas itself.

drogen is especially difficult to observe as it has no permanent electric dipole. The available quadrupole radiation requires high excitation temperatures and remains extremely weak in conditions in which molecular gas resides.

In addition to non-relativistic gas, the ISM also contains particles which were accelerated to relativistic speeds. These relativistic particles are named *cosmic rays*. These highly energetic particles (nuclei, electrons) have energies between 100 MeV and 1 TeV (Gaisser 2006; Draine 2011b; Blasi 2014; Klessen & Glover 2016).

*Interstellar dust* is a general term for metal agglomerations (e.g. polycyclic aromatic hydrocarbonates (PAHs), silicates, graphites) with sizes between 50 to 2500 Å (Draine & Lee 1984; Weingartner & Draine 2001). It is commonly assumed that the dust is correlated to the total gas column density with an almost constant gas-to-dust ratio of 100 (Hildebrand 1983; Klessen & Glover 2016). Despite the fact that the total dust mass is only 1 percent of the gas mass, dust is considered as a key ingredient in the ISM. It efficiently interacts with radiation (absorption, re-emission, shielding) and provides a large surface area for chemical reactions (van Dishoeck & Blake 1998). The structures in Fig. 1 are revealed by dust emission in the infrared regime with a wavelength dependent on the grain size distribution and the incident radiation (Tielens 2005).

The ISM in the solar neighbourhood is filled with the diffuse *interstellar radiation field* (ISRF), which influences the chemical and physical state of the gas and dust. Its spectral energy distribution consists of the cosmic microwave background emission (frequency  $\nu \sim 10^{10}$  Hz, Black 1994), far-infrared emission by dust ( $\nu \sim 10^{11}$  Hz, Dupac et al. 2003; Shetty et al. 2009a,b), infrared emission from PAHs ( $\nu \sim 3 \times 10^{13}$  Hz), and emission of starlight. The older stellar population is predominant in the optical regime. Young, massive, and hot stars influence the far-UV range (Habing 1968; Draine 1978; Mathis et al. 1983). Minor contribution to the ISRF are from synchrotron emission in the radio regime and X-rays from hot plasma (Snowden et al. 1997).

Small and large scale *magnetic fields* are important sources of energy and pressure in the ISM. The field strength in the solar neighbourhood is  $\sim 5 \mu\text{G}$  but can reach higher values in high density gas (Troland et al. 1996; Crutcher 1999). Observationally, magnetic fields are detectable by e.g. the partial alignment of elongated dust grains along the magnetic field lines which polarize optical and infrared radiation (Andersson et al. 2015) or Zeeman-splitting of the 21-cm atomic hydrogen hyperfine structure line (Troland & Heiles 1982; Crutcher et al. 1999; Draine 2003).

### 1.1.2

#### MOLECULAR CLOUDS

*Molecular clouds* (MC) are cold and dense clouds in the ISM which contain almost half of the ISM mass in less than 1 percent of the total ISM volume. These clouds are especially interesting because they host star formation. Fig. 2 shows the infrared emission from the closest site of active high mass star formation in the Galaxy, the Orion A molecular cloud (Meingast et al. 2016).

The most abundant molecule in MCs is  $\text{H}_2$ . It is deeply embedded in the most dense regions of the clouds, however a direct observation is challenging (as described in Section 1.1.1). To investigate the dense MC structures, observations rely on the second most abundant molecule, CO ( $^{12}\text{C}^{16}\text{O}$ ) and its isotopologues (e.g.  $^{13}\text{C}^{16}\text{O}$ ,  $^{13}\text{C}^{18}\text{O}$ ,  $^{12}\text{C}^{17}\text{O}$ ). The distribution of MCs in the Galaxy is observed using CO maps and the following relations were found.



Figure 2: Observation in the infrared wavelength regime of the *Orion A* molecular cloud, the closest site of active massive star formation in the Galaxy. In the center a massive star cluster, the *Trapezium* cluster, has ionized the environment. The surrounding clouds are still molecular and region of active star formation. Credit: ESO/J. Emerson/VISTA

some physical processes counteract gravitational collapse and it is suggested that supersonic, turbulent motions support the cloud (Mac Low et al. 2004; Ballesteros-Paredes et al. 2007). This can be expressed by the virial parameter  $\alpha_{\text{vir}}$ , which relates the gravitational energy  $E_{\text{grav}}$  and the kinetic energy  $E_{\text{kin}}$  with

$$\alpha_{\text{vir}} = \frac{2E_{\text{kin}}}{E_{\text{grav}}} = \frac{5\sigma^2 R}{GM} \quad (1.3)$$

where  $R$  and  $M$  are the radius and the mass of a spherical cloud, respectively,  $G$  is the gravitational constant. The velocity dispersion  $\sigma$  is related to turbulent motions and can be related to the cloud mass and size (Larson 1981; Caselli & Myers 1995):

$$\sigma \propto R^{0.4} \propto M^{0.2}. \quad (1.4)$$

Observationally, it has been shown that the average cloud is close to, but not exactly in virial equilibrium. This uncertainty leaves both interpretations, collapse or equilibrium, open for MCs (Falgarone et al. 2009; Heyer et al. 2009; Roman-Duval et al. 2010).

The cloud-mass distribution is (Dame et al. 1987; Solomon et al. 1987; Scoville et al. 1987; Williams et al. 2000; Heyer & Dame 2015)

$$\frac{dN}{dM} \propto M^{\eta_M} \quad (1.1)$$

where  $N$  is the number of MCs and  $M$  the mass. The scaling index  $\eta_M$  lies between -1.5 and -2.5 dependent on the amount of  $\text{H}_2$  in the inner and outer parts of galaxies (Roman-Duval et al. 2010; Gratier et al. 2012). The observed cloud masses range from  $10^3$ - $10^7 M_\odot$ . Usually clouds with masses above  $10^4 M_\odot$  are classified as *giant molecular clouds* (Dobbs et al. 2014).

As with the mass, the cloud-size distribution is given with

$$\frac{dN}{dR} \propto R^{\eta_R} \quad (1.2)$$

where  $R$  is the cloud size. The scaling index  $\eta_R$  was found to be between -3.3 and -3.9 (Solomon et al. 1987; Elmegreen & Falgarone 1996; Heyer et al. 2001; Roman-Duval et al. 2010).

These two scaling relations hold over a wide range of MCs (Goldsmith & Langer 1978). This is interpreted, that

## 1.1.3

## MASSIVE STAR FORMATION AND STELLAR FEEDBACK

Massive stars ( $8 M_{\odot} < M \lesssim 120 M_{\odot}$ ) and the energy released by stellar feedback are essential for the ISM. Massive star formation takes place in MCs with masses around  $10^3 M_{\odot}$  or higher (McKee & Ostriker 2007). The mass distribution of stars where they are entering the main sequence<sup>3</sup> is reflected in the *initial mass function* (IMF). It was first described for stars between 0.1 and  $10 M_{\odot}$  by Salpeter (1955) with

$$\epsilon(M)\Delta M = \epsilon_0 \left( \frac{M}{M_{\odot}} \right)^{-2.35} \left( \frac{\Delta M}{M_{\odot}} \right) \quad (1.5)$$

where  $\epsilon(M)\Delta M$  is the number of stars with masses inside a mass range  $M$  to  $\Delta m$  and  $\epsilon_0$  the number of stars between 1 and  $2 M_{\odot}$ . Later, the IMF was updated such that multiple power-laws describe the turn-over to the lower mass regime (Chabrier 2001; Kroupa 2001; Chabrier 2003; Bastian et al. 2010). The IMF shows that the ISM is dominated by lower mass stars and the number of massive stars decreases with  $M^{-2.3}$  with an upper limit between 100-150  $M_{\odot}$  (Massey 2003). The formation time of a massive star is short, of the order of  $10^5$  yr. These stars are nearly always formed as part of a star cluster, rather than in isolation (Carpenter et al. 1997; Hartmann et al. 2001; Lada & Lada 2003).

The rate with which stars are forming is related to the amount of mass provided by MCs. On galactic scales, this relation is given by the *Schmidt-Kennicutt law*,

$$\Sigma_{\text{SFR}} \propto \Sigma_{\text{gas}}^{\alpha} \quad (1.6)$$

where  $\Sigma_{\text{SFR}}$  is the star formation surface density,  $\Sigma_{\text{gas}}$  the total gas surface density and the scaling index  $\alpha$ , which was initially found to be 1.4 (Schmidt 1959; Kennicutt 1998). Further investigations revealed that a linear relation can be obtained with the  $\text{H}_2$  surface density  $\Sigma_{\text{H}_2}$  but not with atomic gas (Bigiel et al. 2008; Schruba et al. 2011). From these results it was found that the star formation is inefficient with only a few percent of the gas being converted into stars (Evans et al. 2009; Murray et al. 2011). The gas depletion time<sup>4</sup> was found to be long around a few Gyr (Genzel et al. 2015).

Massive stars (O and B stars) are sources of kinetic, thermal, and radiative energy. The most energetic feedback processes are ionizing radiation and stellar winds during the stellar life time which ends in a core-collapse SN. Ionizing radiation becomes important early in the evolution of a massive star (Peters et al. 2010; De Pree et al. 2014). The embedding environment becomes photoionized and heated. HII regions expand with typical velocities of  $< 10 \text{ km s}^{-1}$ . Fig. 2 shows an HII region caused by a cluster of massive stars. The Trapezium cluster is located in the center, which drives a shock into the molecular part of Orion A (Meingast et al. 2016). The layer between the dense and ionized gas is a chemically complex region, which is called a *photo dissociation regions* (Röllig et al. 2007).

Stellar wind is gas that is driven from the surface of a massive star by radiation pressure (Kudritzki & Puls 2000; Vink 2011). Dependent on the luminosity and the metallicity of the star it can reach velocities of a few  $1000 \text{ km s}^{-1}$  and mass loss rates around  $10^{-6} M_{\odot} \text{ yr}^{-1}$  (Scuderi et al. 1998; Kudritzki & Puls 2000; Markova et al. 2004). The winds can be identified by modified spectral line profiles as the

<sup>3</sup>The main sequence in the Hertzsprung-Russell diagram includes stars that create their energy mainly by fusion of hydrogen.

<sup>4</sup>The depletion time is the time that is needed for star formation to use up the available mass.



emitted mass absorbs stellar radiation (P Cygni profile in the UV). Observationally, winds can be directly observed by X-ray emission and via bow-shocks in moving gas (Draine 2011b).

Finally massive stars end as core-collapse SNe which release  $\sim 10^{51}$  erg and 2 to 5  $M_{\odot}$  of gas with supersonic velocities between 6000 and 7000  $\text{km s}^{-1}$  (Weiler & Sramek 1988; Dwek & Arendt 1992; Janka et al. 2012). The SN type-II rate is observed to be  $\sim 1$  per century in the solar neighbourhood (McKee 1989; Adams et al. 2013). The SN shocks can directly be observed by X-ray and synchrotron emission and cooling by metal lines.

## 1.2

### PHYSICAL PROCESSES IN THE INTERSTELLAR MEDIUM

The thermodynamic state of the gas results from the balance of heating and cooling processes that directly influence gas excitation, ionization, composition and temperature. This affects the dynamics and sets the energy balance (Tielens 2005). The net rate of energy change per volume is defined as

$$\dot{u}_{\text{heat}} = n^2 \Lambda - n\Gamma \quad (1.7)$$

where  $n$  is the particle density,  $n^2 \Lambda$  the total cooling rate and  $n\Gamma$  the heating rate from all available processes. Thermal equilibrium, defined as  $\dot{u}_{\text{heat}} = 0$ , exists for a special set of parameters in pressure, temperature, and density space.

#### 1.2.1

##### HEATING PROCESSES

*Photoelectric heating* is the most important heating process in the diffuse ISM. Dust grains absorb UV photons; the residual energy above the ionization barrier of the dust is converted to kinetic energy which thermalizes the environment (Draine 1978). The heating rate depends on the size and charge distribution of the dust, i.e. negatively charged dust grains are stripped of electrons more easily. Photoelectric heating also depends on the strength of the incident UV field. Dust self-shielding, caused by high dust densities, reduce the UV photon flux and therefore the strength of the incident UV field. At visual extinctions with values above  $A_V > 1$  mag photoelectric heating decreases rapidly and the formation of  $\text{H}_2$  becomes possible (Klessen & Glover 2016).

*$\text{H}_2$  dissociation heating* and  *$\text{H}_2$  pumping* are the two processes where a UV photon interacts with  $\text{H}_2$  and leads to heating. During  $\text{H}_2$  dissociation two H atoms emerge which have higher kinetic energies compared to the mean kinetic energy within the ambient gas, thus leading to the heating of the environment. On average each  $\text{H}_2$  dissociation event provides 0.4 eV (Black & Dalgarno 1977) but the probability for this process is only  $\sim 15$  percent (Draine & Bertoldi 1996). The more frequent process is *UV pumping*, where the excited  $\text{H}_2$  loses energy by de-excitation, either radiating near-infrared photons in low density environments or through collisions with the ambient gas with  $n \gtrsim 1000 \text{ cm}^{-3}$ . The mean released energy per  $\text{H}_2$  pumping event is 2 eV (Draine 2011b; Klessen & Glover 2016).

*Photoionization heating*,  $\Gamma_{\text{ph}}$ , of hydrogen by UV photons with energies  $h\nu > 13.6 \text{ eV}$  is an important process in regions surrounding strong UV sources (massive stars



or star clusters). Through this process hydrogen gets ionized and the photon excess energy is transferred to kinetic energy which heats the vicinity of the star to  $T \sim 8000$  K.

*Cosmic ray heating* is the main heating process in dense gas, where radiation with a lower energy is already absorbed. Cosmic rays have an energy spectrum with a steep power law slope between -2 and -3, that makes the low-energy ( $\sim 100$  MeV) cosmic rays responsible for most of the ionization and heating. However, the densest parts of MCs seem to remain unaffected (Padovani et al. 2009). The primary ionization event releases kinetic energies around 10 – 20 eV, which is sufficient for consequent secondary ionizations (Dalgarno et al. 1999; Glassgold et al. 2012; Klessen & Glover 2016). *X-ray* heating occurs in a similar fashion but release less energy and affect lower column densities (Wolfire et al. 1995).

A variety of *chemical reactions* and *dynamical processes* contribute to the heating of the ISM. A very important chemical example is the recombination of H to the energetically favourable  $H_2$ . This process release 4.48 eV of binding energy. However, the efficiency to convert this energy into heat is uncertain (Congiu et al. 2009; Le Bourlot et al. 2012; Klessen & Glover 2016). Finally, dynamical processes heat the gas in the ISM e.g. adiabatic compression, turbulent dissipation, and shocks.

### 1.2.2

#### COOLING PROCESSES

*Radiative cooling* is an essential process in the ISM. To discuss radiative cooling the gas is separated by the optical depth  $\tau$  into optically thin and optically thick gas. In *optically thin* gas ( $\tau < 1$ ) with a static population, no incident radiation field and no self-emitted radiation is absorbed. The emission of photons from the gas are reduced to processes of collisional excitation, collisional de-excitation and spontaneous emission. An excited electron cascades to a lower energy level by either collisional de-excitation or by emitting a photon. The probability to remove energy by photon emission is given by the *critical density*,  $n_{\text{crit}}$ , which is proportional to the ratio between spontaneous emission and collisional de-excitation. The typical densities  $n$  for the corresponding electron transition in the ISM is below the critical density,  $n < n_{\text{crit}}$ , where de-excitation is dominated rather by emitting photons than collisionally. The cooling rate scales as  $n^2\Lambda$  and it depends on the number of emitters and the number of collisional partners in the gas. In case  $n_{\text{crit}} < n$ , the number of collisional partners is large and energy is preferentially redistributed by collisional de-excitation. In this case, energy is not removed by emitting photons and radiative cooling becomes inefficient with  $n\Lambda$ . The gas approaches the local thermal equilibrium. The excited states of the gas are set by the temperature of the gas rather than the collisional excitation rate. In the *optically thick* regime ( $\tau > 1$ ), emitted photons are immediately absorbed locally. The number of photons trapped by the atoms population increases. This lowers the critical density at which the thermal equilibrium is reached and prevents spontaneous emission. This introduction to radiative cooling is simplified as either chemical species with individual, multi-level systems or incident radiation is considered (Spitzer 1978; Rybicki & Lightman 2004; Klessen & Glover 2016).

*Cooling by permitted transitions*, i.e. cooling by free-free emission and metal line

emission cooling, is the prominent cooling within the typical ISM conditions. The cooling rates can be calculated assuming an equilibrium between collisional ionization and radiative recombination. The dependence of the cooling rates reduces to temperature and metallicity. The cooling curve above  $T > 3 \times 10^4$  K has a double peaked maximum at  $10^5$  K with metal line cooling from carbon (C) and oxygen (O). Between  $10^6$  K and  $10^7$  K iron (Fe) is the main coolant. At even higher temperatures, even Fe becomes fully ionized and free-free bremsstrahlung from hydrogen electrons and protons becomes increasingly important (Sutherland et al. 1993; Gnat & Ferland 2012).

*Fine structure lines* from atomic hydrogen, (mainly) Lyman- $\alpha$  emission is the main coolant around  $T \sim 10^4$  K. As the temperature drops the fine-structure line emission from  $C^+$  and O dominates where the latter becomes negligible in the temperature range below 1000 K. The dominant cooling comes from atomic carbon in cold, dust shielded regions and from the rotational transitions of CO in MCs (Glover & Mac Low 2007b,a; Glover et al. 2010).

### 1.2.3

#### A MULTIPHASE DESCRIPTION OF THE INTERSTELLAR MEDIUM

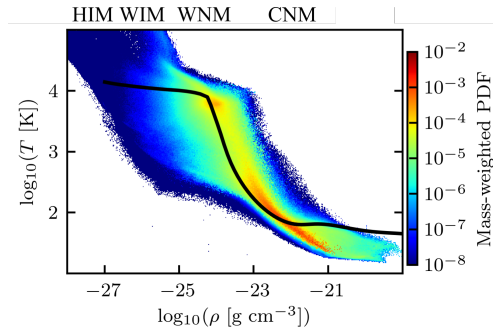


Figure 3: Mass-weighted density pressure distribution of a stratified disc simulation taken from simulation in *Paper II*. The black line shows the thermal equilibrium curve with a constant column density of  $10^{21} \text{ cm}^{-2}$ . The phases of the ISM are indicated at the top.

$n \sim 50 \text{ cm}^{-3}$ ). The coexistence of two atomic phases in pressure equilibrium in the ISM was demonstrated by Field et al. (1969) and later extended by McKee & Ostriker (1977) with a third, additional phase, the *hot ionized medium* (HIM,  $T \sim 10^6$  K,  $n \sim 10^{-3} \text{ cm}^{-3}$ ) which originates from SN explosions. Not part of the classical phases is the *warm ionized gas* (WIM,  $T \sim 8000$  K,  $n \sim 0.1 \text{ cm}^{-3}$ ) which appear in HII bubbles due to ionizing radiation. The cooling time  $t_{\text{cool}}$  of these phases is given with

$$t_{\text{cool}} = \frac{nk_B T}{n^2 \Lambda}. \quad (1.8)$$

Fig. 3 shows the mass-weighted gas distribution from a simulation of a SN-driven, multiphase ISM in part of the galactic disk from *Paper I*. It relates the density  $\rho$  with the pressure over the Boltzmann's constant  $P/k_B$  for each cell in the computational domain. The theoretical thermal equilibrium is evaluated with Eq. 1.7 assuming the aforementioned heating and cooling processes and is shown as black solid line (assuming a constant column density). The gas above this line is dominated by heating, the gas below by cooling. The density range between  $\sim 3 \times 10^{-24}$  and  $\sim 3 \times 10^{-22} \text{ g cm}^{-3}$  is called the thermally unstable regime, where gas is prone to heating into the *warm neutral medium* (WNM,  $T \sim 8000$  K,  $n \sim 0.1 \text{ cm}^{-3}$ ) or cooling to the *cold neutral medium* (CNM,  $T \sim 50$  K,

## 1.3

## STELLAR FEEDBACK PROCESSES

Stellar feedback processes are all interactions of stars with the ISM. This includes protostellar jets, stellar winds, ionizing radiation, radiation pressure, and SNe. The importance of the individual process can be measured by its impact on the ISM. This includes the ability to move gas by momentum as well as to increase the thermal energy. Hence, stellar feedback processes are distinguishable as momentum-driven and energy-driven. Cooling in the ISM is very efficient at low temperatures but this efficiency drops at higher temperatures and lower densities. The larger the cooling time  $t_{\text{cool}}$  over the crossing time  $t_{\text{cross}}$  ratio<sup>5</sup>, the more energy conserving the feedback process is. A longer cooling time also increases the energy sustainability. If the cooling time is shorter, energy is lost and momentum drives the expansion (Krumholz 2015). The following section will discuss a selection of feedback processes which is especially important in this work.

## 1.3.1

## STELLAR WIND

Massive stars emit stellar winds. The typical mass loss rate and wind velocity for massive stars are of the order of  $1 M_{\odot} \text{ Myr}^{-1}$  and a few  $1000 \text{ km s}^{-1}$ , respectively. However, the most massive stars ( $60 M_{\odot}$  and more) can easily exceed these values. The resulting cumulative wind luminosity over the lifetime of a star is of the order of  $10^{51} \text{ erg}$ , which is equivalent to the energy released in a SN explosion (Puls et al. 1996; Naab & Ostriker 2017). The highly supersonic wind creates a primary shock as it expands into the ISM, where it decelerates. The primary shock front is slower than the wind gas that follows. The gas in the primary shock is overtaken and heated to temperatures around  $10^6 \text{ K}$ . A secondary, outer shock establishes which can travel up to some 100 pc (Castor et al. 1975; Weaver et al. 1977; Kudritzki & Puls 2000).

The importance of stellar winds is highly discussed (Matzner 2002; Krumholz 2015; Naab & Ostriker 2017). In numerical simulations of structured clouds the impact of stellar winds is modest (Freyer et al. 2003, 2006; Dale et al. 2014; Geen et al. 2015b). The coupling to the dense, molecular gas is weak and the wind will rather leak out of the clouds through low density channels (Pittard 2013; Wareing et al. 2017). Nevertheless, stellar wind acts on dense gas and is more efficient to remove it compared to ionizing radiation (Rogers & Pittard 2013). At galactic scales, cosmological simulations suggest that winds are negligible (Hopkins et al. 2014). However, Gatto et al. (2015) indicate that stellar winds are a strong regulator for the star formation rate, as they prevent gas accretion on stars and reduce Jeans-unstable gas at larger scales (Gatto et al. 2017).

## 1.3.2

## IONIZING RADIATION

Ionizing radiation is the most energetic feedback process. A massive star emits up to a few  $10^{49}$  Lyman continuum photons per second. Integrated over the lifetime of the star  $10^{53} \text{ erg}$  are released into the ISM. Initially, the surroundings of the star are ionized to the *Strömgren radius*, which is determined by the equilibrium of ion-

<sup>5</sup>The crossing time is the time that a signal with a specific velocity needs to cross a distance.

izations and recombinations. Ionization heating increases the pressure inside this HII region and a shock with a few  $10 \text{ km s}^{-1}$  travels into the medium up to radii of 100 pc (Strömgren 1939; Spitzer 1978; Hosokawa & Inutsuka 2006). As previously mentioned, the energy of the ionizing photons is primarily used to sustain ionization. The byproduct is ionization heating from the excess energy of the Lyman continuum photons. Therefore, the impact on larger scales is limited (Walch et al. 2012; Klessen & Glover 2016). But the local impact of ionizing radiation on the ISM is significant as the radiative shock disperses intermediate dense gas and is able to trigger star formation within the gas swept-up by the shock front (Dale et al. 2012; Walch et al. 2012, 2013; Dale et al. 2014). However, it is unclear how much of the radiative energy is converted into momentum. If the efficiency is high then the radiative contribution to turbulence is non-negligible (Murray et al. 2005, 2010, 2011; Agertz & Kravtsov 2015; Geen et al. 2015b). Nevertheless, dense regions are typically more compressed than dispersed, but this is dependent on the time scale and the mass of the cloud (Krumholz 2006; Walch et al. 2012). In general, ionizing radiation lowers the ISM density for the SNe which are shown to increase the momentum input by up to 50 percent (Walch et al. 2015).

Additional momentum originates from the absorption of photons in the UV on gas and dust grains. This radiation pressure is suggested to be a minor by-product of ionizing radiation at the typical densities in the ISM (Arthur et al. 2004; Krumholz & Matzner 2009; Sales et al. 2014) but might contribute to turbulent driving in dense molecular clouds (Gritschneider et al. 2009).

### 1.3.3

#### SUPERNOVAE

The explosion of a massive star as a core-collapse SN is the singular and final event of its life. A SN explosion releases  $10^{51}$  erg of energy, which causes a highly supersonic shock to expand into the ISM. The SN remnant distributes metals and is a major source of X-rays and cosmic rays. The ambient medium is heated to temperatures above  $10^6$  K, which is essentially the third phase of the ISM (see Section 1.2.3). SNe explosions create hot gas as well as imparting momentum into the gas during a multi staged evolution. Initially the SN ejecta, with masses between  $2\text{--}5 M_{\odot}$ , expands freely. When the swept-up mass becomes equal to the ejecta mass the Sedov-Taylor phase begins. A thin shock is adiabatically driven into the ambient medium. Most of the radial momentum is imparted in this part of the SN evolution. The swept-up gas accumulates in the shock and cooling processes become increasingly important. During the pressure-driven snowplough phase the blast wave slows down and the interior density is reduced. When the interior and ambient pressure become similar the last phase (momentum-driven snowplough phase) starts in which the shell is moving only by the previously gained momentum (McKee & Ostriker 1977; Cioffi et al. 1988; Ostriker & McKee 1988; Petruk 2006; Li et al. 2015).

Numerical simulations show that the positioning of SNe is crucial to the evolution of the ISM. In the extreme case of all SNe exploding in the hot, diffuse phase, the SN remnants interact without significantly cooling. A single stable hot phase fills almost the entire volume with small, extremely dense clumps that contain most of the mass. This system is described as thermal runaway (Gatto et al. 2015; Li et al. 2015; Girichidis et al. 2016b). In contrast, when all SNe are located in density peaks the SN remnant suffers from significant radiative losses and the HIM does not de-

velop. The adiabatic phase is interrupted early and the momentum injection is diminished (Gatto et al. 2015; Girichidis et al. 2016a). Hence, a two phase medium develops and the scale height of the ISM is set by the turbulent pressure (Draine 2011b; Kim et al. 2011; Ostriker & Shetty 2011; Shetty & Ostriker 2012; Kim et al. 2013; Kim & Ostriker 2015). Based on the idea of runaway stars (Gies & Bolton 1986), a mix of 50 percent SNe in density peaks and 50 percent at rather random locations gives a bimodal density distribution with a stable hot phase and dense cold clouds. In this model, gas expands into the galactic halo and galactic outflows are driven (de Avillez 2000; Girichidis et al. 2016a).

Single SNe events destroy MCs (Iffrig & Hennebelle 2015; Gatto et al. 2015; Walch et al. 2015), locally suppress star formation but create new MCs, which in turn could spawn new stars and star clusters (Elmegreen & Lada 1977; Wünsch et al. 2011; Ngoumou et al. 2015). Multiple SNe appear to maintain the observed level of turbulence in the ISM (Elmegreen & Scalo 2004; Scalo & Elmegreen 2004; Mac Low et al. 2004; Padoan et al. 2016), reproduce the HIM (McKee & Ostriker 1977; de Avillez & Breitschwerdt 2007), regulate scale heights (Ostriker & Shetty 2011; Kim & Ostriker 2015), and drive galactic out- and fountain flows (Shapiro & Field 1976; Chevalier & Clegg 1985; Girichidis et al. 2016b).

#### 1.3.4

##### SUPERSONIC TURBULENCE

Turbulence describes a fluid being highly irregular. The turbulent properties are indicated by the Reynold number  $Re$ ,

$$Re \approx \frac{vL}{\nu} \quad (1.9)$$

where  $v$  is the velocity of the fluid with the characteristic length scale  $L$  and  $\nu$  the kinematic viscosity of the fluid. Turbulent motions with a large  $Re$  are almost dissipationless, whereas energy is dissipated at  $Re \sim 1$ .

In a subsonic, incompressible, isotropic turbulent fluid, the power spectrum shows hierarchical behaviour with an energy cascade from large to small scales. At large scale, energy is fed into the fluid, e.g. by a SN shock and the energy in these eddies is dissipationless. Eddies break up, the energy cascades until the dissipation range with  $Re \sim 1$  is reached and energy is lost. A direct energy transfer from the largest to the smallest scales is not possible in incompressible flows<sup>6</sup>. The resulting power spectrum  $E(k)$  has a scale  $k$  dependence with the Kolmogorov exponent,  $E(k) \propto k^{-5/3}$ . The velocity dispersion  $\sigma$  of this fluid is proportional to the characteristic size,  $\sigma \propto L^{1/3}$ . The resulting turbulent heating is  $\gamma_{\text{turb}} \propto \sigma^3 L^{-1}$  with gives rates between  $10^{-30} \text{ erg cm}^{-3} \text{ s}^{-1}$  and  $10^{-28} \text{ erg cm}^{-3} \text{ s}^{-1}$  in the WNM and in prototypical MCs, respectively (Pan & Padoan 2009).

However, the turbulence in the ISM is rather supersonic which implies the formation of shocks. These are the main sources of energy loss and create a power spectrum with an exponent of -2. The turbulent density field of an isothermal medium is well described by a log-normal distribution with a dispersion, which has to be determined by numerical simulations (Federrath et al. 2008, 2010; Padoan &

<sup>6</sup>On the contrary, in compressible flows, shocks introduce dissipation over an arbitrary number of scales.

(Nordlund 2011; Federrath & Klessen 2012; Molina et al. 2012) to be

$$\sigma^2 \sim \ln \left( 1 + b^2 M^2 \frac{\beta}{\beta + 1} \right) \quad (1.10)$$

where  $M$  is the Mach number and  $\beta$  the ratio between the thermal and magnetic pressure.  $b$  is the forcing parameter which varies depending on the mixing ratio between the two extreme driving modes, solenoidal (divergence-free,  $b = 1/3$ ) or compressive (curl-free,  $b = 1$ ).

The importance of turbulence in the ISM is based on observational evidence. During the gravitational collapse of a MC with only thermal support stars would form within a free-fall time,

$$t_{\text{ff}} = \left( \frac{3\pi}{32G\rho} \right)^{0.5} \quad (1.11)$$

where  $G$  is the gravitational constant. This rapid star formation is not observed (Kennicutt & Evans 2012). Turbulence is believed to act as an addition process supporting the cloud against its collapse (Elmegreen & Scalo 2004). However, the turbulent energy is dissipated on a time-scale that is argued to be comparable to the turbulent crossing time (Mac Low 1999; Elmegreen 2000)

$$t_{\text{d}} \sim \frac{L}{\sigma}. \quad (1.12)$$

This means that external or internal driving mechanism have to continuously inject energy to support the cloud. External mechanism are external SNe (Walch & Naab 2015; Padoan et al. 2016), tidal forces, colliding flows (Vázquez-Semadeni et al. 2006; Ballesteros-Paredes et al. 2009a), accretion flows (Klessen et al. 2000; Goldbaum et al. 2011; Heitsch 2013), and the collapse of the cloud (Ibáñez-Mejía et al. 2017). Ionizing radiation (Walch et al. 2012; Dale et al. 2014), stellar winds, and embedded SNe (Gatto et al. 2015; Iffrig & Hennebelle 2015) are suggested as internal driving mechanisms. However, the importance of these processes is unclear and highly debated.



## 2

## METHODOLOGY

---

The methodology of this thesis are numerical simulations which are based on the equations of magneto-hydrodynamics (MHD). In this chapter, the basic set of MHD equations is introduced. To treat shocks, a simplified one-dimensional hydrodynamic description is discussed. The last part introduces the adaptive-mesh refinement (AMR), MHD code FLASH 4. As general literature, the following are recommended [Landau & Lifshits \(1959\)](#), [Shu \(1992\)](#), and [Krumholz \(2015\)](#).

### 2.1

#### MAGNETO-HYDRODYNAMICS

The straightforward way to describe the properties of a gas is to use Newton's equations and calculate for each particle the individual trajectory, momentum and energy. With some statistics, the average state of the gas is evaluated. Unfortunately, this approach quickly becomes unaffordable as the number of gas particles increases.

A more economical way to obtain informations about a gas is to see the individual gas particles as one ensemble. Under the assumption of a local thermal equilibrium and that the free-mean path is smaller than the characteristic length of interest, a parcel of gas can be described as a fluid by its averaged properties velocity  $\mathbf{v}$ , temperature  $T$  and magnetic field  $\mathbf{B}$ . Variables in bold face denote vectors. The ideal MHD equations are given as

$$\frac{\partial \rho}{\partial t} + \nabla \cdot (\rho \mathbf{v}) = 0 \quad (2.1)$$

$$\frac{\partial \rho \mathbf{v}}{\partial t} + \nabla \cdot \left[ \rho \mathbf{v} \mathbf{v}^T + \left( P + \frac{B^2}{8\pi} \right) \mathbf{I} - \frac{\mathbf{B} \mathbf{B}^T}{4\pi} \right] - \rho \mathbf{g} - \dot{q}_{\text{inj}} = 0 \quad (2.2)$$

$$\frac{\partial \epsilon}{\partial t} + \nabla \cdot \left[ (\epsilon + P) \mathbf{v} - \frac{(\mathbf{B} \cdot \mathbf{v}) \mathbf{B}}{4\pi} \right] - \rho \mathbf{v} \mathbf{g} - \dot{u}_{\text{heat}} - \dot{u}_{\text{inj}} = 0 \quad (2.3)$$

$$\frac{\partial \mathbf{B}}{\partial t} - \nabla \times (\mathbf{v} \times \mathbf{B}) = 0 \quad (2.4)$$

where these four equations express the conservation of mass, momentum, energy, and magnetic flux (from top to bottom). Here,  $t$  is the time,  $\rho$  is the volume density,  $P$  is the thermal pressure,  $\epsilon$  is the total energy,  $u$  is the internal energy,  $\dot{q}_{\text{inj}}$  and  $\dot{u}_{\text{inj}}$  are the momentum and internal energy injected by external processes,  $\dot{u}_{\text{heat}}$  is the net internal energy rate due to heating/cooling (see Eq. 3), and  $\mathbf{g}$  is the gravitational acceleration. All energy rates are given per volume.  $\mathbf{I}$  is the identity matrix,  $\mathbf{B} \mathbf{B}^T$  and  $\mathbf{v} \mathbf{v}^T$  are the outer products of the magnetic and velocity field, respectively.

The magnetic field is constrained to be divergence free by

$$\nabla \cdot \mathbf{B} = 0 \quad (2.5)$$

The pressure  $P$  and the total energy  $\epsilon$  are given by

$$P = (\gamma - 1) u, \quad (2.6)$$

$$\epsilon = u + \frac{\rho v^2}{2} + \frac{B^2}{8\pi}, \quad (2.7)$$

where  $\gamma$  is the adiabatic index.

The gravitational acceleration,  $\mathbf{g} = -\nabla\Phi$ , can be obtained by the Poisson's equation,

$$\nabla^2\Phi = 4\pi G\rho \quad (2.8)$$

where  $\Phi$  is the gravitational potential and  $G$  the gravitational constant. In numerical schemes,  $\mathbf{g}$  can have contribution from gas self-gravity  $\mathbf{g}_{\text{sg}}$  and from point sources  $\mathbf{g}_{\text{si}}$ , e.g. stars.

## 2.2

### ONE-DIMENSIONAL SHOCK DESCRIPTION

The basic MHD equations are based on the assumption that the mean free path of the fluid is smaller than the characteristic length scale. A discontinuity is thin and the characteristic length scale approaches zero, thus the assumption is violated. The shown MHD equations are capable to treat shocks. However, it is possible to derive the relations between the thermodynamic properties in the ambient medium (subscript 0) and the post-shock gas (subscript 1). These two regions are separated by the shock interface. The following considerations are made in the inertial frame of the discontinuity.

The set of one-dimensional hydrodynamic equations without gravitational forces and magnetic fields is

$$\rho_0 v_0 = \rho_1 v_1 \quad (2.9)$$

$$\rho_0 v_0^2 + P_0 = \rho_1 v_1^2 + P_1 \quad (2.10)$$

$$\epsilon_0 + P_0 = \epsilon_1 + P_1 \quad (2.11)$$

with the equation of mass conservation, momentum conservation, and energy conservation (from top to bottom). Mass can flow not only across the interface but also parallel to it. The corresponding equation for velocities parallel  $v_{\parallel}$  to the discontinuity is

$$\rho_0 v_0 v_{\parallel,0} = \rho_1 v_1 v_{\parallel,1}. \quad (2.12)$$

In case of zero velocities,  $v_0 = v_1 = 0$ , the pressure difference across the interface is  $P_0 - P_1 = 0$ . This discontinuity is termed *contact discontinuity* as fluids are not exchanged. The flow along the discontinuity becomes generally unstable in case of non-zero, parallel velocities,  $v_{\parallel,0} \neq v_{\parallel,1} \neq 0$ .

In case of non-zero velocities a *shock* evolves with  $v_0 > v_1$  and  $v_{\parallel,0} = v_{\parallel,1}$ . The pressure difference is given with

$$P_1 - P_0 = \rho_0 v_0 (v_0 - v_1) \quad (2.13)$$

where  $P_1 > P_0$ . The *Rankine-Hugoniot jump conditions* describe the ratios of the pressures, densities and temperature between the ambient medium and the post-



shock gas. For a plan parallel shock, the conditions are

$$\frac{P_1}{P_0} = 1 + \frac{2\gamma}{\gamma+1}(M_0^2 - 1) \quad (2.14)$$

$$\frac{\rho_1}{\rho_0} = \frac{(\gamma+1)M^2}{(\gamma-1)M^2 + 2} = \frac{v_0}{v_1} \quad (2.15)$$

$$\frac{T_1}{T_0} = 1 + \frac{2(\gamma-1)}{(\gamma+1)^2} \frac{(\gamma M^2 + 1)(M^2 - 1)}{M^2} \quad (2.16)$$

with the Mach number in the ambient medium  $M \equiv v/c$  and  $c$  being the sound speed  $c = (\gamma P/\rho)^{1/2}$ . The Mach number is also equivalent to the ratio of the ram pressure to the thermal pressure with

$$M = \left( \frac{\rho v^2}{\gamma P} \right)^{1/2}. \quad (2.17)$$

For a monoatomic gas the compression factor is  $(\gamma+1)/(\gamma-1) = 4$ . In case of a strong shock,  $M \gg 1$ ,  $\rho_1/\rho_0 = v_0/v_1 \sim 4$ . This shows that the gas enters the interface supersonically and leaves subsonically. The infalling gas is compressed. The mean free path becomes comparable to the characteristic length and as a consequence viscous processes become important. A significant part of the kinetic energy is dissipated into heat.

## 2.3

### FLASH 4

This section gives a short overview of the FLASH 4 code, developed by the FLASH Center for Computational Science of the University of Chicago<sup>1</sup>. FLASH is a three-dimensional, adaptive mesh refinement (AMR), magento-hydrodynamic code. It has a multi-modular architecture and is parallelized by domain decomposition (Fryxell et al. 2000; Dubey et al. 2008). A variety of solvers are provided but in this thesis the directionally split, five-wave Bouchut MHD solver HLL5R is used (Bouchut et al. 2007; Waagan 2009; Bouchut et al. 2010; Waagan et al. 2011). The most important physical modules for this work are shortly described in the following and in the numeric sections of *Paper I* and *Paper II*.

The *gravity* module calculates the gravitational acceleration  $\mathbf{g}$  caused by gas self-gravity  $\mathbf{g}_{\text{sg}}$ , an external potential  $\mathbf{g}_{\text{pot}}$ , and the interaction of point sources  $\mathbf{g}_{\text{si}}$ , i.e. stars and star clusters. For self-gravity  $\mathbf{g}_{\text{sg}}$  the Poisson equation (Eq. 2.8) is solved by a tree-based algorithm, based on a Barnes-Hut type octal-spatial tree (Barnes & Hut 1986; Wünsch et al. 2018). If needed, an external potential  $\mathbf{g}_{\text{pot}}$  can be included. In the case of galactic disc simulations, the gravitational potential of the old stellar component is included as an isothermal sheet with a certain stellar surface density and scale height (Spitzer 1942). Contributions from dark matter are neglected. The interaction of point sources and the gas is calculated using

$$\mathbf{g}_{\text{si}} = - \sum_{i=0}^N \frac{GM_i}{\mathbf{r}_i^3} \quad (2.18)$$

<sup>1</sup><http://flash.uchicago.edu/site/>

where  $i$  is the index of stars or star clusters,  $N$  is the total number of stars or star clusters,  $M_i$  are their masses and  $r_i$  the distance between the cell and the particle. The total gravitational acceleration is  $\mathbf{g} = \mathbf{g}_{\text{sg}} + \mathbf{g}_{\text{si}} + \mathbf{g}_{\text{pot}}$ .

*Sink particles* describe the unresolved collapse of gas and the formation of stars or star clusters. The public release of FLASH includes a generic sink particle module (Federrath et al. 2010). The conditions to create sink particles are i) ambient densities over a user-defined density threshold, ii) all cells within the accretion radius have to be on the highest level of refinement, iii) the gas inside the accretion radius has to be a converging flow, iv) the gas is Jeans unstable, v) the gas is gravitationally bound, and vi) the central cell has to be in a gravitational potential minimum (Truelove et al. 1997; Walch et al. 2015). The sink particles accrete gas and convert a fraction into massive stars. Therefore, every  $120 M_{\odot}$  of accreted gas a new massive star between 9 and  $120 M_{\odot}$  is randomly sampled from the standard IMF (Salpeter 1955). The residual mass is converted into low-mass stars.

Within the *feedback sink* module the internal population of massive stars is coupled to a stellar evolution model to treat stellar feedback processes. Each massive star individually follows the Geneva stellar tracks from the zero-age main sequence to the Wolf-Rayet phase. An initial proto-stellar phase is not included (Puls et al. 2008; Ekström et al. 2012; Gatto et al. 2017; Peters et al. 2017). The feedback sink module treats the energy input from stellar wind and SNe. It provides the information about the emitted ionizing radiation to the radiative transfer module.

TREERAY calculates the transfer of ionizing radiation (Wünsch et al., in prep.). It is an extension of the FLASH tree-solver described in (Wünsch et al. 2018). The one-dimensional radiative transfer equation is solved along discrete directions (Górski et al. 2005) assuming a temperature dependent absorptions coefficient  $\alpha_B$ , an emission coefficient proportional to the number of emitted Lyman continuum photons, and the On-the-Spot approximation. For more details on the algorithm see Bisbas et al. (2015), Wünsch et al., (in prep), and *Paper II*.

The aforementioned stellar tracks provide the number of Lyman continuum photons  $\dot{N}_{\text{Lyc}}$  and the effective stellar temperature (Peters et al. 2017). In TREERAY this information is processed to get the average photon energy  $E_{\bar{\nu}-\nu_T}$  above the hydrogen ionization threshold  $\nu_T$  assuming a stellar black-body spectrum. The heating rate  $\Gamma_{\text{ph}}$  is calculated in ionization-recombination equilibrium with (Rybicki & Lightman 2004; Tielens 2005),

$$\Gamma_{\text{ph}} = F_{\text{ph}} \sigma E_{\bar{\nu}-\nu_T} = n_{\text{H}}^2 \alpha_{\text{B}} h (\bar{\nu} - \nu_T) \quad (2.19)$$

where  $\sigma$  is the hydrogen photoionization cross-section,  $n_{\text{H}}$  the hydrogen number density,  $F_{\text{ph}}$  the photon flux, and  $E_{\bar{\nu}-\nu_T} = h(\bar{\nu} - \nu_T)$  is the average energy per photon between  $\nu_T = 13.6 \text{ eV}$  and the average photon frequency  $\bar{\nu}$ . The ionization heating rate and number of ionizing photons are provided to the CHEMISTRY module, where the temperature is self-consistently increased by balancing heating and cooling processes and the mean hydrogen ionization state is updated using the given photoionization rate (see *Paper I*).

A simple *chemical network* is included which is explained in detail in Walch et al. (2015). It is based on Glover & Mac Low (2007a), Glover & Mac Low (2007b), Glover et al. (2010), and Nelson & Langer (1997) to follow the abundances of seven chem-

ical species: molecular, atomic and ionized hydrogen as well as carbon monoxide, ionized carbon, atomic oxygen and free electrons ( $\text{H}_2$ ,  $\text{H}$ ,  $\text{H}^+$ ,  $\text{CO}$ ,  $\text{C}^+$ ,  $\text{O}$ ,  $\text{e}^-$ ). The gas has solar metallicity (Sembach et al. 2000) with fixed elemental abundances of carbon, oxygen and silicon ( $x_{\text{C}} = 1.14 \times 10^{-4}$ ,  $x_{\text{O}} = 3.16 \times 10^{-4}$ ,  $x_{\text{Si}} = 1.5 \times 10^{-5}$ ) and the dust-to-gas mass ratio is set to 0.01. It includes an ISRF of homogeneous strength  $G_0 = 1.7$  (Habing 1968; Draine 1978). The ISRF is attenuated in shielded regions depending on the column densities of total gas,  $\text{H}_2$ , and  $\text{CO}$ . Thus, dust shielding and molecular (self-)shielding for  $\text{H}_2$  and  $\text{CO}$  (Glover et al. 2010) is considered by calculating the shielding coefficients with the TREE-RAY OPTICAL-DEPTH module, described and tested in Wünsch et al. (2018).

The gas with temperatures above  $\sim 10^4$  K is modelled with cooling rates according to Gnat & Ferland (2012) in collisional ionization equilibrium. Non-equilibrium cooling for the respective species is applied at lower temperatures (also for Lyman  $\alpha$ ). Within the  $\text{H II}$  region, both  $\text{C}^+$  and  $\text{O}$  cooling are neglected because these species are predominantly in a higher ionization state. Heating rates include the photoelectric effect, cosmic rays ionization with a rate of  $\zeta = 3 \times 10^{-17} \text{ s}^{-1}$ , X-ray ionization by Wolfire et al. (1995), and photoionization heating.

## THE RESEARCH

---

The importance of stellar feedback from massive stars is highly debated. On MC scales, the star formation efficiency is low with on average a few percent of gas that is finally converted into stars (Zuckerman & Evans 1974; Evans et al. 2009; Murray 2011). If not all the gas mass is converted into stellar mass, a mechanism is needed to counteract accretion. It is generally assumed that some physical processes, internal or external, cause supersonic turbulence which supports the clouds against gravitational collapse, and hence, halts the formation of stars (Mac Low & Klessen 2004; Mac Low et al. 2004). Possible external processes are SNe (Walch et al. 2015; Padoan et al. 2016), colliding flows (Vázquez-Semadeni et al. 2006; Ballesteros-Paredes et al. 2009b), accretion flows (Goldbaum et al. 2011; Heitsch 2013), the collapse of the cloud (Ibáñez-Mejía et al. 2017), and on Galactic scale shear flows around spiral arms (Dobbs & Pringle 2013). Ionizing radiation (Walch et al. 2012; Dale et al. 2014), stellar wind, and embedded SNe (Gatto et al. 2015; Iffrig & Hennebelle 2015; Geen et al. 2015b) are internal drivers of turbulence.

The impact of stellar feedback is dispersing by nature. It changes the density structures within star forming regions, interrupts gas accretion locally, might disperse the cloud (Whitworth 1979; Krumholz 2006; Krumholz et al. 2009; Walch et al. 2012; Dale 2015) and triggers star formation in redistributed gas (Elmegreen & Lada 1977; Gritschneder et al. 2009; Walch et al. 2013). However, the impact of feedback and the underlying physical processes are not well understood (Ostriker et al. 2010; Dobbs et al. 2014; Hopkins et al. 2014; Krumholz 2014; Naab & Ostriker 2017). If the feedback processes are simply ranked by the net energy emitted by a massive star, the importance of the processes increases from stellar winds (over the life time of 23  $M_{\odot}$  star,  $E_{\text{src}} \sim 10^{50}$  erg) to SNe ( $E_{\text{src}} \sim 10^{51}$  erg) and to ionizing radiation ( $E_{\text{src}} \sim 10^{53}$  erg). However, the efficiency to couple this energy to the ambient medium is the crux. A simple homogeneous model can be used to study individual scientific questions. In any way, it captures the complexity of the structures in MCs with the wide range of environmental properties. Studies show that MCs are not isolated but are highly linked to the galactic environment (Brunt et al. 2009; Hughes et al. 2013; Colombo et al. 2014; Rey-Raposo et al. 2017; Seifried et al. 2017).

To understand how different feedback mechanisms disperse clouds, recent simulations use isolated turbulent clouds (Dale et al. 2005; Walch et al. 2012; Dale et al. 2012; Geen et al. 2015b,a; Howard et al. 2017). The typical structures are dense and cold. In these simulations the natal MC masses range from a few  $10^3$  to some  $10^5 M_{\odot}$  (Dale et al. 2012, 2014; Geen et al. 2015b,a). Mass-rich clouds are almost unaffected by ionizing radiation. Stellar winds show no importance whenever gravity is strong and the structures are dense. However, low-mass clouds get dispersed by ionizing radiation (Walch et al. 2012) and stellar winds are able to ablate dense material and even drive dense gas out of the clouds through low density channels (Rogers & Pittard 2013; Wareing et al. 2017).

SNe mark the end a massive star's life. The powerful impact affects the ISM up to larger, galactic scales (de Avillez & Breitschwerdt 2004; Joung & Mac Low

2006; Kim et al. 2013, *Paper III*). Locally, SNe disperse MCs (Mac Low et al. 2004; Dib et al. 2006; Gent et al. 2013) by using low density channels carved by stellar winds and ionizing radiation (Pittard 2013; Wareing et al. 2017). Spatially and temporally correlated SNe might interact to form super-bubbles filled with hot gas (McCray & Kafatos 1987; Mac Low & McCray 1988; Tenorio-Tagle & Bodenheimer 1988; Sharma et al. 2014). SNe are possible candidates to drive galactic outflows and galactic winds (Larson 1974; Mac Low 1999; Ostriker et al. 2010; Dalla Vecchia & Schaye 2012; Hill et al. 2012; Girichidis et al. 2016b; Naab & Ostriker 2017). All these works show that the importance of the environmental properties to determining the SN impact.

This thesis aims for a better understanding of the impact of stellar feedback from massive stars in the ISM. The three aforementioned processes, stellar winds, ionizing radiation, and SNe, are discussed in detail. The initial environments are homogeneous, have a turbulent density distribution, or are self-consistently evolved MC. Within these media, the three feedback mechanisms and their impacts are analysed both individually and in combination with one another. The main goals of this thesis are, therefore, to investigate the relative impact of the aforementioned processes, to understand the dependency of feedback on the properties of the ambient medium, and how this dependency can be applied to produce more realistic ISM simulations. Three scientific publications are the core of this thesis. The order is not chronological but follows the evolution of massive stars: stellar winds and ionizing radiations are followed by the final SN explosion. In the following, the three publications are shortly introduced. The full articles are provided in Chapter 4, 5, and 6. In the final Chapter 7, the results are shortly discussed.

*Paper I - The relative impact of photoionizing radiation and stellar winds on different environments* (Haid et al., MNRAS, 478, 2018)

The focus of this paper is to understand the individual and combined impact of stellar winds and ionizing radiation in different homogeneous media. The core aspect is the efficiency with which the provided net stellar energy is coupled to the environment. By determining the feedback-specific cooling processes a media dependence is revealed and the relative impact obtained. For this purpose, a series of hydrodynamical simulations are performed with the FLASH code. It includes the novel radiative transfer scheme TREERAY which treats ionizing radiation in the Lyman continuum. It is coupled to a chemical network to self-consistently calculate the corresponding ionization heating by using the On-the-Spot approximation with a temperature-dependent recombination coefficient. The ambient media have initial conditions with properties of the WIM and CNM. As sources, massive stars with masses between 12 and 60  $M_{\odot}$  are selected. The main results are shown in Fig. 4.

*Paper II - SILCC-Zoom: The early impact of ionizing radiation on forming molecular clouds* (Haid et al., MNRAS, 482, 2019)

In this paper, the impact of ionizing radiation feedback on MC evolutions is investigated. Two clouds which form self-consistently out of the multi-phase, SN-driven ISM are selected and their evolutions are followed for three Myrs. Each cloud is discussed regarding the morphological changes and the star formation efficiency. To perform this study the FLASH code including TREERAY was used. The zoom-in technique is applied to spatially resolve the clouds down to 0.122 pc. The radiative

feedback is coupled to sink particles. Two simulations are performed where one without feedback is used as a reference for the radiative feedback run. The main results are shown in Fig. 5.

*Paper III - Supernova blast waves in wind-blown bubbles, turbulent, and power-law ambient media* (Haid et al., MNRAS, 460, 2016)

In this paper, the media-dependence of the impact of SN remnants is investigated. For this purpose a simple and fast one-dimensional shock code is developed. As in previous studies the adiabatic Sedov-Taylor phase is included but the SN evolution is extended with radiative cooling processes to also follow the pressure-driven snowplough phase until the momentum conserving phase is reached. In homogeneous media, this model reproduces the results from analytic estimates and numerical simulations. It is applied to media, which are preshaped by stellar winds and ionizing radiation. Taking this into account, the blast wave expands into a low-density bubble which is surrounded by a dense shock shell. Finally, the one-dimensional, radial behaviour of the model is utilized to treat a SN remnant in a turbulent environment. Thereby, the ambient densities are randomly sampled from a lognormal density distribution with a given dispersion that is related to the turbulence in the gas by the Mach number. From the combination of many ambient media the momentum and energy input of a SN remnant can be obtained. The results are shown in Fig. 6.





# The relative impact of photoionizing radiation and stellar winds on different environments

S. Haid,<sup>1</sup>★ S. Walch,<sup>1</sup> D. Seifried,<sup>1</sup> R. Wunsch,<sup>2</sup> F. Dinnbier<sup>1</sup> and T. Naab<sup>3</sup>

<sup>1</sup>*I. Physikalisches Institut, Universität zu Köln, Zùlpicher-Strasse 77, 50937 Cologne, D-Germany*

<sup>2</sup>*Astronomický Ústav, Akademie vd Žesky Republiky, BoŽení II 1401, CZ-14131 Praha, Czech Republic*

<sup>3</sup>*Max-Planck-Institut für Astrophysik, Karl-Schwarzschild-Strasse 1, D-85741 Garching, Germany*

Accepted 2018 May 8. Received 2018 April 27; in original form 2017 October 20

## ABSTRACT

Photoionizing radiation and stellar winds from massive stars deposit energy and momentum into the interstellar medium (ISM). They might disperse the local ISM, change its turbulent multi-phase structure, and even regulate star formation. Ionizing radiation dominates the massive stars' energy output, but the relative effect of winds might change with stellar mass and the properties of the ambient ISM. We present simulations of the interaction of stellar winds and ionizing radiation of 12, 23, and 60  $M_{\odot}$  stars within a cold neutral (CNM,  $n_0 = 100 \text{ cm}^{-3}$ ), warm neutral (WNM,  $n_0 = 1, 10 \text{ cm}^{-3}$ ), or warm ionized (WIM,  $n_0 = 0.1 \text{ cm}^{-3}$ ) medium. The FLASH simulations adopt the novel tree-based radiation transfer algorithm TREERAY. With the On-the-Spot approximation and a temperature-dependent recombination coefficient, it is coupled to a chemical network with radiative heating and cooling. In the homogeneous CNM, the total momentum injection ranges from  $1.6 \times 10^4$  to  $4 \times 10^5 M_{\odot} \text{ km s}^{-1}$  and is always dominated by the expansion of the ionized  $\text{H II}$  region. In the WIM, stellar winds dominate ( $2 \times 10^2$  to  $5 \times 10^3 M_{\odot} \text{ km s}^{-1}$ ), while the input from radiation is small ( $\sim 10^2 M_{\odot} \text{ km s}^{-1}$ ). The WNM ( $n_0 = 1 \text{ cm}^{-3}$ ) is a transition regime. Energetically, stellar winds couple more efficiently to the ISM ( $\sim 0.1$  percent of wind luminosity) than radiation ( $< 0.001$  percent of ionizing luminosity). For estimating the impact of massive stars, the strongly mass-dependent ratios of wind to ionizing luminosity and the properties of the ambient medium have to be considered.

**Key words:** ISM: bubbles,  $\text{H II}$  regions – MHD – radiative transfer.

## 1 INTRODUCTION

Feedback from massive stars in the form of ionizing radiation, stellar winds, and supernova (SN) explosions modifies the density distribution, changes the chemical composition, and influences the energy budget of the environment. For young, massive stars, which are still embedded in a gravitationally collapsing cloud, these processes can counteract the contraction and prevent further accretion of material onto the star. Hence, feedback by stellar winds and ionizing radiation provides one feasible way to locally suppress star formation by dispersing the cold gas in the molecular cloud out of which the massive star has been born (Whitworth 1979; Krumholz 2006; Krumholz et al. 2009; Walch et al. 2012; Dale 2015). As a result, the SN at the end of the stars' lifetime explodes into the pre-blown bubble, which is already hot and ionized (Walch & Naab 2015). On the other hand, stellar feedback can also trigger star formation in the surrounding cloud at distances of several parsec from the massive

star (Elmegreen & Lada 1977; Whitworth 1979; Krumholz 2006; Gritschneider et al. 2009; Krumholz et al. 2009; Gritschneider et al. 2010; Walch et al. 2012, 2013; Dale 2015).

On scales larger than individual molecular clouds or cloud cores, the impact of persistent stellar energy emission is still highly debated (Ostriker, McKee & Leroy 2010; Dobbs et al. 2014; Hopkins et al. 2014; Krumholz 2014; Naab & Ostriker 2017). It is likely that a more detailed understanding of the local interaction of stellar winds and ionizing radiation from massive stars, in addition to SNe, are the key to answering some of the major questions in star formation and galaxy evolution (Naab & Ostriker 2017), e.g. galactic outflows might be driven by stellar feedback processes.

Followed by the first theoretical model of the effect of ionizing radiation (Strömgren 1939), the description of the expansion of an  $\text{H II}$  region into a homogeneous medium has been derived by Spitzer (1978) and extended to account for the inertia of the shell by Hosokawa & Inutsuka (2006). Many modern codes have tested these analytic expressions (Bisbas et al. 2015 and references therein). Recent three-dimensional simulations modify the ambient density distribution to be fractal (Walch et al. 2012) or include dense self-

\* E-mail: haid@ph1.uni-koeln.de



gravitating objects (Matzner 2002; Dale et al. 2005). Depending on the escape velocity (Dale, Ercolano & Bonnell 2012), an embedded ionizing source might be able to disrupt a cloud or not (Geen et al. 2015b; Howard, Pudritz & Klessen 2017).

Wind-blown bubbles were first analytically discussed by Castor, McCray & Weaver (1975) and Weaver et al. (1977) for homogeneous media. Later, power-law environmental density distributions were studied (Franco, Tenorio-Tagle & Bodenheimer 1990; Koo & McKee 1992; Garcia-Segura & Mac Low 1995a; Pittard, Dyson & Hartquist 2001). The complexity of numerical simulations increased with even more realistic ambient media and the interaction with other feedback processes (Falle 1975; Garcia-Segura & Mac Low 1995b; Garcia-Segura, Langer & Mac Low 1996; Arthur 2007; Dwarakadas 2007; Toalá & Arthur 2011; Rogers & Pittard 2013).

However, the relative impact of stellar winds with respect to ionizing radiation is still highly debated. Judging from the amount of energy provided by the star, the first process should be negligible (Matzner 2002). However, the conversion of radiative energy to kinetic energy is highly inefficient (Walch et al. 2012) and thus, both processes could be important.

Analytic estimates (Dyson & Williams 1980) and two-dimensional simulations (Freyer, Hensler & Yorke 2003; Kröger, Hensler & Freyer 2006; Hensler, Kroeger & Freyer 2008) indicate that stellar winds couple efficiently with the environmental gas, which means that a significant fraction of the wind input energy is received by the environmental gas in form of thermal and kinetic energy. In addition, the wind momentum input is fully retained. However, the impact of the wind on a surrounding molecular cloud could still be small (Mackey, Langer & Gvaramadze 2013; Dale et al. 2014; Geen et al. 2015b). The wind of a single B-star in the presence of a self-gravitating cloud is surely too weak to counteract the gravitational collapse (Geen et al. 2015b). In simulations with Smoothed Particle Hydrodynamics, momentum-driven winds from a massive,  $30 M_{\odot}$ , O-star also show little destructive behaviour (Dale & Bonnell 2008) but compress gas in a shell. If the shell becomes unstable or the wind expands into a medium with turbulent sub-structures, then the gas with low (lower than average) density is channelled into rarefied regions where it can leak out of the cloud (Harper-Clark & Murray 2009; Dale et al. 2013; Rogers & Pittard 2013; Rosen et al. 2014). These ‘paths of least resistance’ allow for the following SN to disperse the cloud (Pittard 2013; Wareing et al. 2017).

Studies of the impact of stellar feedback processes generally consider that the sources are embedded in dense molecular clouds where stars are born (e.g. Freyer, Hensler & Yorke 2006; Arthur et al. 2011; Dale, Ercolano & Bonnell 2012; Walch et al. 2012; Ngoumou et al. 2015; Geen et al. 2015b). However, the environment of a massive star is likely to change rapidly. It might become warm and ionized (e.g. Felli, Churchwell & Massi 1984) due to previously born stars in the same cluster. In addition, stars are not static. About 20–40 percent of O stars (Gies & Bolton 1986; Stone 1991) are estimated to be runaway stars, migrating at typical velocities of tens of km/s up to several hundreds of km/s into the warm ionized or hot medium (Hoogerwerf, de Bruijne & de Zeeuw 2000; Huthoff & Kaper 2002). Runaway stars reach distances of several hundreds of parsecs from their birthplaces in a few Myr. This motivates us to study the interaction of ionizing radiation and stellar winds not only with the cold dense phase of the ISM, but also with the more rarefied warm ionized phase.

In this paper, we address the question with which efficiencies of stellar winds and ionizing radiation couple the provided energy and momentum to the environment. We investigate different ambient

media, ranging from the prototypical cold neutral medium to a warm ionized medium. In addition, we present the first application of the novel, three-dimensional, tree-based radiative transfer method *TREERAY*. We use a single energy band to treat ionizing radiation and couple it to the employed chemical network. The network follows the evolution of seven species ( $H_2$ , H,  $H^+$ , CO,  $C^+$ , O,  $e^-$ ). We are able to self-consistently treat heating and cooling of the ambient gas.

In Section 2, we briefly describe the simulation code *FLASH 4* and the simulation setup. We also introduce the novel radiative transfer method *TREERAY* and how it is coupled to the chemical network, and compare the resulting temperature of the different  $H_{II}$  regions with the ionizing radiation Monte-Carlo code *MOCASSIN*. In Section 3, we discuss the impact of the combination of stellar winds and ionizing radiation and in Section 4, we show the individual and relative impact of both processes. In Section 5, we take a look at energy coupling efficiencies and the implications on the emission of radiative recombination cooling and X-rays. We summarize in Section 7.

## 2 NUMERICAL METHOD

We use the Eulerian, adaptive mesh refinement, magnetohydrodynamics (MHD) code *FLASH 4* (Fryxell et al. 2000; Dubey et al. 2008) with the directionally split, Bouchut HLL5R solver (Bouchut, Klingenberg & Waagan 2007, 2010; Waagan 2009; Waagan, Federrath & Klingenberg 2011). In addition, self-gravity, radiative transfer, and radiative cooling and heating (from the ionizing radiation as well as from a constant background interstellar radiation field), shielding of molecular hydrogen and CO (Wünsch et al. 2017), and a chemical network is included (Glover & Mac Low 2007b, a; Glover et al. 2010, for the implementation into *FLASH* see Walch et al. 2015). We use a stellar evolution model with a momentum-driven wind (Gatto et al. 2017) and chemistry-coupled ionizing radiation. In this work, we do not treat magnetic fields. In the next subsections, we will describe the implementations in more detail.

### 2.1 Stellar winds

To simulate the impact of stellar winds, we partly follow the procedure of Gatto et al. (2017). The evolution of massive stars (possible masses of  $9\text{--}120 M_{\odot}$ ) is modelled using the Geneva stellar evolution tracks from the zero-age main sequence to the Wolf-Rayet phase (Ekström et al. 2012). An initial proto-stellar phase is not included.

The wind mass-loss rates  $\dot{M}_w$  are taken from the tracks by Ekström et al. (2012). The corresponding terminal wind velocities  $v_w$  are estimated according to the evolutionary status (Puls et al. 2009, in Section 2.4 in Gatto et al. 2017 and the references therein). Fig. 1 shows the time evolution of  $v_w$  (top panel) and  $\dot{M}_w$  (second panel) of stars with initial masses  $M_s = 12, 23$ , and  $60 M_{\odot}$ . The radiative luminosities,  $L_{\text{IRad}}$ , (dashed) and mechanical luminosities,  $L_{\text{Wind}} = 0.5 \dot{M}_w v_w^2$ , (solid) are shown in the third panel. The cumulative energy inputs from the sources ( $E_{\text{src}}(t) = \int_0^t L dt$ , with  $L = L_{\text{IRad}}$  or  $L = L_{\text{Wind}}$ ) are provided in the bottom panel.

#### 2.1.1 Wind implementation

The wind model, as implemented in *FLASH 4*, is based on the injection of momentum in a given spherical volume defined by the *injection radius* (see Section 2.4). In the reference frame of the star, the

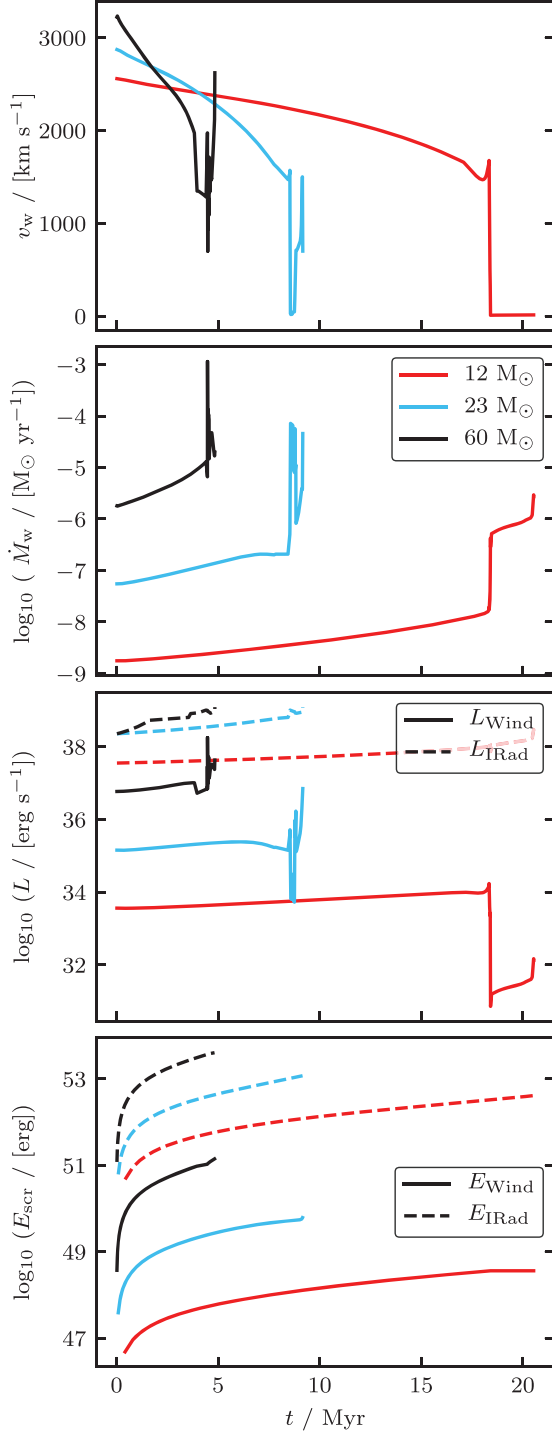


**Figure 1.** Wind velocities (top panel), wind mass-loss rates (second panel), as well as luminosities (third panel) and energies (bottom panel) of stellar winds (solid) and radiation (dashed) of stars with  $M_* = 12$  (red), 23 (blue), and  $60 M_\odot$  (black).

wind momentum points radially outward and is assumed to have a spherically symmetric distribution. Therefore, for a given  $v_w$ , the wind velocity vector in the reference frame of the star,  $\mathbf{v}_w^s$ , that is added to every cell within the injection radius is

$$\mathbf{v}_w^s = v_w \frac{\mathbf{x} - \mathbf{x}_s}{\|\mathbf{x} - \mathbf{x}_s\|} \quad (1)$$

where  $\mathbf{x}_s$  is the position of the star. We apply a Galilei transformation to obtain the wind velocity in the rest frame as

$$\mathbf{v}_w = \mathbf{v}_w^s + \mathbf{v}_s \quad (2)$$

where  $\mathbf{v}_s$  is the velocity of the star.

The total momentum  $\mathbf{p}'$  in a cell after the wind is injected is

$$\mathbf{p}' = m' \mathbf{v}' = m_g \mathbf{v}_g + m_w \mathbf{v}_w \quad (3)$$

where  $m' \mathbf{v}'$  is the cell mass times the cell velocity after the wind injection and  $m_g \mathbf{v}_g$  the initial momentum of the gas in the cell. The wind momentum to be injected is  $m_w \mathbf{v}_w$  with  $m_w = \dot{M}_w(t) \Delta t (\Delta x)^3 V_{inj}^{-1}$ , where  $\Delta t$  is the time-step,  $\Delta x$  the cell size, and  $V_{inj}$  the volume into which the wind is injected.

Since we inject the mass lost by the massive star,  $m_w$ , we have to increase the internal energy<sup>1</sup> in every cell of the injection region. To compute the required internal energy input, we make the ansatz

$$E'_{kin} + E'_{int} = (E_{kin,g} + \Delta E_{kin,w}) + (E_{int,g} + \Delta E_{int,w}), \quad (4)$$

where the left-hand side corresponds to the total energy after the wind injection. The right-hand side comprises the kinetic and internal energies of the gas,  $E_{kin,g}$  and  $E_{int,g}$ , and the kinetic and internal energy of the wind,  $\Delta E_{kin,w}$  and  $\Delta E_{int,w}$ . Since we only inject momentum,  $\Delta E_{int,w} = 0$  by definition. With  $E'_{kin} = \frac{p'^2}{2m'}$  and

$$\Delta E_{kin,w} = E'_{kin} - E_{kin,g} = \frac{p'^2}{2m'} - \frac{(m_g \mathbf{v}_g)^2}{2m_g}, \quad (5)$$

we can solve equation (4) for  $E'_{int}$  and obtain

$$E'_{int} = E_{int,g} + \frac{1}{2} \frac{m_g m_w}{m_g + m_w} (\mathbf{v}_g - \mathbf{v}_w)^2. \quad (6)$$

### 2.1.2 Analytic solution

In a uniform medium, the momentum from the adiabatic, thin-shell evolution of stellar winds can be calculated analytically (Weaver et al. 1977; Garcia-Segura & Mac Low 1995a, b; Everett & Churchwell 2010). The time evolution of the shock radius is (Weaver et al. 1977; Pittard 2013)

$$R_{Wind} = \left( \frac{125}{154\pi} \right)^{0.2} \left( \frac{0.5 \dot{M}_w v_w^2}{\rho_0} \right)^{0.2} t^{0.6}. \quad (7)$$

The resulting momentum input  $p_{theo, Wind}$  is

$$p_{theo, Wind} = \frac{4\pi}{3} \rho_0 0.6 \frac{R_{Wind}^4}{t}, \quad (8)$$

where  $\rho_0$  is the density of the uniform, ambient medium (Krumholz & Matzner 2009).

<sup>1</sup>Note that the specific internal energy is not changed since  $m_w$  has been added to the cell.

## 2.2 Ionizing radiation and radiative heating

### 2.2.1 Analytic solution

For the analytic treatment of ionizing radiation we consider all Lyman continuum photons with an energy of  $h\bar{\nu} \geq 13.6$  eV, which can ionize hydrogen immediately. In ionization-recombination equilibrium, the result is an  $H_{II}$  region which extends to the Strömgen radius  $R_{St}$  with

$$R_{St} = \left( \frac{3}{4\pi} \frac{\dot{N}_{LC} m_p^2}{\alpha_B \rho_0^2} \right)^{1/3}, \quad (9)$$

where  $\dot{N}_{LC}$  is the number of emitted Lyman continuum photons per second,  $m_p$  the proton mass,  $\rho_0$  the ambient density, and  $\alpha_B$  the radiative recombination rate of hydrogen to all levels above the ground state (case B recombination)

$$\alpha_B = 2.56 \times 10^{-13} \left( \frac{T}{10^4 \text{ K}} \right)^{-0.83} [\text{cm}^3 \text{ s}^{-1}], \quad (10)$$

in the range of  $T = [5000, 20000]$  K (Tielens 2005).

The temperature inside the  $H_{II}$  region is immediately increased due to photoionization heating. A pressure gradient establishes at  $R_{St}$  and drives a shock with the shock velocity

$$v_S = c_i \sqrt{\frac{4}{3} \frac{R_{St}^{1.5}}{R_{IRad}^{1.5}} - \frac{\mu_i T_0}{2\mu_0 T_i}} \quad (11)$$

where  $T_0$  and  $\mu_0$  are the ambient temperature and mean molecular weight and  $c_i$ ,  $T_i$ , and  $\mu_i$  are the isothermal sound speed, the temperature, and the mean molecular weight of the ionized medium. Under the assumption that  $v_S$  is larger than the ambient sound speed,  $R_{IRad}$  is the shock radius which evolves with the Hosokawa–Inutsuka modification of the analytic Spitzer solution as (Spitzer 1978; Hosokawa & Inutsuka 2006; Bisbas et al. 2015)

$$R_{IRad} = R_{St} \left( 1 + \frac{7}{4} \sqrt{\frac{4}{3}} \frac{c_i t}{R_{St}} \right)^{4/7}. \quad (12)$$

The resulting momentum is

$$p_{IRad} = \frac{4}{3} \pi (R_{IRad}^3 - R_{St}^3) \rho_0 v_S. \quad (13)$$

### 2.2.2 TREERAY

The transfer of ionizing radiation is calculated by a new module for the FLASH code called TREERAY. It is an extension of the FLASH tree solver for calculating self-gravity and the optical depth in every cell of the computational domain as described in Wünsch et al. (2017). Here, we only give a basic information about TREERAY. A detailed description alongside with accuracy and performance tests will be presented in Wünsch et al. (in prep).

TREERAY uses the octal-tree data structure constructed and updated in each time-step by the tree solver, and shares it with the Gravity and Optical-Depth modules. Each node of the octal-tree represents a cuboidal collection of grid cells and stores the total gas mass contained in it, masses of individual chemical species, and the position of the mass centre. In addition to that, TREERAY stores for each node the total amount of the radiation luminosity generated inside the node, radiation energy flux passing through the node, and the node volume.

Before the tree is traversed for each grid cell (called *target cell*), a system of rays pointing from the target cell to all directions is

constructed. The directions are determined by the HEALPIX algorithm (Górski et al. 2005), which tessellates the unit sphere into elements of equal spatial angle. Each ray is then divided into segments with lengths increasing linearly with the distance from the target cell. In this way, the segment lengths correspond approximately to sizes of nodes interacting with the target cell during the tree walk if the Barnes-Hut criterion for node acceptance is used. When the tree is traversed, node densities, radiation luminosities, and energy fluxes are mapped onto ray segments according to a degree of the intersection of the node volume and the volume belonging to the ray segment.

Finally, after the tree walk, the one-dimensional radiative transport equation is solved along each ray. In this work, this equation has a form corresponding to the physical processes and approximations (On-the-Spot) used in Section 2.2.1, i.e. the absorption coefficient is proportional to  $\alpha_B(T)\rho^2$  and the emission coefficient is proportional to  $\dot{N}_{LC}$  for a given source. As the radiation flux passing through a given segment from different directions has to be taken into account, the solution has to be searched for iteratively, repeating the whole process of tree construction, tree walk, and radiation transport equation solving until a desired accuracy is reached. Fortunately, the solution from the previous hydrodynamic time-step can be used, and as the radiation field typically changes only slightly between times-steps, in most cases only one or two iterations in each time-step are needed.<sup>2</sup>

For the performed simulations, we use 48 rays and the tree solver with the Barnes–Hut acceptance criterion with limit angle  $\theta_{lim} = 0.5$ . The code is benchmarked for the expanding  $H_{II}$  region (Bisbas et al. 2015). In this paper, we extend the prescription with a temperature-dependent recombination coefficient and couple TREERAY to the chemical network.

The main advantage of TREERAY is that the computational cost is basically independent of the number of sources. Therefore, it can be readily used to simulate the radiative feedback of many stars in e.g. clusters in full three-dimensional MHD simulations.

### 2.2.3 Ionizing radiation heating

We assume that all sources emit a black-body spectrum with an effective stellar temperature  $T_*$  given by the aforementioned stellar tracks. Thus, the mean ionizing photon energy  $h\bar{\nu}$  is

$$h\bar{\nu} = \frac{\int_{\nu_T}^{\infty} B_\nu d\nu}{\int_{\nu_T}^{\infty} \frac{B_\nu}{h\nu} d\nu} = \frac{F}{F_{ph}} \quad (14)$$

where  $h$  is the Planck constant,  $\nu_T = 13.6$  eV  $h^{-1}$  is the threshold frequency for hydrogen ionization,  $B_\nu = B_\nu(T_*)$  is the Planck function,  $F$  the energy flux, and  $F_{ph}$  the photon flux (Rybicki & Lightman 2004). Both fluxes are provided by TREERAY for every cell in the computational domain.

The heating rate  $\Gamma_{ih}$  in ionization–recombination equilibrium is calculated with (Tielens 2005)

$$\Gamma_{ih} = F_{ph} \sigma E_{\bar{\nu}-\nu_T} = n_H^2 \alpha_B h (\bar{\nu} - \nu_T), \quad (15)$$

where  $E_{\bar{\nu}-\nu_T} = h(\bar{\nu} - \nu_T)$  is the average excess energy of the ionizing photons,  $\sigma$  is the hydrogen photoionization cross-section,  $n_H$  the hydrogen number density, and  $\alpha_B$  (see equation 10) the radiative recombination rate.

<sup>2</sup>Note that the FLASH code uses global time-steps and that the time-step is always limited by the CFL condition of the fast stellar wind, which is much more restrictive than the progress of the D-type ionization front.

The heating rate and number of ionizing photons are provided to the chemistry module (see Section 2.3). There, the temperature will be increased self-consistently by balancing heating and cooling processes and the hydrogen species will be updated using the given photoionization rate.

### 2.3 Gas cooling, heating, and chemistry

We include a simple chemical network, which is explained in detail in Walch et al. (2015). It is based on Glover and Mac Low (2007a, b); Glover et al. (2010), and Nelson & Langer (1997) to follow the abundances of seven chemical species: molecular, atomic, and ionized hydrogen as well as carbon monoxide, ionized carbon, atomic oxygen, and free electrons ( $\text{H}_2$ ,  $\text{H}$ ,  $\text{H}^+$ ,  $\text{CO}$ ,  $\text{C}^+$ ,  $\text{O}$ ,  $\text{e}^-$ ). The gas has solar metallicity (Sembach et al. 2000) with fixed elemental abundances of carbon, oxygen, and silicon ( $x_{\text{C}} = 1.4 \times 10^{-4}$ ,  $x_{\text{O}} = 3.16 \times 10^{-4}$ ,  $x_{\text{Si}} = 1.5 \times 10^{-5}$ ) and the dust-to-gas mass ratio is set to 0.01. We include a background interstellar radiation field (ISRF) of homogeneous strength  $G_0 = 1.7$  (Habing 1968; Draine 1978). To assume the ISRF to be constant near a massive star is an approximation. However, even a 100 times higher radiation strength increases the temperature in the medium by only 12 percent (see Section A in the Appendix). Thus, the ambient pressure counteracting the expanding shock would change only marginally. For this reason, we here only focus on the case of  $G_0 = 1.7$ . The ISRF is attenuated in shielded regions depending on the column densities of total gas,  $\text{H}_2$ , and  $\text{CO}$ . Thus, we consider dust shielding and molecular (self-) shielding for  $\text{H}_2$  and  $\text{CO}$  (Glover et al. 2010; Walch et al. 2015) by calculating the shielding coefficients with the TREERAY Optical-Depth module, described and tested in (Wünsch et al. 2017).

For gas with temperatures above  $\sim 10^4$  K, we model the cooling rates according to Gnat & Ferland (2012) in collisional ionization equilibrium. Non-equilibrium cooling for the respective species is applied at lower temperatures (also for Lyman  $\alpha$ ). Within the  $\text{H}_{\text{II}}$  region, we neglect both  $\text{C}^+$  and  $\text{O}$  cooling because these species are assumed to be in a higher ionization state.

Heating rates include the photoelectric effect, cosmic ray ionization with a rate of  $\xi = 3 \times 10^{-17} \text{ s}^{-1}$ , and X-ray ionization by Wolfire et al. (1995). In this work, we additionally include the heating by photoionization from the central star (see equation 15).

Note that, since we only consider the radiative transfer in a single energy band (all photons in the Lyman continuum), we do not distinguish between the direct ionization of  $\text{H}$  and  $\text{H}_2$ , as necessary for detailed models of photon-dominated regions (Röllig et al. 2007). However, photon-dominated regions in an early evolutionary stage are considered thin and unresolved in three-dimensional simulations of feedback in MCs (see equation (1) in Bisbas et al. 2015). During the evolution, this region will widen, however the treatment of this late stage is beyond the scope of our simulations.

### 2.4 Simulation setup

We use cubic boxes with a side length of 51 pc. The generic grid resolution is 0.4 pc with a maximum resolution of 0.2 pc refining on the source and the density fluctuations of the shell. The computational domain is homogeneously filled with initially warm and ionized gas (WIM) or with cold, predominantly neutral gas (CNM). The initial densities are  $\rho_0 = 2.1 \times 10^{-25} \text{ g cm}^{-3}$  and  $2.1 \times 10^{-22} \text{ g cm}^{-3}$  and temperatures  $T_0 = 10^4$  K and 20 K, respectively. The ac-

**Table 1.** We list the simulations with the employed stellar process(es), ambient medium, and mass of the central star. Abbreviations: WIM warm ionized medium ( $n_0 = 0.1 \text{ cm}^{-3}$ ,  $T_0 = 10^4$  K), CNM cold neutral medium ( $n_0 = 100 \text{ cm}^{-3}$ ,  $T_0 = 20$  K).

Wind	IRad	Media	Sources [ $M_{\odot}$ ]
X	X	WIM, CNM	12, 23, 60
X		WIM, CNM	12, 23, 60
X	X	WIM, CNM	12, 23, 60

cording number densities for an assumed mean molecular weight<sup>3</sup> of 1.4 are  $n_0 = 0.1$  and  $100 \text{ cm}^{-3}$ .

The chemical species are initialized using fractional abundances. In the WIM, the initial  $\text{H}^+$  abundance  $n_{\text{H}^+}/n_{\text{H,tot}} = 0.98$ , and the other 2 percent are neutral. In the CNM, we initialize  $n_{\text{H}}/n_{\text{H,tot}} = 0.5$  and  $n_{\text{H}_2}/n_{\text{H,tot}} = 0.25$ . Independent of the medium, carbon is always ionized,  $n_{\text{C}^+}/n_{\text{C,tot}} = 1$ .

We consider three different single stars with initial masses of  $M_* = 12, 23$ , and  $60 M_{\odot}$ . The star is always placed in the centre of the domain and emits a stellar wind and/or ionizing radiation. The spherical wind injection region is 12 cells in radius on the highest level of refinement, corresponding to 2.4 pc. Table 1 summarizes the 18 simulations, which were performed for this section.

### 2.5 Benchmark with MOCASSIN

First, we compare the results to the three-dimensional Monte-Carlo photoionization code MOCASSIN (Ercolano et al. 2003). For this purpose, we use three FLASH simulations of massive stars with  $M_* = 12, 23$ , and  $60 M_{\odot}$ , which are the sources of ionizing radiation only and embedded in the CNM. As input for MOCASSIN, we deliver the CNM conditions, the mean stellar temperature of each star,  $T_* = 2.8 \times 10^4$ ,  $3.7 \times 10^4$ , and  $4.7 \times 10^4$  K, and a constant ionizing photon rate of  $2.4 \times 10^{48}$ ,  $3.2 \times 10^{49}$ , and  $2.4 \times 10^{50} \text{ s}^{-1}$  for increasing stellar masses. Both parameters are time averages from the stellar tracks over the initial period of 2.5 Myr.

Fig. 2 compares the radial profiles of MOCASSIN (blue) to the FLASH results (black) at  $t = 2.5$  Myr. With increasing stellar mass, the relative errors of the position of the shock front are 6, 8, and 11 percent. The temperature structure inside the  $\text{H}_{\text{II}}$  region as calculated by MOCASSIN cannot be reproduced by our single-energy-band model because we are not able to treat the hardening of the radiation field at increasing distance from the central star. Yet, the volume-averaged mean temperatures agree to within 8, 5, and  $\sim 1$  percent (see Table 2). Therefore the mean temperatures are representative.

For the WIM, we obtain a constant radial temperature profile inside the computational domain. This is due to the fact that the Strömgren radius lies at a few 100 pc (see equation 9). It is impossible that an expanding shock establishes as the pressure gradient over the shell in this medium is negligible.

## 3 COMBINED IMPACT OF STELLAR WIND AND IONIZING RADIATION

Fig. 3 demonstrates the impact of the combination of both, stellar winds and ionizing radiation feedback, with  $M_* = 12, 23$ , and

<sup>3</sup>Although the mean molecular weight is computed self-consistently using the FLASH Multispecies module, and thus the resulting number densities are not exactly equal to 0.1 and  $100 \text{ cm}^{-3}$  we refer rather to  $n_0$  than  $\rho_0$  throughout most of the paper.



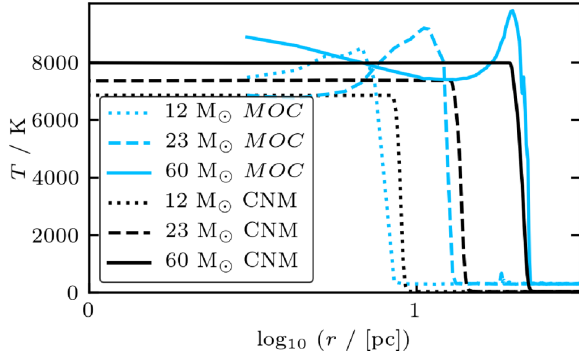


**Figure 2.** The radial temperature distributions obtained from the simulations of ionizing radiation in the CNM (black), which are compared to simulations with the photoionization Monte-Carlo code MOCASSIN (blue). The profiles are shown for stars with  $M_* = 12$  (dotted), 23 (dashed), and 60  $M_\odot$  (solid) at  $t = 2.5$  Myr.

**Table 2.** Comparison of the mean  $H_{II}$  region temperatures with  $M_* = 12$ , 23, and 60  $M_\odot$  in WIM and CNM. The second and third columns are values obtained from the code MOCASSIN. The last two columns show the mean temperatures inside the  $H_{II}$  regions from the FLASH simulations.

Sources	MOCASSIN		FLASH	
	$\bar{T}_{WIM}$ [K]	$\bar{T}_{CNM}$ [K]	$\bar{T}_{WIM}$ [K]	$\bar{T}_{CNM}$ [K]
12 $M_\odot$	7190	7730	7190	7160
23 $M_\odot$	7760	7710	7700	7340
60 $M_\odot$	8220	7990	8150	7940

60  $M_\odot$  (from left to right), each in the CNM at  $t = 0.76$  Myr (top) and the WIM at  $t = 0.2$  Myr (bottom). The first time is chosen as a representative example and at the second time, the wind shock of the star with  $M_* = 60 M_\odot$  has reached the computational boundary. Density (left-hand subpanels) and temperature (right-hand subpanels) structures are shown as slices in the  $z = 0$  plane. Note the different length scales in the top and bottom panels. The green, dashed lines show the theoretically predicted shock radii. In the CNM, we only show these for ionizing radiation  $R_{Irad}$  (equation 12) and in the WIM only for stellar winds  $R_{Wind}$  (equation 7). The predicted shock radii are essentially equivalent to the computed, radially averaged shock radii, which increase with stellar mass from 5.1 pc, to 8.2 pc and 12.5 pc in the CNM and from 5.0 pc, to 11.8 pc, and 23.9 pc in the WIM for  $M_* = 12$ , 23, and 60  $M_\odot$ , respectively.

Inspecting Fig. 3, we find that the gas inside the bubble has distinctive temperatures, depending on the driving process. The warm and ionized gas with a temperature of  $\sim 8000$  K is produced by ionizing radiation. The hot material with temperatures of some  $10^7$  K is shock-heated by stellar winds.

In the CNM (top panels), the shock is driven by ionizing radiation. The impact of stellar winds increases with the mass of the stellar source, respectively with the emitted wind luminosity (see Fig. 1). For the star with  $M_* = 12 M_\odot$ , the emitted wind energy is negligible compared to the emitted radiative energy. Around the star with  $M_* = 23 M_\odot$ , the innermost  $\sim 2$  pc are shock-heated by the wind. Around the most massive star, about 80 percent of the expanding  $H_{II}$  region is filled with hot but rarefied gas. Only the outer  $\sim 4$  pc are not yet affected by wind. In the centre a so-called free-wind region establishes, where the wind expands hypersonically and undisturbed.

In the case of the WIM (bottom panels), stellar winds are driving the expansion. The kinematic effect of ionizing radiation is negligible as the region, which is photoionized by the central source, is not able to expand supersonically into the warm medium. However, radiation still influences the ambient medium by preventing recombination and by providing extra heating which counteracts the cooling of the gas. Thus, the temperature remains at  $\sim 8000$  K. Without radiative support, the temperature would cool down to  $\sim 6000$  K within  $\sim 1.8$  Myr.

Given the agreement of shock radii and the different theoretical predictions, as well as the fact that radiation has a stronger impact in the CNM, whereas in the WIM it is vice versa, shows that the impact of each stellar process is media-dependent.

In Fig. 4, we show the time evolution of the radial momenta  $p$  from the combination of stellar winds and ionizing radiation for the  $M_* = 12$  (dotted), 23 (dashed), and 60 (solid)  $M_\odot$  in the CNM (black) and the WIM (red). For comparison, we show the corresponding momentum input of SNe obtained at the beginning of the momentum-conserving snowplough phase (dashed-dotted lines, Haid et al. 2016). This SN model assumes that the blast wave expands into a uniform ambient medium with CNM or WIM conditions and the corresponding momentum input should therefore be understood as an upper limit. Since stellar wind and ionizing radiation feedback evacuate a bubble and compress the swept-up mass in a dense shell long before the SN explosion, SN remnants might instantaneously experience significant radiative cooling when hitting the swept-up shell. This would drastically lower the final momentum input of the SN (Walch & Naab 2015; Haid et al. 2016).

Although we consider this maximum momentum input of a type II SN, we find that the momentum input caused by a massive star with  $M_* = 60 M_\odot$  exceeds the SN momentum input in CNM conditions with  $p = 2.5 \times 10^5 M_\odot \text{ km s}^{-1}$  after only 1.5 Myr. We predict that at a later time ( $\sim 3$  Myr) also the star with  $M_* = 23 M_\odot$  will rise above the momentum input from a single SN. The momentum input in the WIM is systematically lower than in the CNM. The relative difference is a factor of  $\sim 12$ , 6, and 2 for increasing stellar masses.

### 3.1 Radial profiles of chemical abundances

By coupling the chemistry and the radiative transfer module, we are able to reproduce chemical transitions in shocked regions. In Fig. 5, we show the radially averaged profiles around a star with  $M_* = 12$ , 23, and 60  $M_\odot$  embedded in the CNM at  $t = 0.76$  Myr. Density  $\rho$  (solid, left axis) and temperature  $T$  (dashed, right axis) share the top panel. The bottom panel includes the mass-weighted abundance  $f$  of the species H (red, solid),  $H_2$  (red, dashed),  $H^+$  (red, dotted), CO (blue), and  $C^+$  (black). The mass-weighted abundance is defined as  $f_x \equiv M_x/M_{tot}$  where  $M_x$  is the mass of species  $x$  and  $M_{tot}$  the total mass.

The density and temperature profiles correspond to radiation-driven bubbles (Bisbas et al. 2015) with central wind-heated regions in different stages of their evolution. With increasing stellar mass, the shock positions move to larger radii.

Around the star with  $M_* = 12 M_\odot$ , an  $H_{II}$  region evolves with an average temperature and average density of  $\sim 7200$  K and  $2.1 \times 10^{-23} \text{ g cm}^{-3}$ . Stellar winds show no influence.

In the vicinity ( $r < 1.9$  pc) of the star with  $M_* = 23 M_\odot$ , the wind establishes a small region filled with hot, rarefied gas ( $n \sim 0.1 \text{ cm}^{-3}$ ,  $T \sim 10^8 \text{ K}$ ). This compresses the gas in the  $H_{II}$  region to an average density of  $4.2 \times 10^{-23} \text{ g cm}^{-3}$ . The corresponding average temperature increases to  $\sim 7300$  K.

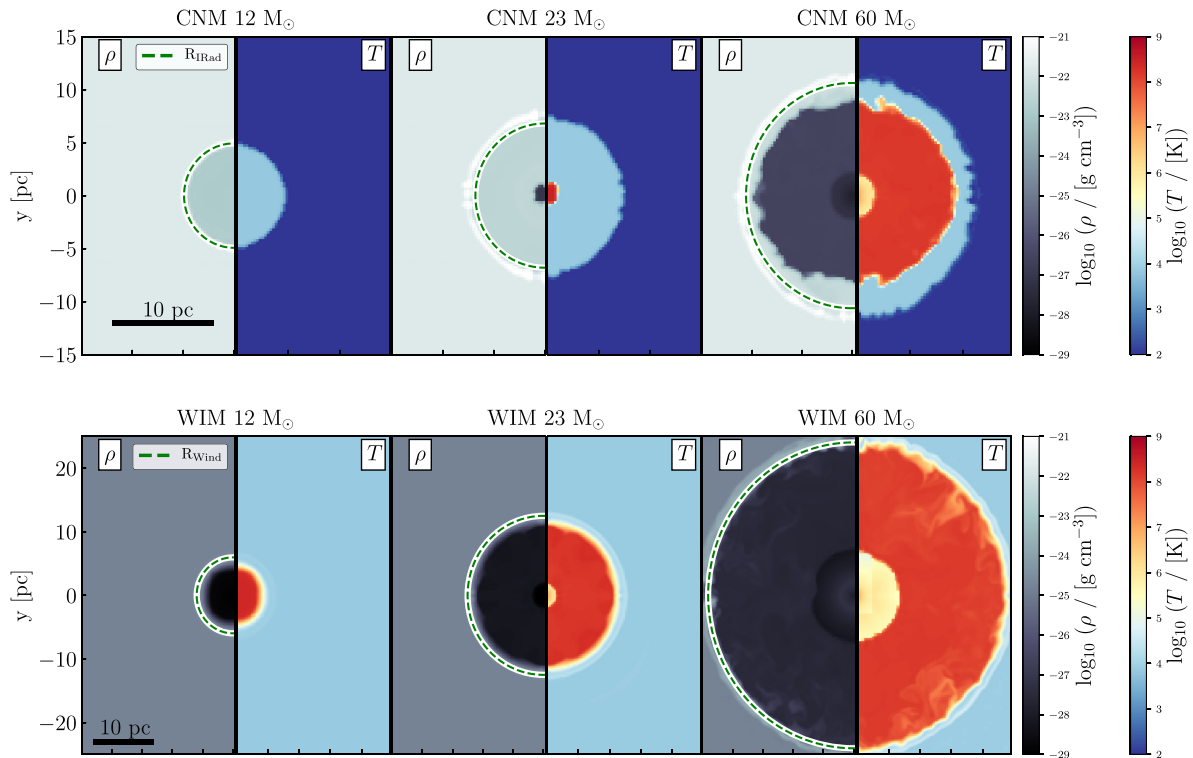


**Figure 3.** Effect of ionizing radiation and stellar wind with  $M_* = 12, 23$ , and  $60 M_\odot$  (from left to right) after  $0.76$  Myr in the CNM ( $n_0 = 100 \text{ cm}^{-3}$ ,  $T_0 = 20 \text{ K}$ , top) and after  $0.2$  Myr in the WIM ( $n_0 = 0.1 \text{ cm}^{-3}$ ,  $T_0 = 10^4 \text{ K}$ , bottom). Shown are slices through the  $z = 0$  plane in density (left-hand subpanel) and temperature (right-hand subpanel) for each source. The simulations in the same row share the same length and color scale. The top row is a zoom of the total computational domain with a length scale of  $30 \text{ pc}$ . The green lines indicate the theoretical radiation-driven shock radius (top row; equation 12) and the analytic wind-driven shock radius (bottom row; equation 7).

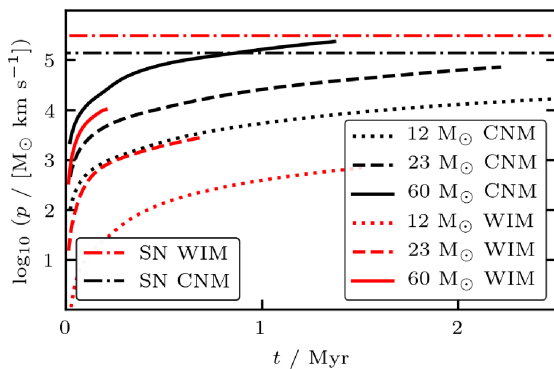


**Figure 4.** Evolution of the radial momentum  $p$  in the CNM (black) and the WIM (red) for sources with  $M_* = 12$  (dotted),  $23$  (dashed), and  $60$  (solid)  $M_\odot$  created by the combination of stellar wind and ionizing radiation. Lines terminate when the front shock has reached the boundary of the computational domain. The corresponding SN momenta in the WIM and CNM at the beginning of the momentum-conserving snowplough phase (Haid et al. 2016) are shown as horizontal, dash-dotted lines.

Around the star with  $M_* = 60 M_\odot$ , the region filled with the shocked stellar wind occupies around 80 per cent of the volume,

which is enclosed by the ionization front. The hot but rarefied gas in the wind bubble has an average temperature of  $T \sim 10^8 \text{ K}$  and an average density of  $\sim 3 \times 10^{-2} \text{ cm}^{-3}$ . The remaining  $\text{H}_{\text{II}}$  region is compressed into a layer of thickness  $\sim 4 \text{ pc}$ . There, the average temperature and density is  $\sim 8200 \text{ K}$  and  $\sim 8.6 \times 10^{-23} \text{ g cm}^{-3}$ . In the centre a free-wind region evolves.

The radial profiles of the chemical abundances are qualitatively and quantitatively very similar for different  $M_*$ . Inside the  $\text{H}_{\text{II}}$  region, almost all hydrogen is ionized but the abundance of atomic hydrogen increases with increasing distance to the source. Ionized hydrogen drops by 6 orders of magnitude at the ionization front. The abundance of  $\text{C}^+$  drops by 3 orders of magnitude and CO forms as the ionizing radiation becomes increasingly shielded. The outside medium contains predominantly molecular hydrogen.

We refer to the Appendix (Appendix B and Fig. B1) for the radial profiles of stars with  $M_* = 12, 23$ , and  $60 M_\odot$  in the WIM and addition profiles of e.g. pressure and radial velocity.

#### 4 RELATIVE IMPORTANCE OF STELLAR WIND AND IONIZING RADIATION

As indicated in Section 3, the structure of the developing feedback bubble depends on the ambient medium (CNM or WIM), which suggests that the impact of stellar winds and ionizing radiation

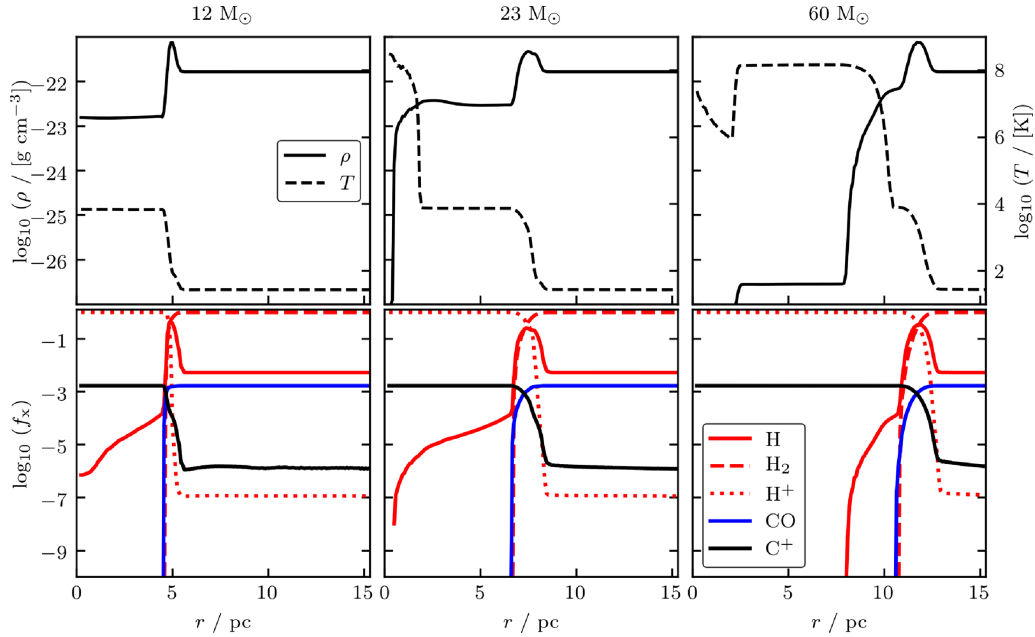


**Figure 5.** Radial profiles of the simulations with ionizing radiation and stellar winds for stars with  $M_* = 12, 23,$  and  $60 M_\odot$  in the CNM at  $t = 0.76$  Myr. We show the radially averaged density  $\rho$  (solid, left axis) and temperature  $T$  (dashed, right axis) in the top panels and the mass-weighted abundances  $f_x$  of the species H (red, solid),  $H_2$  (red, dashed),  $H^+$  (red, dotted), CO (blue), and  $C^+$  (black) in the bottom panels.

strongly depend on the medium they interact with. In order to study this more quantitatively, we carry out 12 additional simulations (see Table 1) with either wind feedback or ionizing radiation feedback.

In Fig. 6, we compare the evolution of radial momenta measured in the gaseous environment of stars with  $M_* = 12, 23,$  and  $60 M_\odot$  (from left to right) for simulations with either ionizing radiation (middle panel, dashed) or stellar winds (bottom panel, dotted) in the CNM (black) and the WIM (red). For comparison, the results from the combination of both feedback processes are shown in the top row (solid lines; same as Fig. 4). Note, that some evolutions stop before 2.5 Myr because the feedback bubble expands out of the computational domain. Therefore, when we evaluate the momentum at the end of the simulation we provide the corresponding time.

We include the analytic estimates for ionizing radiation  $p_{\text{theo, IRad}}$  (thin, dashed lines, top and middle panel, equation 13) and for stellar winds  $p_{\text{theo, Wind}}$  (thin, dotted lines, top and bottom panel, equation 8). We also show the emitted wind momentum  $p_{\text{src}}(t) = \int_0^t \dot{M}_w v_w dt$  (blue, dotted lines) in the bottom panel. The momentum  $p_{\text{src}}$  is the minimum radial momentum injected into the ambient medium. Similar to an expanding SN blast wave (Haid et al. 2016), the feedback-driven, expanding shell gains additional radial momentum as a function of time. Therefore, the computed momenta are always larger than  $p_{\text{src}}$  if a stellar wind is present. For the radiation feedback, there is no minimum momentum input, because no mass-loss of the star is associated with photoionization heating. Radial outward momentum can only be generated if the radiation couples, i.e. interacts with the ambient gas. However, emitted UV radiation generates additional momentum by radiation pressure (see Appendix C). We want to point out, that this second process floors the minimum radiative momentum input.

In the CNM (black), the momentum input at  $t = 2.5$  Myr from ionizing radiation (middle panels) is  $1.6 \times 10^4$ ,  $8.4 \times 10^4$ , and  $4.0$

$\times 10^5 M_\odot \text{ km s}^{-1}$  with increasing stellar mass. The momentum evolution closely follows the analytic estimate and agrees with previous works by e.g. Bisbas et al. (2015) and Geen et al. (2015b). For stellar winds (bottom row) the corresponding momenta are  $3.0 \times 10^2$  ( $t = 2.5$  Myr),  $1.9 \times 10^3$  ( $t = 2.5$  Myr), and  $10^4 M_\odot \text{ km s}^{-1}$  ( $t = 1.1$  Myr). These values differ significantly from the theoretical predictions as the momentum evolution in Section 2.1 assumes no radiative losses. We find that the temperature in the simulated wind bubble is slightly lower and the density is slightly higher than in the adiabatic case due to cooling, where radiative cooling sets in at about 0.1 Myr. Therefore, the shock speed is lower and the shock radius lags behind  $R_{\text{wind}}$ , leading to a smaller swept-up mass and less radial momentum gain. The momentum gained by the combination of both feedback processes differs little from the momentum gained by ionizing radiation alone, with a relative difference of  $\sim 1, 9,$  and  $23$  percent for increasing stellar mass. Thus, ionizing radiation is the dominant source of momentum, driving a shock in the CNM, and the contribution of stellar winds is small (see also Fig. 3 and Fig. 4, top panel; this agrees with previous results by e.g. Dale & Bonnell 2008; Ngoumou et al. 2015).

In the WIM (red), ionizing radiation does not fully couple to the ambient medium. Therefore, it creates very little radial momentum of  $\sim 10^2 M_\odot \text{ km s}^{-1}$ , independent of the stellar mass. The theoretical predictions disagree with the simulation results because they assume that the interior sound speed is significantly larger than the ambient sound speed. This requirement is not fulfilled in the WIM. Stellar winds generate approximative momenta between some  $10^2$  up to a few  $10^3 M_\odot \text{ km s}^{-1}$ , which is almost the same as gained in the CNM.

In the WIM, we find that the combination of both processes is dominated by stellar winds. Interestingly, the simulations with

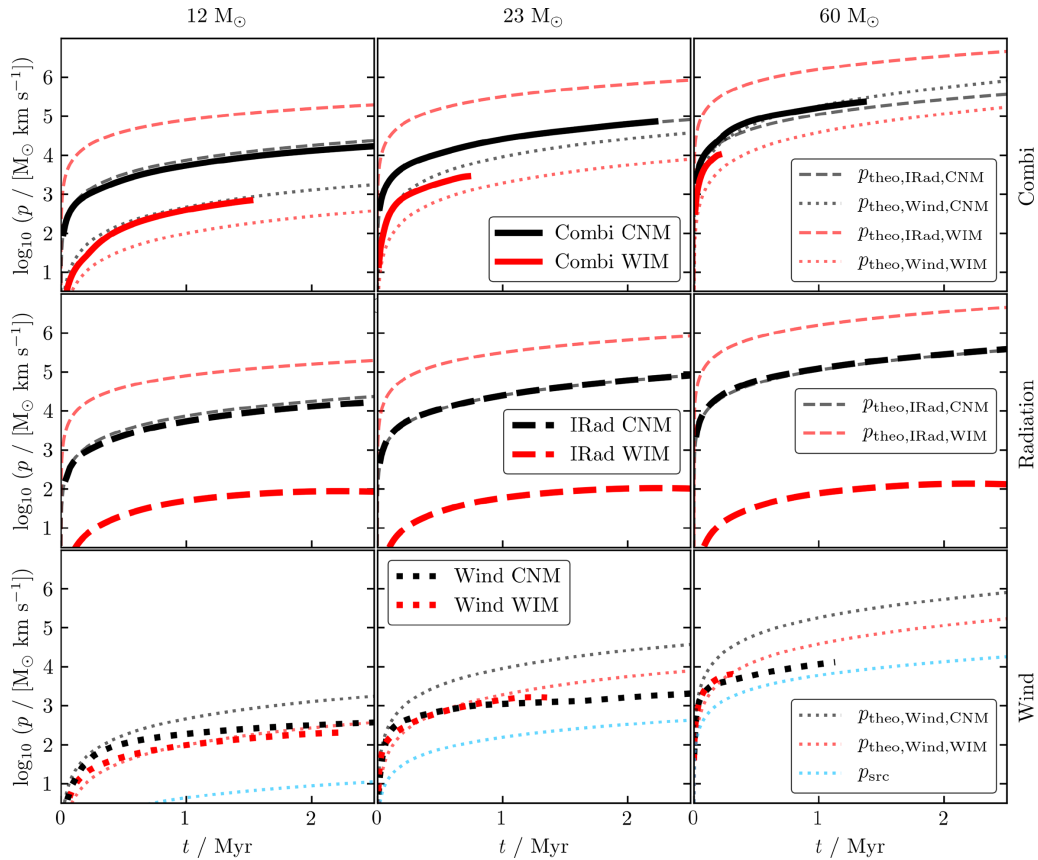


**Figure 6.** Evolution of the radial momentum input in the ambient medium from stars with  $M_* = 12, 23$ , and  $60 M_\odot$  (from left to right) in a homogeneous WIM (red) or CNM (black) from ionizing radiation (middle row, dashed), stellar winds (bottom row, dotted), and both processes (top row, solid; see Fig. 4). The thin lines show the theoretical momentum input  $p_{\text{theo}}$  (for radiation see equation (13), for wind see equation (8)). The blue lines in the bottom row indicate the wind momentum input from the source  $p_{\text{src}}$ . In case the shown lines stop before 2.5 Myr, the feedback bubble expands out of the computational domain.

combined feedback (top row) follow the analytical estimates for a longer time than the simulations with wind feedback only.

Overall, we find that stellar winds dominate in the WIM. Ionizing radiation dominates in the CNM, but is unable to expand significantly into ambient media with temperatures similar or higher to its interior. Note that the sum of momenta from individual processes is not necessarily equal to the momentum input from combined stellar feedback,  $p_{\text{theo,IRad}} + p_{\text{theo,Wind}} \neq p_{\text{Combi}}$  (Freyer et al. 2003). In the CNM, the feedback from both processes  $p_{\text{Combi}}$  is larger than  $p_{\text{IRad}} + p_{\text{Wind}}$  by  $\sim 1, 3$ , and  $23$  percent with increasing stellar mass. In the WIM, the difference is a factor of  $\sim 3.2, 2.8$ , and  $1.9$ .

#### 4.1 The relative impact of stellar winds and ionizing radiation

In order to compare the momentum input of ionizing radiation and stellar winds, we define the relative impact  $I_p$  as

$$I_p \equiv \frac{p_{\text{Wind}} - p_{\text{IRad}}}{p_{\text{Wind}} + p_{\text{IRad}}}, \quad (16)$$

where  $p_{\text{Wind}}$  and  $p_{\text{IRad}}$  is the input of momentum from stellar winds and ionizing radiation, respectively. Thus,  $I_p$  is a measure for the predominance of one feedback process and values around zero indicate equality in momentum input. We name a process ‘dominant’

when the relative impact is close to unity. In this analysis, we assume that the sum of radiation and wind momentum input is representative for the combined momentum input. As discussed at the end of Section 4, this is a lower limit.

For each comparison, we use two simulations with identical initial conditions including either stellar winds or ionizing radiation. Fig. 7 shows the relative impact  $I_p$  of stellar winds and ionizing radiation as a function of the source environment time.  $I_p$  is the time-averaged value in a time period, which both simulations have in common. The vertical lines show the maximum and minimum values of  $I_p$  obtained during the course of the simulation. Six data points are obtained from higher resolution (full markers,  $0.2 \text{ pc}$ ) simulations with stars  $M_* = 12$  (red),  $23$  (blue), and  $60 M_\odot$  (black) embedded in the WIM and CNM (see Table 1). In addition, we include simulations with a lower uniform resolution (empty markers) of  $0.4 \text{ pc}$  in two additional, warm, neutral media, WNM<sub>1</sub> and WNM<sub>2</sub> with number densities  $n_0$  of  $\sim 1$  and  $\sim 10 \text{ cm}^{-3}$  and temperatures  $T_0$  of  $\sim 2 \times 10^3 \text{ K}$  and  $\sim 2 \times 10^2 \text{ K}$  (see Table 3).

Thin lines show the relative impact derived from the analytic estimates in equation (13) and equation (8) which are shifted according with the corresponding simulations. This prediction makes use of the heating and cooling balance of the ISM to relate density and temperatures.



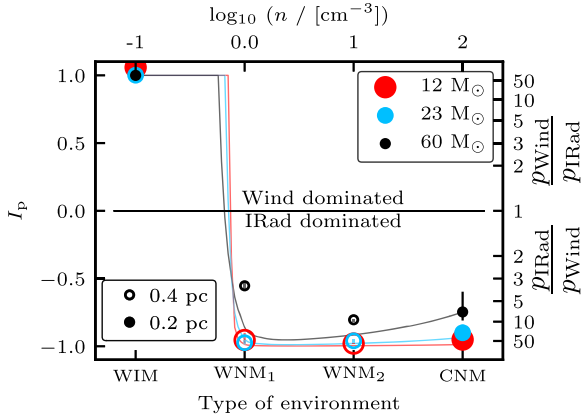


**Figure 7.** The relative impact of stellar winds and ionizing radiation gives an estimate which process is dominant. The horizontal line separates the wind-dominated (upper part) from the radiation-dominated (lower part). The markers show the time average relative impact  $I_p$  of the two feedback processes. The colours represent  $M_* = 12$  (red),  $23$  (blue), and  $60 M_\odot$  (black). The lines show the relative impact derived from the analytic estimates. The vertical lines show the maximum and minimum values during the evolution. Full and empty markers show simulations with effective resolutions of  $0.2$  pc and  $0.4$  pc, respectively. The right ordinate shows the fraction of the dominant to the subordinate process (upper part  $\frac{P_{\text{Wind}}}{P_{\text{IRad}}}$ , lower part  $\frac{P_{\text{IRad}}}{P_{\text{Wind}}}$ ). We investigate  $I_p$  in four different environments. In warm ambient media the wind momentum input dominates, whereas the opposite applies in cold ambient media.

**Table 3.** We list the feedback processes, media, and masses of the stellar sources of performed simulations with lower effective resolution of  $0.4$  pc. Abbreviations:  $WNM_1$  warm neutral medium ( $n_0 = 1 \text{ cm}^{-3}$ ,  $T_0 = 2 \times 10^3$  K, neutral),  $WNM_2$  warm neutral medium ( $n_0 = 10 \text{ cm}^{-3}$ ,  $T_0 = 200$  K, neutral).

Wind	IRad	Media	Sources [ $M_\odot$ ]
	X	$WNM_1$ , $WNM_2$	12, 23, 60
X		$WNM_1$ , $WNM_2$	12, 23, 60

The right ordinate shows the factor of the dominant to the subordinate process with  $\frac{P_{\text{Wind}}}{P_{\text{IRad}}}$  above and  $\frac{P_{\text{IRad}}}{P_{\text{Wind}}}$  below the equality of momentum,  $\frac{P_{\text{Wind}}}{P_{\text{IRad}}} = \frac{P_{\text{IRad}}}{P_{\text{Wind}}} = 1$ . Note that this factor diverges when  $I_p$  approaches unity. Fig. 7 reflects the results from Section 4, that stellar winds are important in the WIM and dominate radiation by a factor  $\frac{P_{\text{Wind}}}{P_{\text{IRad}}}$  of  $10^2$  around a  $12 M_\odot$  star and up to  $10^4$  around a  $60 M_\odot$  star. In the CNM, ionizing radiation is dominant with factors  $\frac{P_{\text{IRad}}}{P_{\text{Wind}}}$  around 50 for all considered stars. Going from the WIM to the WNM, the media change from being wind to ionizing radiation dominated. Hence, with densities larger than  $n_0 = 1 \text{ cm}^{-3}$  the media are radiation dominated.

The simulated and analytic values of  $I_p$  agree in the WIM for all star masses. In environments similar to the  $WNM_1$ , a steep transition happens from the wind dominated to radiation dominated regime. The density where  $I_p$  changes for the star with  $M_* = 60 M_\odot$  is smaller compared to the others because the temperature inside the  $H_{II}$  region is higher for more massive stars, hence a pressure gradient establishes at lower densities. In the  $WNM_2$  and the CNM, the analytic treatment agrees with the simulated values. In the  $WNM_1$  and  $WNM_2$  around the star with  $M_* = 60 M_\odot$ ,  $I_p$  the analytical

description is a factor  $\sim 3$  in  $\frac{P_{\text{IRad}}}{P_{\text{Wind}}}$  off the simulated values. The difference arises from the assumption in the analytic model, that the temperature inside the  $H_{II}$  region is not media-dependent and set to be constant. In addition, the shocks leave the computational domain early with the result of a lower momentum imposed by the ionizing radiation.

Our results disagree with the results for the low-density environment discussed in the work of Geen et al. (2015a). The reason is that the authors set a low temperature of  $62$  K in their low density environment with  $n_0 = 0.1 \text{ cm}^{-3}$ , which disagrees with the equilibrium temperature of  $\sim 10^4$  K derived from the chemical network we employ. The authors choice of parameters enables ionizing radiation to create an overpressured bubble and therefore overestimates the impact of radiation in their low-density model.

Based on the analytic model, we can specify the media dependence. In Fig. 8, we show  $I_p$  (color) as a function of the assumed constant ambient density and temperature for a star with  $M_* = 23 M_\odot$ . The black dashed line indicates the temperature inside the corresponding  $H_{II}$  region. The black solid line shows the number density-temperature relation in equilibrium used in the analytic model described in the context of Fig. 7. The white crosses show the ambient media assumed in this work. Fig. 8 shows that above the temperature set by photoionization, the medium is wind dominated. In addition at low densities ( $n < \sim 1 \text{ cm}^{-3}$ ) and corresponding temperatures above  $5000$  K, the influence of radiation decreases and  $I_p$  approaches 1. At higher densities and lower temperatures, the radiative-driven expansion dominates.

The simulations and our model assume solar metallicities. For environments with lower metallicities, the temperature inside an  $H_{II}$  region is higher as metal line cooling is reduced. Hence, we expect the resulting radiative momentum to increase as well. The result would be that the wind-dominated region is shifted to higher temperatures.

## 5 ENERGY COUPLING AND RADIATIVE COOLING

### 5.1 The coupling efficiency of stellar winds and ionizing radiation

The coupling efficiency,  $\epsilon$ , is a measure of how much emitted energy from a source,<sup>4</sup>  $E_{\text{src}}$ , remains in the system,  $E_{\text{sys}}$ , which then is able to drive radial momentum. We define  $E_{\text{src}}$  as (Freyer et al. 2003, 2006)

$$E_{\text{src}}(t) = \int_0^t L(t') dt', \quad (17)$$

where  $L$  is the source luminosity with  $L = L_{\text{IRad}}$  for ionizing radiation,  $L = L_{\text{Wind}}$  for stellar winds or  $L = L_{\text{IRad}} + L_{\text{Wind}}$  for the combination of both processes (see Fig. 1, bottom panel).

$E_{\text{sys}}$  is the part of the inserted energy that remains in the system in the form of kinetic and thermal energy. It is defined as

$$E_{\text{sys}}(t) = E(t) - E_0(t) \quad (18)$$

where  $E(t)$  is the total energy at time  $t$  and  $E_0(t)$  is the (thermal) energy of the gas in a reference box, which is evolved in isolation and slowly cooling down.

<sup>4</sup>An additional subscript indicates the stellar feedback process, which is source of the energy, e.g.  $E_{\text{src, IRad}}$ .

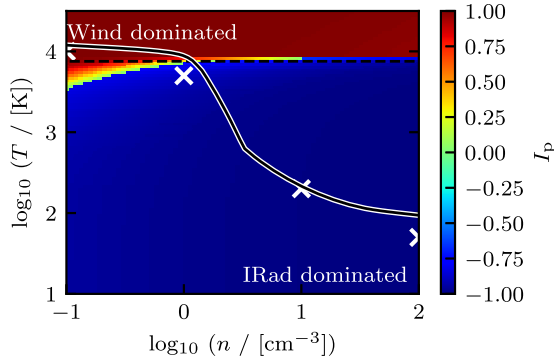


**Figure 8.** Time-average relative impact  $I_p$  (color) as a function of constant ambient density and temperature around a star with  $M_* = 23 M_\odot$ . The temperature inside the corresponding HII region is indicated as a black, dashed line. The black, solid line corresponds to the condition of heating and cooling balance, which are the bases for the analytic predictions in Fig. 7. The white crosses indicate the media used in this work (from left to right: WIM, WNM1, WNM2, CNM).

The coupling efficiency  $\epsilon$  is then defined as

$$\epsilon \equiv \frac{E_{\text{sys}}}{E_{\text{src}}}. \quad (19)$$

In Fig. 9, we show the coupling efficiencies  $\epsilon$  of ionizing radiation (middle, dashed), stellar winds (right, dotted) and the combination of both processes (left, solid) in the WIM (red) and CNM (black) for a star with a mass of  $23 M_\odot$ . We note that for different  $M_*$ , we find similar efficiencies and a similar time-dependent evolution. Two features are characteristic for all simulations. The initial coupling efficiency is high with  $\epsilon = 0.9$ , thus almost perfect, but drops rapidly within the first 0.1 Myr. Second, stellar winds couple more efficiently to the ambient medium than ionizing radiation.

In the CNM, the efficiency of ionizing radiation drops to  $\sim 10^{-5}$ . For stellar winds, we obtain values of  $\sim 10^{-4}$ . However, despite the higher  $\epsilon$ , the wind is not important since  $E_{\text{src,IRad}}/E_{\text{src,Wind}} \approx 10^3$ . In the WIM, ionizing radiation couples to the ambient gas with  $\epsilon < 10^{-6}$ , whereas we get  $\epsilon \sim 10^{-3}$  for the stellar wind. The coupling efficiency of the combination of both processes has values of  $\sim 10^{-5}$ , again because the radiation is more energetic than the wind but does not couple.

Overall, stellar winds couple more efficiently to the ambient medium than ionizing radiation in both, the WIM and the CNM. Ionizing radiation couples to the medium by ionizing and heating the gas, which is an inefficient process and susceptible to radiative cooling (see Section 5.2). This agrees with previous work, that show that the conversion of radiative to kinetic energy is highly inefficient (e.g. Walch et al. 2012).

## 5.2 Radiative cooling

Contrary to many previous papers, we self-consistently compute radiative heating and cooling everywhere in the computational domain. In this section, we discuss the importance of three, selected cooling processes by post-processing our simulations. These are radiative recombination of hydrogen (case B recombination, see Section 2.3), free-free emission of hydrogen, and soft X-ray emission in the energy band of 0.5 to 2 keV. The corresponding cooling rates are  $\Lambda_{\text{rc}}$  (Cen 1992),  $\Lambda_{\text{ff}}$  (Shapiro & Kang 1987) and  $\Lambda_{\text{X}}$ . For the last rate, we use tables generated with the ASTROPHYSICAL PLASMA

EMISSION CODE (APEC, Smith et al. 2001) from the collisional ionization database ATOMDB (Foster et al. 2010, [www.atomdb.org](http://www.atomdb.org)).

In Fig. 10, we show the calculated cooling rates associated with radiative recombination (dashed), free-free emission (dash-dotted) and X-ray emission (dotted) for the two simulations where a star with  $M_* = 23 M_\odot$  injecting a stellar wind and ionizing radiation has been placed in the WIM (red) or in the CNM (black). For comparison we show the input wind luminosity  $L_{\text{Wind}}$  (blue, dotted) and the radiation luminosity  $L_{\text{IRad}}$  (blue, dashed).

In the CNM, radiative recombination is the dominant cooling process with  $\Lambda_{\text{rc}} \sim 9 \times 10^{37} \text{ erg s}^{-1}$  while free-free emission is a factor of 3 smaller. X-ray emission saturates at a rate of  $\Lambda_{\text{X}} \sim 10^{30} \text{ erg s}^{-1}$ . About 50 percent of the total stellar luminosity,  $L_{\text{src}} = L_{\text{Wind}} + L_{\text{IRad}}$ , is lost by these three cooling processes. The residual energy is mostly lost by metal line cooling.

In the WIM, the radiative emission with  $\sim 10^{37} \text{ erg s}^{-1}$  is 3 orders of magnitude larger than the free-free emission, which is much smaller than the cooling rates found in the CNM. The total X-ray luminosity approaches a constant value of  $\sim 10^{29} \text{ erg s}^{-1}$ . Only  $\sim 1$  percent of the total stellar luminosity is lost by the three cooling processes.

This indicates that the difference in coupling efficiency  $\epsilon$  between ionizing radiation and stellar wind is due to cooling by radiative recombination. The interior of an HII region and the emissivity peak of radiative recombination have very similar temperatures (see equation (10)).

In both CNM and WIM, the energy loss by soft X-ray emission is small with  $\Lambda_{\text{X}} \sim 10^{30} \text{ erg s}^{-1}$  or  $\sim 10^{-8} L_{\text{src}}$ , respectively. Therefore, the X-ray emission predicted in our model is well below the results shown by Arthur (2007) and also below observed X-ray luminosities (e.g. Garcia-Segura & Mac Low 1995a; Wrigge et al. 2005). The reason is that they consider the early evolution of the wind-blown bubble (up to  $\sim 20,000$  years) where the density inside the bubble is presumably much higher and the temperature is lower, such that more soft X-ray emission is expected. Generally, X-ray emission has the peak emissivity in a temperature range of  $10^6 \text{ K} - 10^7 \text{ K}$  (Toalá & Arthur 2016). In the presented simulations, the X-ray emitting wind bubbles have typical temperatures of  $\sim 10^8 \text{ K}$  (see Fig. 5 and Fig. B1).

## 6 APPLICATION OF THE MODEL TO OBSERVED FEEDBACK BUBBLES

We select two representative observed bubbles, the predominantly radiation-driven bubble RCW 120 and NGC 7635 (including the S162 complex), where wind and radiation are acting in combination. We initialize our semi-analytic model presented in the Sections 2.1.2 and 2.2.1 and applied in Fig. 7 with the physical properties of these examples to estimate the relative impact of wind and radiation. The results presented in the following are rough approximations and assume spherical symmetry with homogeneous mass distribution and emission.

The HII region RCW 120 evolves around a  $\sim 30 M_\odot$  star of the age of 0.2 – 0.4 Myr within an environment with densities  $n_0 \sim 1400 - 3000 \text{ cm}^{-3}$  (Zavagno et al. 2007; Mackey et al. 2015; Figueira et al. 2017). When applying the semi-analytic model to a  $30 M_\odot$  star in a homogeneous medium with  $1500 \text{ cm}^{-3}$  we can estimate the relative impact to be  $I_p \sim -0.85$ , indicating that radiative feedback is indeed dominant. According to our model, the star imparts  $\sim 6.3 \times 10^5 M_\odot \text{ km s}^{-1}$  of momentum within 2 Myr.

RCW 120 is observed in  $\text{H}_\alpha$  and dust emission but shows no evidence of excited metal lines (Zavagno et al. 2007). This missing

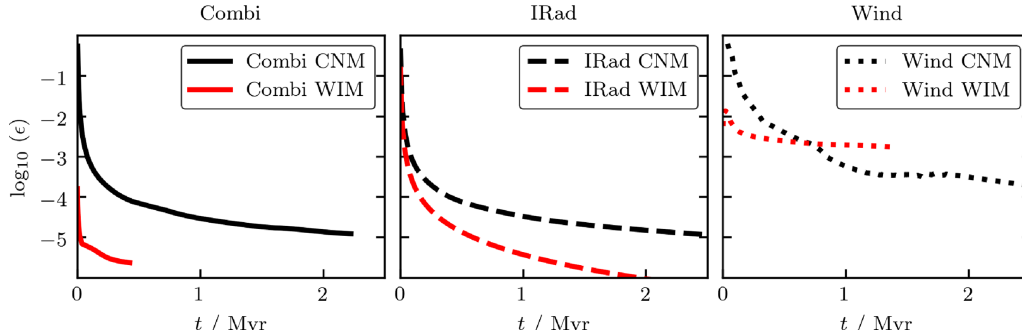


**Figure 9.** The evolution of the coupling efficiencies  $\epsilon$  is shown for a source with  $23 M_{\odot}$ . We distinguish between two media, WIM (red) and CNM (black). Ionizing radiation (middle, dashed) and stellar winds (right, dotted) are compared to the combination of both processes (left, solid). In all simulations, where the lines stop before 2.5 Myr, the feedback bubble expands out of the computational domain.

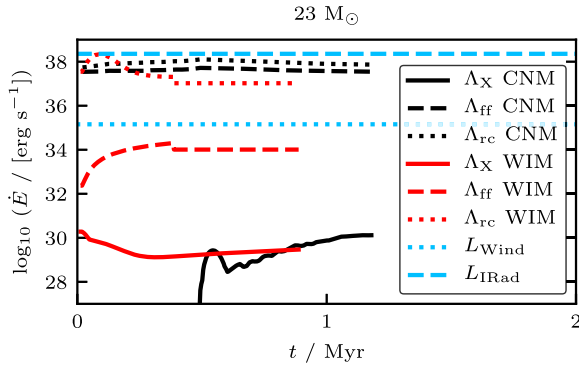


**Figure 10.** We compare different cooling processes in the WIM (red) and the CNM (black) when a bubble of ionizing radiation and stellar winds from a  $M_* = 23 M_{\odot}$  expands into it. We show the cooling rates associated with radiative recombination,  $\Lambda_{\text{rc}}$  (dashed), free-free emission,  $\Lambda_{\text{ff}}$  (dash-dotted), and X-ray emission,  $\Lambda_{\text{X}}$  (dotted). For comparison we show the wind luminosity  $L_{\text{Wind}}$  (blue, dotted) and the radiation luminosity  $L_{\text{IRad}}$  (blue, dashed) emitted by the star.

line emission indicates that the bubble is indeed radiation-driven, which agrees with our results that stellar winds are unimportant for the early evolution in the CNM. In contrast, the other, clearly wind-driven bubbles like NGC 6888 appear bright in  $H_{\alpha}$  as well as metal line emission e.g. [OIII] (Toalá et al. 2012; Toalá & Guerrero 2013). This evolved bubble is fully filled with wind-heated gas (compare with Fig. 3).

An example for combined feedback is NGC 7635. The entire object emits  $H_{\alpha}$  radiation while only the central part emits [OIII] in addition. From these observations and the previous discussion we can distinguish between the central, 2 pc wide, spherical, wind-driven region and the surrounding  $H_{\text{II}}$  region with a diameter between 2.5 – 3.1 pc (Christopoulou et al. 1995; Moore et al. 2002b). The mean densities inside the wind-blown bubble and the  $H_{\text{II}}$  region are estimated with,  $n_{\text{Wind, obs}} = 100 \text{ cm}^{-3}$  and  $n_{\text{IRad, obs}} = 300 \text{ cm}^{-3}$ , respectively (Thronson et al. 1982; Christopoulou et al. 1995; Moore et al. 2002b; Mesa-Delgado & Esteban 2010). The central source is a 0.3 Myr old, O6.5 star with a wind mass-loss rate of  $\sim 10^{-6} M_{\odot} \text{ yr}^{-1}$ , a wind velocity of  $\sim 2500 \text{ km s}^{-1}$ , and an estimated flux of  $\dot{N}_{\text{LC}} \sim 10^{49} \text{ s}^{-1}$  (Icke 1973; Moore et al. 2002b, a), thus similar to the  $23 M_{\odot}$  star considered in this work.

The wind-blown bubble has an observed mass,  $M_{\text{Wind, obs}}$ , of 3 – 14  $M_{\odot}$  and a radial expansion velocity of 4 – 25  $\text{km s}^{-1}$  (Thronson et al. 1982; Mesa-Delgado & Esteban 2010). With this, the resulting radial momentum of the wind driven-gas,  $p_{\text{Wind, obs}}$ , ranges from 12 to 350  $M_{\odot} \text{ km s}^{-1}$ . However, for the surrounding  $H_{\text{II}}$  region the corresponding properties can only be crudely estimated as measurements are insufficient. With an approximated mass,  $M_{\text{IRad, obs}}$ , of 26 – 91  $M_{\odot}$  (spherical shell with  $n_{\text{IRad, obs}}$ ) and a velocity of  $\sim 4$  – 5  $\text{km s}^{-1}$  (expansion of 2.5 to 3.1 pc within 0.3 Myr) we obtain a momentum of  $p_{\text{IRad, obs}} \sim 110$  – 450  $M_{\odot} \text{ km s}^{-1}$ .

We can also make use of our semi-analytic model to estimate the impact of the  $H_{\text{II}}$  region: for this, we assume a  $23 M_{\odot}$  star and an environmental density of  $n_{\text{IRad, obs}} = 300 \text{ cm}^{-3}$ . The model obtains a relative impact of  $I_p \sim -0.9$  with the total radial momentum imparted by radiation,  $p_{\text{IRad, mod}}$ , to be  $\sim 4700 M_{\odot} \text{ km s}^{-1}$  and the corresponding momentum from stellar winds  $p_{\text{Wind, mod}}$ , to be  $\sim 1300 M_{\odot} \text{ km s}^{-1}$ . The modelled and observed momenta differ by up to a factor of 10. The modelled bubble radius in case of wind feedback is 2.4 pc (a factor of  $\sim 2.4$  larger than the observed radius of 1 pc) and the modelled radius in case of radiative feedback is 3.1 pc (a factor of 2 – 2.4 larger than the observed radius with 1.25 – 1.55 pc). These differences are closely linked to the significant uncertainties of the observed densities and velocities, the estimated mass of the central star as well as the assumption of homogeneity in the model. To obtain comparable momenta from the model assuming a  $23 M_{\odot}$  star, the ambient density has to be increased to a few  $1000 \text{ cm}^{-3}$  which is comparable to the densities observed in the northern part of NGC 7635. The bubbles have expanded to the observed radii after 0.4 Myr. The relative impact is then reduced to -0.6.

Finally, we want to estimate the relative impact of feedback in NGC 7635 by comparing the observed  $H_{\alpha}$  emission from the  $H_{\text{II}}$  and the wind-blown region. The corresponding luminosities for the wind-driven,  $L_{H_{\alpha}, \text{Wind, obs}}$ , and the radiation-driven bubble,  $L_{H_{\alpha}, \text{IRad, obs}}$ , are  $4.9 \times 10^{35} \text{ erg s}^{-1}$  and  $1.0$  –  $1.5 \times 10^{36} \text{ erg s}^{-1}$ , respectively (assuming an averaged flux over a representative part of the regions, Moore et al. 2002a, b). To obtain the relative impact,  $I_p$ , we follow the idea of equation (16) and substitute the momenta,  $p_{\text{IRad}}$  and  $p_{\text{Wind}}$ , by  $L_{H_{\alpha}, \text{IRad, obs}}$  and  $L_{H_{\alpha}, \text{Wind, obs}}$ . The resulting relative impact  $I_p$  ranges from -0.4 to -0.6. This is in reasonable agreement with the estimates from the semi-analytic model,  $I_p = -0.6$  – -0.9. In both cases, the relative impact in NGC 7635 is clearly dominated by radiative feedback but the wind increases in impor-

tance. We expect even better agreement when relaxing the assumptions of homogeneity (as e.g. done for supernova-driven bubbles in Haid et al. 2016).

## 7 SUMMARY

In this paper, we investigate the impact and the coupling efficiencies of stellar winds and ionizing radiation from single massive stars. We perform a series of hydrodynamic simulations with the AMR code FLASH 4 including the novel radiative transfer scheme TREERAY, which is coupled to a chemical network. We use the On-The-Spot approximation with a temperature-dependent recombination coefficient and account for ionization heating within the  $H_{II}$  region. The initial conditions of homogeneous ambient media match the properties of the WIM ( $10^4$  K,  $0.1 \text{ cm}^{-3}$ , ionized), the WNM (2000 K,  $1 \text{ cm}^{-3}$ ), and the CNM (20 K,  $100 \text{ cm}^{-3}$ , predominantly neutral). Stars with  $M_* = 12, 23$ , and  $60 M_\odot$  are used as sources. We expect magnetic fields, omitted in this work, to affect the shape of the feedback bubble but not change the results found here in a qualitative way.

We benchmark the coupling of the radiative transfer implementation with the chemistry module against the Monte-Carlo photoionization code MOCASSIN and recover comparable mean temperatures within the  $H_{II}$  regions for the different stars.

With ionization and stellar winds included, the radiation-driven shock is always ahead of the wind-driven shock. This implies that the wind-blown bubble is always surrounded by a  $H_{II}$  region. The differential impact of stellar winds and ionizing radiation - tested separately - is highly dependent on the properties of the ambient ISM. Within the CNM, ionizing radiation dominates the momentum input ( $1.6 \times 10^4$  to  $4 \times 10^5 M_\odot \text{ km s}^{-1}$ ). Stellar winds are only shock-heating a small inner bubble and contribute a negligible amount of momentum in comparison with radiation. When comparing these results to the impact of single SNe in the CNM, we find an equal or higher momentum input for stars with a mass of  $23 M_\odot$  and above. In the WIM, the momentum input of stellar winds is similar to the CNM ( $2 \times 10^2$  to  $5 \times 10^3 M_\odot \text{ km s}^{-1}$ ), while ionizing radiation falls short ( $\sim 10^2 M_\odot \text{ km s}^{-1}$ ). With both processes at work, ionizing radiation supports the wind-driven expansion by preventing the rarefied environment from cooling and recombining. We also show that the warm neutral medium is a transition regime from ionization dominated momentum injection in the CNM to wind dominated injection in the WIM. We introduce an analytic model to predict in which homogeneous media ionizing radiation or stellar wind is dominating. The values from this description are similar to the results from the numerical simulations.

Energetically, stellar winds couple more efficiently to the ISM ( $\sim 0.1$  percent of wind luminosity) than ionizing radiation ( $< 0.001$  percent of ionizing luminosity). The low coupling efficiency of ionizing radiation results from the high cooling rate associated with radiative recombination and free-free emission.

For estimating the global impact of massive stars on different surrounding media, the strongly mass-dependent ratios of wind luminosity to ionizing luminosity (see Fig. 1) have to be considered. It is likely, that a massive star interacts with vastly different environments during its lifetime due to the short dispersal time scales of young star clusters and the significant fraction of runaway massive stars. In summary, this study shows that the relative impact of stellar winds and ionizing radiation depends on the stellar mass considered but even more strongly on the properties of the ambient medium.

## ACKNOWLEDGEMENTS

SH, SW, DS, and FD acknowledge the support by the Bonn-Cologne Graduate School for Physics and Astronomy which is funded through the German Excellence Initiative. SH, SW, and DS also acknowledge funding by the Deutsche Forschungsgemeinschaft (DFG) via the Sonderforschungsbereich SFB 956 ‘Conditions and Impact of Star Formation’ (subproject C5). SH, SW, DS, FD and TN acknowledge the support by the DFG Priority Program 1573 ‘The physics of the interstellar medium’. SH and SW acknowledge funding by the European Research Council through ERC Starting Grant No. 679852 ‘RADFEEDBACK’. TN acknowledges support from the DFG cluster of excellence ‘Origin and Structure of the Universe’. R.W. acknowledges support by the Albert Einstein Centre for Gravitation and Astrophysics via the Czech Science Foundation grant 14-37086G and by the institutional project RVO:67985815 of the Academy of Sciences of the Czech Republic. The software used in this work was developed in part by the DOE NNSA ASC- and DOE Office Science ASCR-supported FLASH Center for Computational Science at University of Chicago. The authors gratefully acknowledge the Gauss Centre for Supercomputing e.V. ([www.gauss-centre.eu](http://www.gauss-centre.eu)) for funding this project by providing computing time on the GCS Supercomputer SuperMUC at Leibniz Supercomputing Centre (<http://www.lrz.de>). We thank the YT-PROJECT community (Turk et al. 2011) for the yt analysis package, which we used to analyse and plot most of the data. We thank the anonymous referees for the constructive input.

## REFERENCES

- Arthur S. J., 2007, in *Revista Mexicana de Astronomia y Astrofisica Conference Series*, 30
- Arthur S. J., Henney W. J., Mellema G., de Colle F., Vázquez-Semadeni E., 2011, *MNRAS*, 414, 1747
- Bisbas T. G., et al., 2015, *MNRAS*, 453, 1324
- Bouchut F., Klingenberg C., Waagan K., 2007, *Num. Math.*, 108, 7
- Bouchut F., Klingenberg C., Waagan K., 2010, *Num. Math.*, 115, 647
- Castor J., McCray R., Weaver R., 1975, *ApJ*, 200, L107
- Cen R., 1992, *ApJS*, 78, 341
- Christopoulou P. E., Goudis C. D., Meaburn J., Dyson J. E., Clayton C. A., 1995, *A&A*, 295, 509
- Dale J. E., 2015, *New Astron. Rev.*, 68, 1
- Dale J. E., Ercolano B., Bonnell I. A. 2012, *MNRAS*, 424, 377
- Dale J. E., Bonnell I. A., 2008, *MNRAS*, 391, 2
- Dale J. E., Bonnell I. A., Clarke C. J., Bate M. R., 2005, *MNRAS*, 358, 291
- Dale J. E., Ngoumou J., Ercolano B., Bonnell I. A., 2013, *MNRAS*, 436, 3430
- Dale J. E., Ngoumou J., Ercolano B., Bonnell I. A., 2014, *MNRAS*, 442, 694
- Dobbs C. L., Krumholz M. R., Ballesteros-Paredes J. et al., 2014, *Protostars and Planets VI*, 3
- Draine B. T., 1978, *ApJS*, 36, 595
- Dubey A., Fisher R., Graziani C. et al., 2008, in *Pogorelov N. V., Audit E., Zank G. P., eds., Astronomical Society of the Pacific Conference Series*, 385, Numerical Modeling of Space Plasma Flows, Astronomical Society of the Pacific, San Francisco, p. 145
- Dwarkadas V. V., 2007, *ApJ*, 667, 226
- Dyson J. E., Williams D. A., 1980, *Physics of the Interstellar Medium*, Halsted Press, New York
- Ekström S., Georgy C., Eggenberger P. et al., 2012, *A&A*, 537, A146
- Elmegreen B. G., Lada C. J. 1977, *ApJ*, 214, 725
- Ercolano B., Barlow M. J., Storey P. J., Liu X.-W., 2003, *MNRAS*, 340, 1136
- Everett J. E., Churchwell E., 2010, *ApJ*, 713, 592
- Fall S. M., Krumholz M. R., Matzner C. D., 2010, *ApJ*, 710, L142



- Falle S. A. E. G., 1975, *A&A*, 43, 323
- Felli M., Churchwell E., Massi M., 1984, *A&A*, 136, 53
- Figueira M., Zavagno A., Deharveng L. et al., 2017, *A&A*, 600, A93
- Foster A., Smith R. K., Brickhouse N. S., Kallman T. R., 2010, *Bull/ Am. Astron. Soc.*, 42, 524
- Franco J., Tenorio-Tagle G., Bodenheimer P., 1990, *ApJ*, 349, 126
- Freyer T., Hensler G., Yorke H. W., 2003, *ApJ*, 594, 888
- Freyer T., Hensler G., Yorke H. W., 2006, *ApJ*, 638, 262
- Fryxell B., Olson K., Ricker P. et al., 2000, *ApJS*, 131, 273
- Garcia-Segura G., Mac Low M.-M., 1995a, *ApJ*, 455, 145
- Garcia-Segura G., Mac Low M.-M., 1995b, *ApJ*, 455, 160
- Garcia-Segura G., Langer N., Mac Low M.-M., 1996, *A&A*, 316, 133
- Gatto A., Walch S., Naab T. et al., 2017, *MNRAS*, 466, 1903
- Geen S., Hennebelle P., Tremblin P., Rosdahl J. 2015a, *MNRAS*, 454, 4484
- Geen S., Rosdahl J., Blaizot J., Devriendt J., Slyz A., 2015b *MNRAS*, 448, 3248
- Gies D. R., Bolton C. T. 1986, *ApJS*, 61, 419
- Glover S. C. O., Mac Low M.-M., 2007b, *ApJ*, 659, 1317
- Glover S. C. O., Mac Low M.-M., 2007a, *ApJS*, 169, 239
- Glover S. C. O., Federrath C., Mac Low M.-M., Klessen R. S. 2010, *MNRAS*, 404, 2
- Gnat O., Ferland G. J., 2012, *ApJS*, 199, 20
- Górski K. M., Hivon E., Banday A. J. et al., 2005, *ApJ*, 622, 759
- Gritschneider M., Naab T., Walch S., Burkert A., Heitsch F., 2009, *ApJ*, 694, L26
- Gritschneider M., Burkert A., Naab T., Walch S., 2010, *ApJ*, 723, 971
- Habing H. J., 1968, *Bull. Astron. Inst. Netherlands*, 19, 421
- Haid S., Walch S., Naab T. et al., 2016, *MNRAS*, 460, 2962
- Harper-Clark E., Murray N., 2009, *ApJ*, 693, 1696
- Hensler G., Kroeger D., Freyer T., 2008, in *Israelian G., Meynet G., eds. The Metal-Rich Universe*, Cambridge University Press, Cambridge, p. 327
- Hoogerwerf R., de Bruijne J. H. J., de Zeeuw P. T., 2000, *ApJ*, 544, L133
- Hopkins P. F., Kereš D., Oñorbe J. et al., 2014, *MNRAS*, 445, 581
- Hosokawa T., Inutsuka S.-i., 2006, *ApJ*, 646, 240
- Howard C., Pudritz R., Klessen R., 2017, *ApJ*, 834, 40
- Huthoff F., Kaper L., 2002, *A&A*, 383, 999
- Icke V., 1973, *A&A*, 26, 45
- Koo B.-C., McKee C. F., 1992, *ApJ*, 388, 93
- Kröger D., Hensler G., Freyer T., 2006, *A&A*, 450, L5
- Krumholz M. R., 2006, *ApJ*, 641, L45
- Krumholz M. R., 2014, *Phys. Rep.*, 539, 49
- Krumholz M. R., Matzner C. D., 2009, *ApJ*, 703, 1352
- Krumholz M. R., Klein R. I., McKee C. F., Offner S. S. R., Cunningham A. J., 2009, *Science*, 323, 754
- Mackey J., Langer N., Gvaramadze V. V., 2013, *MNRAS*, 436, 859
- Mackey J., Gvaramadze V. V., Mohamed S., Langer N., 2015, *A&A*, 573, A10
- Matzner C. D., 2002, *ApJ*, 566, 302
- Mesa-Delgado A., Esteban C., 2010, *MNRAS*, 405, 2651
- Moore B. D., Hester J. J., Scowen P. A., Walter D. K., 2002a *AJ*, 124, 3305
- Moore B. D., Walter D. K., Hester J. J. et al., 2002b *AJ*, 124, 3313
- Murray N., Ménard B., Thompson T. A., 2011, *ApJ*, 735, 66
- Naab T., Ostriker J. P., 2017, *ARA&A*, 55, 59
- Nelson R. P., Langer W. D., 1997, *ApJ*, 482, 796
- Ngoumou J., Hubber D., Dale J. E., Burkert A., 2015, *ApJ*, 798, 32
- Ostriker E. C., McKee C. F., Leroy A. K., 2010, *ApJ*, 721, 975
- Pittard J. M., 2013, *MNRAS*, 435, 3600
- Pittard J. M., Dyson J. E., Hartquist T. W., 2001, *A&A*, 367, 1000
- Puls J., Sundqvist J. O., Najarro F., Hanson M. M., 2009, in *Hubeny I., Stone J. M., MacGregor K., Werner K., eds., American Institute of Physics Conference Series*, Vol. 1171, p. 123
- Rahner D., Pellegrini E. W., Glover S. C. O., Klessen R. S., 2017, *MNRAS*, 470, 4453
- Rogers H., Pittard J. M., 2013, *MNRAS*, 431, 1337
- Röllig M., Abel N. P., Bell T. et al., 2007, *A&A*, 467, 187
- Rosen A. L., Lopez L. A., Krumholz M. R., Ramirez-Ruiz E., 2014, *MNRAS*, 442, 2701
- Rybicki G. B., Lightman A. P., 2004, *Radiative Processes in Astrophysics*, Wiley-VCH Verlag, Weinheim
- Sales L. V., Marinacci F., Springel V., Petkova M., 2014, *MNRAS*, 439, 2990
- Sembach K. R., Howk J. C., Ryans R. S. I., Keenan F. P., 2000, *ApJ*, 528, 310
- Shapiro P. R., Kang H., 1987, *ApJ*, 318, 32
- Smith R. K., Brickhouse N. S., Liedahl D. A., Raymond J. C., 2001, *ApJ*, 556, L91
- Spitzer L., 1978, *Physical Processes in the Interstellar Medium*, Wiley-Interscience, New York
- Stone R. C., 1991, *AJ*, 102, 333
- Strömgren B., 1939, *ApJ*, 89, 526
- Thronson H. A., Jr., Lada C. J., Harvey P. M., Werner M. W., 1982, *MNRAS*, 201, 429
- Tielens A. G. G. M., 2005, *The Physics and Chemistry of the Interstellar Medium*, Cambridge University Press, Cambridge
- Toalá J. A., Arthur S. J., 2011, *ApJ*, 737, 100
- Toalá J. A., Arthur S. J., 2016, *MNRAS*, 463, 4438
- Toalá J. A., Guerrero M. A., 2013, *A&A*, 559, A52
- Toalá J. A., Guerrero M. A., Chu Y.-H. et al., 2012, *ApJ*, 755, 77
- Turk M. J., Smith B. D., Oishi J. S. et al., 2011, *ApJS*, 192, 9
- Waagan K., 2009, *Journal of Computational Physics*, 228, 8609
- Waagan K., Federrath C., Klingenberg C., 2011, *J. Comput. Phys.*, 230, 3331
- Walch S., Naab T., 2015, *MNRAS*, 451, 2757
- Walch S. K., Whitworth A. P., Bisbas T., Wünsch R., Hubber D., 2012, *MNRAS*, 427, 625
- Walch S., Whitworth A. P., Bisbas T. G., Wünsch R., Hubber D. A., 2013, *MNRAS*, 435, 917
- Walch S., Girichidis P., Naab T. et al., 2015, *MNRAS*, 454, 238
- Wareing C. J., Pittard J. M., Falle S. A. E. G., 2017, *MNRAS*, 470, 2283
- Weaver R., McCray R., Castor J., Shapiro P., Moore R., 1977, *ApJ*, 218, 377
- Whitworth A., 1979, *MNRAS*, 186, 59
- Wolfire M. G., Hollenbach D., McKee C. F., Tielens A. G. G. M., Bakes E. L. O., 1995, *ApJ*, 443, 152
- Wrigge M., Chu Y.-H., Magnier E. A., Wendker H. J. 2005, *ApJ*, 633, 248
- Wünsch R., Walch S., Whitworth A. P., Dinnbier F. 2017, *MNRAS*, in press
- Zavagno A., Pomarès M., Deharveng L. et al., 2007, *A&A*, 472, 835

## APPENDIX A: INTERSTELLAR RADIATION FIELD

As discussed in Section 2.3, we include a background interstellar radiation field (ISRF) of homogeneous strength  $G_0 = 1.7$  (Habing 1968; Draine 1978). To assume the ISRF to be constant near a massive star is an approximation. In Fig. A1, we show the influence of the ISRF on the WIM, hence the temperature evolution. We expect the FUV radiation to penetrate deeper into the rarefied medium and choose three homogeneous strength of  $G_0 = 1.7$  (solid), 17 (dashed) and 170 (dotted). The initial drop of temperature is slowed down as the ISRF is increased. However, the maximum possible temperature difference is 20 percent with an average difference of under 10 percent between the  $G_0 = 1.7$  and 170. We conclude, that a homogeneous ISRF is valid for the presented simulations.

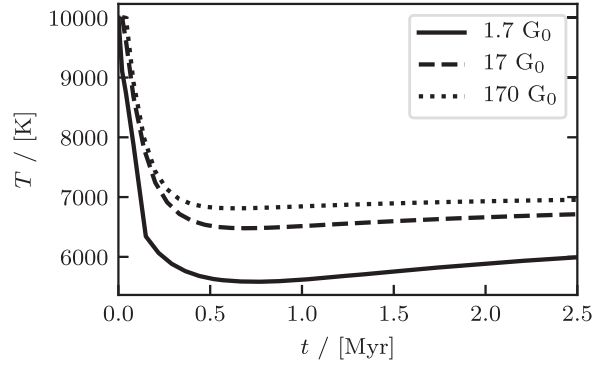


**Figure A1.** Temperature evolution of the WIM without a massive star under the conditions of a homogeneous ISRF with  $G_0 = 1.7$  (solid), 17 (dashed), and 170 (dotted).

## APPENDIX B: RADIAL PROFILES

In Fig. B1, we show the radial profiles of density  $\rho$  (top), the temperature  $T$  (second), the pressure over the Boltzmann constant  $P/k_B$  (third) and the mean momentum of a cell  $\bar{p}_i$  (bottom) for simulations with stellar winds and ionizing radiation in the CNM (left) and the WIM (right) for stars with  $M_* = 12$  (dotted), 23 (dashed), and 60 (solid)  $M_\odot$ .

In the CNM, the shock position increases with increasing mass of the star. The behaviour of density and temperature are discussed in Section 3.1. The third panel shows, that the expansion is pressure driven with a pressure contrast of almost 2 orders of magnitude. The resulting shock carries most of the radial momentum. The interior expands too but with a significant lower momentum.

In the WIM, the shock density is a factor of  $\sim 4$  higher than the ambient density. Within the almost homogeneous interior the density drops to  $\sim 10^{-28}$  g cm $^{-3}$  with a temperature of  $\sim 10^8$  K. The result are pressures between  $\sim 3 \times 10^3$  K cm $^{-3}$  and  $\sim 2 \times 10^4$  K cm $^{-3}$  for the star with  $M_* = 12$  and 60  $M_\odot$ , respectively. The wind-driven shock contains a significant fraction of the radial momentum. The momentum in the shock is 3 orders of magnitude higher compared to the interior.

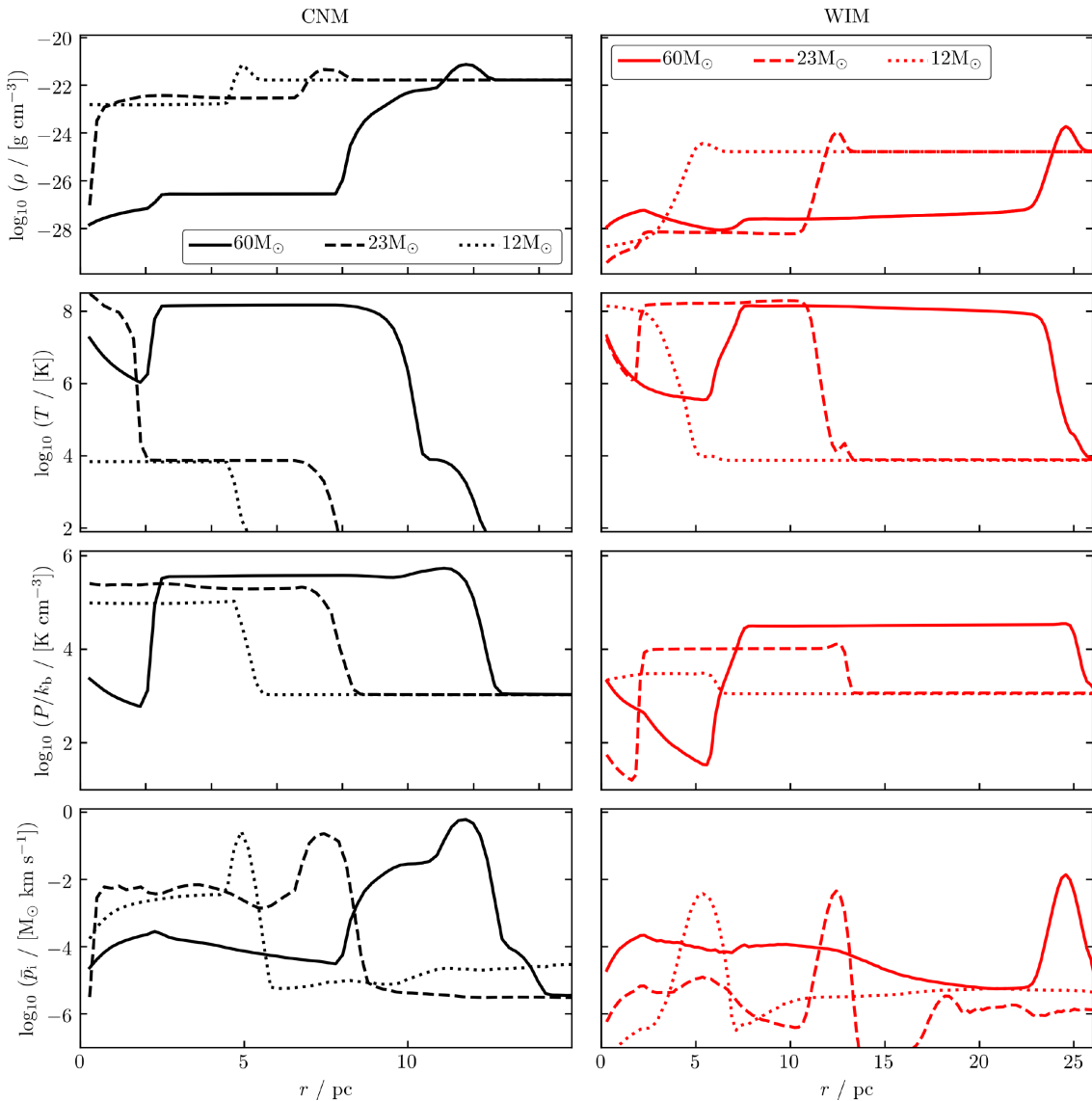


**Figure B1.** The radial profiles of the combination of stellar winds and ionizing radiation which were obtained from the simulation for Fig. 3. The left (red) and the right (black) column shows the radially averaged values in the WIM and the CNM. Each panel includes the structure from stars with  $M_* = 12$  (dotted), 23 (dashed) and 60 (solid)  $M_\odot$ . For top to bottom, we show the density  $\rho$ , the temperature  $T$ , the pressure over the Boltzmann constant  $P/k_B$ , and the mean momentum of a cell  $\bar{p}_i$ . The x-axis match the zoom-in length scale of Fig. 3 with 25 and 15 pc.

## APPENDIX C: IMPACT OF RADIATION PRESSURE

The impact of radiation pressure is highly debated. This process is considered to be unimportant in the CNM (Rahner et al. 2017) and with a source luminosity  $L_{\text{Rad}}$  from a single star with  $M_* \approx 23 M_\odot$  (Krumholz et al. 2009; Fall Krumholz & Matzner 2010; Murray, Ménard & Thompson 2011; Sales et al. 2014).

In Fig. C1, we compare the momentum evolution from ionizing radiation feedback with (dash-dotted) and without radiation pressure (dashed) on gas in the CNM. At  $t = 2.5$  Myr, the momentum input from the radiation only simulation is  $8.4 \times 10^4 M_\odot \text{ km s}^{-1}$  and increases by about 20 percent with additional radiation pressure. We conclude that radiation pressure is subdominant. In the WIM, the impact of radiation pressure is expected to be even smaller, due to the inefficient coupling of the radiation.

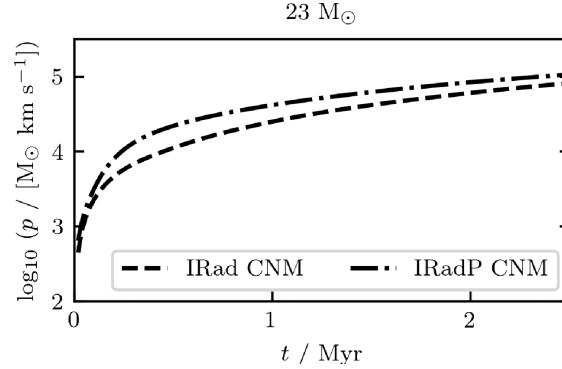


**Figure C1.** Momentum evolution of ionization feedback from a  $23 M_\odot$  source in the CNM. We compare the radiation feedback without (dashed) and with (dash-dotted) radiation pressure.

This paper has been typeset from a  $\text{\LaTeX}$  file prepared by the author.







# SILCC-Zoom: The early impact of ionizing radiation on forming molecular clouds

S. Haid<sup>1</sup>,<sup>\*</sup> S. Walch,<sup>1</sup> D. Seifried<sup>1</sup>, R. Wünsch,<sup>2</sup> F. Dinnbier<sup>1</sup> and T. Naab<sup>3</sup>

<sup>1</sup>*I. Physikalisches Institut, Universität zu Köln, Zùlpicher-Strasse 77, D-50937 Cologne, Germany*

<sup>2</sup>*Astronomický Ústav, Akademie věd české republiky, Benf II 1401, CZ-14131 Praha, Czech Republic*

<sup>3</sup>*Max-Planck-Institut für Astrophysik, Karl-Schwarzschild-Strasse 1, D-85741 Garching, Germany*

Accepted 2018 October 22. Received 2018 October 17; in original form 2018 February 18

## ABSTRACT

As part of the SILCC-Zoom project, we present our first sub-parsec resolution radiation-hydrodynamic simulations of two molecular clouds self-consistently forming from a turbulent, multiphase ISM. The clouds have similar initial masses of few  $10^4 M_\odot$ , escape velocities of  $\sim 5 \text{ km s}^{-1}$ , and a similar initial energy budget. We follow the formation of star clusters with a sink-based model and the impact of radiation from individual massive stars with the tree-based radiation transfer module TREERAY. Photoionizing radiation is coupled to a chemical network to follow gas heating, cooling, and molecule formation and dissociation. For the first 3 Myr of cloud evolution, we find that the overall star formation efficiency is considerably reduced by a factor of  $\sim 4$  to global cloud values of  $< 10$  per cent as the mass accretion of sinks that host massive stars is terminated after  $\lesssim 1$  Myr. Despite the low efficiency, star formation is triggered across the clouds. Therefore, a much larger region of the cloud is affected by radiation and the clouds begin to disperse. The time-scale on which the clouds are dispersed sensitively depends on the cloud sub-structure and in particular on the amount of gas at high visual extinction. The damage of radiation done to the highly shielded cloud ( $MC_1$ ) is delayed. We also show that the radiation input can sustain the thermal and kinetic energy of the clouds at a constant level. Our results strongly support the importance of ionizing radiation from massive stars for explaining the low-observed star formation efficiency of molecular clouds.

**Key words:** hydrodynamics – methods: numerical – stars: formation – ISM: clouds – ISM: kinematics and dynamics.

## 1 INTRODUCTION

Molecular clouds (MCs) condense out of the diffuse, interstellar medium (ISM). These dense regions host filamentary sub-structures of molecular gas with an atomic envelope (André et al. 2014; Dobbs et al. 2014; Klessen & Glover 2016). Massive stars form in infrared dark clouds, which are the densest parts of MCs (Goldreich & Kwan 1974; Lada & Lada 2003; Rathborne, Jackson & Simon 2006; Klessen 2011; Ragan et al. 2012). During their lifetime, massive stars emit ionizing radiation and eject high-velocity winds, which result in the deposition of momentum, kinetic, and thermal energy in the ISM and change the chemical composition. The underlying physical processes are collectively termed *stellar feedback*, i.e. stellar winds (Castor, McCray & Weaver 1975; Weaver et al. 1977; Wünsch et al. 2011), ionizing radiation (Spitzer 1978; Hosokawa & Inutsuka 2006; Dale, Ercolano & Bonnell 2012; Walch et al. 2012), radiation pressure (Krumholz & Matzner 2009; Fall, Krumholz &

Matzner 2010; Murray, Quataert & Thompson 2010), and supernovae (Sedov 1958; Ostriker & McKee 1988; Walch & Naab 2015; Körtgen et al. 2016). Feedback modifies density structures, counteracts the gravitational collapse, interrupts mass accretion, and directly influences the cycle of star formation. However, the detailed impact on MCs evolution is still a matter of discussion (Whitworth 1979; Krumholz 2006; Krumholz et al. 2009; Walch et al. 2012; Dale 2015). It seems clear that stellar feedback can change the local and global multiphase structure of the ISM with dramatic consequences for star formation (Naab & Ostriker 2017).

MCs are complex. Observations indicate that they are embedded in their galactic environment (Mac Low, de Avillez & Korpi 2004) and coupled to large-scale (some 100 pc) motions (Hughes et al. 2013; Colombo et al. 2014). Galactic turbulent velocity fields seem to be inherited (Brunt, Heyer & Mac Low 2009) with consequences for the star formation rate (Rey-Raposo, Dobbs & Duarte-Cabral 2015). Hence, it is likely that the cloud properties are already imprinted during early formation and continuously reshaped by physical processes on galactic scales (Dobbs, Pringle & Burkert 2012;

\* E-mail: haid@ph1.uni-koeln.de

Walch et al. 2015; Girichidis et al. 2016; Seifried et al. 2017; Rey-Raposo et al. 2017). This also suggests that the possible support of MCs by internal stellar feedback is highly variable and depends on the cloud structure. Analytical models, which are usefully guiding our theoretical understanding, may not fully reflect the complexity of self-consistently evolving MCs (Matzner 2002).

Early studies treat MCs in isolated environments to investigate gravitational collapse and implications for the star formation rate (Shu 1977; Foster & Chevalier 1993; Hetem & Lepine 1993; Klessen, Heitsch & Mac Low 2000; Dale et al. 2005; Gavagnin et al. 2017). Follow-up studies started to investigate connections to the surrounding ISM with idealized gas replenishing scenarios such as colliding flows (Heitsch et al. 2005; Vázquez-Semadeni et al. 2007, 2010) or cloud–cloud collisions (Whitworth et al. 1994; Inoue & Fukui 2013; Balfour et al. 2015; Dobbs, Pringle & Duarte-Cabral 2015). In galactic-scale simulations (de Avillez & Breitschwerdt 2005; Slyz et al. 2005; Joung & Mac Low 2006; Hill et al. 2012; Kim, Ostriker & Kim 2013; Hennebelle & Iffrig 2014; Smith et al. 2014a; Dobbs 2015; Walch et al. 2015; Girichidis et al. 2016), the statistical properties of MCs are analysed and the global importance of individual feedback processes are estimated (Girichidis et al. 2016; Padoan et al. 2016; Gatto et al. 2017; Padoan et al. 2017; Peters et al. 2017; Kim & Ostriker 2018). Recent progress in computational performance enables us to simulate a galactic-scale environment and simultaneously increase the spatial and time resolution in forming MC. This technique is referred to as a *zoom-in* simulation (Clark et al. 2012; Bonnell, Dobbs & Smith 2013; Smith, Glover & Klessen 2014b; Dobbs 2015; Butler et al. 2017; Ibáñez-Mejía et al. 2017; Kuffmeier, Haugbølle & Nordlund 2017; Nordlund et al. 2017; Pettitt et al. 2017; Seifried et al. 2017). The advantage is that large-scale influences (e.g. supernova shocks) are propagated down to MC-scales and cloud formation can be studied in a self-consistently evolved environment.

The impact of stellar feedback strongly depends on the mass of the star, hence the UV-luminosity (Geen et al. 2018), and its environment. A massive star with  $M_* \approx 23 M_\odot$  emits a factor of  $\sim 100$  less energy in a wind than it releases in radiative energy (Matzner 2002) but higher/lower mass stars have stronger/weaker winds relative to radiation. Furthermore, stellar winds are inefficiently coupled to dense environment (Haid et al. 2018). Therefore, in massive MCs ( $M \gtrsim 10^5 M_\odot$ ), the impact of stellar winds seems negligible (Dale et al. 2014; Geen et al. 2015; Ngoumou et al. 2015; Howard, Pudritz & Klessen 2017). However, in low-mass MCs ( $M \approx 10^4 M_\odot$ ), winds are able to reshape the clouds, ablate dense material, and even drive gas out of the clouds through low-density channels (Rogers & Pittard 2013). Winds are also more important than radiation if the environment of the massive star is already warm or hot because in this case the radiation does not couple to the surrounding ISM and the radiative energy cannot be deposited in the gas (i.e. low coupling efficiency; Haid et al. 2018). Ionizing radiation also struggles to impact bound, massive MCs (Dale et al. 2012, 2013), while clouds with the sound speed of the photoionized gas being similar to the escape velocity can be dispersed completely within a few Myr (Walch et al. 2012). In any case, both processes shape the environment for the final supernova explosions to leak out, thereby dispersing the clouds effectively (Harper-Clark & Murray 2009; Pittard 2013; Rosen et al. 2014; Gatto et al. 2017; Naab & Ostriker 2017; Peters et al. 2017; Wareing, Pittard & Falle 2017).

The observed star formation in MCs is low with only a few per cent of gas that is converted into stars during one free-fall time (Zuckerman & Evans 1974; Evans et al. 2009; Murray 2011). This inefficiency suggests that processes inside a cloud op-

pose the gravitational collapse. Stellar feedback is discussed to be an internal driver of supersonic turbulence with a velocity dispersion of a few  $\text{km s}^{-1}$  (Mac Low et al. 2004; Mac Low & Klessen 2004; Mellema et al. 2006; Walch et al. 2012). However, numerical simulations fail to reproduce this low level of star formation (Klessen et al. 2000; Vázquez-Semadeni, Ballesteros-Paredes & Klessen 2003; Dale et al. 2014).

Therefore, two aspects of the interaction of stellar feedback with the MC environment remain a matter of discussion. Is star formation limited to the low-observed values of a few per cent as a consequence of internal feedback processes? What is the role of MC sub-structure and filling factor on the coupling efficiencies of stellar winds and ionizing radiation (Haid et al. 2018)?

To address these questions, we present 3D, radiation–hydrodynamic adaptive mesh refinement (AMR) simulations of MCs as part of a supernova-driven, multiphase ISM in a piece of a galactic disc (within the SILCC project; Walch et al. 2015; Girichidis et al. 2016). We apply a zoom-in technique to follow the formation and evolution of two MCs with total gas masses of a few  $10^4 M_\odot$  with an effective resolution of 0.122 pc (Seifried et al. 2017). Sink particles are integrated by our novel predictor–corrector scheme (Dinnbier et al., in preparation). With a model of star cluster formation within sink particles, we couple ionizing radiation to the ambient medium (Haid et al. 2018). The radiation is treated by the novel, tree-based radiative transfer scheme TREERAY (Wünsch et al., in preparation) based on the tree solver for gravity and diffuse radiation implemented in FLASH (Wünsch et al. 2018). For now, we neglect stellar winds, as their contribution in the early, dense phase of MCs is likely subordinate to ionizing radiation (Dale et al. 2014; Haid et al. 2018). We focus on the interplay of ionizing radiation and the particular MC morphology and star formation efficiency.

The paper is organized as follows. In Section 2, we present the numerical method. In Section 3, we give an overview of the simulation set-up. We discuss the morphological impact of ionizing radiation in Section 4. We depict the effect of radiative feedback on the environment around the stellar component (Section 5). The evolution of global cloud properties is shown in Section 6 and the differences between the two clouds are discussed in Section 7. Finally, we conclude in Section 8.

## 2 NUMERICAL METHOD

We use the 3D AMR magneto-hydrodynamics code FLASH 4 (Fryxell et al. 2000; Dubey et al. 2008) with the directionally split, Bouchut HLLSR solver (Bouchut, Klingenberg & Waagan 2007, 2010; Waagan 2009; Waagan, Federrath & Klingenberg 2011) including self-gravity, a chemical network to follow molecule formation and dissociation, the novel radiative transfer module TREERAY, sink particles, and the stellar evolution of massive stars.

### 2.1 Sink particles

Sink particles represent the unresolved formation of stars or clusters by gravitational collapse. In the simulations, we use a new particle module (Dinnbier et al., in preparation) that uses a Hermite predictor–corrector integrator and is coupled to the Barnes-Hut tree (Wünsch et al. 2018). The sink formation and accretion criteria are the same as in Federrath et al. (2010). In this work, sink particles represent star clusters (hereafter also simply called sinks) within which multiple massive stars (hereafter also stars) can form. For further information on the cluster sink implementation, we refer to Gatto et al. (2017).

A sink particle can only be formed in a computational cell and followed through the computational domain if the harbouring cell lives on the highest refinement level (smallest spatial resolution) in the AMR hierarchy. The accretion radius  $r_{\text{accr}}$  is set to  $r_{\text{accr}} = 2.5 \times \Delta x = 0.31$  pc. We further demand that the gas, within  $r_{\text{accr}}$  is Jeans unstable, is in a converging flow and represents a local gravitational potential minimum (Federrath et al. 2010). Under the assumption of an isothermal gas with a temperature  $T = 100$  K, we derive the density threshold above which sinks can form,  $\rho_{\text{si}} = 1.1 \times 10^{-20} \text{ g cm}^{-3}$  following the Jeans criterion:

$$\rho_{\text{si}} = \frac{\pi k_B}{m_p G} \frac{T}{4r_{\text{accr}}^2} \quad (1)$$

where  $k_B$  is the Boltzmann constant and  $G$  the gravitational constant (Truelove et al. 1997; Gatto et al. 2017).

Sink particles accrete gas. A fraction of the accreted gas is turned into massive stars by means of the star cluster sub-grid model. Assuming a Kroupa stellar initial mass function (IMF), one new massive star ( $9 M_\odot \leq M_* \leq 120 M_\odot$ ) is randomly sampled for every  $120 M_\odot$  accreted on a sink (Kroupa 2001). We assume the Salpeter slope of  $-2.35$  in the high-mass regime of the IMF (Salpeter 1955). Each sink with a mass  $M_{\text{si}}$  can contain  $N_*$  stars with individual initial masses  $M_*$  and individual stellar evolutions tracks (see Ekström et al. 2012, Gatto et al. 2017, Peters et al. 2017 and references therein). We refer to the number of massive stars,  $N_*$ , in a sink as the *active stellar component*,  $M_{*,\text{tot}}$ , with  $M_{*,\text{tot}} = \sum_{i=1}^{N_*} M_{*,i}$ . The residual gas is converted into low-mass stars, which are not recorded individually as they currently provide no feedback to the surrounding medium.

Each sink particle is subject to the gravitational attraction of the gas and the other sink particles. Their trajectories are integrated by a predictor–corrector scheme, which is inspired by the two nested fourth-order Hermite predictor–corrector integrators used in the NBODY6 code (Makino 1991; Makino & Aarseth 1992; Aarseth 1999, 2003). Here, the outer (regular) integrator takes into account the slowly varying force due to the gas, while the inner (irregular) integrator takes into account the fast-varying force due to the other sink particles. It is an analogue to the Ahmad–Cohen scheme (Ahmad & Cohen 1973), where the division to regular and irregular forces is based on the kind of interaction (gas or sink particles) instead of physical proximity. The regular time-step corresponds to the hydrodynamical time-step, while the irregular time-step  $\Delta t_{\text{irr}}$  is calculated according to the standard formula (Aarseth 2003)

$$\Delta t_{\text{irr}} = \left( \frac{\eta(|\mathbf{a}||\ddot{\mathbf{a}}| + |\dot{\mathbf{a}}|^2)}{|\dot{\mathbf{a}}||\ddot{\mathbf{a}}| + |\ddot{\mathbf{a}}|^2} \right)^{1/2}, \quad (2)$$

and then quantized to bins differing by factor of 2 in time. We set the constant for integration  $\eta$  to be  $\eta = 0.01$ . The quantities  $\mathbf{a}$ ,  $\dot{\mathbf{a}}$ ,  $\ddot{\mathbf{a}}$ , and  $\ddot{\mathbf{a}}$  are the acceleration and the higher time derivatives acting on the particle due to the other sink particles. The scheme uses the softening kernel described in Monaghan & Lattanzio (1985) with softening length corresponding to  $2.5 \times \Delta x = 0.31$  pc at the highest refinement level. Likewise, gas is attracted by sink particles, which are placed to the tree to facilitate the force evaluation. We present the detailed description of the sink particle integrator as well as numerical tests in Dinbier et al. (in preparation).

## 2.2 Ionizing radiation and radiative heating

The transfer of ionizing radiation is calculated by a new module for the FLASH code called TREERAY. It is an extension of the FLASH tree solver described in Wünsch et al. (2018). TREERAY uses the

octal-tree data structure constructed and updated at each time-step by the tree solver and shares it with the GRAVITY (calculates gas self-gravity, see Wünsch et al. 2018), OPTICAL-DEPTH (calculates the optical depth and parameters for the total,  $\text{H}_2$  and CO shielding, see Walch et al. 2015; Wünsch et al. 2018), and EUV modules. The latter is the new module that calculates the local flux of ionizing radiation. Here, we only give basic information about TREERAY; a detailed description alongside with accuracy and performance tests will be presented in Wünsch et al. (in preparation). TREERAY has already been benchmarked in Bisbas et al. (2015) and applied in homogeneous media (Haid et al. 2018).

Each node of the octal-tree represents a cuboidal collection of grid cells and stores the total gas mass contained in it, masses of individual chemical species, and the position of the mass centre. In addition to that, TREERAY stores for each node the total amount of the radiation luminosity generated inside the node, the radiation energy flux passing through the node, and the node volume. Before the tree is traversed for each grid cell (called *target cell*), a system of  $N_{\text{pix}}$  rays pointing from the target cell to different directions is constructed. The directions are determined by the HEALPIX algorithm (Górski et al. 2005), which tessellates the unit sphere into elements of equal spatial angle. We use  $N_{\text{pix}} = 48$ . Each ray is then divided into segments with lengths increasing linearly with the distance from the target cell. In this way, the segment lengths correspond approximately to the sizes of the nodes interacting with the target cell during the tree walk if the Barnes–Hut (BH) criterion for node acceptance is used. Here, we use the BH criterion with an opening angle of  $\theta_{\text{lim}} = 0.5$ . When the tree is traversed, node densities, radiation luminosities, and energy fluxes are mapped on to the ray according to the node and the volume belonging to the ray segment.

Finally, after the tree walk, the 1D radiative transport equation is solved using the *On-the-Spot approximation* along each ray using the case B recombination coefficient  $\alpha_B$  with the temperature dependence in the range of  $T = [5000, 20000]$  K given by (Draine 2011)

$$\alpha_B = 2.56 \times 10^{-13} \text{ cm}^3 \text{ s}^{-1} \left( \frac{T}{10^4 \text{ K}} \right)^{-0.83}. \quad (3)$$

The radiative transfer equation along the ray towards the target cell is given by

$$F_0 = \sum_{i=N-1}^0 \left[ \frac{\epsilon_i}{4\pi r_i^2} - \sum_{j=i+1}^N \alpha_B \frac{F_{i,j}^2}{F_{\text{tot},i}} dV_{ij} \right], \quad (4)$$

where  $F_0$  is the received flux in the target cell,  $N$  is the number of segments along a ray,  $\epsilon_i$  is the emission coefficient in segment  $i$ ,  $F_{\text{tot},i}$  the total flux coming into segment  $i$ ,  $F_{i,j}$  the source in a segment if a source exists,  $r_i$  the distance from the segment to the target cell, and  $dV_{ij}$  the volume of the segment. As the radiation flux passing through a given segment from different directions has to be taken into account, the solution has to be searched for iteratively, repeating the whole process of tree construction, tree walk, and solving the radiation transport equation until the maximum relative error drops below 0.01. To speed up convergence, we use the result of the previous hydrodynamic time-step as the radiation field typically changes only slightly between time-steps, in most cases only one or two iterations are needed in each time-step.

We use the prescription given in Gatto et al. (2017) and Peters et al. (2017) to simulate the evolution, and in particular the radiative energy output, of massive stars using the Geneva stellar tracks from the zero-age main sequence to the Wolf–Rayet phase (Kudritzki &

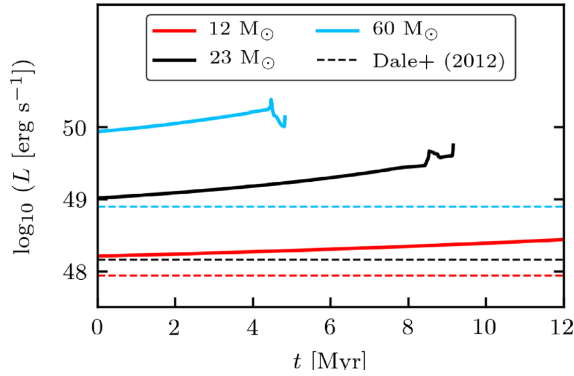


**Figure 1.** Time evolution of the radiative luminosities  $L_{\text{RAD}}$  of stars with  $M_* = 12$  (red),  $23$  (black), and  $60 M_\odot$  (blue). The dashed lines show the values used in the simulations of Dale et al. (2012). Note that the end of the evolution of the  $12 M_\odot$  is not shown here.

Puls 2000; Markova et al. 2004; Markova & Puls 2008; Puls, Vink & Najarro 2008; Ekström et al. 2012). An initial proto-stellar phase is not included. The corresponding time evolution of the radiative luminosity  $L$  is shown in Fig. 1 for three stars with  $M_* = 12$  (red),  $23$  (black), and  $60 M_\odot$  (blue). For the later discussion, we include dashed horizontal lines that correspond to the luminosities used in Dale et al. (2012, 2014) based on stellar models of Diaz-Miller, Franco & Shore (1998).

The aforementioned stellar tracks provide the time-dependent number of Lyman continuum photons,  $\dot{N}_{\text{Lyc}}$ , and the effective stellar temperature (Peters et al. 2017). In TREERAY, this information is processed to get the average excess photon energy,  $E_{\bar{\nu}-\nu_T}$ , between  $\nu_T = 13.6 \text{ eV } h^{-1}$  and the average photon frequency,  $\bar{\nu}$ , by assuming a black-body spectrum for each star and integrating it in the Lyman continuum (Rybicki & Lightman 2004). Note that since we only consider the radiative transfer in a single energy band (all photons in the Lyman continuum), we do not distinguish between the direct ionization of H and  $\text{H}_2$ , as necessary for detailed models of photon-dominated regions (Röllig et al. 2007; Baczynski, Glover & Klessen 2015).

We calculate the heating rate,  $\Gamma_{\text{ih}}$ , in the ionization–recombination equilibrium with (Tielens 2005)

$$\Gamma_{\text{ih}} = F_{\text{ph}} \sigma E_{\bar{\nu}-\nu_T} = n_{\text{H}}^2 \alpha_{\text{B}} h (\bar{\nu} - \nu_T), \quad (5)$$

where  $F_{\text{ph}}$  is the photon flux,  $\sigma$  the hydrogen photoionization cross-section,  $n_{\text{H}}$  the hydrogen number density, and  $h$  is the Planck constant. The ionization heating rate and number of ionizing photons are provided to the CHEMISTRY module (see Section 2.3), where the temperature is self-consistently increased by balancing heating and cooling processes, the mean hydrogen ionization state is updated using the given photoionization rate (Haid et al. 2018) and CO is dissociated. In ionization–recombination equilibrium, an H II region develops around the sink particle with interior temperatures between  $\sim 7000$ – $9000$  K. In homogeneous media, this is well explained by the ionization of the Strömgren sphere followed by the *Spitzer* expansion (Strömgren 1939; Spitzer 1978; Hosokawa & Inutsuka 2006). However, the equilibrium temperature strongly depends on the density of the ionized gas within the H II region and can be significantly lower in young, embedded H II regions, which are still quite dense (see Section 5.2).

## The early impact of ionizing radiation 4065

### 2.3 Gas cooling, heating, and chemistry

We include a simple chemical network, which is explained in detail in Walch et al. (2015). It is based on Glover & Mac Low (2007a,b), Glover et al. (2010), and Nelson & Langer (1997) to follow the abundances of seven chemical species: molecular, atomic, and ionized hydrogen as well as carbon monoxide, ionized carbon, atomic oxygen, and free electrons ( $\text{H}_2$ , H,  $\text{H}^+$ , CO,  $\text{C}^+$ , O, and  $\text{e}^-$ ). The gas has solar metallicity (Sembach et al. 2000) with fixed elemental abundances of carbon, oxygen, and silicon ( $x_{\text{C}} = 1.14 \times 10^{-4}$ ,  $x_{\text{O}} = 3.16 \times 10^{-4}$ ,  $x_{\text{Si}} = 1.5 \times 10^{-5}$ ) and the dust-to-gas mass ratio is set to 0.01. We include a background interstellar radiation field (ISRF) of homogeneous strength  $G_0 = 1.7$  (Habing 1968; Draine 1978). So far, TREERAY does not treat the far-ultraviolet (FUV) regime. The effect of radiation in the FUV energy band will be discussed in a follow-up paper. For the cloud dynamics, we still expect photoionization to be the dominant process (Peters et al. 2010b; Walch et al. 2012; Baczynski et al. 2015) with typical temperatures around  $\sim 8000$  K almost independently of gas densities. FUV radiation is considered to be important in photodissociation regions that are forming ahead of the ionization shock fronts. As we show in Section 5.2, a hypothetical FUV field of  $1000 \times G_0$  increases the gas temperature in such dense ( $\sim 10^{-21} \text{ g cm}^{-3}$ ) photodissociation regions to a few 100 K at most. Therefore, the predicted dynamical effect resulting from the FUV heating is considered to be negligible with respect to the EUV heating.

The ISRF is attenuated in shielded regions depending on the column densities of total gas,  $\text{H}_2$ , and CO. Thus, we consider dust shielding and molecular (self-) shielding for  $\text{H}_2$  and CO (Glover et al. 2010) by calculating the shielding coefficients with the TREERAY OPTICAL-DEPTH module (Wünsch et al. 2018). From the effective column density in each cell the visual extinction,  $A_{\text{v}}$ , is calculated by

$$A_{\text{v}} = \frac{N_{\text{H}}}{1.8 \times 10^{21} \text{ cm}^2}, \quad (6)$$

where the total gas column density  $N_{\text{H}}$  is given by  $N_{\text{H}} = \Sigma_{\text{H}} / (\mu m_{\text{p}})$  where  $\Sigma_{\text{H}}$  is the surface density,  $\mu$  is the mean molecular weight, and  $m_{\text{p}}$  is the proton mass.

For gas with temperatures above  $10^4$  K, we model the cooling rates according to Gnat & Ferland (2012) in collisional ionization equilibrium. Non-equilibrium cooling (also for Lyman  $\alpha$ ) is followed at lower temperatures through the chemical network. Within the H II region, we neglect both  $\text{C}^+$  and O cooling because these species are predominantly in a higher ionization state. Heating rates include the photoelectric effect, cosmic ray ionization with a rate of  $\xi = 3 \times 10^{-17} \text{ s}^{-1}$ , X-ray ionization by Wolfire et al. (1995), and photoionization heating (see Section 2.2).

## 3 SIMULATION SET-UP

### 3.1 The SILCC simulation

The SILCC simulation (Walch et al. 2015; Girichidis et al. 2016) is the basic set-up and is used to self-consistently study the evolution of the supernova-driven multiphase ISM. The computational domain with an extent of  $500 \text{ pc} \times 500 \text{ pc} \pm 5 \text{ kpc}$  has a disc mid-plane with galactic properties at low red-shift similar to the solar neighbourhood. The boundary conditions for the gas are periodic in  $x$ - and  $y$ -direction and outflow in  $z$ -direction. For gravity, the boundary conditions are periodic in  $x$ - and  $y$ -direction and isolated in  $z$ -direction (see Wünsch et al. 2018 for mixed gravity boundary



**Table 1.** Overview of the total (top, subscript *tot*) and the central part (bottom, subscript *CoV*) of MC<sub>1</sub> and MC<sub>2</sub> with the centre *c* in *x*, *y*, *z* coordinates (second column), the side length *d* in *x*, *y*, *z* direction (third column), the gas mass *M* (fourth column), and the escape velocity *v*<sub>esc</sub> of the cloud (last column) at *t*<sub>0,MC1</sub> = 13.51 Myr and *t*<sub>0,MC2</sub> = 13.40 Myr.

Cloud	<i>c</i> <sub>tot</sub> (pc)	<i>d</i> <sub>tot</sub> (pc)	<i>M</i> <sub>tot</sub> (M <sub>⊙</sub> )	<i>v</i> <sub>esc</sub> (km s <sup>−1</sup> )
MC <sub>1</sub>	157, −115, 0	88, 87, 77	$1.0 \times 10^5$	5.3
MC <sub>2</sub>	45, 196, −3	87, 87, 71	$8.5 \times 10^4$	4.5
	<i>c</i> <sub>CoV</sub> [pc]	<i>d</i> <sub>CoV</sub> (pc)	<i>M</i> <sub>CoV</sub> (M <sub>⊙</sub> )	<i>v</i> <sub>esc</sub> (km s <sup>−1</sup> )
MC <sub>1</sub>	127, −112, −4	40, 40, 40	$4.0 \times 10^4$	7.1
MC <sub>2</sub>	55, 192, 1	40, 40, 40	$2.7 \times 10^4$	5.2

conditions). The base grid resolution, denoted as *l*<sub>ref</sub> = 5 in the following, is Δ*x* = 3.9 pc.

Initially, the disc has a gas surface density of Σ<sub>Gas</sub> = 10 M<sub>⊙</sub> pc<sup>−2</sup>, and the density profile follows a Gaussian distribution in the vertical direction:

$$\rho(z) = \rho_0 \exp \left[ -\frac{1}{2} \left( \frac{z}{h_z} \right)^2 \right], \quad (7)$$

where the scale height of the gas *h*<sub>z</sub> = 30 pc and the mid-plane density ρ<sub>0</sub> = 9 × 10<sup>−24</sup> g cm<sup>−3</sup>. The initial temperature of the gas near the mid-plane is 4500 K and the disc is made up of H and C<sup>+</sup>. The density is floored to 10<sup>−28</sup> g cm<sup>−3</sup> with a temperature of 4 × 10<sup>8</sup> K in the gas at high altitudes above and below the galactic plane.

The simulation includes a static background potential to model the old and inactive stellar component in the disc, which is modelled as an isothermal sheet with a stellar surface density Σ<sub>\*</sub> = 30 M<sub>⊙</sub> pc<sup>−2</sup> and a scale height of 100 pc (Spitzer 1942). This static potential is added to the gravitational potential of the self-gravitating gas that is calculated in every time-step.

For the first *t*<sub>ZI</sub> = 11.9 Myr from the start of the simulations, the development of a multiphase ISM is driven by supernova explosions. Therefore, we inject supernovae at a fixed rate of 15 Myr<sup>−1</sup>. The supernova rate bases on the Kennicutt–Schmidt relation (Schmidt 1959; Kennicutt 1998) and a standard IMF for Σ<sub>Gas</sub>. We use mixed supernova driving, where supernovae explode in density peaks and at random positions by an equal share (1:1 ratio). In *z*-direction, the positioning of the random supernovae is weighted with a Gaussian distribution with a scale height of 50 pc (see Walch et al. 2015 and Girichidis et al. 2016 for more details).

A single supernova injects 10<sup>51</sup> erg of energy. Whether the energy is injected in the form of internal energy or momentum depends on the ability to resolve the Sedov–Taylor radius. The spherical injection region has a minimum radius of four grid cells. In case the density is low, the Sedov–Taylor radius is resolved and the energy thermally injected. If it is unresolved, the temperature in the region is raised to *T* = 10<sup>4</sup> K and the supernova bubble is momentum driven (Blondin et al. 1998; Gatto et al. 2015; Walch et al. 2015; Haid et al. 2016).

### 3.2 Initial conditions for this work: the zoom-in simulations

We refer to the resimulation of selected clouds with a higher spatial resolution as *zoom-in*. Two different MCs, MC<sub>1</sub> and MC<sub>2</sub>, are selected from the SILCC-Zoom simulation (Seifried et al. 2017). The selected domains (see Table 1) are traced back in time to properly model the formation process from the beginning. The zoom-in

starts at *t*<sub>ZI</sub> = 11.9 Myr where supernova driving is suspended and the typical number densities in the selected zoom-in regions do not exceed some 10 cm<sup>−3</sup>.

During the zoom-in simulation, the resolution is gradually increased in both MCs. Starting from the SILCC base grid resolution of Δ*x* = 3.9 pc (*l*<sub>ref</sub> = 5), we allow adaptive refinement down to Δ*x* = 0.122 pc (*l*<sub>ref</sub> = 10). Two refinement criteria are used. The refinement on the second derivative of gas densities, which picks up density fluctuations, is limited to a maximum refinement of 0.5 pc. Further refinement to the smallest Δ*x* depends on the local Jeans length, *L*<sub>Jeans</sub>, which is computed for each cell. We require that *L*<sub>Jeans</sub> is resolved with at least 16 cells in each spatial dimension, otherwise we refine.

The zoom-in is not carried out in a single time-step. Starting from the base grid resolution, we increase the refinement step-by-step and require about 200 time-steps in between two steps. On the one hand, this choice allows the relaxation of the gas to prevent filamentary grid artefacts, which appear in case of an instantaneous zoom-in (Seifried et al. 2017). On the other hand, it avoids the formation of large-scale, rotating, disc-like structures in case of a slower zoom-in in which case compressive motions are dissipated too efficiently. The zoom-in simulation reaches the highest refinement level at *t*<sub>ZE</sub> = 13.2 Myr.

### 3.3 Simulation overview

In this work, we continue from the zoom-in simulation at *t*<sub>ZE</sub> = 13.2 Myr and allow for the formation of cluster sink particles. From this time we start two simulations. The reference run, ZI<sub>NOFB</sub>, does not include any stellar feedback. In the second simulation, ZI<sub>RAD</sub>, the forming, active stellar component provides ionizing radiation.

Note that each simulation contains both MCs, MC<sub>1</sub> and MC<sub>2</sub> with similar volumes *V*<sub>tot</sub>, in which the zoom-in is enabled, and total gas masses *M*<sub>tot</sub> within 10 percent. Table 1 summarizes the initial properties of the clouds. Each cloud develops its own sink evolution, i.e. star formation history. The first sink in MC<sub>1</sub> forms at *t*<sub>0,MC1</sub> = 13.51 Myr and in MC<sub>2</sub> at *t*<sub>0,MC2</sub> = 13.40 Myr. As radiation feedback sets in, the clouds start to evolve differently. Therefore, we define six times *τ*<sub>*i*</sub> relative to *t*<sub>0</sub>, which we use for the analysis of the clouds as

$$\tau_i \equiv t_i - t_0 \text{ with } i \in [0, 1.0, 1.5, 2.0, 2.5, 3.0]. \quad (8)$$

The subscript *i* indicates the time in Myr after *t*<sub>0</sub>, i.e. *τ*<sub>0</sub> = 0 Myr refers to *t*<sub>0</sub> and *τ*<sub>3.0</sub> = 3.0 Myr after *t*<sub>0</sub>. A second subscript is used to indicate the respective MC.

Fig. 2 shows the total gas column density, Σ<sub>gas</sub>, in the *y*-*z* plane in MC<sub>1</sub> (top) and MC<sub>2</sub> (bottom) at *τ*<sub>0</sub>. To obtain Σ<sub>gas</sub>, we integrate the density ρ along the *x*-direction within the volume *V*<sub>tot</sub> (see Table 1). The black frames indicate the central sub-regions (later referred to as centre of volume, CoV) to be shown in more detail in Figs 3 and 4 with properties summarized in Table 1.

## 4 THE MORPHOLOGY OF THE MOLECULAR CLOUDS

The masses and volumes of MC<sub>1</sub> and MC<sub>2</sub> are comparable (see Table 1). However, their formation out of the turbulent, multiphase ISM leads to different morphologies (see Fig. 2). MC<sub>1</sub> contains a highly collimated, dense (Σ<sub>gas</sub> ≈ 500 M<sub>⊙</sub> pc<sup>−2</sup>), T-shaped filament, where the bar is one horizontal structure with extended ends. The vertical trunk is divided into two, roughly parallel sub-structures.

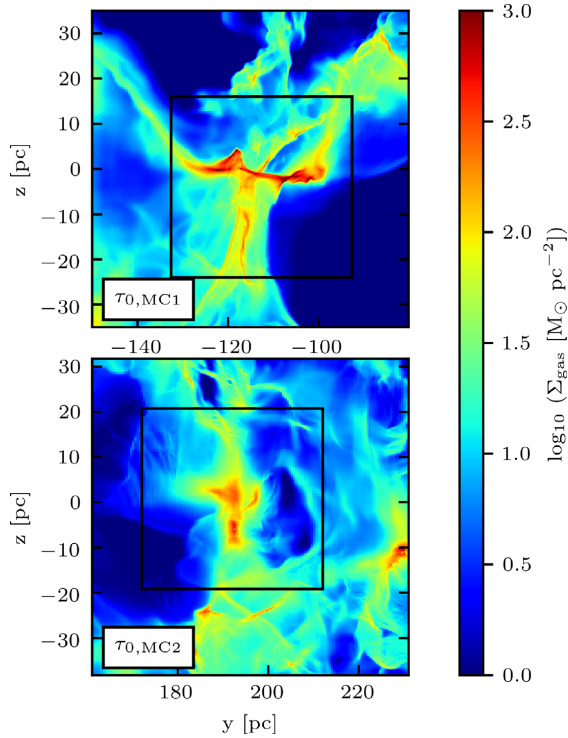


**Figure 2.** Gas column density  $\Sigma_{\text{gas}}$  in the  $y$ - $z$ -plane for the total volume  $V_{\text{tot}}$  of cloud MC<sub>1</sub> (top) and MC<sub>2</sub> (bottom) at the formation time of the first massive star, at  $t_{0,\text{MC1}} = 13.73$  and  $t_{0,\text{MC2}} = 13.55$  Myr. The black frames indicate the central volume  $V_{\text{CoV}}$  to be shown in more detail in Figs 3 and 4.

Each of the dense filaments is surrounded by an ‘envelope’ with intermediate column densities ( $\Sigma_{\text{gas}} \approx 5 - 50 \text{ M}_{\odot} \text{ pc}^{-2}$ ). To the bottom right, a low column density ( $\Sigma_{\text{gas}} \approx 0.05 - 0.5 \text{ M}_{\odot} \text{ pc}^{-2}$ ) cavity is situated, which originates from a previous supernova explosion outside the cloud. In MC<sub>2</sub>, the main filamentary structure is vertically elongated and less condensed with a central, hub-like condensation. Qualitatively, the surface density maps of MC<sub>1</sub> and MC<sub>2</sub> span the same dynamic range.

In Figs 3 and 4, we show the time evolution (from top to bottom) of the column densities of MC<sub>1</sub> and MC<sub>2</sub> without (leftmost column) and with radiative feedback (second column). Sink particles without and with active stellar components are indicated with circles and stars, respectively, with their age indicated by a second colour scheme ranging from 0 to 3 Myr. The third and fourth column show the column densities of molecular hydrogen and ionized hydrogen for the runs with radiation. Here, we only show the central ( $40 \text{ pc} \times 40 \text{ pc}$ ) sub-region of the clouds (see Table 1, bottom, subscript ‘CoV’) and therefore the column densities are obtained from the integration along the  $x$ -direction over the corresponding  $40 \text{ pc}$ , henceforth  $V_{\text{CoV}}$ . By comparing the maximum values of  $\Sigma_{\text{gas}}$  in Fig. 2 with Figs 3 and 4, one can see that only lower density gas from the fore and background has been cut.

Without feedback (runs ZLNOFB), gravity is further condensing the initial structures, while the lower column density gas surrounding the main filaments is accreted. In MC<sub>2</sub>, the gas is gravitationally collapsing, but the global structure of the cloud does not change

significantly and is still recognizable at  $\tau_{3.0}$ . In both clouds, sink formation occurs in the densest filament(s) and its debris.

Radiative feedback (runs ZLRAD) does not significantly alter the global dynamics of MC<sub>1</sub> during the first 2 Myr but more filamentary sub-structures appear, while the existing sub-structures seem to be locally supported against gravitational collapse. The dense regions are puffed up by the expanding radiative shocks. Multiple radiation-driven, partly or fully embedded bubbles develop (see  $\Sigma_{\text{H}+}$  in the right columns of Figs 3 and 4). Some active sinks do not form a noticeable bubble of ionized hydrogen, in particular if the contained massive stars that are less massive than  $20 \text{ M}_{\odot}$ . During the last Myr, the clouds decompose and a variety of filamentary sub-structures evolve into all directions. The envelope is widened and heated gas is expelled into the cavity. Star formation takes place in the bar and its remnants but primarily in the central dense clump (compare to  $\Sigma_{\text{H}2}$  in the third column of Fig. 3). In MC<sub>2</sub>, the bottom half of the cloud forms massive stars quickly, while the upper half forms only low-mass and hence inactive sink particles. Feedback from the bottom half disrupts the cloud into an upper, crescent-shaped filament (compare to  $\Sigma_{\text{H}2}$  in Fig. 4, third column) and some left-over, dispersed gas below (see  $\Sigma_{\text{H}+}$  at  $\tau_{3.0}$  in Fig. 4, fourth column). At later time, the emerging feedback triggers a second generation ( $y = 195 \text{ pc}$ ,  $z = 5 \text{ pc}$ ) of massive stars in the upper part. The low-density envelope is replenished with expelled gas.

MC<sub>1</sub> and MC<sub>2</sub> with radiative feedback show a significant difference in morphology. The first cloud evolves into one massive structure with multiple embedded HII regions and is surrounded by a low-density envelope, which is only slowly evolving. The central structure hosts almost all stars and star formation continues. The second cloud is partly destroyed by a rapidly forming first generation of stars in the lower cloud filament. A new generation of stars is triggered in the upper part of the central sub-region, which demonstrates that not only the mass (which is roughly similar for both clouds) but also the morphology prior to stellar feedback influences its impact. We investigate this further in Section 6.

## 5 CLOUD ENVIRONMENTS WITH MASSIVE STARS

In runs ZLNOFB, the total numbers of sinks in MC<sub>1</sub> and MC<sub>2</sub> at time  $\tau_{3.0}$  is 39 and 19 with masses of  $\sim 1.8 \times 10^4$  and  $1.5 \times 10^4 \text{ M}_{\odot}$ , respectively. In ZLRAD, the two clouds host 31 sinks with  $\sim 5900 \text{ M}_{\odot}$  and 23 sinks with  $\sim 3300 \text{ M}_{\odot}$ , respectively (see top panel of Fig. B1). Hence, in MC<sub>1</sub> more sinks with a smaller average mass per sink particle are formed than in MC<sub>2</sub>. The different fragmentation properties of the two clouds is caused by the different cloud sub-structure. In MC<sub>2</sub>, the total number of sinks is slightly increased by radiative feedback, although the mass in sinks is dramatically reduced. This shows that radiative feedback may regulate star formation and, at the same time, trigger star formation. A more detailed investigation of triggered star formation is postponed to a follow-up paper.

The IMF for massive stars in MC<sub>1</sub> (red) and MC<sub>2</sub> (black) is shown in Fig. 5 for the simulations ZLNOFB (thick, transparent lines) and ZLRAD (thin, opaque lines) at time  $\tau_{3.0}$ . The blue line indicates the Salpeter slope of the IMF in the high-mass range proportional to  $M_*^{-2.35}$  (Salpeter 1955). In the runs ZLRAD, 31 and 23 massive stars form with  $M_{*,\text{tot}} \approx 830$  and  $480 \text{ M}_{\odot}$  in the total volume of MC<sub>1</sub> and MC<sub>2</sub>, respectively. Within the period of 3 Myr, a small number of massive stars are forming, which

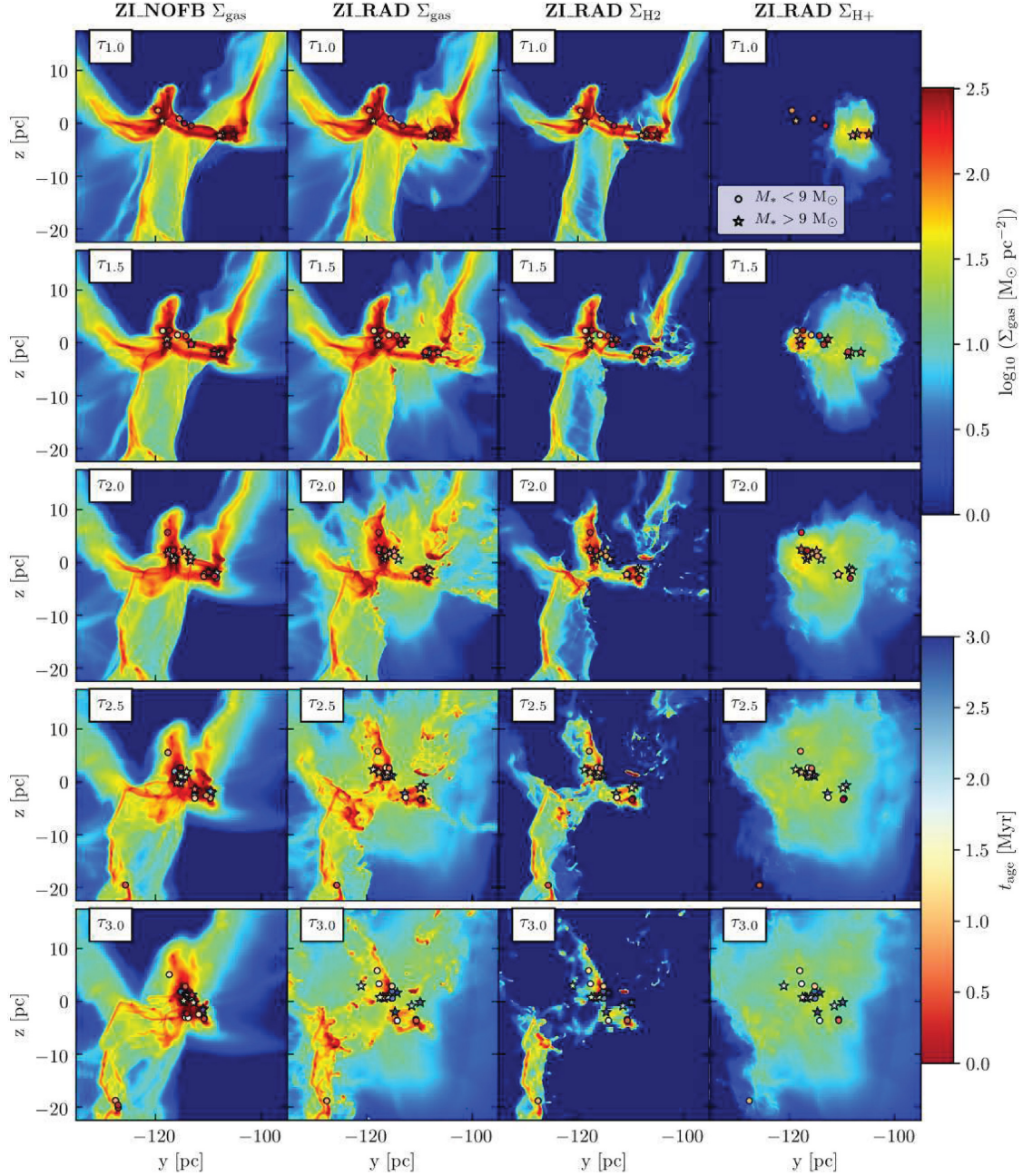


**Figure 3.** Time evolution of the central volume  $V_{\text{CoV}}$  of size  $(40 \text{ pc})^3$  (see Fig. 2 and Table 1) of MC1 in the simulations ZLNOFB (left) and ZLRAD (second to fourth), respectively, at times  $\tau_{1.0}$ – $\tau_{3.0}$  (from top to bottom). The first two columns show the gas column density  $\Sigma_{\text{gas}}$  in the  $y$ - $z$  plane. The third and fourth show the  $\text{H}_2$  and  $\text{H}^+$  column densities. The circles indicate sink particles without an active stellar component, i.e. without massive stars. Star-shaped markers are cluster sink particles with active stellar feedback. The colour of the markers indicates their age.

leaves the high-mass end of the IMF undersampled. Hypothetical sampling of low-mass stars ( $M_* < 9 M_\odot$ ) from the residual sink mass results in a well-represented low-mass end of the Kroupa IMF. The corresponding formation history of the massive stars is shown in Fig. B3.

Sink particles accrete gas from their environment as long as the gas is, e.g. gravitationally bound. When accretion stops the sink particle has reached its maximum mass,  $M_{\text{si,max}}$ . It is useful to investigate the accretion time,  $\Delta t_{\text{acc}}$ , which is the time elapsed from the formation of the sink until the maximum sink mass is reached,



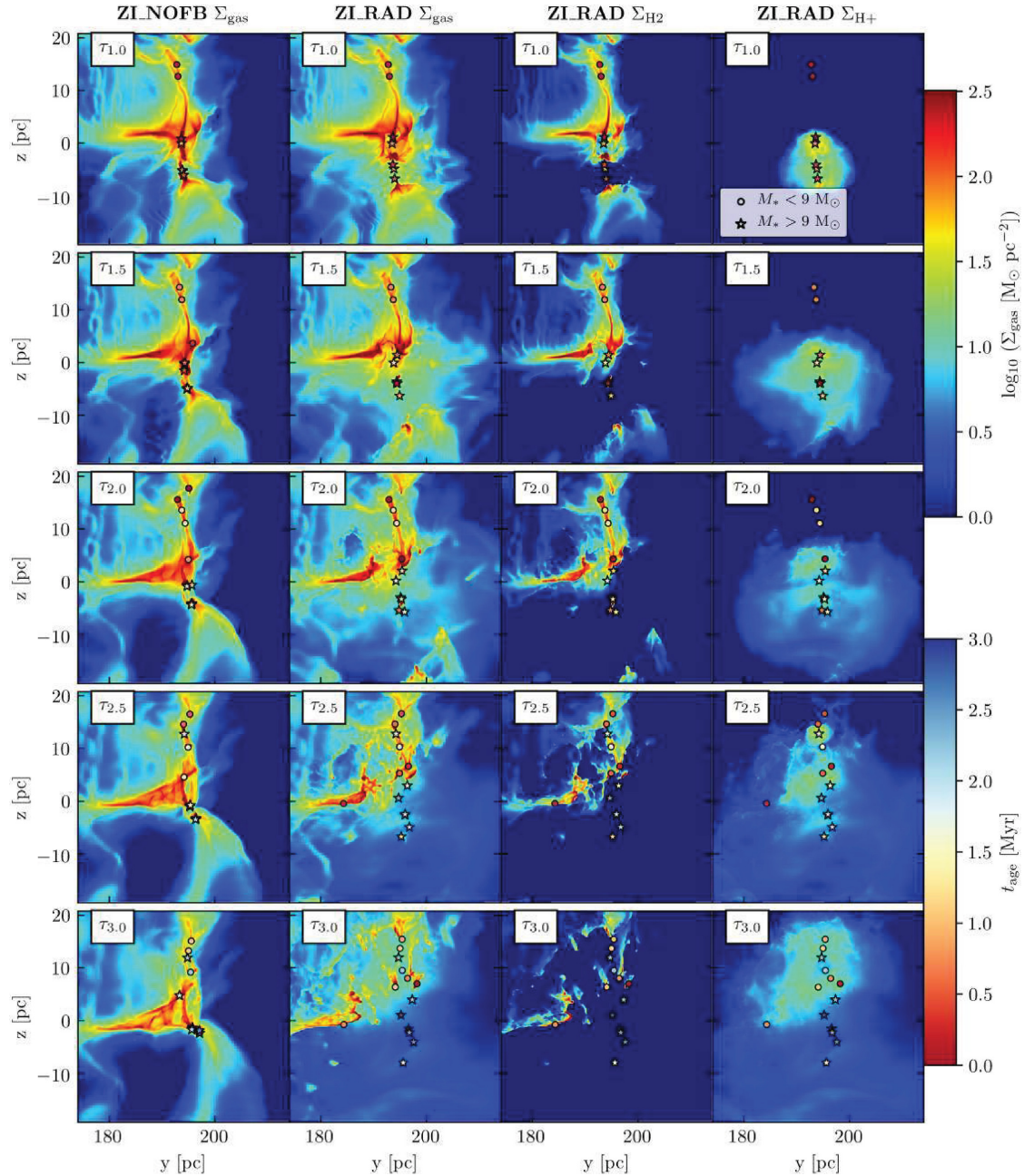
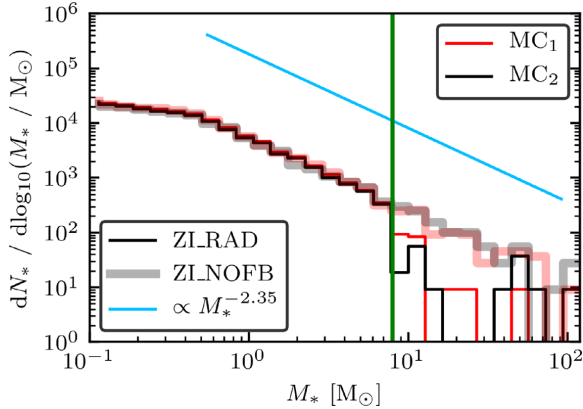


Figure 4. Same figure as in Fig. 3 but for MC<sub>2</sub>.

which quantitatively demonstrates the impact of radiative feedback on the local star formation rate. In Fig. 6, we show  $\Delta t_{\text{acc}}$  as a function of  $M_{\text{si,max}}$  for the simulations of MC<sub>1</sub> (red) and MC<sub>2</sub> (black) with (ZI.RAD; full markers) and without radiative feedback (ZI.NOFB; open markers) within  $V_{\text{COV}}$ . Transparent markers are sinks with masses below the massive star formation limit of  $120 M_{\odot}$ . The blue crosses indicate that the accretion on to the corresponding sink has stopped. In ZI.NOFB, the accretion times stretch over a wider temporal range and sinks grow to a few  $1000 M_{\odot}$  because

accretion cannot be halted. In ZI.RAD, the accretion time is less than  $\sim 1$  Myr. Sink particles with masses above the star formation threshold not only stop their own accretion but effect or even interrupt the mass accretion of any nearby companion. This results in a large fraction of sinks that remain below the star formation mass threshold. We expect that short accretion times are accompanied by a drastic change in the environmental density of the sink particles as a function of time. This is investigated in the following Section.



**Figure 5.** IMF in MC<sub>1</sub> (red) and MC<sub>2</sub> (black) for simulation ZI.NOFB (thick) and ZI.RAD (thin) at  $\tau_{3,0}$ . The blue line indicates the Salpeter slope proportional to  $M_*^{-2.35}$  (Salpeter 1955). With radiation within this first 3 Myr, 31 and 23 massive stars form within MC<sub>1</sub> and MC<sub>2</sub>, respectively. Hence, the high-mass range ( $M_* > 9 M_\odot$ ) suffers from low number statistics. However, sampling low-mass stars from the residual sink mass shows that the underlying Kroupa IMF is well represented (Kroupa 2001). The green, vertical line indicates the boarder between the low-mass and high-mass regime at  $9 M_\odot$ .

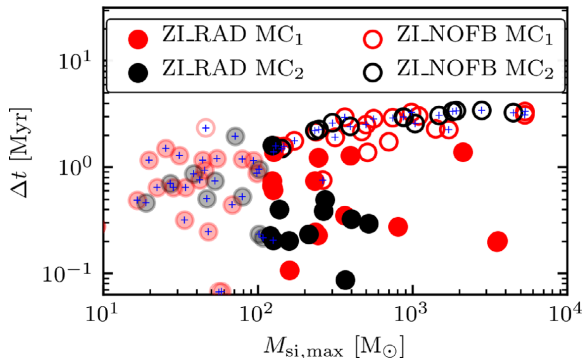


**Figure 6.** Accretion time  $\Delta t_{\text{acc}}$  counted from the formation time of the sink as a function of the maximum sink mass  $M_{\text{si,max}}$  for the simulations ZI.RAD (full markers) and ZI.NOFB (open markers) within  $V_{\text{COV}}$  of MC<sub>1</sub> (red) and MC<sub>2</sub> (black). The transparent markers indicate that the sink mass does not exceed the  $120 M_\odot$  high-mass star-forming threshold. The blue crosses display that the accretion has stopped. Radiative feedback stops accretion on to active sink particles quicker (after  $\approx 1$  Myr).

### 5.1 Environmental densities

Over the lifetime of massive stars, their environmental densities are continuously changing. The ambient density determines the impact of radiative feedback (Haid et al. 2018). Right after a star is born, the surrounding gas is typically dense so that the young H II region is confined (Wood & Churchwell 1989; Peters et al. 2010a). The bubble then expands hydrodynamically, while more gas is ionized. However, once the environmental density has significantly decreased (after the ionized gas has leaked out of the bubble or the star has moved out of the dense star-forming filament), the ionization front spreads out and the impact of radiative feedback is not locally confined.

In Fig. 7, we show the cumulative distribution of the number of sinks (top,  $N_{\text{si}}$ ) and the cumulative sink mass (bottom,  $M_{\text{si}}$ ) as a function of the environmental density obtained by averaging the ambient density of each sink in a sphere with a radius of 1 pc,  $\bar{\rho}_{1\text{pc}}$ . We show MC<sub>1</sub> (left) and MC<sub>2</sub> (right) with (ZI.RAD; thin lines) and without feedback (ZI.NOFB; thick lines) at two times: the formation time of a sink particle is denoted with  $\tau_{\text{si},0}$  (red) and the end time  $\tau_{3,0}$  (black). The green vertical line indicates the sink formation threshold density,  $\rho_{\text{si}}$ .

First of all, when comparing ZI.RAD and ZI.NOFB in MC<sub>2</sub>, we can see that with radiative feedback more sinks are formed, which hints towards triggered star formation. However, the higher number of sink contains a significantly lower total mass (see bottom panels), which indicates that feedback limits the accretion on to star-forming dense regions (see also Fig. 6). Furthermore, we can see that the sinks' environmental densities are severely changed by radiative feedback. All sinks are born in very dense gas ( $\bar{\rho}_{1\text{pc}} > 10^{-21} \text{ g cm}^{-3}$ ) and without feedback most of them also stay there (modulo some wandering off a bit). This implies that there is a large enough gas reservoir to feed the sink particles for the simulated time, even if their mass has grown significantly. With radiative feedback, however, the distribution is significantly shifted towards lower densities at  $\tau_{3,0}$  compared to  $\tau_{\text{si},0}$ . Even though there is still a number of sinks at  $\bar{\rho}_{1\text{pc}} > 10^{-21} \text{ g cm}^{-3}$ , these are mostly the young sink particles that did not have time to disperse their environment. In MC<sub>1</sub>, about 60 per cent of all sinks are surrounded by gas with  $\bar{\rho}_{1\text{pc}} < 10^{-21} \text{ g cm}^{-3}$ . The dispersal of MC<sub>2</sub> has progressed farther and  $\sim 80$  per cent of all sinks are found at  $\bar{\rho}_{1\text{pc}} < 10^{-21} \text{ g cm}^{-3}$ .

Fig. 7 shows that the environmental densities for more than 90 and 60 per cent of the sink particles in MC<sub>1</sub>, respectively, MC<sub>2</sub> lie between  $10^{-23}$  and  $10^{-20} \text{ g cm}^{-3}$  at  $\tau_{3,0}$ . These are conditions, where stellar winds were shown not to be important (Geen et al. 2015; Haid et al. 2018). Therefore, we do not include this additional feedback process in this work. Nevertheless, the environmental densities are continuously reduced by radiative feedback. At later stages ( $\tau > \tau_{3,0}$ ) stellar wind might become important.

### 5.2 The multiphase evolution

We show the mass-weighted (colour) density–temperature, and density–pressure (pressure over the Boltzmann constant) distributions  $V_{\text{COV}}$  for both clouds in Figs 8 and 9, respectively. Note that, according to the Jeans criterion, the depicted gas density is fully resolved, even at the high-density end. For each cloud (MC<sub>1</sub>, top panels; MC<sub>2</sub>, bottom panels), we show different times  $\tau_{1,0}$ ,  $\tau_{2,0}$ , and  $\tau_{3,0}$  from top to bottom. To guide the eye, the black lines show the thermal equilibrium curves calculated using a stand-alone version of the chemistry module with increasing  $G_0$  of 1.7 (solid), 17 (dashed), 170 (dash-dotted), and 1700 (dotted) in units of Habing fields. The thermal equilibrium curve can be assumed to be the transition to the CO-dominated gas (Röllig et al. 2007). In each row, the left-hand column shows the runs without radiative feedback (ZI.NOFB) and the three panels to the right base on run ZI.RAD. The second panel shows the total gas within  $V_{\text{COV}}$ , while the third and fourth panel show gas above and below a visual extinction,  $A_v = 1$  mag, which is computed self-consistently for every cell in the computational domain using the TREERAY OPTICAL-DEPTH module (see Section 2.3). The markers indicate the average environmental density, temperature, and pressure of sinks without (circles) and with active stellar components (stars) within a sphere of radius 1 pc around each sink particle,  $\bar{\rho}_{1\text{pc}}$ ,  $\bar{T}_{1\text{pc}}$ , and  $P/k_{\text{B}1\text{pc}}$ .

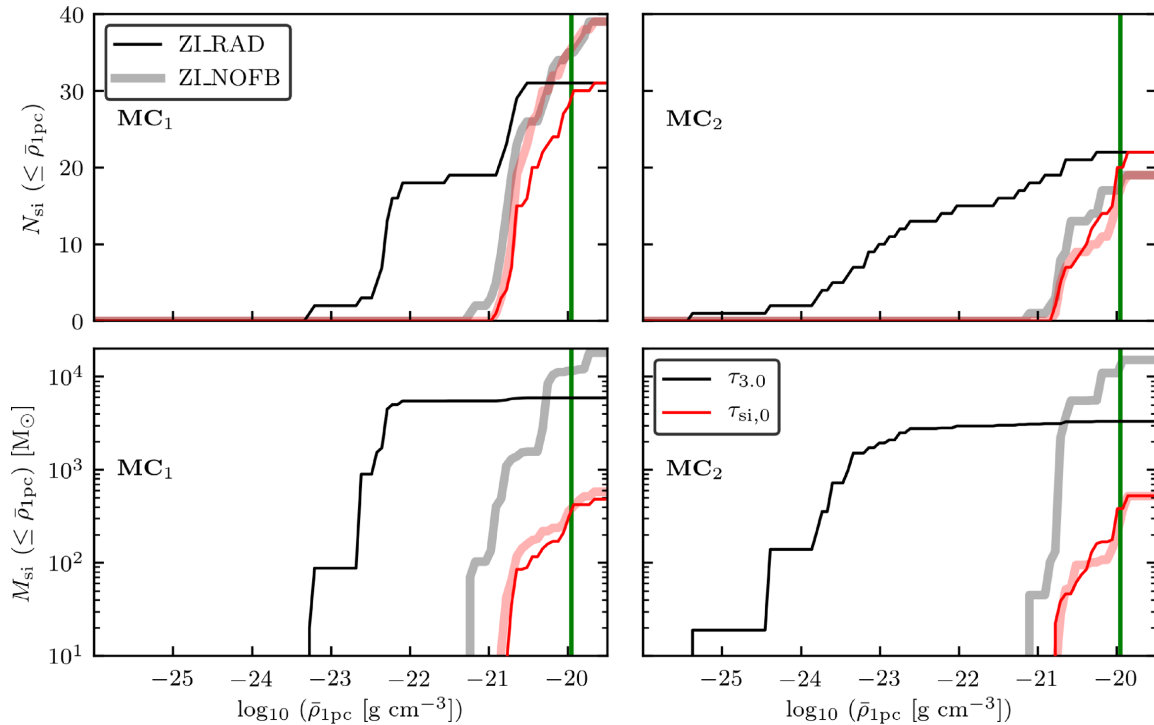


**Figure 7.** Cumulative cluster sink particles mass  $M_{\text{si}}$  (top) and number  $N_{\text{si}}$  (bottom panel) distribution dependent on the environmental densities at different sink ages,  $\tau_{\text{si},0}$  (red, formation time),  $\tau_{\text{si},1.0}$  (black), and  $\tau_{\text{si},1.5}$  (blue) for simulation ZLNOFB (thick) and ZLRAD (thin). The top and bottom panels correspond to the total domain of MC<sub>1</sub> (left) and MC<sub>2</sub> (right), respectively. The green, vertical line shows the sink formation density threshold,  $\rho_{\text{si}}$ .

The numbers in the lower left corners indicate the mass within  $V_{\text{CoV}}$  at given time or the fraction of mass at high and low  $A_v$  relative to  $M_{\text{CoV}}$ , respectively. It can be seen that MC<sub>1</sub> has a significantly higher fraction of shielded gas than MC<sub>2</sub> (for further analysis see Section 6.1). The sinks are shown in the respective high-/low- $A_v$  panels depending on their average  $A_v$  within the surrounding 1 pc radius.

The gas distributions of runs ZLNOFB (Figs 8 and 9, left-hand column) are more or less constant in time and follow the computed equilibrium curves. For  $\rho \gtrsim 10^{-22} \text{ g cm}^{-3}$ , most of the gas is more deeply embedded and cools down to  $\sim 10 \text{ K}$ . For runs with radiative feedback, the phase diagrams change significantly as a lot of gas is lifted above the equilibrium curve towards high temperatures and pressures. Several new horizontal branches become apparent in the temperature–density diagram. Young and deeply embedded H II regions first appear in the  $A_v > 1 \text{ mag}$  distribution (see Fig. A2 for the ionization state of this gas). With time, these embedded bubbles grow, burst out of the dense filament and leak into the low-density environment. Fully developed H II regions are heated up to temperatures between 8000 and 10000 K occurring at  $A_v < 1 \text{ mag}$ .

Inactive stars are usually deeply embedded inside the cloud (at high density and low temperature), unless they reside near an active sink that influences their environment. The H II regions seem to expand until the pressure gradient between ambient medium and H II region across their outer boundary is diminished, which can be seen from Fig. 9 where the gas inside the H II region joins the rising equilibrium pressure branch of the warm ambient medium.

## 6 THE INTERACTION BETWEEN MOLECULAR CLOUDS AND RADIATIVE FEEDBACK

MC<sub>1</sub> and MC<sub>2</sub> were chosen as two clouds with similar initial parameters (see Seifried et al. 2017, and Table 1). Nevertheless, the clouds evolve differently in the presence of radiative feedback (see Figs 3 and 4), where MC<sub>1</sub> seems less affected than MC<sub>2</sub>. In this Section, we discuss the physical property of the cloud, i.e. the local extinction, which we ultimately (after a careful and extensive analysis) identify to be responsible for the apparent differences. Next, we discuss the energy content and the star formation properties of both clouds.

### 6.1 Extinction matters!

Fig. 10 shows the fraction of cloud mass constrained by different extinction thresholds in MC<sub>1</sub> (red) and MC<sub>2</sub> (black) in the total cloud ( $M_{A_v}/M_{\text{tot}}$ , top) and the central sub-region ( $M_{A_v}/M_{\text{CoV}}$ , bottom) as a function of time in simulations ZLRAD (thin) and ZLNOFB (thick). Note that the evolutions of  $M_{\text{tot}}$  and  $M_{\text{CoV}}$  are shown in Fig. A1. We evaluate the mass with the extinction below (dashed) and above (solid) a visual extinction of  $A_v = 1 \text{ mag}$ . For both simulations, ZLNOFB and ZLRAD, the evolutions are similar for the first 1.5 Myr. In the total domain of MC<sub>1</sub> and MC<sub>2</sub>, most mass resides at  $A_v \leq 1 \text{ mag}$  with  $\sim 0.7$  of the total mass,  $M_{\text{tot}}$ . Hence, only a small fraction of the gas is well shielded with  $A_v > 1 \text{ mag}$  and the well-shielded mass fraction is higher in MC<sub>1</sub> than in MC<sub>2</sub> by  $\sim 30$  per cent at  $\tau_0$  up to  $\sim 80$  per cent at  $\tau_{2.0}$  and finally becomes similar at  $\tau_{3.0}$ . In the central sub-regions, the evolutions of the well-



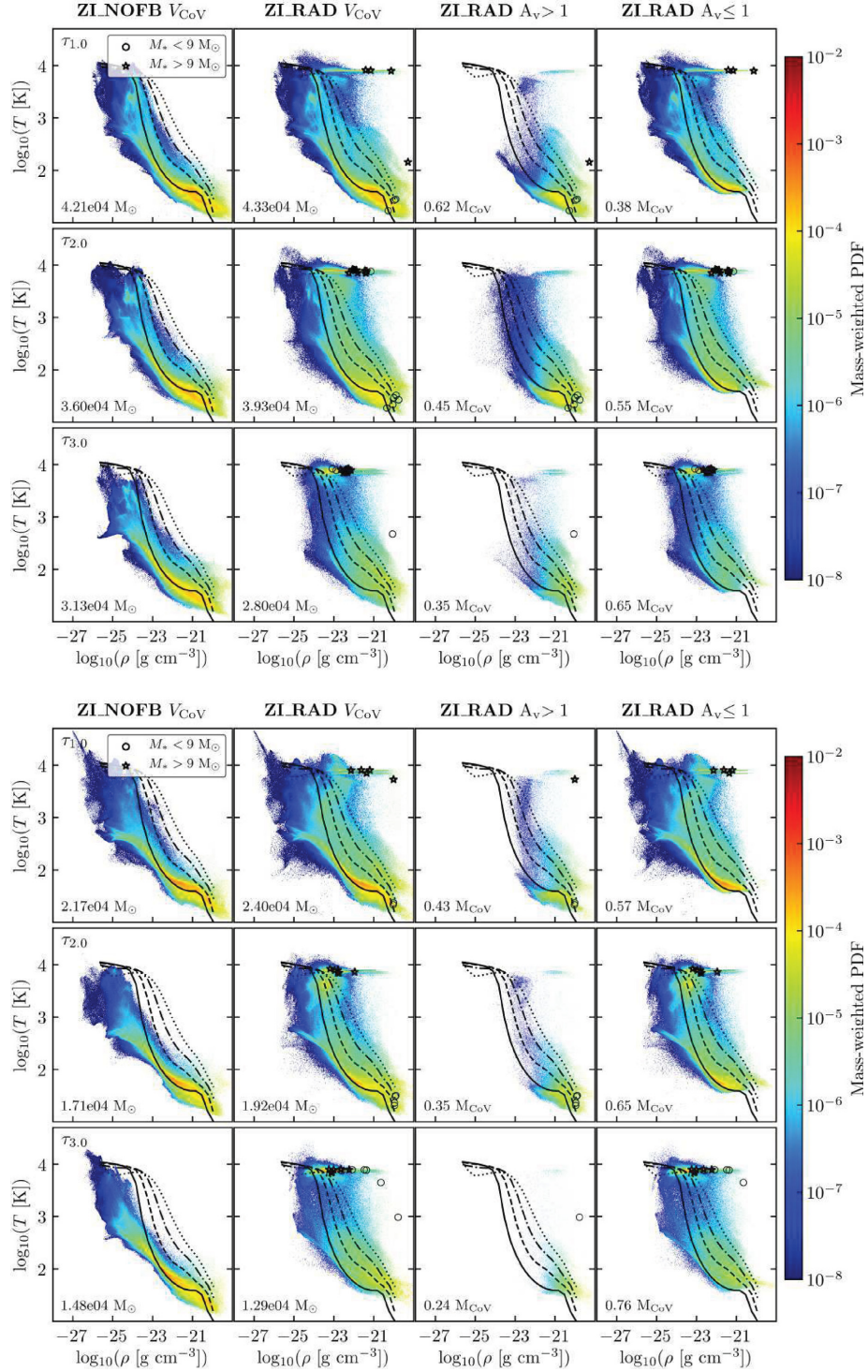


**Figure 8.** Mass-weighted (colour) density–temperature distribution of the of the central sub-region ( $V_{\text{CoV}}$ ) of MC1 (top) and MC2 (bottom) at times  $\tau_{1.0}$  (top),  $\tau_{2.0}$  (centre), and  $\tau_{3.0}$  (bottom) for simulation ZLNOFB (left-hand column) and ZLRAD (right). The left and second column show the total gas distributions. The third and fourth columns show only gas above/below an  $A_v$  of 1 mag. The markers indicate sink particles with an active stellar component (star symbol) and without massive stars (circles). The black lines show the thermal equilibrium curve derived for  $G_0$  of 1.7 (solid), 17 (dashed), 170 (dash-dotted), and 1700 (dotted) in units of Habing fields. The numbers in the lower left corners indicate the total gas mass in  $V_{\text{CoV}}$  (first and second column) and the fraction of mass above/below  $A_v = 1$  (third and fourth column), respectively.

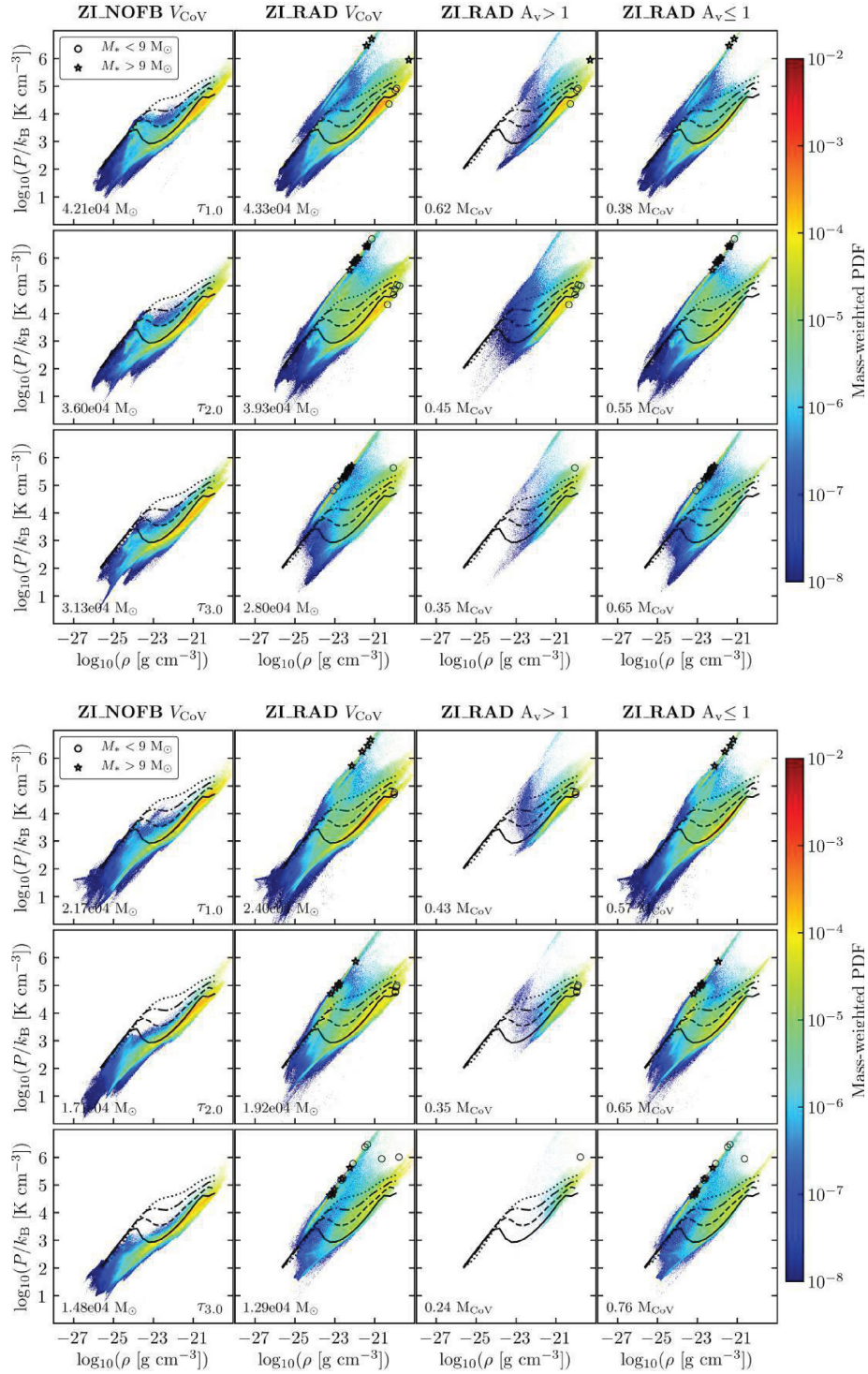
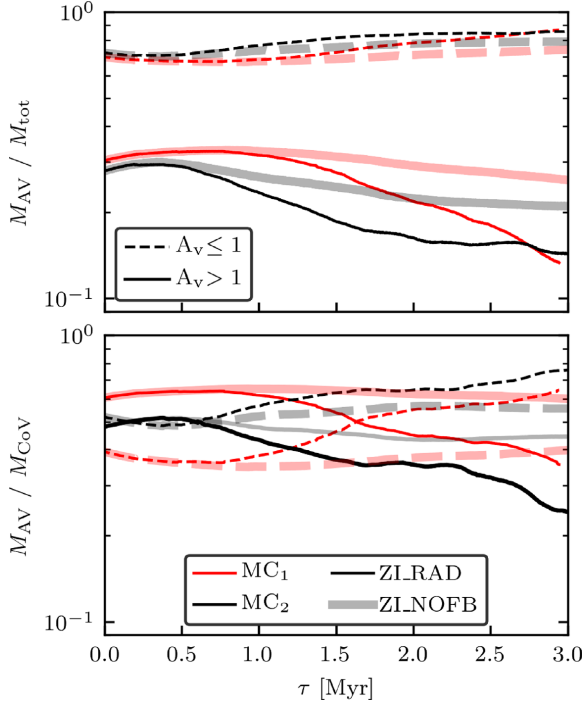


Figure 9. Same figure as in Fig. 8 but for the mass-weighted pressure-density distributions.



**Figure 10.** Time evolution of the fraction of total gas mass found below (dashed) and above (solid lines) an  $A_v$  of 1 mag for the total (top) and the central sub-region (bottom) MC<sub>1</sub> (red) and MC<sub>2</sub> (black). The differences in simulations with radiative feedback (thin lines) and without radiative feedback (thick lines) are minor, but MC<sub>1</sub> has more mass at  $A_v > 1$  than MC<sub>2</sub>.

shielded gas follow the larger volume with higher initial fractions of  $\sim 60$  per cent and to  $\sim 50$  per cent of  $M_{\text{Cov}}$ . During the evolution, gas is dispersed by feedback and the fraction of  $A_v < 1$  mag dominates (compare to Figs 8 and 9).

In Fig. 11, we show the mass-weighted (top) and volume-weighted (bottom) density (left) and column density probability density function (PDF, right) in simulation ZI\_RAD at  $\tau_{1.0}$  (top panels) and  $\tau_{3.0}$  (bottom panel). The PDF includes gas within  $V_{\text{Cov}}$  for MC<sub>1</sub> (red) and MC<sub>2</sub> (black). The dotted lines indicate the density PDF of gas with  $A_v > 1$  mag. This  $A_v$  is calculated for every cell in the computational domain via the TREERAY OPTICAL-DEPTH module. We find that the mass-weighted and volume-weighted total gas density distributions of MC<sub>1</sub> and MC<sub>2</sub> are similar over a wide range of densities and at  $\tau_{1.0}$  and  $\tau_{3.0}$ . The column density PDFs (right-hand column) of the clouds are slightly different: While MC<sub>1</sub> dominates in the high  $\Sigma$  regime ( $\Sigma \gtrsim 100 M_\odot \text{ pc}^{-2}$ ), MC<sub>2</sub> hosts more gas at lower column densities.

The differences between the two clouds become apparent when inspecting the high- $A_v$  gas (blue, green). MC<sub>1</sub> has more mass in gas at high  $A_v$  than MC<sub>2</sub> and this gas occupies a larger fraction of the cloud volume. Also, there is basically no difference between the two time-steps  $\tau_{1.0}$  and  $\tau_{3.0}$  for MC<sub>1</sub>, apart from the very high density tail in the mass-weighted density PDF, which forms at  $\tau_{3.0}$ . This indicates that the gas in MC<sub>1</sub> is still relatively confined at  $\tau_{3.0}$ . On the other hand, MC<sub>2</sub> has less mass at high  $A_v$ , and this mass occupies a smaller fraction of the cloud volume. Also, the mass

and volume fractions of gas at high  $A_v$  are clearly decreasing as a function of time, which is a clear sign of cloud dispersal.

Overall, we find that the impact of radiative feedback is very sensitive to the detailed cloud sub-structure. In this regard, even if the volume density distributions are similar, the distribution of the 3D, visual extinction may be different, and these differences are enhanced when the cloud is exposed to radiative feedback.

## 6.2 Energy evolution

In Fig. 12, we show the evolution of the internal (red,  $E_{\text{int}}$ ) and kinetic (black,  $E_{\text{kin}}$ ) energy of the gas for the simulations ZI\_RAD (thin) and ZI\_NOFB (thick) for MC<sub>1</sub> (top) and MC<sub>2</sub> (bottom), respectively. Note that we only consider the gas, while the contribution to  $E_{\text{kin}}$  from sink particles is neglected. The initial kinetic and internal energies are similar for both MCs with  $E_{\text{int}} \approx 3 \times 10^{48}$  erg and  $E_{\text{kin}} \approx 2 \times 10^{49}$  erg. Both clouds are initially bound with virial parameters of  $\sim 0.72$  and  $\sim 0.89$  as calculated for  $M_{\text{tot}}$  in  $V_{\text{tot}}$ . In ZI\_NOFB, the energies in both clouds decrease as no-feedback energy is injected. With radiative feedback, the internal energy increases following the formation of massive stars. Radiative feedback also clearly enhances the kinetic energy content of the clouds, i.e. it drives turbulence (see e.g. Gritschneider et al. 2009; Walch et al. 2012).

In both clouds, we see jumps in  $E_{\text{int}}$  by up to 50 per cent. This behaviour is linked to the confinement of radiative bubbles. Initially, they are embedded in dense structures, only a small volume is affected and the radiative impact is delayed. But as soon as the H II regions open, radiation and ionized material leak out and increase the internal energy in a larger domain. As the average rate of ionizing photons in the central volume is comparable for both clouds with a factor of  $\sim 2$  difference (see Fig. B3), the final energetic states are similar.

## 6.3 Star formation

A common way to separate the diffuse ISM from the dense gas is to choose a density threshold. With the subscript ‘100’, we refer to gas with number density  $n > 100 \text{ cm}^{-3}$  ( $\rho > 3.84 \times 10^{-22} \text{ g cm}^{-3}$ ). To trace predominantly molecular gas, we use the subscript ‘H2’, which means that the mass fraction of  $\text{H}_2$  in every cell is equal or greater than 50 per cent (see Seifried et al. 2017). A general way to indicate either of the two constraints is a subscript ‘x’.

The instantaneous star formation rate surface density  $\Sigma_{\text{SFR,inst}}$  assumes that all gas that is accreted on to a sink particle is immediately forming an ensemble of low- and high-mass stars. It is defined as

$$\Sigma_{\text{SFR,inst}} = \frac{1}{A} \sum_{j=1}^{N_{\text{sl}}} \dot{M}_{\text{sl},j}(\Delta t) [M_\odot \text{ Myr}^{-1} \text{ pc}^{-2}] \quad (9)$$

where  $\Delta t = 0.1 \text{ Myr}$ ,  $A$  is the area of the cloud, and  $\dot{M}_{\text{sl},j}$  the mass accretion rate of the sinks over a time period  $\Delta t$  (Matzner & McKee 2000; Gatto et al. 2017).  $A$  is calculated from the mass-weighted radius, which we calculate from the distance of all cells above a given threshold relative to the centre of mass in the volume  $V_{100}$ .

In Fig. 13, we depict  $\Sigma_{\text{SFR,inst}}$  for MC<sub>1</sub> (top) and MC<sub>2</sub> (bottom) for the simulations ZI\_RAD (thin) and ZI\_NOFB (thick), respectively. We compute the mass-weighted cloud area from all cells with  $n > 100 \text{ cm}^{-3}$ . The time-averaged values for the simulation ZI\_NOFB are 1.9 and 1.3  $M_\odot \text{ Myr}^{-1} \text{ pc}^{-2}$  as well as 0.6 and 0.3  $M_\odot \text{ Myr}^{-1} \text{ pc}^{-2}$  in run ZI\_RAD for MC<sub>1</sub> and MC<sub>2</sub>, respectively. This shows that



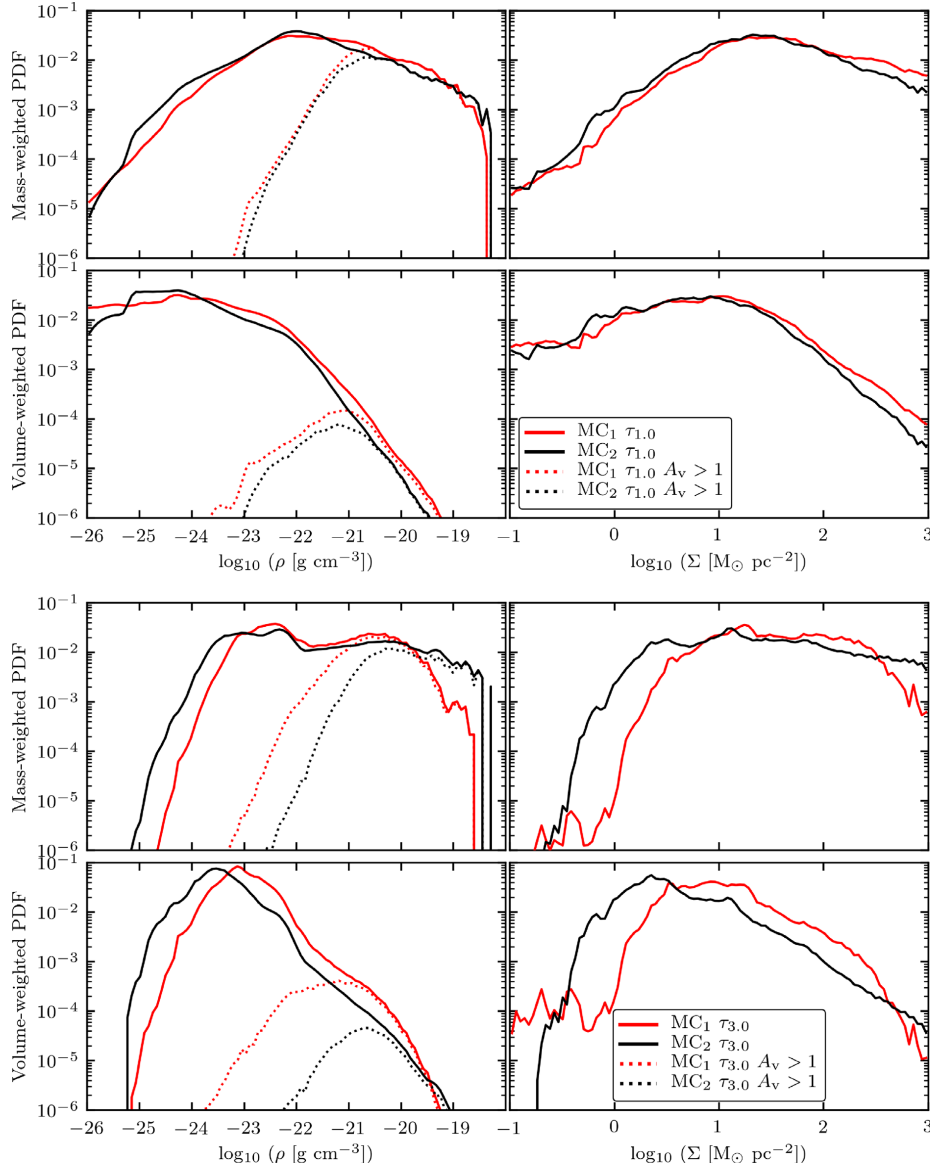


**Figure 11.** Mass-weighted (top) and volume-weighted (bottom) density (left) and column density PDF (right) in simulation ZLRAD. We show the distributions at  $\tau_{1,0}$  (top four panels) and  $\tau_{3,0}$  (bottom four panels) of central sub-region of MC<sub>1</sub> (red) and MC<sub>2</sub> (black). The dotted lines (left column) indicate the density PDF of gas with  $A_v > 1$  mag. Although the overall PDFs of the two clouds are nearly indistinguishable, MC<sub>2</sub> contains a lot less well-shielded gas than MC<sub>1</sub>. Also, the dispersal of MC<sub>2</sub> can be seen because the fraction of gas with  $A_v > 1$  is reduced from  $\tau_{1,0}$  to  $\tau_{3,0}$ .

radiative feedback reduces the star formation rate surface density by a factor of  $\sim 4$ . Similar values are obtained for a radius constrained with molecular hydrogen dominated gas.

The *star formation efficiency per free-fall time* ( $\text{SFE}_{\text{ff},x}$ ) is the dimensionless ratio of the mass in stars  $M_{\text{st}}$  that forms within a free-fall time  $\tau_{\text{ff},x}$  divided by the mass of the cloud  $M_x$  with  $x = [100, \text{H}_2]$ . In this paper, the mass in stars is equivalent to the mass in the sink particles,  $M_{\text{st}} = M_{\text{si}}$ . The free-fall time is given with  $\tau_{\text{ff},x} = (3\pi/(32G\rho_x))^{0.5}$ , where  $\rho_x = M_x/V_x$ . This gives

$$\text{SFE}_{\text{ff},x} = \frac{\dot{M}_{\text{si}}}{M_x \tau_{\text{ff},x}} \quad (10)$$

where  $\dot{M}_{\text{si}} = dM_{\text{si}}/dt$  (Krumholz & Tan 2007; Murray 2011; Dale et al. 2014).

In Fig. 14, we show  $\text{SFE}_{\text{ff},x}$  for simulation ZLRAD in MC<sub>1</sub> (top) and MC<sub>2</sub> (bottom) for  $\rho_{100}$  (red) and  $\rho_{\text{H}_2}$  (black), respectively. The time-averaged values are shown as horizontal, solid lines. The horizontal, dashed lines are the time-averaged values from the corresponding simulations without radiative feedback, ZLNOFB. The time-averaged free-fall times  $t_{\text{ff},x}$  are 2.7, 2.4 Myr in MC<sub>1</sub> and 2.8, 1.8 Myr in MC<sub>2</sub> for the thresholds  $x = [100, \text{H}_2]$ , respectively. For the number density threshold  $\rho_{100}$  and the  $\text{H}_2$ -based threshold  $\rho_{\text{H}_2}$ , the time-averaged  $\text{SFE}_{\text{ff}}$  are 9 and 13 percent in MC<sub>1</sub> and 5 and

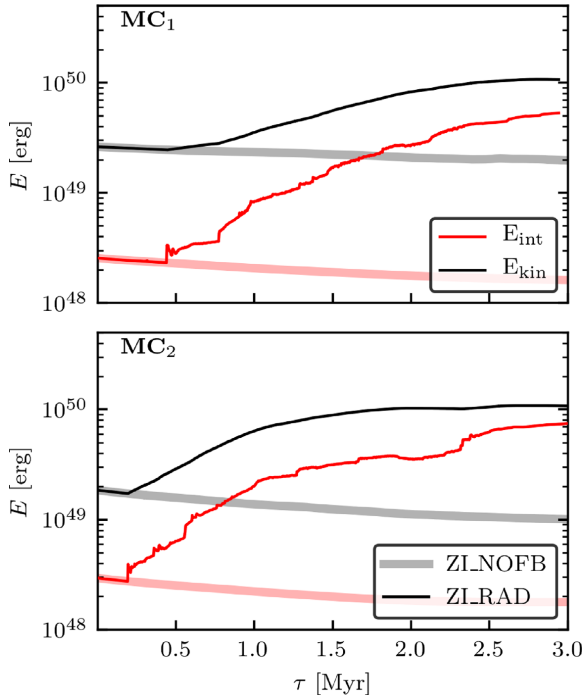


**Figure 12.** Time evolution of the internal (red,  $E_{\text{int}}$ ) and kinetic (black,  $E_{\text{kin}}$ ) energy in the simulations ZLRAD (thin) and ZLNOFB (thick) in MC<sub>1</sub> (top) and MC<sub>2</sub> (bottom). The jumps in the evolution of the internal energy are due to embedded H II regions that open and release radiation into the ambient medium.

6 per cent in MC<sub>2</sub> with radiative feedback, and 29 and 40 per cent in MC<sub>1</sub>, respectively, 31 and 37 per cent in MC<sub>2</sub> without feedback. Thus, in the simulations ZLNOFB the average values are  $\sim 4$  times higher and in agreement with the findings for  $\Sigma_{\text{SFR,inst}}$ . In general, we obtain somewhat higher average values due to short episodes of high star formation, although the  $\text{SFE}_{\text{ff},100}$  regularly drops down to the 5-per cent regime (green, shaded area). Note that  $\text{SFE}_{\text{ff},\text{H2}}$  is larger due to a smaller mass that is available for star formation (see equation 10).

Values for  $\text{SFE}_{\text{ff}}$  are observed for low-mass clouds to be around a few per cent (Krumholz & Tan 2007; Evans et al. 2009). In clouds, which are more massive and/or have longer free-fall times, the efficiency can increase up to 30 per cent (Murray 2011). Isolated, bound MCs in numerical simulations by Dale et al. (2012, 2014) show  $\text{SFE}_{\text{ff}}$  without and with feedback of 16 and 11 per cent, respectively, which indicates that radiative feedback is inefficient in regulating star formation. This contradicts our findings, where ionizing radiation reduces the  $\text{SFE}_{\text{ff}}$  on average by a factor of 4. Similar values are found by Howard, Pudritz & Harris (2016). One reason for the inefficiency of radiative feedback in Dale et al. (2012) and Dale et al. (2014) can be found in the underlying model of Diaz-Miller et al. (1998), which systematically underestimates the ionizing luminosities. These differ from the presented model by up to a factor of 10 lower values with increasing stellar mass (see Fig. 1).

Fig. 15 compares the  $\text{SFE}_{\text{ff}}$  obtained from the simulations with resolved observations of Milky Way MCs, kpc-scale observations of Local Group galaxies, and from unresolved observations of both disc and starburst galaxies in the local Universe and at high red-

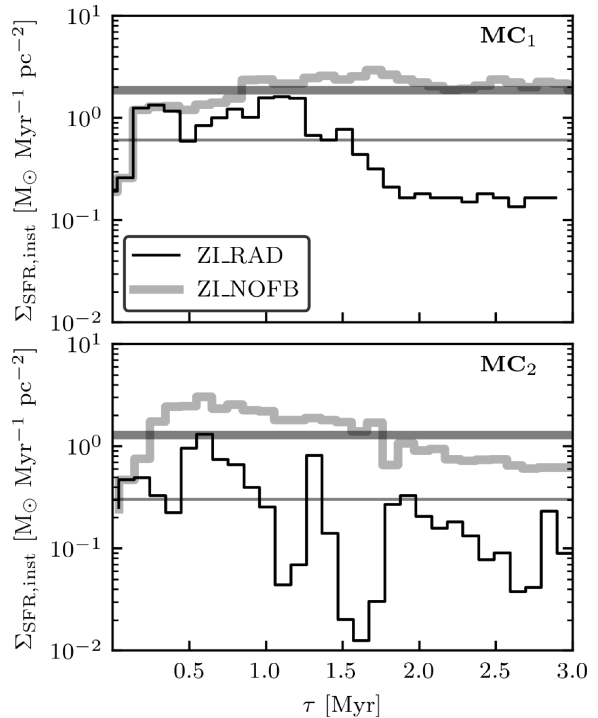


**Figure 13.** Instantaneous star formation rate surface density  $\Sigma_{\text{SFR,inst}}$  calculated for all gas within the zoom-in region of MC<sub>1</sub> (top) and MC<sub>2</sub> (bottom) that has a number density  $n > 100 \text{ cm}^{-3}$ . We show simulations with (ZLRAD; thin) and without radiative feedback (ZLNOFB; thick). Radiative feedback reduces  $\Sigma_{\text{SFR,inst}}$  by a factor of  $\sim 4$ .

shift published in Lada, Lombardi & Alves (2010) and Heiderman et al. (2010). We relate the star formation rate surface density  $\dot{\Sigma}_* = \Sigma_{\text{SFR,inst}}(\Delta t = 3 \text{ Myr})$  with the surface density over the free-fall time  $\Sigma/t_{\text{ff}}$  derived for MC<sub>1</sub> (red) and MC<sub>2</sub> (black) for the simulations ZLRAD (full markers) and ZLNOFB (empty markers) at  $\tau_{3.0}$ . For each cloud, we only consider gas within its  $V_{\text{tot}}$  above the number density threshold  $n > 100 \text{ cm}^{-3}$ . The black line and grey shaded area show the fitted behaviour found in Krumholz, Dekel & McKee (2012, 2013) and the associated uncertainty.

The  $\text{SFE}_{\text{ff}}$  obtained for the ZLNOFB runs are too high and clearly offset from the observed relation. However, both clouds with radiative feedback are right on top of the relation, with MC<sub>2</sub> at slightly lower  $\dot{\Sigma}_*$  than MC<sub>1</sub>. The two observed points that sit directly on top of our results correspond to the Taurus and Ophiuchus MCs (points near MC<sub>2</sub>) and Lupus 3 (point on top of MC<sub>1</sub> result). This result is reassuring because these observed clouds lie in the solar neighbourhood – the environment simulated here – and have total masses and other physical properties that are comparable to our simulated clouds.

## 7 DISCUSSION: DIFFERENCES BETWEEN MC<sub>1</sub> AND MC<sub>2</sub>

MC<sub>1</sub> and MC<sub>2</sub> condense out of the same multiphase ISM. They were selected to have similar initial properties such as masses around  $10^4 M_{\odot}$ , similar volumes, comparable kinetic, and internal energies, and similar virial parameters of 0.72 and 0.89. However, during the evolution under the influence of ionizing radiation both clouds seem



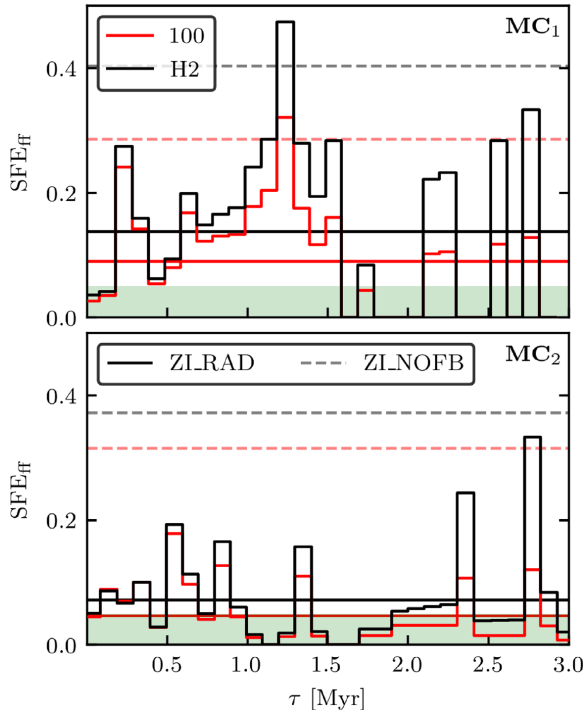


**Figure 14.** The evolution of the star formation efficiency per free-fall time  $SFE_{ff,x}$  in the total domain of MC<sub>1</sub> (top) and MC<sub>2</sub> (bottom) for the simulation ZI\_RAD with the constraints  $x = [100$  (red), H<sub>2</sub> (black)]. The solid, horizontal lines show the time average. The dashed horizontal lines show the time average of the same parameter in the simulation ZI\_NOFB. The shaded green area indicates an efficiency below 5 percent.

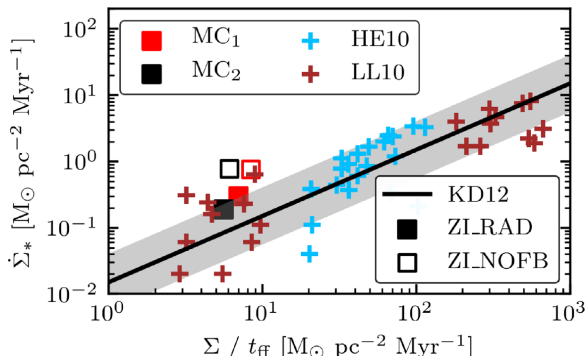


**Figure 15.** Relation between the star formation surface density  $\Sigma_*$  and surface density over the free-fall time  $\Sigma/t_{ff}$  for MC<sub>1</sub> (red square) and MC<sub>2</sub> (black square) for the simulations ZI\_RAD (full markers) and ZI\_NOFB (empty markers) at  $\tau_{3.0}$ . The black line shows the fitted behaviour found in Krumholz et al. (2012) surrounded by the scatter in grey. The data are taken from Lada et al. (2010) and Heiderman et al. (2010). Our simulated clouds are closest to three nearby low-mass star-forming MC, Taurus, Ophiuchus, and Lupus 3.

to diverge with respect to their morphologies, meaning that most of the gas in MC<sub>1</sub> remains (see Fig. 3) while MC<sub>2</sub> is almost fully dispersed at  $\tau_{3.0}$  (see Fig. 4).

In Fig. 7, we show that the environmental densities of sink particles gradually decrease with age and particularly the sinks in MC<sub>2</sub>

are embedded in low-density media. Together with Fig. 11, where we show that this cloud has much less well-shielded gas with  $A_V > 1$  mag, we interpret that MC<sub>1</sub> has more deeply embedded dense structures and a thicker envelope. The density–temperature distribution of the central region of the clouds (see Fig. 8) with  $A_V > 1$  mag indicates that some sources are deeply embedded in these well-shielded regions. Therefore, radiative feedback is confined to small bubbles in MC<sub>1</sub>. The radiative impact is delayed until the radiative bubbles open into the ambient medium, ionized gas and radiation leak out and induce kinetic motions.

It is important to mention, that the emitted radiative energy is similar in both central regions (see Fig. B3 for the rate of UV-photons). There are also massive stars forming in the rest of the cloud. The most relevant stars have high masses. In our simulations, almost all of those are situated far away from the central sub-region. With distance and with decreasing mass, the UV-photon rates per volume decrease and easily drop below the values expected from a star with a mass of  $9 M_\odot$ , hence are considered as minor. The effect of feedback from massive stars outside the sub-regions on the dense structures is minor. Otherwise it should also be visible in the mass evolution of well-shielded gas (see Fig. 10 and compare ZI\_NOFB with ZI\_RAD) and in the density–temperature distribution, but both remain almost unchanged (see Figs 8 and 9).

Concerning the star formation in both clouds, ionizing radiation is able to lower the star formation rate surface density by a factor of  $\sim 4$ . The star formation efficiency constrained by gas above  $100 \text{ cm}^{-3}$  is found to be on average  $\sim 5$ –9 percent in both clouds (see Figs 14 and 13). In ZI\_NOFB, a few, massive sink particles evolve, whereas in ZI\_RAD in cloud MC<sub>2</sub> the sink masses are significantly reduced but their number increased. Star formation is triggered by radiative feedback.

The comparison of MC<sub>1</sub> and MC<sub>2</sub> shows that, not only the cloud masses (Dale et al. 2012, 2013), the corresponding luminosities (Geen et al. 2018) and escape velocities influence the impact from radiative feedback, but that the initial cloud sub-structure significantly determines the cloud evolution. The initial conditions are imprinted during the formation process of the cloud (Brunt et al. 2009; Rey-Raposo et al. 2017). We find that the fully 3D shielding properties determine the time-scales of molecule formation (Seifried et al. 2017) as well as the time-scales for cloud dispersal (this paper).

## 8 CONCLUSIONS

In this paper, we investigate the impact of ionizing radiation feedback from massive stars in the early evolution of MCs up to 3 Myr. We perform hydrodynamic simulations with the AMR code FLASH 4 and include the novel radiative transfer scheme TREERAY, which is coupled to a chemical network to treat the effect of ionizing radiation. We self-consistently follow the formation of two, initially bound MCs from an supernova-driven, multiphase ISM down to a resolution of  $0.122 \text{ pc}$  within the SILCC-Zoom project. We allow for sink particle formation on the highest refinement level. In the simulation ZI\_RAD, ionizing radiation is coupled to massive stars. Simulation ZI\_NOFB is the reference run without feedback process. In the following we list the main conclusions.

(i) Despite the similar initial masses of the two MCs, the morphological evolutions under the influence of ionizing radiations is different. In MC<sub>1</sub>, a central blob of gas remains, whereas a part of MC<sub>2</sub> is fully dispersed. We show that this difference is linked to the mass of internal sub-structures of dense and well shielded gas,

which embeds, and delays radiative feedback. The sub-structures are imprinted during the formation of the clouds.

(ii) We show that the total gas density PDFs are nearly identical for the different MCs. However, the well-shielded gas ( $A_V > 1$  mag) reveals cloud-specific properties. In this work, MC<sub>1</sub> shows more volume-filling gas at intermediate densities, i.e. a thicker envelope surrounding the densest, star-forming filaments. These are responsible for sustaining the cloud structure despite the impact of radiative feedback. MC<sub>2</sub> contains less of this gas, hence becomes more easily dispersed.

(iii) In the simulation, we find for some massive stars that the environmental densities are high and the radiative bubbles are embedded in sub-structures. When the radiative bubble opens into the ambient medium, internal energy and hot, ionized gas is released and the embedded phase is terminated. This behaviour is reflected by small jumps in the internal energy evolution. In this phase, the ionized gas inside the H II region is heated to the prototypical  $\sim 8000$  K.

(iv) Star formation can be regulated by radiative feedback. In simulation ZLRAD, the star formation efficiency drops by a factor of  $\sim 4$  compared to the ZLNOFB in both clouds. The star formation efficiency in gas with densities above  $100 \text{ cm}^{-3}$  lies at  $\sim 5$ –9 per cent. This indicates that internal morphologies regulate the impact of photoionizing radiation, hence the star formation.

(v) Without feedback, a few sink particles accrete a significant fraction of the cloud mass. Radiative feedback significantly reduces the sink mass and instead may increase its number. This seems to be triggered star formation, even though the overall star formation efficiency is so severely reduced.

(vi) When comparing with observational data, we find that our two clouds, which were simulated using typical solar neighbourhood conditions, lie on top of the results derived for Taurus, Ophiuchus, and Lupus 3, three low-mass, star-forming, nearby MC with similar total masses.

## ACKNOWLEDGEMENTS

SH, SW, DS, and FD acknowledge the support by the Bonn-Cologne Graduate School for physics and astronomy, which is funded through the German Excellence Initiative. SH, SW, and DS also acknowledge funding by the Deutsche Forschungsgemeinschaft (DFG) via the Sonderforschungsbereich SFB 956 'Conditions and Impact of Star Formation' (subproject C5). SH, SW, DS, FD, and TN acknowledge the support by the DFG Priority Program 1573 'The physics of the interstellar medium'. SH and SW acknowledge funding by the European Research Council through ERC Starting Grant No. 679852 'RADFEEDBACK'. TN acknowledges support from the DFG cluster of excellence 'Origin and Structure of the Universe'. RW acknowledges support by the Albert Einstein Centre for Gravitation and Astrophysics via the Czech Science Foundation grant 14-37086G and by the institutional project RVO:67985815 of the Academy of Sciences of the Czech Republic. The software used in this work was developed in part by the DOE NNSA ASC- and DOE Office Science ASCR-supported FLASH Center for Computational Science at University of Chicago. The authors gratefully acknowledge the Gauss Centre for Supercomputing e.V. ([www.gauss-centre.eu](http://www.gauss-centre.eu)) for funding this project (pr62su) by providing computing time on the GCS Supercomputer SuperMUC at Leibniz Supercomputing Centre (<http://www.lrz.de>). We thank the YT-PROJECT community (Turk et al. 2011) for the YT analysis package, which we used to analyse and plot most of the data. We thank the anonymous referee for the constructive input.

## REFERENCES

- Aarseth S. J., 1999, *PASP*, 111, 1333  
Aarseth S. J., 2003, *Gravitational N-Body Simulations*. Cambridge Univ. Press, Cambridge, p. 430  
Ahmad A., Cohen L., 1973, *J. Comput. Phys.*, 12, 389  
André P., Di Francesco J., Ward-Thompson D., Inutsuka S.-I., Pudritz R. E., Pineda J. E., 2014, in Beuther H., Klessen R. S., Dullemond C. P., Henning T., eds, *Protostars and Planets VI*. Univ. Arizona Press, Tucson, AZ, p. 27  
Baczynski C., Glover S. C. O., Klessen R. S., 2015, *MNRAS*, 454, 380  
Balfour S. K., Whitworth A. P., Hubber D. A., Jaffa S. E., 2015, *MNRAS*, 453, 2471  
Bisbas T. G. et al., 2015, *MNRAS*, 453, 1324  
Blondin J. M., Wright E. B., Borkowski K. J., Reynolds S. P., 1998, *ApJ*, 500, 342  
Bonnell I. A., Dobbs C. L., Smith R. J., 2013, *MNRAS*, 430, 1790  
Bouchut F., Klingenberg C., Waagan K., 2007, *Numer. Math.*, 108, 7  
Bouchut F., Klingenberg C., Waagan K., 2010, *Numer. Math.*, 115, 647  
Brunt C. M., Heyer M. H., Mac Low M.-M., 2009, *A&A*, 504, 883  
Butler M. J., Tan J. C., Teyssier R., Rosdahl J., Van Loo S., Nickerson S., 2017, *ApJ*, 841, 82  
Castor J., McCray R., Weaver R., 1975, *ApJ*, 200, L107  
Clark P. C., Glover S. C. O., Klessen R. S., Bonnell I. A., 2012, *MNRAS*, 424, 2599  
Colombo D. et al., 2014, *ApJ*, 784, 3  
Dale J. E., 2015, *New Astron. Rev.*, 68, 1  
Dale J. E., Bonnell I. A., Clarke C. J., Bate M. R., 2005, *MNRAS*, 358, 291  
Dale J. E., Ercolano B., Bonnell I. A., 2012, *MNRAS*, 424, 377  
Dale J. E., Ngoumou J., Ercolano B., Bonnell I. A., 2013, *MNRAS*, 436, 3430  
Dale J. E., Ngoumou J., Ercolano B., Bonnell I. A., 2014, *MNRAS*, 442, 694  
de Avillez M. A., Breitschwerdt D., 2005, *A&A*, 436, 585  
Diaz-Miller R. I., Franco J., Shore S. N., 1998, *ApJ*, 501, 192  
Dobbs C. L., 2015, *MNRAS*, 447, 3390  
Dobbs C. L., Pringle J. E., Burkert A., 2012, *MNRAS*, 425, 2157  
Dobbs C. L. et al., 2014, in Beuther H., Klessen R. S., Dullemond C. P., Henning T., eds, *Protostars and Planets VI*. Univ. Arizona Press, Tucson, AZ, p. 3  
Dobbs C. L., Pringle J. E., Duarte-Cabral A., 2015, *MNRAS*, 446, 3608  
Draine B. T., 1978, *ApJS*, 36, 595  
Draine B. T., 2011, *Physics of the Interstellar and Intergalactic Medium*. Princeton Univ. Press, Princeton, NJ  
Dubey A. et al., 2008, in Pogorelov N. V., Audit E., Zank G. P., eds, *ASP Conf. Ser. Vol. 385, Numerical Modeling of Space Plasma Flows*. Astron. Soc. Pac., San Francisco, p. 145  
Ekström S. et al., 2012, *A&A*, 537, A146  
Evans N. J., II, et al., 2009, *ApJS*, 181, 321  
Fall S. M., Krumholz M. R., Matzner C. D., 2010, *ApJ*, 710, L142  
Federrath C., Banerjee R., Clark P. C., Klessen R. S., 2010, *ApJ*, 713, 269  
Foster P. N., Chevalier R. A., 1993, *ApJ*, 416, 303  
Fryxell B. et al., 2000, *ApJS*, 131, 273  
Gatto A. et al., 2015, *MNRAS*, 449, 1057  
Gatto A. et al., 2017, *MNRAS*, 466, 1903  
Gavagnin E., Bleuler A., Rosdahl J., Teyssier R., 2017, *MNRAS*, 472, 4155  
Geen S., Rosdahl J., Blaizot J., Devriendt J., Slyz A., 2015, *MNRAS*, 448, 3248  
Geen S., Watson S. K., Rosdahl J., Bieri R., Klessen R. S., Hennebelle P., 2018, *MNRAS*, 481, 2548  
Girichidis P. et al., 2016, *MNRAS*, 456, 3432  
Glover S. C. O., Mac Low M.-M., 2007a, *ApJS*, 169, 239  
Glover S. C. O., Mac Low M.-M., 2007b, *ApJ*, 659, 1317  
Glover S. C. O., Federrath C., Mac Low M.-M., Klessen R. S., 2010, *MNRAS*, 404, 2  
Gnat O., Ferland G. J., 2012, *ApJS*, 199, 20  
Goldreich P., Kwan J., 1974, *ApJ*, 189, 441  
Górski K. M., Hivon E., Banday A. J., Wandelt B. D., Hansen F. K., Reinecke M., Bartelmann M., 2005, *ApJ*, 622, 759

- Gritschneider M., Naab T., Walch S., Burkert A., Heitsch F., 2009, *ApJ*, 694, L26
- Habing H. J., 1968, *Bull. Astron. Inst. Neth.*, 19, 421
- Haid S., Walch S., Naab T., Seifried D., Mackey J., Gatto A., 2016, *MNRAS*, 460, 2962
- Haid S., Walch S., Seifried D., Wünsch R., Dinnbier F., Naab T., 2018, *MNRAS*, 478, 4799
- Harper-Clark E., Murray N., 2009, *ApJ*, 693, 1696
- Heiderman A., Evans N. J., II, Allen L. E., Huard T., Heyer M., 2010, *ApJ*, 723, 1019
- Heitsch F., Burkert A., Hartmann L. W., Slyz A. D., Devriendt J. E. G., 2005, *ApJ*, 633, L113
- Hennebelle P., Iffrig O., 2014, *A&A*, 570, A81
- Hetem A., Jr., Lepine J. R. D., 1993, *A&A*, 270, 451
- Hill A. S., Joung M. R., Mac Low M. -M., Benjamin R. A., Haffner L. M., Klingenberg C., Waagan K., 2012, *ApJ*, 750, 104
- Hosokawa T., Inutsuka S. -I., 2006, *ApJ*, 646, 240
- Howard C., Pudritz R., Klessen R., 2017, *ApJ*, 834, 40
- Howard C. S., Pudritz R. E., Harris W. E., 2016, *MNRAS*, 461, 2953
- Hughes A. et al., 2013, *ApJ*, 779, 46
- Ibáñez-Mejía J. C., Mac Low M. -M., Klessen R. S., Baczynski C., 2017, *ApJ*, 850, 62
- Inoue T., Fukui Y., 2013, *ApJ*, 774, L31
- Joung M. K. R., Mac Low M. -M., 2006, *ApJ*, 653, 1266
- Kennicutt R. C., Jr., 1998, *ApJ*, 498, 541
- Kim C. -G., Ostriker E. C., 2018, *ApJ*, 853, 173
- Kim C. -G., Ostriker E. C., Kim W. -T., 2013, *ApJ*, 776, 1
- Klessen R. S., 2011, *EAS Publ. Ser.*, 51, 133
- Klessen R. S., Glover S. C. O., 2016, *Star Formation in Galaxy Evolution: Connecting Numerical Models to Reality*, Saas-Fee Advanced Course, Vol. 43. Springer-Verlag, Berlin Heidelberg, p. 85
- Klessen R. S., Heitsch F., Mac Low M. -M., 2000, *ApJ*, 535, 887
- Körtgen B., Seifried D., Banerjee R., Vázquez-Semadeni E., Zamora-Avilés M., 2016, *MNRAS*, 459, 3460
- Kroupa P., 2001, *MNRAS*, 322, 231
- Krumholz M. R., 2006, *ApJ*, 641, L45
- Krumholz M. R., Matzner C. D., 2009, *ApJ*, 703, 1352
- Krumholz M. R., Tan J. C., 2007, *ApJ*, 654, 304
- Krumholz M. R., Klein R. I., McKee C. F., Offner S. S. R., Cunningham A. J., 2009, *Science*, 323, 754
- Krumholz M. R., Dekel A., McKee C. F., 2012, *ApJ*, 745, 69
- Krumholz M. R., Dekel A., McKee C. F., 2013, *ApJ*, 779, 89
- Kudritzki R. -P., Puls J., 2000, *ARA&A*, 38, 613
- Kuffmeier M., Haugbølle T., Nordlund Å., 2017, *ApJ*, 846, 7
- Lada C. J., Lada E. A., 2003, *ARA&A*, 41, 57
- Lada C. J., Lombardi M., Alves J. F., 2010, *ApJ*, 724, 687
- Mac Low M. -M., Klessen R. S., 2004, *Rev. Mod. Phys.*, 76, 125
- Mac Low M. -M., de Avillez M. A., Korpi M. J., 2004, in Alfaro E. J., Pérez E., Franco J., eds, *Astrophysics and Space Science Library* Vol. 315, *How Does the Galaxy Work? A Galactic Tertulia with Don Cox and Ron Reynolds*. Kluwer, Dordrecht, p. 339
- Makino J., 1991, *ApJ*, 369, 200
- Makino J., Aarseth S. J., 1992, *PASJ*, 44, 141
- Markova N., Puls J., 2008, *A&A*, 478, 823
- Markova N., Puls J., Repolust T., Markov H., 2004, *A&A*, 413, 693
- Matzner C. D., 2002, *ApJ*, 566, 302
- Matzner C. D., McKee C. F., 2000, *ApJ*, 545, 364
- Mellema G., Arthur S. J., Henney W. J., Iliev I. T., Shapiro P. R., 2006, *ApJ*, 647, 397
- Monaghan J. J., Lattanzio J. C., 1985, *A&A*, 149, 135
- Murray N., 2011, *ApJ*, 729, 133
- Murray N., Quataert E., Thompson T. A., 2010, *ApJ*, 709, 191
- Naab T., Ostriker J. P., 2017, *ARA&A*, 55, 59
- Nelson R. P., Langer W. D., 1997, *ApJ*, 482, 796
- Ngoumou J., Hubber D., Dale J. E., Burkert A., 2015, *ApJ*, 798, 32
- Nordlund Å., Ramsey J. P., Popovas A., Kuffmeier M., 2018, *MNRAS*, 477, 624
- Ostriker J. P., McKee C. F., 1988, *Rev. Mod. Phys.*, 60, 1
- Padoan P., Pan L., Haugbølle T., Nordlund Å., 2016, *ApJ*, 822, 11
- Padoan P., Haugbølle T., Nordlund Å., Frimann S., 2017, *ApJ*, 840, 48
- Peters T., Mac Low M. -M., Banerjee R., Klessen R. S., Dullemond C. P., 2010a, *ApJ*, 719, 831
- Peters T., Klessen R. S., Mac Low M. -M., Banerjee R., 2010b, *ApJ*, 725, 134
- Peters T. et al., 2017, *MNRAS*, 466, 3293
- Pettitt A. R., Tasker E. J., Wadsley J. W., Keller B. W., Benincasa S. M., 2017, *MNRAS*, 468, 4189
- Pittard J. M., 2013, *MNRAS*, 435, 3600
- Puls J., Vink J. S., Najarro F., 2008, *A&AR*, 16, 209
- Ragan S. et al., 2012, *A&A*, 547, A49
- Rathborne J. M., Jackson J. M., Simon R., 2006, *ApJ*, 641, 389
- Rey-Raposo R., Dobbs C., Duarte-Cabral A., 2015, *MNRAS*, 446, L46
- Rey-Raposo R., Dobbs C., Agertz O., Alig C., 2017, *MNRAS*, 464, 3536
- Rogers H., Pittard J. M., 2013, *MNRAS*, 431, 1337
- Röllig M. et al., 2007, *A&A*, 467, 187
- Rosen A. L., Lopez L. A., Krumholz M. R., Ramirez-Ruiz E., 2014, *MNRAS*, 442, 2701
- Rybicki G. B., Lightman A. P., 2004, *Radiative Processes in Astrophysics*. Wiley, New York
- Salpeter E. E., 1955, *ApJ*, 121, 161
- Schmidt M., 1959, *ApJ*, 129, 243
- Sedov L. I., 1958, *Rev. Modern Phys.*, 30, 1077
- Seifried D. et al., 2017, *MNRAS*, 472, 4797
- Sembach K. R., Howk J. C., Ryans R. S. I., Keenan F. P., 2000, *ApJ*, 528, 310
- Shu F. H., 1977, *ApJ*, 214, 488
- Slyz A. D., Devriendt J. E. G., Bryan G., Silk J., 2005, *MNRAS*, 356, 737
- Smith R. J., Glover S. C. O., Clark P. C., Klessen R. S., Springel V., 2014a, *MNRAS*, 441, 1628
- Smith R. J., Glover S. C. O., Klessen R. S., 2014b, *MNRAS*, 445, 2900
- Spitzer L., Jr., 1942, *ApJ*, 95, 329
- Spitzer L., 1978, *Physical processes in the interstellar medium*. Wiley, New York
- Strömgren B., 1939, *ApJ*, 89, 526
- Tielens A. G. G. M., 2005, *The Physics and Chemistry of the Interstellar Medium*. Cambridge Univ. Press, Cambridge
- Truelove J. K., Klein R. I., McKee C. F., Holliman J. H., II, Howell L. H., Greenough J. A., 1997, *ApJ*, 489, L179
- Turk M. J., Smith B. D., Oishi J. S., Skory S., Skillman S. W., Abel T., Norman M. L., 2011, *ApJS*, 192, 9
- Vázquez-Semadeni E., Ballesteros-Paredes J., Klessen R. S., 2003, *ApJ*, 585, L131
- Vázquez-Semadeni E., Gómez G. C., Jappsen A. K., Ballesteros-Paredes J., González R. F., Klessen R. S., 2007, *ApJ*, 657, 870
- Vázquez-Semadeni E., Colín P., Gómez G. C., Ballesteros-Paredes J., Watson A. W., 2010, *ApJ*, 715, 1302
- Waagan K., 2009, *J. Comput. Phys.*, 228, 8609
- Waagan K., Federrath C., Klingenberg C., 2011, *J. Comput. Phys.*, 230, 3331
- Walch S., Naab T., 2015, *MNRAS*, 451, 2757
- Walch S. et al., 2015, *MNRAS*, 454, 238
- Walch S. K., Whitworth A. P., Bisbas T., Wünsch R., Hubber D., 2012, *MNRAS*, 427, 625
- Wareing C. J., Pittard J. M., Falle S. A. E. G., 2017, *MNRAS*, 470, 2283
- Weaver R., McCray R., Castor J., Shapiro P., Moore R., 1977, *ApJ*, 218, 377
- Whitworth A., 1979, *MNRAS*, 186, 59
- Whitworth A. P., Bhattal A. S., Chapman S. J., Disney M. J., Turner J. A., 1994, *MNRAS*, 268, 291
- Wolfire M. G., Hollenbach D., McKee C. F., Tielens A. G. G. M., Bakes E. L. O., 1995, *ApJ*, 443, 152
- Wood D. O. S., Churchwell E., 1989, *ApJS*, 69, 831
- Wünsch R., Silich S., Palouš J., Tenorio-Tagle G., Muñoz-Tuñón C., 2011, *ApJ*, 740, 75
- Wünsch R., Walch S., Dinnbier F., Whitworth A., 2018, *MNRAS*, 475, 3393
- Zuckerman B., Evans N. J., II, 1974, *ApJ*, 192, L149

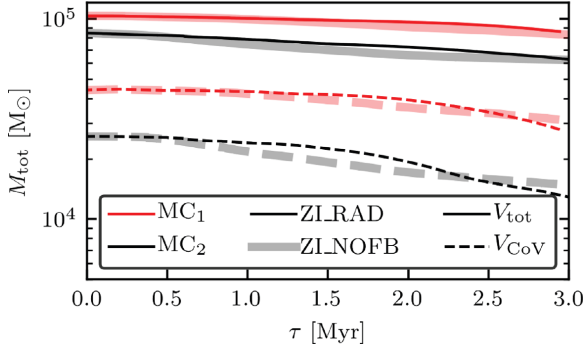


**Figure A1.** Evolution of the mass,  $M_{\text{tot}}$ , in the total volume,  $V_{\text{tot}}$  (solid), and the central sub-region,  $V_{\text{CoV}}$  (dashed), in MC1 (red) and MC2 (black) for simulation ZI\_RAD (thin) and ZI\_NOFB (thick).

#### APPENDIX A: MASS EVOLUTION

Fig. A1 shows the time evolution of the total mass in MC1 (red) and MC2 (black) for simulation ZI\_RAD (thin) and ZI\_NOFB (thick) in the total volume,  $V_{\text{tot}}$  (solid), and the central sub-region,  $V_{\text{CoV}}$  (dashed).

Fig. A2 shows the density–temperature distribution of MC1 (top subpanel) and MC2 (bottom sub-panel) at  $\tau_{1.0}$  (top) and  $\tau_{3.0}$  (bottom). The molecular hydrogen fraction (left) and ionized hydrogen fraction (right) is indicated by colour.

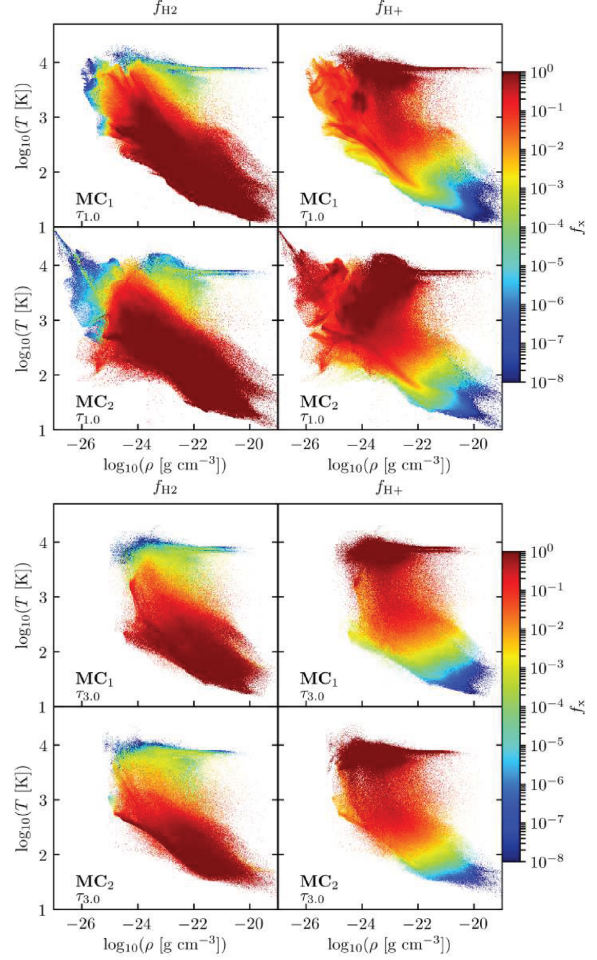


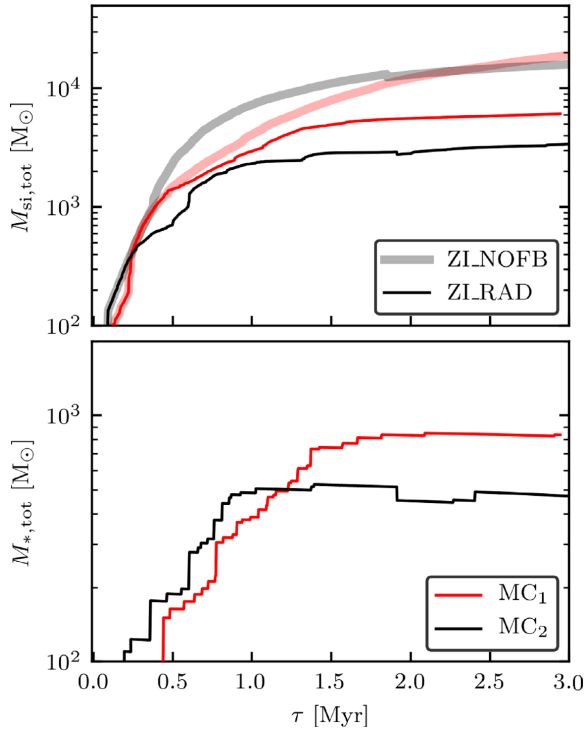
**Figure A2.** Density–temperature distribution of MC1 (top) and MC2 (bottom) with the molecular hydrogen fraction (left) and ionized hydrogen fraction (right) at the  $\tau_{1.0}$  (top panels) and  $\tau_{3.0}$  (bottom panels).

#### APPENDIX B: STELLAR MASS EVOLUTION

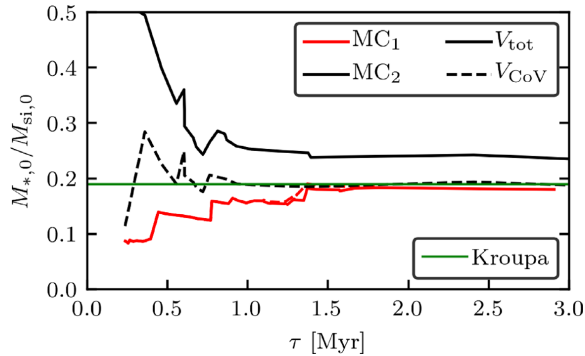
Fig. B1 shows the time evolution of the sink mass,  $M_{\text{si,tot}}$ , (top) and the total mass of massive stars,  $M_{\text{s,tot}}$ , (bottom) in the total volume  $V_{\text{tot}}$  of MC1 (red) and MC2 (black) for simulation ZI\_NOFB (thick, only top) and ZI\_RAD (thin), respectively. The initial phase of  $M_{\text{s,tot}}$  shows oscillations, which is due to two particles, which move out of the domain.

Fig. B2 shows the ratio between the stellar and sink mass at the time of the stellar formation,  $M_{\text{s},0} / M_{\text{si},0}$ , in MC1 (red) and MC2 (black) for simulation ZI\_RAD in the total cloud (solid) and the central sub-regions (dashed). The mass fractions of the high-mass range with respect to the underlying Kroupa IMF lies at 18 per cent (green horizontal line). Hence, a stellar population (in a cloud) that satisfies this ratio represents the IMF well. Ratios above and below indicate that massive stars over- and under-represented the IMF, respectively. After an initial massive star deficit, both central sub-regions and MC2 are well sampling the IMF. The high values in MC1 are caused by an initial  $\approx 100 M_{\odot}$  star.





**Figure B1.** Evolution of the sink mass  $M_{\text{si,tot}}$  (top) and the stellar mass  $M_{*,\text{tot}}$  (bottom) in MC<sub>1</sub> (red) and MC<sub>2</sub> (black) for simulation ZI.RAD (thin, only top) and ZI.NOFB (thick). The evolution of  $M_{*,\text{tot}}$  shows some oscillation at the beginning, which is due to stars, which move out of the MC, hence are not considered in the analysis.



**Figure B2.** Evolution of the ratio between the stellar and sink mass at the time of stellar formation in MC<sub>1</sub> (red) and MC<sub>2</sub> (black) for simulation ZI.RAD in the total cloud (solid) and the central sub-region (dashed). The mass fraction of the high-mass range with respect to the underlying Kroupa IMF is shown as a horizontal, green line. Note that after about 2 Myr star formation has ceased and the mass fraction remains therefore constant.

Fig. B3 shows the time evolution of the initial stellar mass (top), the distance (centre) to the centre of the small, central sub-region of cloud MC<sub>1</sub> (red) and MC<sub>2</sub> (black) and the luminosity of Lyman continuum photons (bottom). The full markers and solid lines and empty markers and dashed lines indicate that the star is located in the central sub-region or the rest of the cloud, respectively.

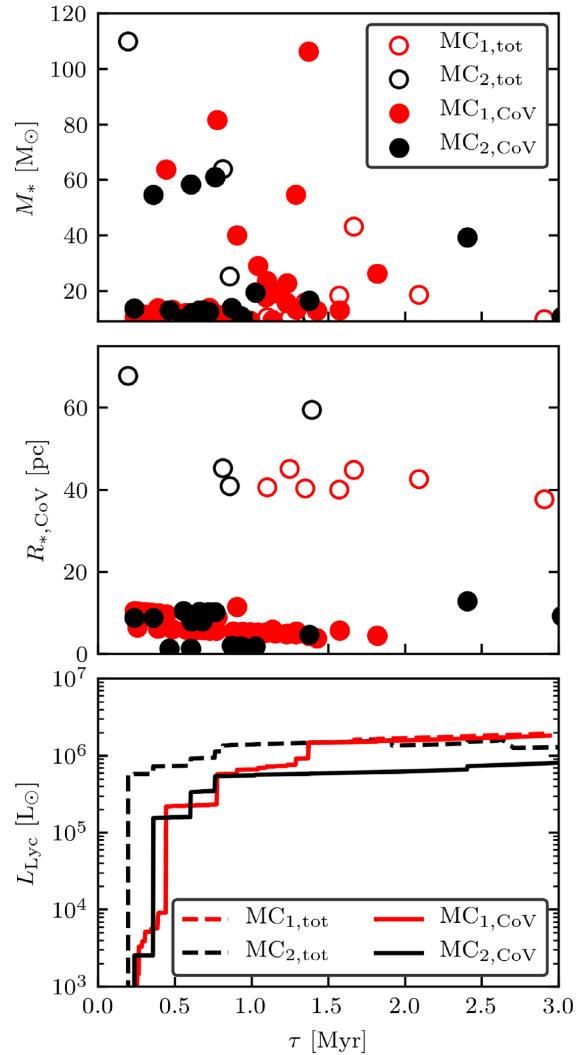


**Figure B3.** The mass of new-born massive stars at their birth time (top), and their distance to the centre of mass (middle panel) of the clouds MC<sub>1</sub> (red) and MC<sub>2</sub> (black) as well as the time evolution of the luminosity of Lyman continuum photons (bottom). The full markers and solid lines indicate that the star is located in the central volume with  $(40 \text{ pc})^3$ , whereas empty markers and dashed lines indicate a position within the rest of the cloud.

## APPENDIX C: OTHER PROJECTIONS

Figs C1 and C2 as well as Figs C3 and C2 show the time evolution of the gas column density  $\Sigma_{\text{gas}}$  in the  $x$ - $z$ -plane and in the  $x$ - $y$  plane for the central sub-region ( $V_{\text{CoV}}$ , see Fig. 2 and Table 1) of MC<sub>1</sub> and MC<sub>2</sub>, respectively. The two columns show simulations ZI.NOFB (left) and ZI.RAD (right), respectively, at times  $\tau_{1.0}$  to  $\tau_{3.0}$  (from top to bottom). The circles indicate sink particles without an active stellar component, i.e. without massive stars. Star-shaped markers are cluster sink particles with active stellar feedback. The colour of the markers indicates the sink age.

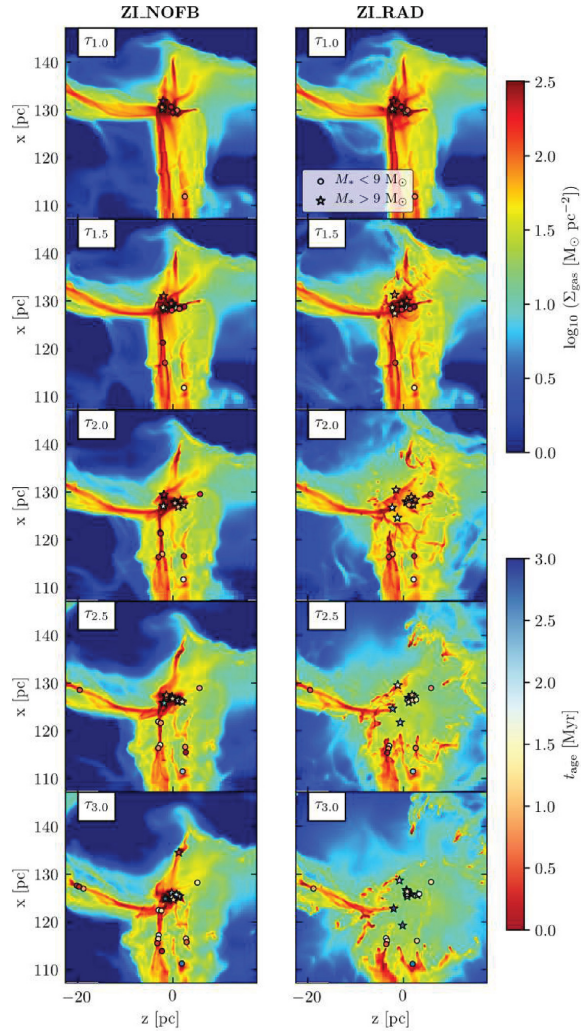


**Figure C1.** Same as the left two columns in Fig. 3 but projected along y-direction.

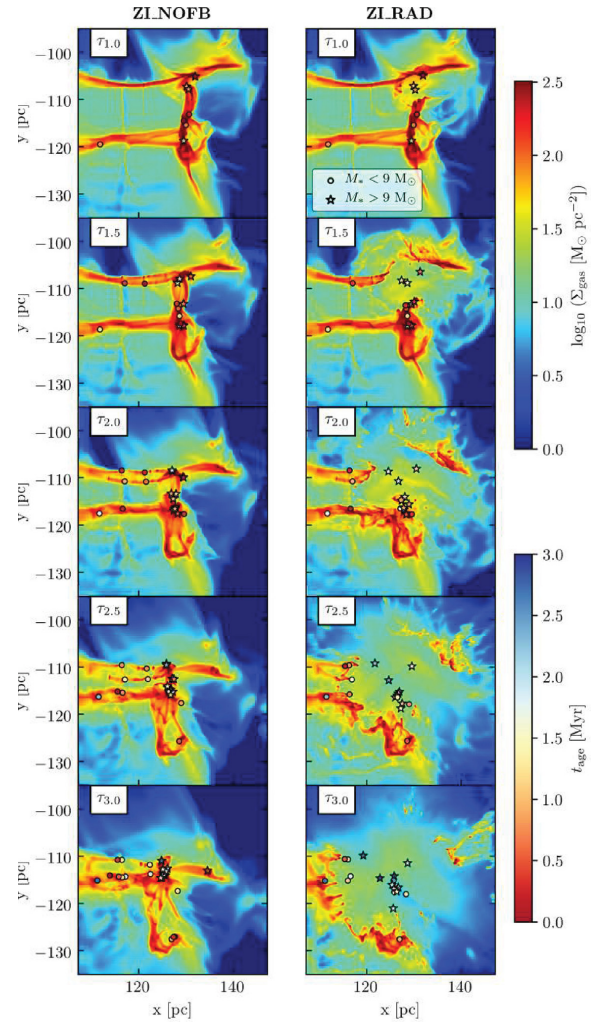


**Figure C2.** Same as the left two columns in Fig. 3 but projected along z-direction.

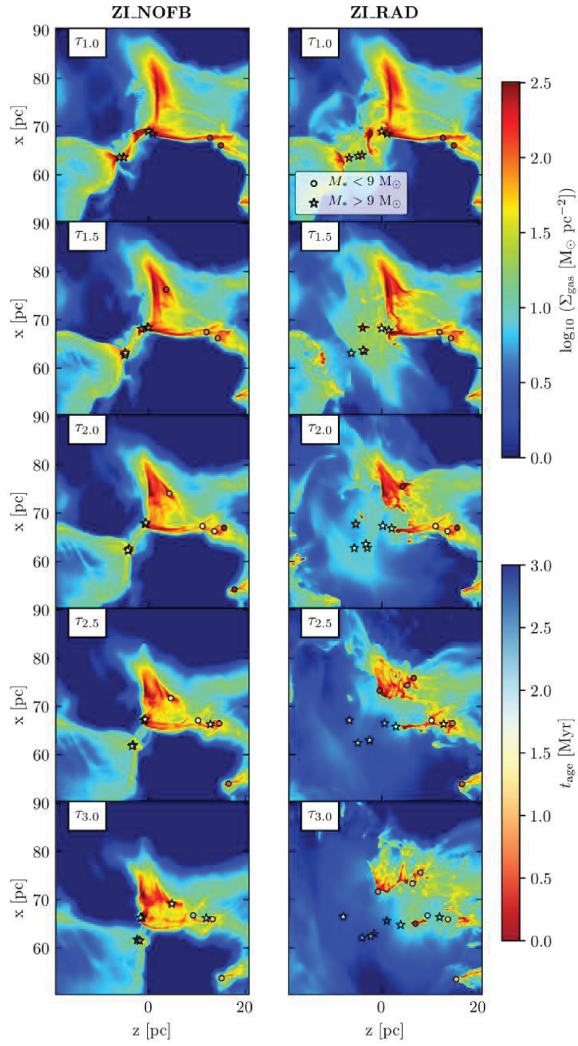


**Figure C3.** Same as the left two columns in Fig. 4 but projected along y-direction.

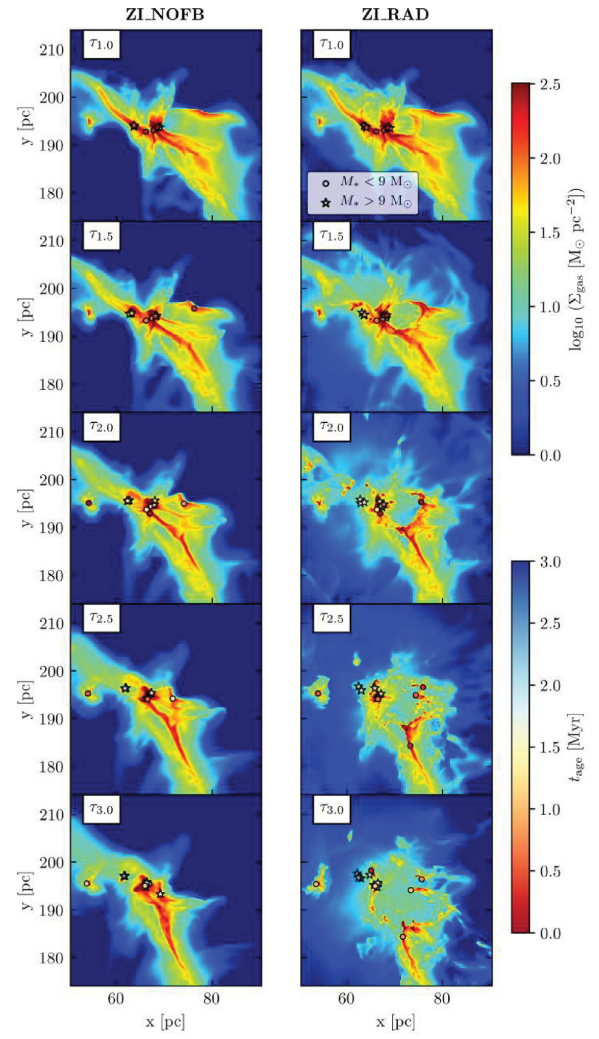


**Figure C4.** Same as the left two columns in Fig. 4 but projected along z-direction.

This paper has been typeset from a  $\text{\LaTeX}$  file prepared by the author.







# Supernova blast waves in wind-blown bubbles, turbulent, and power-law ambient media

S. Haid,<sup>1</sup>★ S. Walch,<sup>1</sup> T. Naab,<sup>2</sup> D. Seifried,<sup>1</sup> J. Mackey,<sup>1,3</sup> and A. Gatto<sup>2</sup>

<sup>1</sup>*I. Physikalisches Institut, Universität zu Köln, Zùlpicher-Strasse 77, D-50937 Cologne, Germany*

<sup>2</sup>*Max-Planck-Institut für Astrophysik, Karl-Schwarzschild-Strasse 1, D-85741 Garching, Germany*

<sup>3</sup>*Dublin Institute for Advanced Studies, School of Cosmic Physics, 31 Fitzwilliam Place, Dublin 2, Ireland*

Accepted 2016 May 4. Received 2016 May 4; in original form 2016 February 9

## ABSTRACT

Supernova (SN) blast waves inject energy and momentum into the interstellar medium (ISM), control its turbulent multiphase structure and the launching of galactic outflows. Accurate modelling of the blast wave evolution is therefore essential for ISM and galaxy formation simulations. We present an efficient method to compute the input of momentum, thermal energy, and the velocity distribution of the shock-accelerated gas for ambient media (densities of  $0.1 \geq n_0 \text{ [cm}^{-3}] \geq 100$ ) with uniform (and with stellar wind blown bubbles), power-law, and turbulent (Mach numbers  $\mathcal{M}$  from 1 to 100) density distributions. Assuming solar metallicity cooling, the blast wave evolution is followed to the beginning of the momentum conserving snowplough phase. The model recovers previous results for uniform ambient media. The momentum injection in wind-blown bubbles depend on the swept-up mass and the efficiency of cooling, when the blast wave hits the wind shell. For power-law density distributions with  $n(r) \sim r^{-2}$  (for  $n(r) > n_{\text{floor}}$ ) the amount of momentum injection is solely regulated by the background density  $n_{\text{floor}}$  and compares to  $n_{\text{uni}} = n_{\text{floor}}$ . However, in turbulent ambient media with lognormal density distributions the momentum input can increase by a factor of 2 (compared to the homogeneous case) for high Mach numbers. The average momentum boost can be approximated as  $p_{\text{turb}}/p_0 = 23.07 \left(\frac{n_{0,\text{turb}}}{1 \text{ cm}^{-3}}\right)^{-0.12} + 0.82(\ln(1 + b^2 \mathcal{M}^2))^{1.49} \left(\frac{n_{0,\text{turb}}}{1 \text{ cm}^{-3}}\right)^{-1.6}$ . The velocity distributions are broad as gas can be accelerated to high velocities in low-density channels. The model values agree with results from recent, computationally expensive, three-dimensional simulations of SN explosions in turbulent media.

**Key words:** shock waves – turbulence – ISM: supernova remnants.

## 1 INTRODUCTION

Supernovae (SNe) play a fundamental role in setting the properties of the multiphase interstellar medium (ISM; e.g. Salpeter 1955; de Avillez & Breitschwerdt 2004; Joung & Mac Low 2006; Kim, Ostriker & Kim 2013; Walch et al. 2015). They not only enrich the ISM with metals but also inject energy and momentum leading to the dispersal of molecular clouds (MCs), the driving of turbulent motions as well as galactic outflows (e.g. Mac Low & Klessen 2004; Dib, Bell & Burkert 2006; Gent et al. 2013; Girichidis et al. 2016). Therefore, SN explosions may locally (and globally) control star formation (Agertz et al. 2013; Hennebelle & Iffrig 2014; Iffrig & Hennebelle 2015; Walch & Naab 2015). Spatially and temporally correlated SNe can interact and drive the expansion of coherent shells, often termed as ‘superbubbles’ (e.g. McCray &

Kafatos 1987; Mac Low & McCray 1988; Tenorio-Tagle & Bodenheimer 1988; Sharma et al. 2014). Large-scale supershells (e.g. Carina Flare; Dawson et al. 2008; Palouš et al. 2009; Dawson et al. 2011) may sweep up enough mass to create new MCs, which in turn could spawn new stars and star clusters (Elmegreen & Lada 1977; Wunsch et al. 2010; Ntormousi et al. 2011). On galactic scales SNe might drive fountain flows or even galactic winds (e.g. Larson 1974; Mac Low & Ferrara 1999; Ostriker, McKee & Leroy 2010; Dalla Vecchia & Schaye 2012; Hill et al. 2012; Creasey, Theuns & Bower 2013; Girichidis et al. 2016). Therefore, SNe might play an important role for regulating the efficiency of galaxy formation and determine galaxy morphology (e.g. Dekel & Silk 1986; Goldbaum et al. 2011; Brook et al. 2012; Aumer et al. 2013; Hopkins et al. 2014; Marinacci, Pakmor & Springel 2014; Übler et al. 2014). All of the above conclusions about the impact of SN explosions have been made on the basis of (at the time) computationally expensive numerical simulations with varying degrees of accuracy.

\*E-mail: haid@ph1.uni-koeln.de

For a long time the evolution of blast waves has been in the focus of theoretical studies (e.g. Sedov 1946; Taylor 1950 and their importance for galactic astrophysics has been realized early on. A key parameter (apart from the explosion energy) determining the fate of an SN remnant (SNR) is the density of the ambient ISM. In numerous analytical studies the evolution of blast waves – also in the presence of cooling – was (mostly) investigated for homogeneous or power-law density distributions (Cox 1972; Chevalier 1976; McKee & Ostriker 1977; Cowie, McKee & Ostriker 1981; Cox & Franco 1981; Cioffi, McKee & Bertschinger 1988; Ostriker & McKee 1988; Franco et al. 1994; Blondin et al. 1998).

For more realistic density distributions similar to the observed ISM it is more challenging (or even impossible) to make accurate analytical predictions. The ISM is structured and is subject to supersonic turbulent motions, which lead to the observed lognormal shape of the column density probability distribution function (PDF; Kainulainen et al. 2009; Schneider et al. 2011). Numerical and analytic work confirms a lognormal surface density (Mac Low & Klessen 2004) as well as volume density PDF in isothermal supersonic flows (Vazquez-Semadeni, Passot & Pouquet 1993; Padoan, Nordlund & Jones 1997a,b; Ostriker, Stone & Gammie 2001; Kritsuk et al. 2006; Federrath, Klessen & Schmidt 2008; Walch et al. 2011; Shetty & Ostriker 2012; Ward, Wadsley & Sills 2014). In addition, the structure of the ISM around massive stars is strongly affected by the massive stars' ionizing radiation (e.g. Kessel-Deynet & Burkert 2003; Dale et al. 2005; Gritschneider et al. 2009; Walch et al. 2012) and stellar winds (e.g. Weaver et al. 1977). These structural changes affect the impact of SN explosions (e.g. Rogers & Pittard 2013; Geen et al. 2015; Walch & Naab 2015).

The efficiency with which energy and momentum from an SN explosion is transferred to the ambient medium depends on the mean ambient density  $n_0$  and its turbulent Mach number  $\mathcal{M}$ . Direct numerical simulations indicate that in dense environments ( $n_{0,\text{turb}} = 100 \text{ cm}^{-3}$ ) and low-Mach-number regimes ( $\mathcal{M} < 10$ ) the input of momentum is moderate in the presence of cooling (Kim & Ostriker 2015; Walch & Naab 2015) with a momentum transfer of  $\sim 10$  times the initial SN momentum  $p_0$  ( $p_0 \sim 10^4 - 3 \times 10^4 \text{ M}_\odot \text{ km s}^{-1}$ , in this work  $p_0 = 14\,181 \text{ M}_\odot \text{ km s}^{-1}$ ), while the momentum input can be  $\sim 2$  times larger for densities  $n_{0,\text{turb}} < 0.1 \text{ cm}^{-3}$ . For lower densities, however, the energy and momentum transfer can be significantly higher. Recent numerical simulations have shown that varying assumptions for typical ambient densities of SN explosions can result in very different evolutionary paths of the ISM. In the most extreme case of SN mainly going off in the diffuse phase, the SNRs can interact without significant cooling and the system can go into thermal runaway or start driving a hot outflow (Gatto et al. 2015; Li et al. 2015; Girichidis et al. 2016).

In cosmological simulations of galaxy formation with typical resolution elements of several hundred parsecs, all the above details – in particular the first phases of blast wave evolution – are unresolved in dense environments, leading to discrepancies between the theoretical expectations and the simulated reality (see e.g. Schaye et al. 2015). In general, this long-known ‘overcooling problem’ appears when the main momentum creating stages, the Sedov–Taylor (ST) and the pressure driven snowplough (PDS) phase, stay unresolved and become artificially short (Balogh et al. 2001; Stinson et al. 2006; Creasey et al. 2011; Tomassetti et al. 2015). The thermal energy is radiated away too quickly and the momentum input is unresolved as too much mass is accelerated to too low velocities (Hu et al. 2016), in particular if the time step is not reduced accordingly (Dalla Vecchia & Schaye 2012; Kim & Ostriker 2015). The properties of the hot phase within the SNR are also predicted inaccurately and the

effect on the global filling factor of the ISM is then biased (McKee & Ostriker 1977; Agertz et al. 2013; Keller, Wadsley & Couchman 2015). A plausible way to overcome these inaccuracies might be the construction of subresolution feedback models with information extracted from small-scale resolved numerical simulations of SNRs. However, this computationally expensive process has to cover all the complexity of SNRs and their surroundings (Kim & Ostriker 2015; Martizzi, Faucher-Giguère & Quataert 2015; Walch & Naab 2015; Thompson & Krumholz 2016).

To better understand the evolution of blast waves in the complex ISM, we present an efficient one-dimensional model, based on the thin-shell approach (Ostriker & McKee 1988), to compute the momentum input from SNe for uniform (see Section 4.1), radial power-law (see Section 4.2), wind-blown bubble (see Section 5) or turbulent environmental density distributions (see Section 6.1). In addition to previous studies (e.g. Cioffi et al. 1988; Ostriker & McKee 1988), we combine the computation of all blast wave phases and their transitions in a single code using tabulated cooling functions. This way we can cover a wide range of ambient medium parameters. The model is easily customized to different SN scenarios as shown in case of a pre-existing wind bubble or a turbulent environment. We test the code results against recent, highly resolved numerical simulations (Kim & Ostriker 2015; Martizzi et al. 2015; Walch & Naab 2015; Thompson & Krumholz 2016) and show that we are able to achieve comparable results at almost negligible computational costs.

The paper is structured as follows. In Section 2, we discuss the set of equations which govern the evolution of the SNR and the momentum transfer to the ISM. Section 3 introduces the model which forms the basis for this work. We discuss cases (i) and (ii) in Section 4. In Section 5, we show the momentum input in a wind-blown bubble. In Section 6, we extend our model to apply it to a turbulent environment and conclude in Section 7.

## 2 THE EVOLUTION OF SUPERNOVA REMNANTS

When a massive star explodes as a core-collapse SN, gas (typically  $\sim 2\text{--}5 \text{ M}_\odot$ ) is ejected with supersonic velocities ( $v_{\text{eject}} \sim 6000\text{--}7000 \text{ km s}^{-1}$ ; Blondin et al. 1998; Janka et al. 2012), and drives a blast wave into the ISM. The evolution of the blast wave can be characterized by the time evolution  $t$  of the shock radius  $r_s$ ,

$$r_s \propto t^\eta, \quad (1)$$

where  $t$  is the time after the explosion and  $\eta$  is the expansion parameter (Klein, McKee & Colella 1994; Cohen, Piran & Sari 1998; Kushnir & Waxman 2010). It can be separated into five different phases (see Fig. 1; McKee & Ostriker 1977; Cioffi et al. 1988; Ostriker & McKee 1988; Petruk 2006; Li et al. 2015).

(i) Pre-Sedov–Taylor (PST) phase. In this first phase after the initial explosion radiative losses are insignificant for the dynamics of the SNR. The supersonically expanding ejecta dominate the evolution with an initial expansion parameter  $\eta = 1$  (free expansion phase). The shock of the blast wave proceeds into the ambient medium. However the shocked material pushes on the ejecta. A reverse shock emerges. It interacts with the freely expanding ejecta causing a pressure gradient between the forward and reverse shock. Part of the kinetic energy of the SN ejecta is converted into heat. In this non-self-similar phase the expansion parameter decreases continuously. When the swept-up mass is comparable to the ejecta

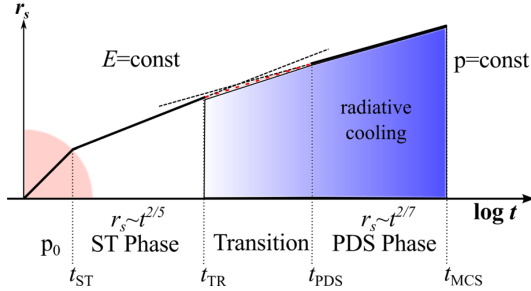


**Figure 1.** Schematic time evolution (times and radius are not to scale) of an SN blast wave radius in a homogeneous environment.  $p_0$  is the initial radial momentum of the SN ejecta. The PST phase (red) terminates at  $t = t_{ST}$  with the beginning of the energy conserving (non-radiative) ST phase ( $r_s \propto t^{2/5}$ ). With radiative losses becoming more important (blue) the blast wave passes through a transition phase ( $t = t_{TR}$ ) and approaches the fully radiative PDS phase at ( $t = t_{PDS}$ ). The shock radius evolves as  $r_s \propto t^{2/7}$  until the MCS phase is reached at ( $t = t_{MCS}$ ). The swept-up material can only gain radial momentum until the end of the PDS phase.

mass  $M_{\text{eject}}$  the expansion parameter is approximately the ST value of 2/5 (Chevalier 1982; Truelove & McKee 1999; Vink 2012).

(ii) ST phase. At the end of the PST phase about 72 per cent of the initial SN energy is converted into thermal energy and the energy conserving ST phase starts at  $t = t_{ST}$  (Taylor 1950; Sedov 1958; McKee & Ostriker 1977),

$$t_{ST} = \left[ r_{s,ST} \left( \frac{\xi E_{SN}}{\rho_0} \right)^{-1/5} \right]^{5/2} \quad (2)$$

with the factor  $\xi \sim 2$  and the shock radius  $r_{s,ST}$ , which can be computed as

$$r_{s,ST} = \left( \frac{3 M_{\text{eject}}}{4 \pi \rho_0} \right)^{1/3}. \quad (3)$$

During the energy conserving ST phase the shock evolves adiabatically with  $r_s \propto t^{2/5}$  and the radial momentum of the swept-up mass increases.

(iii) Transition (TR) phase. The energy conserving phase ends when the rate of change in temperature due to adiabatic expansion is comparable to radiative losses (Ostriker & McKee 1988; Petruk 2006). In this TR phase, starting at  $t = t_{TR}$ , the post-shock cooling time  $t_{\text{cool}}$  becomes comparable to the age of the remnant (see Section 2.1.2)

$$t_{TR} \sim t_{\text{cool}}. \quad (4)$$

The radial momentum can still significantly increase. As the shock front decelerates, the faster post-shock gas compresses the shocked material and forms a thin, dense shell at the end of the TR phase (Cioffi et al. 1988; Ostriker & McKee 1988).

(iv) PDS phase. At the beginning of the PDS, at  $t = t_{PDS}$ , a dense shell has formed behind the radiative shock (Falle 1975). Typically  $t_{PDS}$  is a few times  $t_{TR}$  (see Section 2.1.2). The further evolution is dominated by radiation. The homogeneous pressure inside the bubble drives the expansion into the low-pressure environment (Cox 1972; Gaffet 1983; Cioffi et al. 1988; Cohen et al. 1998). The shock velocity and further momentum input to the ISM decrease.

(v) Momentum-conserving snowplough (MCS) phase. The MCS phase starts at  $t = t_{MCS}$  once the excess thermal energy is radiated away. The momentum of the shell cannot increase any more. Momentum is conserved and inertia becomes the main driver of the

further expansion (Cioffi et al. 1988). We therefore stop and compare our models at  $t_{MCS}$ .

## 2.1 The ambient medium

The structure and the mean density of the ambient medium have a significant influence on the evolution of a blast wave. Here, we consider the general case of a radial power-law density profile (Ostriker & McKee 1988)

$$\rho(r) = \rho_0 B r^{-\omega}, \quad (5)$$

where  $\rho_0$  is the central density,  $\omega$  is the power-law index and  $B$  can be used to normalize the radius (Truelove & McKee 1999).

The mass density is related to the number density,  $n$ , by  $\rho = n \mu m_H$ , with  $m_H$  being the proton mass and the mean molecular weight  $\mu$  (ionized gas with  $\mu_i = 0.61$ ; atomic gas with  $\mu_a = 1.27$ ).

The total mass of the SNR,  $M$ , is

$$M(r) = M_{\text{eject}} + \frac{4}{3 - \omega} \pi \rho_0 B r^{3-\omega} \text{ for } \omega \neq 3, \quad (6)$$

where  $M_{\text{eject}}$  is the mass of the SN ejecta. The second term corresponds to the swept-up mass. As the PST phase is dominated by the mass of the ejecta, we assume a constant density,  $\rho_0$  until  $t_{ST}$ . In the following we describe in detail our numerical model considering the different phases starting with the ST phase.

### 2.1.1 ST phase

At the beginning of the adiabatic ST phase a certain percentage of the initial kinetic energy has thermalized (approximately 75 per cent in a homogeneous medium). The fraction of kinetic to thermal energy stays constant and the total energy is conserved (Chevalier 1976; Cioffi et al. 1988).

At  $r_{s,ST}$  (equation 3) the adiabatic expansion begins with the radial evolution of the shock, described by the Sedov solution (Sedov 1946; Newman 1980; Ostriker & McKee 1988; Klein et al. 1994; Truelove & McKee 1999; Breitschwerdt et al. 2012),

$$r_s(t) = \left( \frac{\xi E}{\rho_0 B} \right)^{\frac{1}{5-\omega}} t^{\frac{2}{5-\omega}} \quad (7)$$

with  $\xi = (5 - \omega)(10 - 3\omega)/8\pi$  and the expansion parameter  $\eta = 2/(5 - \omega)$ .

The expansion speed can be derived by considering the time derivatives of the shock radius  $r_s$  in the ST stage (Cavaliere & Messina 1976):

$$\frac{d}{dt}(r_s) = v = \frac{2}{5 - \omega} \frac{r_s}{t}. \quad (8)$$

Here  $v$  is the shock velocity. The post-shock velocity  $v'$  is

$$v' = 3/4 v. \quad (9)$$

### 2.1.2 TR phase

Between the ST and PDS phases, there is an intermediate period of non-self-similar behaviour which, therefore, cannot be described by a power-law solution as in equation (1). We treat the TR phase independently, which allows a more realistic modelling of the SNR (e.g. Cioffi et al. 1988; Petruk 2006). The description of the ST phase as energy conserving is accurate as long as cooling plays a minor role and the energy loss due to radiation is negligible.

Following Blondin et al. (1998)  $t_{\text{TR}}$  is defined as the time at which the cooling time is comparable to the age of the remnant. We obtain similar results when the rate of change in temperature of the SNR,  $T$ , due to the adiabatic expansion becomes comparable to the radiative losses (Petruk 2006):

$$\frac{d}{dt_{\text{TR}}} (T)_{\text{exp}} \sim \frac{d}{dt_{\text{TR}}} (T)_{\text{cool}}. \quad (10)$$

During the TR phase the post-shock gas velocity approaches the shock speed (Cioffi et al. 1988),

$$v' = K_{01} v_1 v, \quad (11)$$

with the velocity moment,  $K_{01}$ , and the fraction  $v_1$  of the shock velocity  $v$  (see equation 8).

The velocity moment,  $K_{01}$ , is unity in self-similar blast waves but changes whenever this condition is violated, thus at  $t_{\text{TR}}$ ,  $K_{01, \text{TR}} = 0.857$  (Cioffi et al. 1988, but see also Ostriker & McKee 1988 for more details).

We follow Cioffi et al. (1988) and assume that the TR phase lasts until

$$t_{\text{TR}} c = t_{\text{PDS}}, \quad (12)$$

where  $c = (1 + \eta)/(\eta^{1/(1+\eta)})$  with  $\eta = (4(3 - \omega) - 2\omega)/(5 - \omega)$ . We follow the approximation by Petruk (2006) and assume  $c = 1.83$  for the homogeneous medium and  $c = 1$  for  $\omega = 2$ . During this period,  $v_1$  changes as

$$v_1 = \frac{3}{4} + 0.25 \left( \frac{\left( \frac{t}{t_{\text{TR}}} \right)^{2.1} - 1}{\left( \frac{1}{c} \right)^{2.1} - 1} \right). \quad (13)$$

As radiative cooling becomes important,  $v_1$  increases from the ST value of 3/4 to a value of one at  $t_{\text{PDS}}$ . A thin, dense, radiatively cooling shell forms (Gaffet 1983; Cioffi et al. 1988; Ostriker & McKee 1988; Petruk 2006).

The large thermal pressure gradient across the shock drives the expansion under the influence of radiative cooling (Cioffi et al. 1988). We use a set of coupled ordinary differential equations for the further evolution of the SNR starting at  $t_{\text{TR}}$ , throughout the PDS phase until  $t_{\text{MCS}}$ . The time evolution of mean momentum and shock radius then read (see Ostriker & McKee (1988), their equation (2.9) and appendix D):

$$\frac{d}{dt}(\bar{p}) = \frac{4(3 - \omega)\pi}{3} K_{\text{pres}} \bar{p}_{\text{th}} r_s^2 \quad (14)$$

$$\frac{d}{dt}(r_s) = \frac{3}{4r_s^3 \pi \bar{\rho}} \frac{1}{K_{01} v_1} (\bar{p}), \quad (15)$$

where  $K_{\text{pres}}$  is the pressure moment and  $\bar{p}_{\text{th}}$  is the mean thermal pressure within the SNR,

$$\bar{p}_{\text{th}} = \frac{E_{\text{th}}}{2\pi r_s^3}, \quad (16)$$

which depends on the thermal energy  $E_{\text{th}}$  of the SNR changing as

$$\frac{d}{dt}(E_{\text{th}}) = -V \Lambda(\bar{T}) \bar{n}^2. \quad (17)$$

$\Lambda$  is the cooling function (see Section 3) in a volume  $V$  with a mean number density  $\bar{n}$  and a mean temperature  $\bar{T}$ . We consider two volumes, namely that of the shock and the interior. Note that equation (17) is used throughout the entire evolution of the SN blast wave from  $t_{\text{ST}}$  until the end (Ostriker & McKee 1988; Bisnovatyi-Kogan & Silich 1995). During the ST phase almost no thermal

## Supernova blast waves in ambient media 2965

energy is radiated away. Internal structures have minor influence compared to the shock and are therefore neglected.

The pressure moment,  $K_{\text{pres}}$ , can be interpreted as the weighted mean interior pressure of the SNR (see Ostriker & McKee 1988, equation D10a for further details). At the beginning of the TR phase in our SN-model  $K_{\text{pres, TR}} = 0.932$  and approaches  $K_{\text{pres, PDS}} = 1$  (Cioffi et al. 1988; Ostriker & McKee 1988; Bisnovatyi-Kogan & Silich 1995).

### 2.1.3 PDS phase

The PDS is the first fully radiative phase. It starts with the formation of a thin shocked shell, which contains most of the mass of the SNR and encloses a roughly isobaric and hot cavity (Blondin et al. 1998). Since we restrict ourselves to one dimension, we neglect instabilities or deviations from spherical geometry (Franco et al. 1994).

The evolution during the PDS is also described by the equations introduced in Section 2.1.2 with  $K_{\text{pres}} = K_{01} = v_1 = 1$ . With a dense, uniform, thin shell we can model the flow using a self-similar solution and equation (1) is valid. As we neglect the influence of the inner parts, the expansion parameter  $\eta$  in this case is (Ostriker & McKee 1988; Gaffet 1983),

$$\eta = \frac{2}{2 + 3\gamma - \omega}, \quad (18)$$

where  $\gamma = 5/3$  is the adiabatic index of a mono-atomic gas.

During the PDS almost all thermal energy is radiated away. The thermal pressure inside the cavity becomes equal to the ambient thermal pressure at  $t_{\text{MCS}}$ . At this point we stop the calculation of the PDS phase and assume that afterwards the radial momentum stays constant.

## 3 THE NUMERICAL SETUP

We study the evolution of a single SNR from the ST to the MCS phase by solving the set of ordinary differential equations (ODEs; equations 8, 14, and 15 together with equation 17), based on the thin-shell approach (Cioffi et al. 1988; Ostriker & McKee 1988), described in Section 2.1 via a fifth-order Runge–Kutta–Fehlberg integration scheme (Butcher 1996) with adaptive step-sizing. This spherically symmetric, one-dimensional SN model assumes no instabilities in the shell, no shell perforation or internal structures. An advantage of the presented SN model is, that we can easily and efficiently calculate the evolution of SNe in a large number of different ambient media.

We assume solar metallicity and we model radiative cooling for  $10^4 \text{ K} < T < 10^8 \text{ K}$  using the cooling function by Sutherland, Bicknell & Dopita (1993). For  $T < 10^4 \text{ K}$  a cooling function by Koyama & Inutsuka (2000, 2002) is used with

$$\Lambda = \Gamma \left[ 10^7 \exp \left( \frac{-1.184 \times 10^5}{T + 1000} \right) + 1.4 \times 10^{-2} \sqrt{T} \exp \left( \frac{-92}{T} \right) \right] \text{ erg cm}^3 \text{ s}^{-1} \quad (19)$$

with a fixed heating rate  $\Gamma$  (Koyama & Inutsuka 2002; Walch & Naab 2015),

$$\Gamma = 2 \times 10^{-26} \text{ erg s}^{-1}. \quad (20)$$

The SN is initialized at the beginning of the ST phase by adding  $10^{51} \text{ erg}$  of total energy  $E_{\text{SN}}$  (Ostriker & McKee 1988) and  $2 M_{\odot}$  (Draine 2011) of ejecta mass at the initial ST radius,

**Table 1.** Top section: initial SN properties for all simulations. Bottom section: List of performed simulations. Column 1 gives the considered property, column 2 fixes the density structure of the ambient medium, and column 3 defines the density profile. In columns 4 and 5 we give the turbulent Mach number and number of cones used to simulate the turbulent substructure of the ambient medium (see Section 6). The last column lists the corresponding figures in this paper.

Initial SN properties		SN energy $M_{\text{eject}} = 10^{51}$ erg		Ejecta mass $M_{\text{eject}} = 2 M_{\odot}$	
Property	Structure	Density	Turbulence		Figures
Uniform media ( $\mu_a, \mu_i$ )	Homogeneous	$n_{0,\text{uni}} = 0.1\text{--}100 \text{ cm}^{-3}$	–	–	3
Media with density gradient	Power law	$n_{0,\text{power}} = 0.1\text{--}100 \text{ cm}^{-3}$	–	–	5
Different surrounding media	Power law	$n_{0,\text{power}} = 1 \text{ cm}^{-3}$	–	–	6
Different initial densities	Wind-blown bubble	$n_{0,\text{uni}} = 1\text{--}1000 \text{ cm}^{-3}$	–	–	7
Different initial temperatures	Wind-blown bubble	$n_{0,\text{uni}} = 1 \text{ cm}^{-3}$	–	–	8
Example ( $\mu_a, \mu_i$ )	Turbulent	$n_{0,\text{turb}} = 1 \text{ cm}^{-3}$	$\mathcal{M} = 10$	$N_{\text{cones}} = 12$	10
Density variation	Turbulent	$n_{0,\text{turb}} = 1 \text{ cm}^{-3}$	$\mathcal{M} = 10$	$N_{\text{cones}} = 12\text{--}384$	11 (top)
Momentum variation	Turbulent	$n_{0,\text{turb}} = 1 \text{ cm}^{-3}$	$\mathcal{M} = 10$	$N_{\text{cones}} = 12\text{--}384$	11 (bottom)
Momentum at $t_{\text{MCS}}$	Turbulent	$n_{0,\text{turb}} = 0.1\text{--}100 \text{ cm}^{-3}$	$\mathcal{M} = 0.1\text{--}100$	$N_{\text{cones}} = 192$	12
Mass–velocity distribution	Turbulent	$n_{0,\text{turb}} = 1, 100 \text{ cm}^{-3}$	$\mathcal{M} = 1, 10$	$N_{\text{cones}} = 384$	13

equation (3), corresponding to an initial momentum input of  $p_0 = 14\,181 M_{\odot} \text{ km s}^{-1}$ .

We run simulations with different combinations of ambient medium densities and density distributions (equation 5, see Table 1). The initial number densities for a uniform distribution  $n_{0,\text{uni}}$  and the central density of the power-law distribution  $n_{0,\text{power}}$  vary in a range of  $0.1\text{--}100 \text{ cm}^{-3}$  ( $n_{0,\text{uni}} = n_{0,\text{power}} = 0.1, 0.3, 1, 3, 10, 30, 100 \text{ cm}^{-3}$ ).

At radii smaller than  $R_{\text{ST}}$  we assume the density to be homogeneous as the mass of the ejecta dominates the first phase. At larger radii we consider different density distributions (constant, power-law, turbulent) in the ambient medium. For the power-law distribution we assume a density floor,  $n_{\text{floor}}$ :

$$n_{\text{power}}(r) = \begin{cases} n_{0,\text{power}} & \text{for } r \leq r_{\text{ST}} \\ n_{0,\text{power}} \left( \frac{r}{r_{\text{ST}}} \right)^{-\omega} & \text{for } r > r_{\text{ST}} \\ & \text{and } n_{\text{power}}(r) \geq n_{\text{floor}} \\ n_{\text{floor}} & \text{for } r > r_{\text{ST}} \\ & \text{and } n_{\text{power}}(r) < n_{\text{floor}}. \end{cases} \quad (21)$$

Without this lower limit the mean of the ambient density would drop to non-physical values and the sound speed of the ambient medium with a fixed pressure would increase to infinity (Cavaliere & Messina 1976; Chevalier 1976; Greif et al. 2011; Hennebelle & Falgarone 2012).

A self-consistent treatment of the chemical evolution is not included and it is not possible to consider multiple ionization states of the ambient medium. For simplicity, we choose a neutral environment with solar abundances with  $\mu_a = 1.27$ . Some studies (e.g. Cioffi et al. 1988; Petruk 2006) consider the SN environment to be ionized. To compare with these results, we rerun the simulations in uniform media and for a turbulent example with  $\mu_i = 0.61$  (see Section 4.1 and Section 6.1).

A simulation is terminated at the beginning of the MCS phase,  $t_{\text{MCS}}$  (see Section 2.1.3), after which the momentum is constant. For all environments we assume an universal ambient pressure, because  $P \propto nT \sim \text{const}$  (McKee & Ostriker 1977). All parameters of the model and the performed simulations are summarized in Table 1.

The computational effort to run a single SN depends on the number of time steps. The initial step-size is chosen to be a fraction of

the ST time, which depends on the density of the ambient medium. During the computation we use adaptive step-size control. We compare the local, relative error of the radius and the thermal energy obtained from the applied integration scheme with a global tolerance of  $10^{-3}$  at densities of  $n_{0,\text{uni}} \leq 50 \text{ cm}^{-3}$  and  $10^{-4}$  for denser environments. In case the local error exceeds the global tolerance the time step is adjusted. On a single core (clock speed 3.40 GHz) a simulations needs between  $4 \times 10^3$  ( $n_{0,\text{uni}} = 3 \text{ cm}^{-3}$ ) and  $1.3 \times 10^4$  ( $n_{0,\text{uni}} = 100 \text{ cm}^{-3}$ ) time steps, which corresponds to a CPU time of 1.5–6 s.

## 4 BLAST WAVE EVOLUTION IN IDEALIZED ENVIRONMENTS

### 4.1 Homogeneous density distribution

We apply our model to follow the evolution of blast waves for a single SN in homogeneous media with densities of  $n_{\text{uni}} = 0.1\text{--}100 \text{ cm}^{-3}$ , covering the more tenuous ISM up to average densities of MCs. We assume both an ionized with  $\mu_i$  and a neutral ambient medium with  $\mu_a$ .

The transition times  $t_{\text{TR}}$  and  $t_{\text{PDS}}$  (see Fig. 2) of SNe in homogeneous media, obtained in this work, can be fitted with a power law which depend on the number density  $n_{0,\text{uni}}$  and mean molecular weight  $\mu$  (see Section 4.1):

$$t_{\text{TR},\mu_a} = 4.15 (n_{0,\text{uni}}/1 \text{ cm}^{-3})^{-0.53} \times 10^4 \text{ yr}$$

$$t_{\text{PDS},\mu_a} = 7.80 (n_{0,\text{uni}}/1 \text{ cm}^{-3})^{-0.53} \times 10^4 \text{ yr}$$

$$t_{\text{TR},\mu_i} = 3.18 (n_{0,\text{uni}}/1 \text{ cm}^{-3})^{-0.54} \times 10^4 \text{ yr}$$

$$t_{\text{PDS},\mu_i} = 5.80 (n_{0,\text{uni}}/1 \text{ cm}^{-3})^{-0.54} \times 10^4 \text{ yr}.$$

The definitions for the respective TR times are not unique. Different numerical setups (e.g. Petruk 2006), cooling functions (e.g. Cioffi et al. 1988) and assumptions for the ambient medium (mean molecular weight in ionized,  $\mu_i$ , or neutral,  $\mu_a$ , media) can lead to different results. Fig. 2 compares  $t_{\text{TR}}$  and  $t_{\text{PDS}}$  from previous works (Cioffi et al. 1988; Franco et al. 1994; Blondin et al. 1998; Petruk 2006) to values obtained from this work (black triangles, black



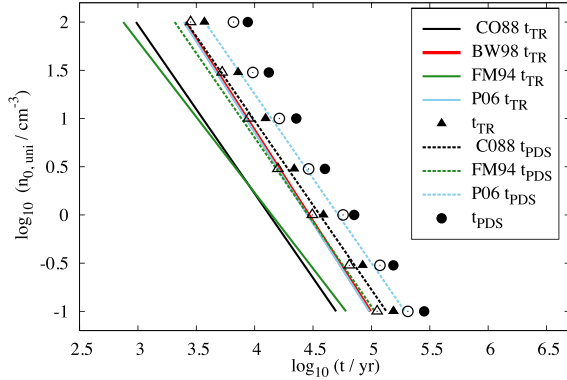


**Figure 2.** Model predictions for the end of the ST phase  $t_{\text{TR}}$  (black triangles) and the beginning of the PDS phase  $t_{\text{PDS}}$  (black circles) in ambient media with different number densities  $n_{0,\text{uni}}$  and different states of ionization of the ambient gas. Full symbols show the case of a neutral ambient medium with solar abundances ( $\mu_a$ ), and open symbols show the case of a fully ionized ambient medium with  $\mu_i$ . Our results are consistent with previous works by Blondin et al. (1998, here BW98) and Petruk (2006, here P06) but differ significantly from Cioffi et al. (1988, here CO88) and Franco et al. (1994, here FM94) for several reasons (see details in the text).

circles) in uniform ambient media with number densities between 0.1 and  $100 \text{ cm}^{-3}$ .

Our results are consistent with previous studies by Blondin et al. (1998) and Petruk (2006) assuming the ambient medium to be ionized (open symbols). The differences in low-density environments are less than 10 per cent. Only at  $n_{0,\text{uni}} = 100 \text{ cm}^{-3}$  the values differ by  $\sim 40$  per cent. In models with a neutral medium (full symbols),  $t_{\text{TR}}$  and  $t_{\text{PDS}}$  are significantly shifted to later times. Cioffi et al. (1988) and Franco et al. (1994) use different setups and show no agreement with the findings of all other authors. For a detailed comparison of important times in the evolution of SNRs we refer to Kim & Ostriker (2015) and Petruk (2006).

In Fig. 3, top-left panel, we show the evolution of the swept-up mass of the SNR. Initially it is dominated by the ejecta mass. The swept-up mass increases rapidly during the ST phase. The final swept-up mass,  $M_{\text{tot}}$ , is  $\sim 1290$  [660]  $M_{\odot}$  in dense environments increasing up to about  $8870$  [4590]  $M_{\odot}$  in an ambient medium with  $n_{0,\text{uni}} = 0.1 \text{ cm}^{-3}$ . This significant increase is a consequence of a 30 times longer evolution in lower density environments. It will be discussed in more detail in Section 6.4.

In Fig. 3 (top-right panel), we show the evolution of the thermal energy starting from the ST phase (71.7 per cent of the initial SN energy) until the onset of the MCS phase (end of lines). Here and in all following plots, the beginning of the TR phase is indicated by triangles and the onset of the PDS phase by circles. Filled symbols and thick solid lines show the results for a neutral ambient medium. The open triangles, circles, and dashed lines correspond to the same models assuming an ionized ambient medium. Hereafter, the values for ionized ambient media are given within square brackets.

As expected, for the highest density ( $n_{0,\text{uni}} = 100 \text{ cm}^{-3}$ , black line) the ST phase terminates already after  $3.6$  [2.8] kyr, while for the lowest density ( $n_{0,\text{uni}} = 0.1 \text{ cm}^{-3}$ , dark yellow line) the ST lasts until  $150$  [112] kyr.

As the density of the shell increases, the post-shock gas starts to radiate. At  $t_{\text{TR}}$  the thermal energy drops significantly at much earlier times for  $n_{0,\text{uni}} = 100 \text{ cm}^{-3}$  than for  $n_{0,\text{uni}} = 0.1 \text{ cm}^{-3}$ . For all densities the PDS phase starts at about  $1.8 t_{\text{TR}}$ . For high

## Supernova blast waves in ambient media 2967

densities ( $n_{0,\text{uni}} = 100 \text{ cm}^{-3}$ ), the PDS phase of  $1.9$  [1.4] kyr is short compared to  $185$  [159] kyr in an ambient density of  $n_{0,\text{uni}} = 0.1 \text{ cm}^{-3}$ . The bubble stays overpressured and drives the evolution throughout the PDS stage. Cooling becomes inefficient (the curves flatten towards the end of the evolution) as the temperature of the SNR drops below  $10^4 \text{ K}$  (Sutherland et al. 1993; Koyama & Inutsuka 2002, see equation 20).

The time evolution of the shell radius is shown in the bottom-left panel of Fig. 3. For all densities the radius evolves as  $r_s \propto t^\eta$  with  $\eta = 2/5$  in the ST phase. At  $t = t_{\text{TR}}$ ,  $\eta$  shifts towards  $2/7$  and the SNR enters the PDS stage. For the highest density the shell expands to a radius of  $3.4$  [3.6] pc during the ST and to  $4.2$  [4.4] pc in the PDS phase. For the lowest density the TR radius is about  $59.5$  [61.6] pc expanding to  $73.5$  [76.2] pc in the TR phase and finally reaches  $85.3$  [90.0] pc at the end of the PDS. The final expansion radius significantly decreases from low- to high-density environments, because the cooling of the shell occurs earlier and therefore the interior pressure drops more rapidly in denser media.

In the bottom-right panel of Fig. 3, we show the corresponding evolution of the radial shell momentum. During the ST phase, the SN momentum increases significantly from  $p_0 \approx 1.4 \times 10^4 M_{\odot} \text{ km s}^{-1}$  by a factor of  $\sim 8$  [6] for  $n_{0,\text{uni}} = 100 \text{ cm}^{-3}$  and up to a factor 20 [14] at  $n_{0,\text{uni}} = 0.1 \text{ cm}^{-3}$ . The following TR phase further increases the momentum by  $\sim 40$  per cent with respect to the ST values. At the beginning of the MCS phase the shell momentum varies between  $13.4$  [9.3]  $p_0$  for the highest density and  $30.9$  [21.3]  $p_0$  for an ambient density of  $0.1 \text{ cm}^{-3}$ . However the momentum increase during the PDS, is almost negligible because the pressure inside the SNR is lowered to values similar to the ambient pressure (see Section 3). Within a high-density environment ( $n_{0,\text{uni}} = 100 \text{ cm}^{-3}$ ) the increase is only  $0.9 p_0$ . The final radial momentum converges as the temperature inside the SNR drops. Shortly before the onset of the MCS phase a final plateau forms. The temperature has dropped below  $10^4 \text{ K}$  and the photoelectric heating starts to compensate the radiative cooling (Koyama & Inutsuka 2002).

In Fig. 4, we compare the final momenta in a density range of  $n_{0,\text{uni}} = 0.1$ – $100 \text{ cm}^{-3}$  from our model with recent numerical simulations (Kim & Ostriker 2015; Li et al. 2015; Martizzi et al. 2015) and with previous works (Cioffi et al. 1988). We show the results for atomic (full black squares) and ionized media (open black squares). The SN model in an ionized medium with a density of  $n_{0,\text{uni}} = 1 \text{ cm}^{-3}$  has a radial momentum input of  $2.3 \times 10^5 M_{\odot} \text{ km s}^{-1}$ , which is in good agreement with  $2.17 \times 10^5 M_{\odot} \text{ km s}^{-1}$  found by Kim & Ostriker (2015) with  $2.66 \times 10^5 M_{\odot} \text{ km s}^{-1}$  by Li et al. (2015) and the semi-analytic solution by Cioffi et al. (1988).

For neutral and ionized gas the final momentum input is

$$p_{\mu_a} = 22.44 (n_{0,\text{uni}} / 1 \text{ cm}^{-3})^{-0.12} p_0$$

$$p_{\mu_i} = 16.52 (n_{0,\text{uni}} / 1 \text{ cm}^{-3})^{-0.12} p_0,$$

respectively. Numerical simulations by Kim & Ostriker (2015) find a lower factor of 19.75 and an exponent of  $-0.16$ .

### 4.2 Power-law density distribution

We now assume a power-law ambient medium density distribution following equation (21) with  $\omega = 2$ . We vary  $n_{0,\text{power}} = 0.1$ – $100 \text{ cm}^{-3}$  (Weaver et al. 1977; Band & Liang 1988).

In the top-left panel of Fig. 5, we show the corresponding evolution of the swept-up mass. We find two distinct regimes for the mass evolution. Where the ambient density distribution follows a power

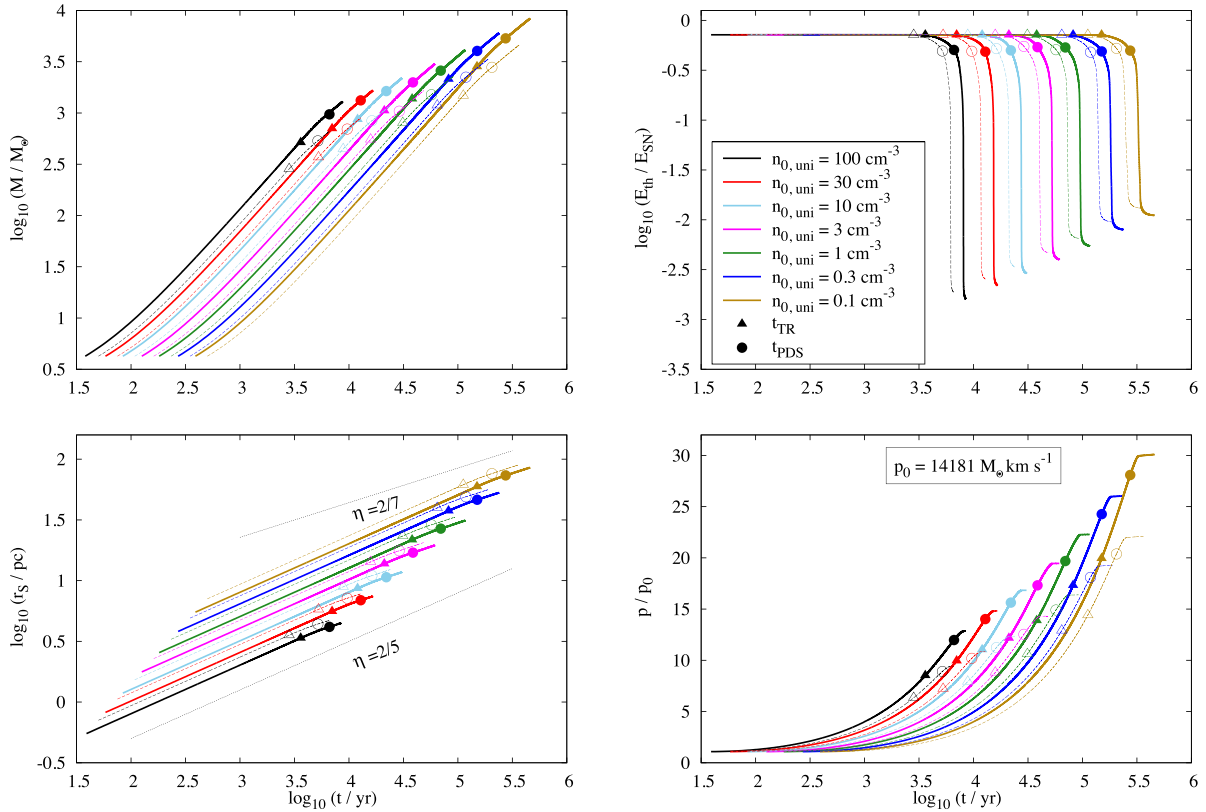


**Figure 3.** Time evolution of SNRs in homogeneous ambient media with densities in the range of  $0.1\text{--}100\text{ cm}^{-3}$ . Triangles indicate the beginning of the TR phase (end of ST phase) at  $t_{\text{TR}}$ , circles the onset of PDS. Open symbols and dashed lines show the corresponding simulation in ionized ambient media. Top-left panel: time evolution of the swept-up mass. Top-right panel: evolution of the normalized thermal energy. The energy losses are highest and most rapid for the densest environments. Bottom-left panel: evolution of the shell radius. The shock radius increases within low-density ambient media (up to 85 pc at  $n_{0,\text{uni}} = 0.1\text{ cm}^{-3}$ ). Black, dashed lines indicate slopes of  $2/5$  during  $t < t_{\text{TR}}$  and  $2/7$  during  $t > t_{\text{PDS}}$ . Bottom-right panel: evolution of the momentum input normalized to the initial SN momentum  $p_0$ .

law with  $M \propto t^{1.95}$ . In this medium and a high density ( $n_{0,\text{power}} = 100\text{ cm}^{-3}$ )  $\sim 155\text{ M}_{\odot}$  is swept-up compared to  $6\text{ M}_{\odot}$  for  $n_{0,\text{power}} = 0.1\text{ cm}^{-3}$ . Once the uniform density floor is reached, the swept-up mass is quickly dominated by the surrounding uniform medium with  $n_{\text{floor}}$ . Independent of  $n_{0,\text{power}}$  the swept-up mass is  $\sim 5000\text{ M}_{\odot}$  at  $t_{\text{TR}}$  and  $1.3 \times 10^4\text{ M}_{\odot}$  at  $t_{\text{MCS}}$ . Compared to the uniform ambient medium with  $n_{0,\text{uni}} = 0.01\text{ cm}^{-3}$ , the total swept-up mass in the power-law distribution is  $\sim 20$  per cent smaller. The expansion proceeds shorter in time and expansion in the latter case because slightly less momentum is created during the evolution.

In Fig. 5 (top-right panel), we show the evolution of the thermal energy normalized to the initial SN energy. The initial thermal energy is  $0.82 E_{\text{SN}}$  (results from equation 7 and the momentum at  $t_{\text{ST}}$ ). Starting with energy conservation during the ST phase, thermal energy is radiated away at the same  $t_{\text{TR}}$  (triangles,  $t_{\text{TR}} \sim 510\text{ kyr}$ ) independent of the profile density. The thermal energy drops significantly during the PDS phase (circles,  $t_{\text{PDS}} \sim 1\text{ Myr}$ ) to  $0.26 E_{\text{SN}}$ . For all central densities the thermal energy is lost only within the last  $\sim 300\text{ kyr}$  of the simulation ( $t_{\text{MCS}} \sim 1.2\text{ Myr}$ ). For comparison, the thermal energy retained at  $t_{\text{PDS}}$  in a uniform ambient medium with  $n_{0,\text{power}} = 0.01\text{ cm}^{-3}$  is  $0.4 E_{\text{SN}}$ .

The time evolution of the shell radius is shown in Fig. 5 (bottom-left panel). For all densities, the radius evolves with an expansion

parameter  $\eta \sim 2/(5 - \omega)$  in the ST phase turning to  $\eta \sim 2/7$  as it reaches the PDS phase within the homogeneous medium. For the highest central density ( $n_{0,\text{power}} = 100\text{ cm}^{-3}$ ) the shell expands to  $155\text{ pc}$  during the ST phase. At  $t_{\text{PDS}}$  the radius is  $204\text{ pc}$  and finally the shell has expanded to  $215\text{ pc}$ . These values are almost independent of the central density and are more comparable to the expansion radius of a homogeneous ambient medium with  $n_{0,\text{power}} = 0.01\text{ cm}^{-3}$ , which expands to  $230\text{ pc}$ .

The radial momentum (Fig. 5; bottom-right panel) depends, among others, on the swept-up mass, which couples the thermal energy to the ambient medium. In a power-law medium, where  $n(r)$  decreases rapidly the mass of the SN ejecta dominates the initial evolution (Fig. 5; bottom-right panel). The momentum increases between  $2.4 p_0$  ( $n_{0,\text{power}} = 0.1\text{ cm}^{-3}$ ) and  $5.1 p_0$  ( $n_{0,\text{power}} = 100\text{ cm}^{-3}$ ) before  $n(r) = n_{\text{floor}}$  is reached. From this point onwards, the momentum increases more rapidly. At  $t_{\text{TR}}$  all simulations converge to a common value of  $\sim 25.3 p_0$ , increase to  $36.3 p_0$  at  $t_{\text{PDS}}$  and finally to  $37.0 p_0$ . For comparison, the momentum in a homogeneous medium with  $n_{0,\text{uni}} = 0.01\text{ cm}^{-3}$  at  $t_{\text{TR}}$  is  $26.6 p_0$  and  $39.0 p_0$  at  $t_{\text{MCS}}$ .

In Fig. 6, we illustrate the impact of different values of  $n_{\text{floor}}$  ( $n_{\text{floor}} = 10^{-2}, 10^{-4}\text{ cm}^{-3}$ ) on the remnant evolution in power-law environments. For comparison, we show the case of a homogeneous ambient medium with  $n_{0,\text{power}} = 1\text{ cm}^{-3}$  (black, solid line),



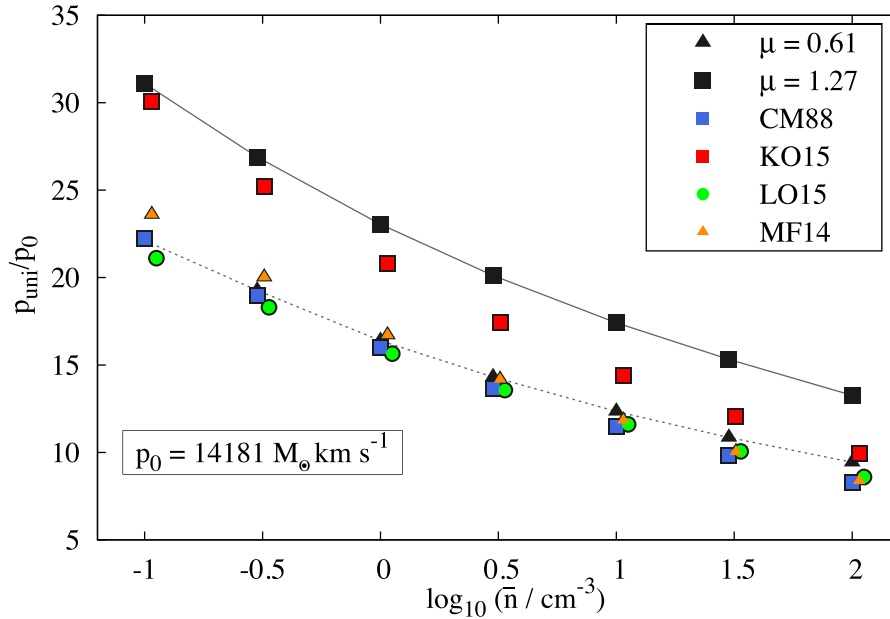


**Figure 4.** Final (at  $t_{\text{MCS}}$ ) radial momentum input  $p_{\text{uni}}$  in homogeneous medium with densities in the range of  $n_{0,\text{uni}} = 0.1\text{--}100\text{ cm}^{-3}$ . For comparison, we add recent numerical simulations of SNe in homogeneous media (coloured symbols) from Kim & Ostriker (2015, here KO15, red squares), Martizzi et al. (2015, here MF14, orange triangles), Cioffi et al. (1988, here CM88, blue squares), and Li et al. (2015, here LO15, green circles).

$n_{0,\text{power}} = 10^{-2}\text{ cm}^{-3}$  (green, dashed line) and  $n_{0,\text{power}} = 10^{-4}\text{ cm}^{-3}$  (dark yellow, dashed line). We compare the case of an SNR expanding into a warm ionized medium (WIM case; green lines) with  $n_{\text{floor}} = 10^{-2}\text{ cm}^{-3}$ ,  $T = 7000\text{ K}$ , and  $P/k_b = 70\text{ cm}^{-3}\text{ K}$ ; or into a hot ionized medium (HIM case; dark yellow lines) with  $n_{\text{floor}} = 10^{-4}\text{ cm}^{-3}$ ,  $T = 3 \times 10^5\text{ K}$ , and  $P/k_b = 30\text{ cm}^{-3}\text{ K}$ , respectively (McKee 1995). A plain power-law with no density floor (red lines) is also shown. We terminate the latter simulation at 30 Myr. The density distributions are shown in the top-left panel of Fig. 6.

In the top-right panel of Fig. 6 we show the interior pressure,  $P/k_b$  (full lines) and the counteracting ambient pressure (dotted lines). Assuming an isothermal environment, the ambient pressure is directly proportional to the density distribution. The homogeneous ambient medium is isobaric, whereas in the WIM and HIM the pressure decreases with increasing radius down to the isobaric floor. The pressure in the ambient medium with a plain power-law would decrease to zero at infinity. The pressure inside the bubble decreases and drops significantly at  $t_{\text{TR}}$  when radiation becomes important. When the ambient pressure is equal to the interior pressure, the simulation terminates at 98 kyr (homogeneous medium), 1.3 Myr (WIM) and 26 Myr (HIM).

The expansion radius of the SNR (left-bottom panel) increases with lower ambient densities. In a homogeneous medium the radius is the smallest as the shock sweeps-up mass with a constant density. The power-law media with homogeneous surroundings show similar behaviour but different final radii depending on the ambient pressure. The final radius in the WIM is  $\sim 200\text{ pc}$  ( $t_{\text{MCS}} = 1.1\text{ Myr}$ ) and in the HIM  $\sim 1020\text{ pc}$  ( $t_{\text{MCS}} = 5.6\text{ Myr}$ ). For the plain power-law the density drops with the radius. The counteracting swept-up mass is missing and the expansion terminates without forming a dense shell (Ostriker & McKee 1988; Truelove & McKee 1999; Petruk 2006).

The final radial momentum input (Fig. 6, bottom-right panel) increases from  $22.9 p_0$  in the homogeneous medium and almost doubles to  $39.0 p_0$  assuming a WIM. In the HIM the momentum input is  $68.3 p_0$ . The momentum in the plain power-law environment increases continuously.

To summarize, we find that the momentum injection in a power-law environment is small compared to the uniform medium, because the decreasing density suppresses the coupling of the momentum to the gas. If the power-law environment is surrounded by a homogeneous density floor the final momentum can increase. However, the momentum input is always smaller or equal to the case of a uniform ambient medium with  $n_{0,\text{uni}} = n_{\text{floor}}$ , independent of  $n_{0,\text{power}}$ .

## 5 BLAST WAVE EVOLUTION IN WIND-DRIVEN BUBBLES

During the lifetime of a massive star strong stellar winds interact with the ambient medium and blow low-density bubbles (Weaver et al. 1977). The subsequent SNe explode in these bubbles and the evolution of the blast wave is modified. Here we discuss the evolution of SN blast waves in wind-blown bubbles. We assume a simple model for a constant wind expanding into an initially cold (80 K) homogeneous medium with four different initial densities ( $n_{0,\text{uni}} = 1, 10, 100, 1000\text{ cm}^{-3}$ ). In these cold environments, the wind-blown bubble expands supersonically and drives a strong shock into the ambient ISM. The shock is radiative and cools down to  $T_{\text{s,SH}}$ .

We assume a  $20 M_{\odot}$  O-star with a constant wind velocity of  $v_w = 2000\text{ km s}^{-1}$  and a constant mass-loss rate of  $\dot{M}_w = 10^{-7} M_{\odot}\text{ yr}^{-1}$  over a lifetime of  $t_B = 10\text{ Myr}$ . The SN has an ejecta mass  $M_{\text{eject}} = 2 M_{\odot}$  (Puls et al. 2009). The expansion radius  $r_{\text{s,B}}$  of a wind-blown

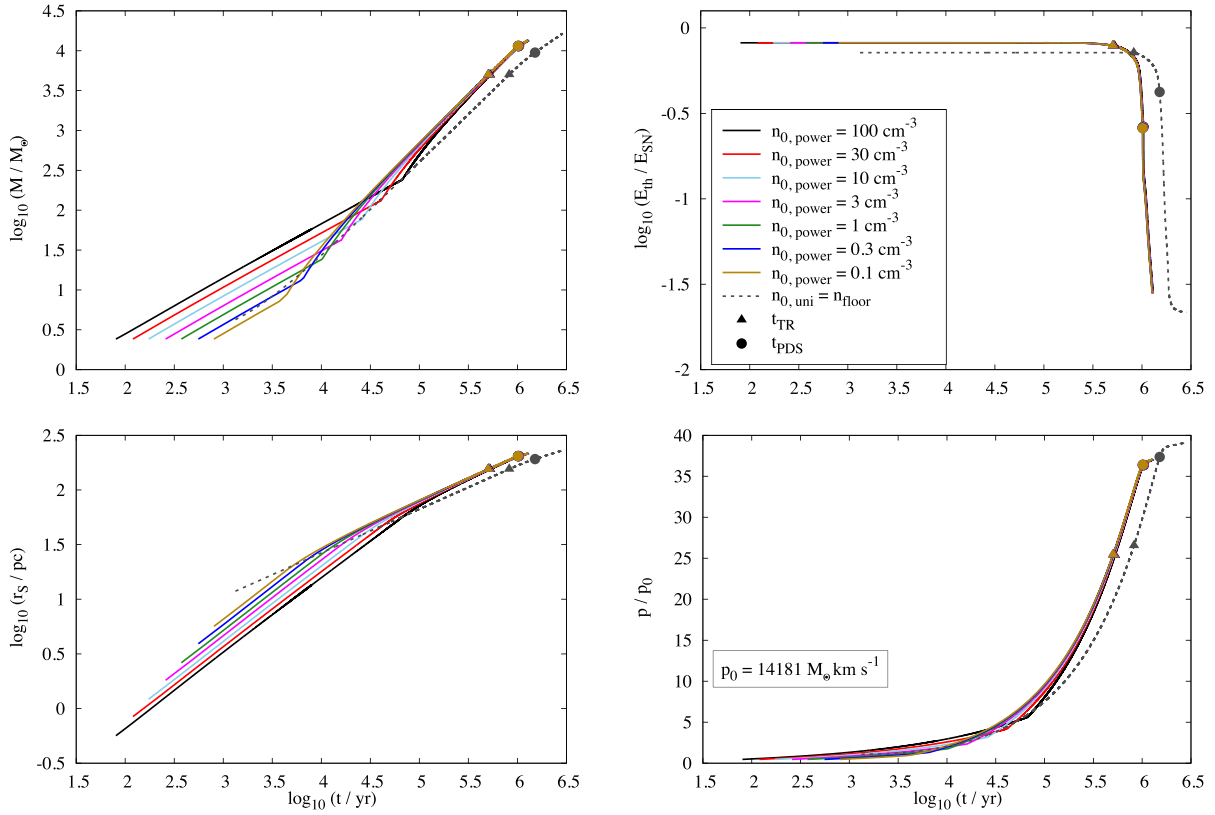


**Figure 5.** Time evolution of SNRs in ambient media with a power-law density distribution and central densities in the range of  $0.1\text{--}100\text{ cm}^{-3}$  (lines with different colours as indicated in the legend) and a density floor of  $0.01\text{ cm}^{-3}$ . Triangles indicate the beginning of the TR phase,  $t_{\text{TR}}$ , circles the onset of the PDS phase. The SN expansion into a homogeneous medium (grey, dashed line) with an ambient density equal to the floor density is shown. It is shifted to later times by a factor of  $10^{0.2} \sim 1.59$ , because it lies on top of the other lines. Top-left panel: mass increase during the evolution up to a collective mass of some  $10^{3.5} M_{\odot}$ . Top-right panel: evolution of the normalized thermal energy. Bottom-left panel: evolution of the shell radius. Bottom-right panel: evolution of the momentum input normalized to the initial SN momentum  $p_0$ .

bubble from a constant stellar wind without heat transfer is given by (Weaver et al. 1977; Pittard 2013)

$$r_{s,B}(t) = \left( \frac{125}{154\pi} \right)^{1/5} \left( \frac{L_{\omega}}{\rho_{0,\text{uni}}} \right)^{1/5} t^{3/5}, \quad (22)$$

where  $\rho_{0,\text{uni}}$  is the density of the initial homogeneous ambient medium with  $\mu = 1$ .  $L_{\omega}$  is the mechanical luminosity

$$L_{\omega} = \frac{1}{2} \dot{M}_{\omega} v_{\omega}^2. \quad (23)$$

The average density  $\rho_B$  within the bubble without mixing is (Dyson 1973; Garcia-Segura & Mac Low 1995; Pittard 2013)

$$\rho_B(t) = \frac{3\dot{M}_{\omega}t}{4\pi r_{s,B}^3}. \quad (24)$$

The density of the wind-shocked shell  $\rho_{s,B}$  can be estimated by the isothermal shock jump condition ( $\gamma = 1$ ),

$$\rho_{s,B} = \rho_{0,\text{uni}} \frac{v_{s,B}^2}{c_0^2}, \quad (25)$$

where  $c_0$  is the sound speed of the ambient medium with  $c_0 = (\gamma P_0 / \rho_{0,\text{uni}})^{1/2}$ . The wind bubble expands supersonically with the velocity  $v_{s,B}$

$$\frac{d}{dt}(r_{s,B}) = v_{s,B} = \frac{3}{5} \frac{r_{s,B}}{t}. \quad (26)$$

The shell thickness  $\delta r_{s,B}$  is

$$\delta r_{s,B} = \frac{c_0^2}{3} \frac{r_{s,B}}{v_{s,B}^2}. \quad (27)$$

In Fig. 7, we show the evolution of an SN in each of the four pre-existing wind-blown bubbles. The densities inside the bubble,  $n_B$ , are  $3.7, 14.8, 59.1$ , and  $235.1 \times 10^{-4} \text{ cm}^{-3}$  for ambient densities of  $n_{0,\text{uni}} = 1, 10, 100, 1000 \text{ cm}^{-3}$  (top-left panel, dashed line). The interior is separated from the ambient medium by a dense shell. The density contrast of between the interior and the shell is constant with  $1.5 \times 10^{-5}$ . The thickness of the shells are  $0.7, 1.2, 1.8$ , and  $2.9 \text{ pc}$ . The density of the SNR follows this evolution until the evolutions stalls.

The SN evolution in the low-density interior is dominated by the ST phase, which immediately ends when the blast wave hits the dense shell (top-left panel). Within  $\sim 2 \text{ kyr}$  80 per cent of the initial thermal energy is radiated away, almost independently of the shell density. The remaining thermal energy is related to the hot,

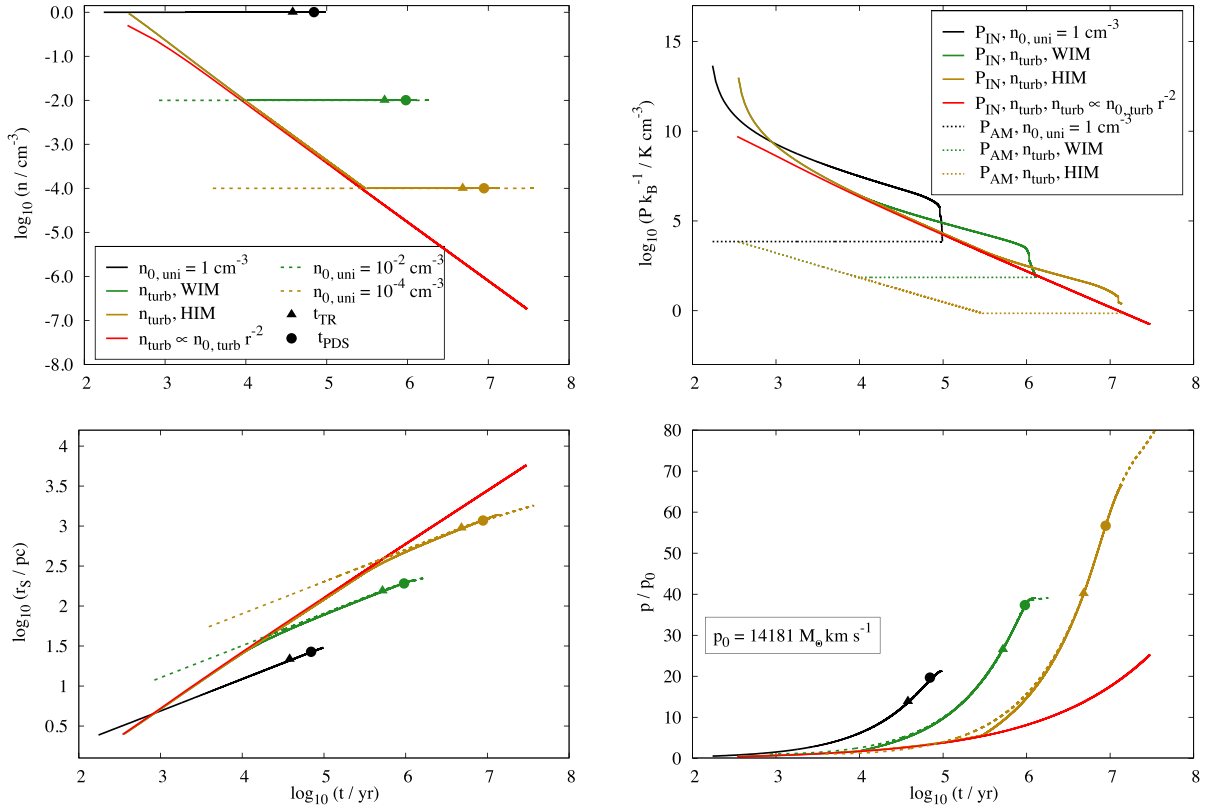


**Figure 6.** Time evolution of a SNR expanding into ambient media with four different density distributions: a homogeneous (black lines) environment with a density of  $n_{0,\text{power}} = 1 \text{ cm}^{-3}$ , media with a power-law distribution  $\omega = 2$  and density floors similar to the WIM (green lines,  $7000 \text{ K}$ ,  $n_{\text{floor}} = 10^{-2} \text{ cm}^{-3}$ ,  $P/k_b = 70 \text{ cm}^{-3} \text{ K}$ ) and the HIM (dark yellow lines,  $3 \times 10^5 \text{ K}$ ,  $n_{\text{floor}} = 10^{-4} \text{ cm}^{-3}$ ,  $P/k_b = 30 \text{ cm}^{-3} \text{ K}$ ) and a power-law distributed medium without a lower limit (red lines). Dashed lines correspond to homogeneous ambient media with  $n_{0,\text{power}} = n_{\text{floor}}$  (HIM, WIM). Triangles indicate the beginning of the TR phase, circles the onset of the PDS phase. *Top left panel:* Evolution of the expansion radius. *Top right panel:* Evolution of the internal pressures (solid lines) and the counteracting ambient pressure (dotted lines). *Bottom left panel:* Number density evolution at the shock front, showing the assumed density floors. *Bottom right panel:* Evolution of the radial momentum input. The simulation without a density floor is terminated after  $\sim 30 \text{ Myr}$ .

low-density interior of the SNR. Previous works (e.g. Dwarkadas 2007) show a similar behaviour of rapid cooling at the shock boundary. Recent numerical simulations (Fierlinger et al. 2016) point out that 1.5 per cent of the SN energy is left after the SNR stalls at the boundary.

Initially the radial evolution (bottom-left panel) is that within a homogeneous medium. For the densest ambient medium ( $n_{0,\text{uni}} = 1000 \text{ cm}^{-3}$ ) the wall of the wind-blown cavity is reached after  $\sim 4.9 \text{ kyr}$  and  $22.0 \text{ pc}$ , while it takes  $\sim 12.2 \text{ kyr}$  and  $87.6 \text{ pc}$  for  $n_{0,\text{uni}} = 10 \text{ cm}^{-3}$ . The final radius corresponds to the inner radius of the bubble.

The density distribution of the wind-bubble is assumed to be static and the shell has no momentum. While in the ST phase, the momentum input by the SN is small because of the low gas density within the bubble. Once the remnant reaches the shell, which is massive compared to the swept-up mass from the SN, it cools quickly and cannot accelerate the shell. As a result the evolution of the SNR stalls. The final momentum input (bottom-right panel) lies between  $\sim 2.4$  and  $2.9 p_0$ .

The density difference between the interior and the shock as well as the density of the wind-blown shell itself determine the final radial momentum. Assuming isothermal behaviour, the ambient temperature of the initial environment is linked to the shell temperature,

which again affects the thickness of the shell. Therefore, in Fig. 8 we show the influence of densities,  $n_B$ , and the temperature of the ambient ISM on the momentum input. We choose  $n_B = 3.7 \times 10^{-4}$  and  $0.37 \text{ cm}^{-3}$ , where the first corresponds to a wind-blown bubble with an initial density  $n_{0,\text{uni}} = 1 \text{ cm}^{-3}$  and the latter corresponds to a bubble which is filled by ionized gas as would be the case for an H II region. We increase the temperatures from  $80$  to  $800 \text{ K}$  and to the temperature ( $3175 \text{ K}$ ), which corresponds to  $v_{s,B} = c_0$ . The dashed lines show the momenta of SNe in uniform media with  $n_B = n_{0,\text{uni}}$ .

For the low-density case ( $n_B = 3.7 \times 10^{-4} \text{ cm}^{-3}$ ), we show how the final momentum increases with temperature from  $2.9 p_0$  at  $80 \text{ K}$  to  $4.4 p_0$  at  $800 \text{ K}$  and up to  $6.5 p_0$  at  $3175 \text{ K}$ . At a higher interior density ( $n_B = 0.37 \text{ cm}^{-3}$ ), the momentum in the cold ( $80 \text{ K}$ ) ambient medium is  $19.3 p_0$  and is comparable to the corresponding homogeneous medium. Recent numerical results of SNe exploding into bubbles blown by a stellar wind and ionizing radiation give a factor of  $\sim 10$  (Geen et al. 2015).

This shows that the ambient density and temperature are essential for the evolution of an SNR in a wind-blown bubble. Higher temperatures broaden the wind-blown shell and reduce the density contrast. This results in a lower cooling and an increase of

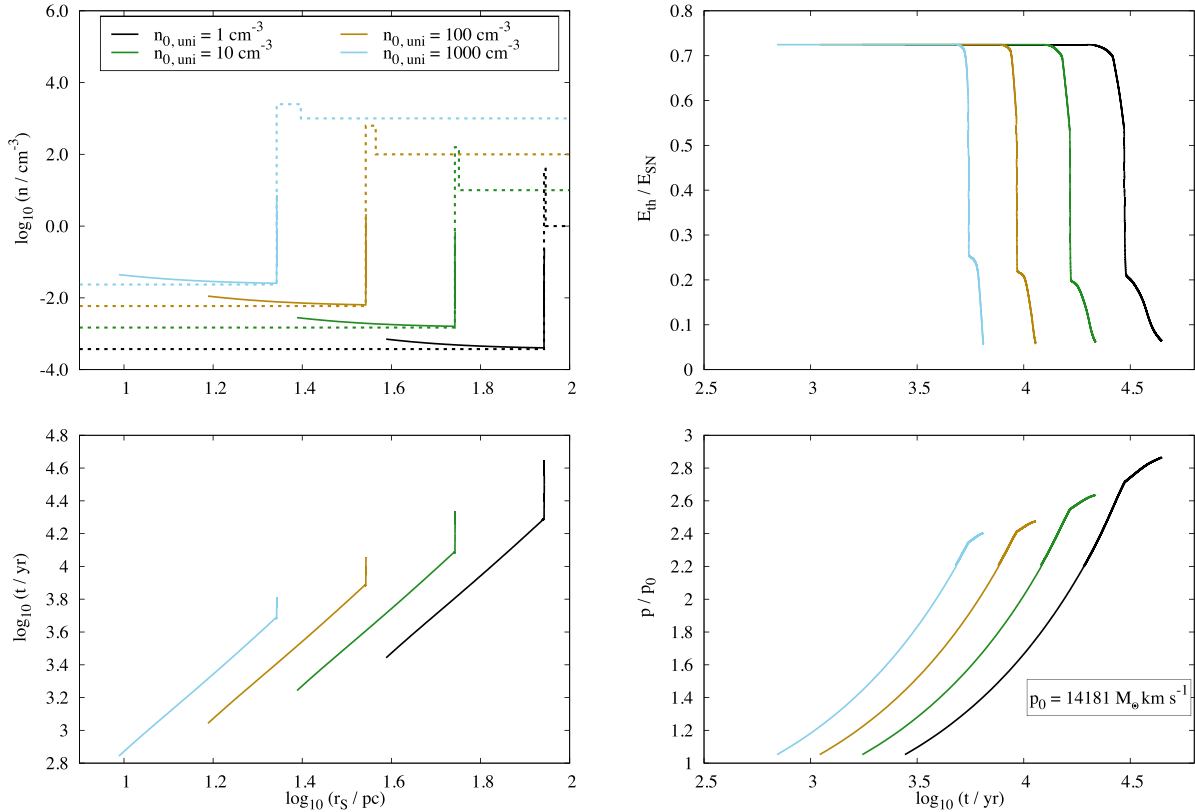


**Figure 7.** Time evolution of an SNR ( $M_{\text{eject}} = 2 M_{\odot}$ ) in a pre-existing bubble from a constant wind expanding into an initially homogeneous medium with densities of  $n_{0,\text{uni}} = 1, 10, 100, 1000 \text{ cm}^{-3}$ , an initial temperature of 80 K and  $P_0/k_B = 80 - 8 \times 10^4 \text{ cm}^{-3} \text{ K}$ . The density in the interior is assumed to be constant (top-left panel) and in a constant density environment. Top-left panel: radial density distribution of the pre-existing wind-blown bubble (dashed lines) and the mean density of the SNR (full lines). Top-right panel: time evolution of the normalized thermal energy. Bottom-left panel: evolution of the time over the SNR shock radius. Bottom-right panel: time evolution of the radial, normalized momentum input.

radial momentum (e.g. Walch & Naab 2015). The influence of the wind-blown bubble on the evolution of the SNR diminishes as the swept-up mass increases compared to the mass of the shell. SNR with a high density inside the bubble and a small difference between the swept-up mass and the mass of the wind-blown shell show a behaviour that is comparable to a uniform medium with that bubble density.

## 6 BLAST WAVE EVOLUTION IN TURBULENT ENVIRONMENTS

We study the evolution of an SNR expanding in a more realistic ambient medium, which is subject to isothermal, supersonic turbulence (Klessen, Burkert & Bate 1998; Klessen, Heitsch & Mac Low 2000; Kainulainen et al. 2009; Schneider et al. 2011; Federrath 2013). Numerical simulations suggest that the volume-weighted density PDF of gas shaped by isothermal turbulent motions can be described by a lognormal distribution (Vazquez-Semadeni et al. 1993; Nordlund et al. 1997; Padoan et al. 1997b; Federrath et al. 2008),

$$q(z) = \frac{1}{\sqrt{2\pi\sigma_{\ln\rho}^2}} \exp\left[-\frac{(z - \bar{z})^2}{2\sigma_{\ln\rho}^2}\right], \quad (28)$$

where  $z = \ln(\rho/\rho_{0,\text{turb}})$  with a mean density of the gas  $\rho_{0,\text{turb}}$ . The median is  $\bar{z} = -\sigma_{\ln\rho}^2/2$  (Vazquez-Semadeni 1994; Thompson &

Krumholz 2016). The dispersion of the density distribution  $\sigma_{\ln\rho}^2$  can be related to the Mach number  $\mathcal{M}$  of turbulent motions (Federrath et al. 2008; Thompson & Krumholz 2016),

$$\sigma_{\ln\rho}^2 \sim \ln(1 + b^2 \mathcal{M}^2). \quad (29)$$

The turbulent driving factor  $b$  is assumed to be 0.5 with a thermal mix of divergence free (solenoidal) and curl free (compressive) turbulence (Federrath et al. 2008; Brunt 2010; Krumholz 2014).

The volume density PDF can also be related to the surface density PDF  $\sigma_{\ln\Sigma}$  (Brunt 2010; Brunt, Federrath & Price 2010a,b). In this case, the dispersion reads

$$\sigma_{\ln\Sigma}^2 = \ln(1 + Qb^2 \mathcal{M}^2) \quad (30)$$

with the conversion factor

$$Q = \sigma_{\ln\Sigma}^2 / \sigma_{\ln\rho}^2. \quad (31)$$

### 6.1 Approximating the turbulent structures of the ambient medium

We adopt our model to compute the SNR evolution in turbulent ambient media, where the density structure is described by the lognormal PDF in equation (28). Since the blast wave evolution is primarily determined by the mean density of the swept-up material

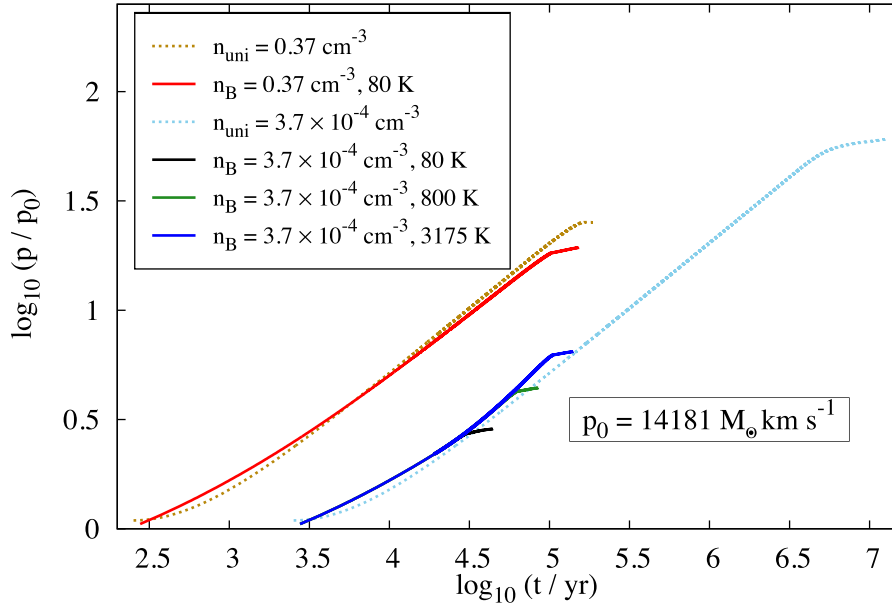


**Figure 8.** Radial momentum of SNR in wind-blown bubbles in different initial media in comparison to uniform media (dashed lines). The densities are  $n_B = n_{\text{uni}} = 3.7 \times 10^{-4} \text{ cm}^{-3}$  and  $0.37 \text{ cm}^{-3}$ . The initial temperatures of the ambient medium, which hosts the wind-blowing star are 80, 800, and 3175 K. At the latter temperature the shock speed is equal to the sound speed of the medium.

(Ostriker & McKee 1988; Padoan et al. 1997b), we assume that small-scale density fluctuations along the radial direction of the SNR have a negligible effect on the evolution. We assume that in different directions, the blast wave will encounter gas with different mean densities.

In this simplified model, we abstain from following winding shock fronts between structures with a large density gradient (e.g. Martizzi et al. 2015) or interaction between different radial directions. The first constraint arises from the simple set of equations used in our model. It is not designed to follow the dynamical evolution but gives a statistical expectation of SNR in turbulent media. For the latter we assume no physical interactions between the different cones and assume that during the ST and TR phase the radially outwards directed velocities of the SNR are large and the interaction has minor effects. At later phases the extent of the different radial directions is sufficient to neglect an interacting boundary.

To model the mean densities in different radial directions, the ambient medium in our model is discretized (see Fig. 9, bottom panel) into  $N_{\text{cones}}$  cones. The cones are defined by equal solid angles and have equal surface areas and volumes. For each cone, we randomly draw a mean density,  $n_i$ , from the lognormal density distribution and run the one-dimensional model of the evolution of an SNR for a uniform medium (see Section 2). The total momentum  $p_{\text{turb}}$  injected by an SN in this pseudo three-dimensional turbulent medium is derived from the sum over all cone momenta  $p_i$ ,

$$\sum_i^{N_{\text{cones}}} p_i = p_{\text{turb}}. \quad (32)$$

Each cone is initialized with the same fraction of the total SN energy, i.e.  $E_{\text{SN}}/N_{\text{cones}}$ . As the expansion radius in each cone is different, the symmetry of the SN bubble is broken (Walch & Naab 2015).

In Fig. 10 we show results using 12 cones, which is the minimum number needed to divide the unit sphere into equal surface area pixels (see Górski et al. 2005). With  $N_{\text{cones}} = 12$  the lognormal PDF is not well sampled (see Section 6.2 for a further discussion). The turbulent Mach number is 10 and the mean number density of the ambient medium, is  $n_{0,\text{turb}} = 1 \text{ cm}^{-3}$ . The sampled densities  $n_i$  have values between  $3 \times 10^{-3} \text{ cm}^{-3}$  and  $4.5 \text{ cm}^{-3}$  according to a PDF with a width of  $\sigma_{\ln \rho} = 1.8$  for  $\mathcal{M} = 10$ . Fig. 10 shows the equal initial momenta (upside down triangles) as well as the individual momenta  $p_i$  at the end of the individual ST (triangles), TR (circles) and PDS (squares) phase for a neutral ( $\mu_a$ , black) and ionized ( $\mu_i$ , red) medium for all mean cone densities  $n_i$  (green line and corresponding y-axis on the right-hand side).

The mean momentum per cone,  $\langle p_i \rangle$ ,

$$\langle p_i \rangle = \frac{p_{\text{turb}}}{N_{\text{cones}}}, \quad (33)$$

in a neutral [ionized] medium at  $t_{\text{TR}}$  is 1.7 [1.2]  $p_0$ , which increases up to 2.4 [1.7]  $p_0$  at  $t_{\text{PDS}}$  ( $p_0 = 14181 \text{ M}_{\odot} \text{ km s}^{-1}$ ). At  $t_{\text{MCS}}$  the mean momentum per cone is 2.6 [1.9]  $p_0$ , as indicated by the black horizontal line (red line for ionized ambient medium). This corresponds to a total momentum of 31.2 [22.8]  $p_0$  ( $2.16 \times 10^5 \text{ M}_{\odot} \text{ km s}^{-1}$ ). Note that  $t_{\text{TR}}$ ,  $t_{\text{PDS}}$ , and  $t_{\text{MCS}}$  are different for cones with different densities. However, since the momentum stays constant after  $t_{\text{MCS}}$ ,  $p(t_{\text{MCS}})$  is considered as the final momentum.

The blast wave simulation in a homogeneous medium with  $n_{0,\text{uni}} = 1 \text{ cm}^{-3}$  injects 22.3 [16.4]  $p_0$  of momentum. Therefore, the increase in momentum is a direct consequence of turbulence. For higher  $\mathcal{M}$ , the PDF becomes broader. The blast wave encounters more low-density regions, which are subject to less radiative cooling and allow for a higher momentum injection.

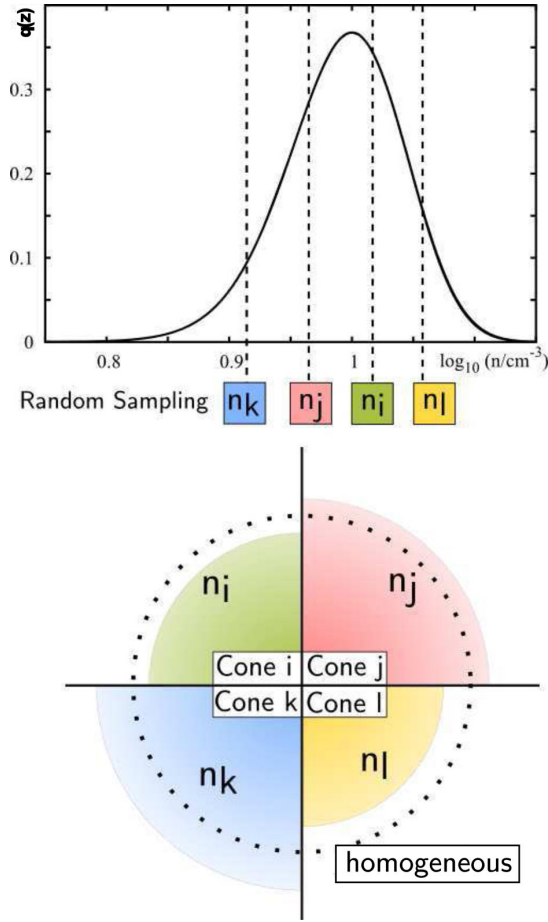


**Figure 9.** Schematic representation of the model for the blast wave evolution into a turbulent medium. Top panel: sampling of densities from a lognormal PDF, which represents turbulent density structures. The number of sampling points corresponds to the number of cones with equal-surface areas. Bottom panel: homogeneously assigning the densities to the cones. The blast wave evolution is then completed for each cone separately. The total momentum input is the sum of the individual solutions.

## 6.2 Accuracy of the model

The fidelity of the SN model depends on the number of sampled densities, i.e.  $N_{\text{cones}}$ . We need a sufficient number in order to accurately represent the underlying density distribution.

We compute the evolution of 50 individual SN explosions in turbulent media, each with an increasing number of equal-volume cones (sampling points of the PDF) from 12 to 384. For each of the 50 runs, we use a different random seed to sample the number densities in each cone from the lognormal density PDF with  $n_{0,\text{turb}} = 1 \text{ cm}^{-3}$  and  $\mathcal{M} = 10$ .

Fig. 11 presents all six sets ( $N_{\text{cones}} = 12, 24, 48, 96, 192, 384$ ; different symbols) with 50 SN simulations each. In the top panel the sampled mean densities of the individual simulations,  $\langle n \rangle = \sum_i^{N_{\text{cones}}} n_i / N_{\text{cones}}$  are shown. Independent of the numbers of cones the mean ambient density ( $n_{0,\text{turb}} = 1 \text{ cm}^{-3}$ ; blue dashed line) is well sampled by the overall mean of the individual simulations (red bars). The variance decreases from 1.2 to 0.9 with increasing number of cones from 12 to 384.

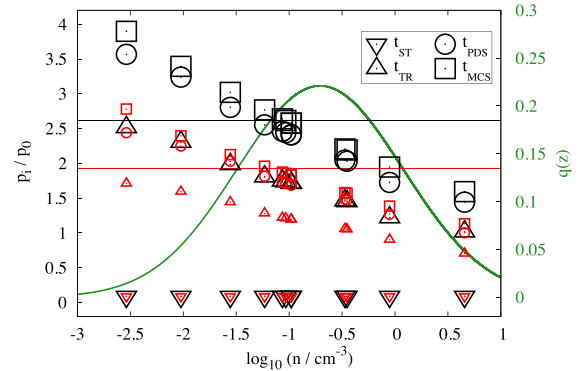


**Figure 10.** Example for the SN momentum injection in a turbulent medium sampled with 12 cones. The number densities are randomly drawn from a lognormal PDF with a mean number density  $n_{0,\text{turb}} = 1 \text{ cm}^{-3}$  and a turbulent Mach number  $\mathcal{M} = 10$ . We show the values at  $t_{\text{ST}}$  (upside down triangles),  $t_{\text{TR}}$  (triangles),  $t_{\text{PDS}}$  (circles), and  $t_{\text{MCS}}$  (squares) within an ionized ambient medium ( $\mu_i$ , red symbols) and an atomic ( $\mu_a$ , black symbols). The individual radial momentum for each cone  $p_i$  is shown as a function of the sampled density  $n$ . At  $t_{\text{PDS}}$  the mean momentum per cone is  $2.6 [1.9] p_0$  (black [red] horizontal line). The underlying lognormal PDF is indicated with a green line.

The bottom panel shows the final momentum  $p_{\text{turb}}$  (normalized to the initial momentum) of the same simulations. The overall mean converges to  $29.4 p_0$  at the highest numbers of cones (blue dashed line). The variance is similar in all runs at about  $4 p_0$ .

To summarize, we show that the combination of high- $\mathcal{M}$ -turbulence and small  $N_{\text{cones}}$  may not accurately represent the turbulent PDF structure. Individual realizations might over/underpredict the mean densities but larger samples and a higher number of cones reduced the variance in the mean density and the momentum input.

## 6.3 Momentum distribution in turbulent media

We perform simulations of SNRs in turbulent media with mean densities of  $n_{0,\text{turb}} = 0.1\text{--}100 \text{ cm}^{-3}$ , and Mach numbers,  $\mathcal{M} = 1\text{--}100$ . Based on the previous section, we decided to use sets of 20 realizations for each turbulent setup with  $N_{\text{cones}} = 192$  and evaluate the total radial momenta up to  $t_{\text{MCS}}$  of the cone with the lowest density cone (Fig. 12).

The mean shell momenta lie between  $13.0 p_0$  ( $n_{0,\text{turb}} = 100 \text{ cm}^{-3}$ ,  $\mathcal{M} = 1$ ) and  $30.6 p_0$  ( $n_{0,\text{turb}} = 0.1 \text{ cm}^{-3}$ ,  $\mathcal{M} = 1$ ). Higher supersonic turbulence ( $\mathcal{M} = 100$ ) boosts the momentum by 60 per cent ( $n_{0,\text{turb}} = 100 \text{ cm}^{-3}$ ) up to 88 per cent ( $n_{0,\text{turb}} = 0.1 \text{ cm}^{-3}$ ) compared to the low- $\mathcal{M}$ -turbulence value.

The radial momentum input of a single SN in a turbulent medium can be quantified in terms of the mean density and the width (Mach number) of the underlying density PDF:

$$p_{\text{turb}}/p_0 = 23.07 (n_{0,\text{turb}}/1 \text{ cm}^{-3})^{-0.12} + 0.82(\ln(1 + b^2 \mathcal{M}^2))^{1.49} (n_{0,\text{turb}}/1 \text{ cm}^{-3})^{-0.17}. \quad (34)$$

The first term corresponds to the momentum transfer from a single SN into a homogeneous medium. The second term depends on a combination of the turbulent Mach number (width of the PDF) and the mean density. The factor in the first term is higher compared to the value (22.44) obtained for the uniform medium. The difference results from the additional turbulent term. The fit was generated over all data points by a Bees algorithm coupled with



Levenberg–Marquardt provided by the fitting tool MAGIX ( $\chi^2 \sim 8$ ; Bernst et al. 2011; Möller et al. 2013).

In Fig. 12 we compare our results to direct, three-dimensional (magneto-) hydrodynamical simulations from different authors, namely, Iffrig & Hennebelle (2015), Martizzi et al. (2015), Kim & Ostriker (2015), Li et al. (2015), and Walch & Naab (2015, coloured symbols). We compare at times similar to our  $t_{\text{MCS}}$ . As the methodology for setting up the ISM conditions varies from author to author, we explain each set of simulations in more detail.

Iffrig & Hennebelle (2015, dark blue diamonds) simulate SNR in highly-resolved (maximum grid resolution 0.05 pc) turbulent MCs with magnetic fields, self-gravity and a cooling function similar to equation (19). The initial conditions for the SN explosion evolve from a spherical cloud with a density gradient  $\propto r^{-2}$  embedded in a low-density environment. The assumed velocity field in the MC represents a Kolmogorov spectrum with a random component. The authors conclude that the influence of magnetic fields is small, rather the position and, therefore, the ambient density of the SN in the MC is determining the final momentum. It is well approximated by the solution of three-dimensional SNR simulations in homogeneous medium with  $18 p_0$  for  $n_0 = 1 \text{ cm}^{-3}$ .

Kim & Ostriker (2015, red squares) pre-evolve the ambient medium from a thermally unstable state with small density perturbations. The SN explodes into a two-phase environment in pressure balance. The fitted final momentum input is comparable to SNe in homogeneous media. The difference to our final momentum in low- $\mathcal{M}$ -turbulent environments is smaller than 15 per cent.

Walch & Naab (2015, dark yellow circles) use an smoothed particle hydrodynamics (SPH) particle code to perform highly resolved (maximum resolution  $0.1 M_\odot$ ) hydrodynamic simulations with interpolating cooling tables by Plewa (1995, for  $T \geq 10^4 \text{ K}$ ) and the cooling function from Koyama & Inutsuka (2002, for  $T < 10^4 \text{ K}$ ). The ambient medium is initialized with fractal substructures, which represent a lognormal density PDF. The resulting variance is translated to a turbulent Mach number,  $\mathcal{M} = 4.4$  (Walch et al. 2011). The normalized final momentum  $p = 25.6 p_0$  is  $\sim 9$  per cent higher compared to values obtained from our SN model ( $n_{0,\text{turb}} = 1 \text{ cm}^{-3}$ ,  $\mathcal{M} = 4.4$ ).

Martizzi et al. (2015, orange triangles) perform hydrodynamic simulations in an ambient medium with a lognormal density field but only cooling by Sutherland et al. (1993) at temperatures above  $10^4 \text{ K}$ . The variance of the distribution uses a parametrization by Lemaster & Stone (2009). The spatial correlations are parametrized by a Burgers power spectrum. The initial velocity field is set to zero. Within these structures (maximum grid resolution 0.05 pc), the SNR evolves along the path of least resistance but cools significantly (down to  $10^4 \text{ K}$ ) when dense structures are hit and merge with the shock. This results in a final momentum input of  $7.3 p_0$  in a supersonic environment ( $\mathcal{M} = 30$ ,  $n_{0,\text{turb}} = 100 \text{ cm}^{-3}$ ), which is lower than the performed fiducial simulation in a homogeneous medium. The final value is  $\sim 2.6$  lower than a similar simulation with our model.

Li et al. (2015, green circles) creates an (artificial) environment with randomly distributed cold clouds and hot intercloud medium with an SN in the centre. The results show no distinctive phases and an expansion between the cold and dense regions on a path of least resistance. Initially the radial momentum input is lower, than the homogeneous comparison and shows an increasing power-law behaviour with radius. As the shock expands further it interacts with the medium in non-radial directions. At the end the momentum is almost constant and similar to values from uniform media. The

## Supernova blast waves in ambient media 2975

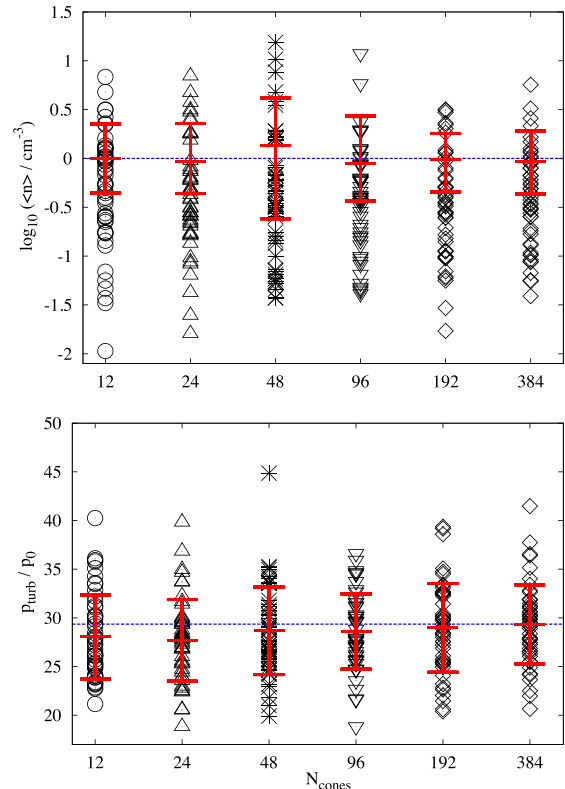


**Figure 11.** Effect of the number of cones  $N_{\text{cones}}$  on the accuracy of the turbulent SN model for the mean density (top panel) and momentum input (bottom panel). The number densities are randomly sampled from a log-normal PDF with a fixed mean density  $n_{0,\text{turb}} = 1 \text{ cm}^{-3}$  and Mach number  $\mathcal{M} = 10$ . Each of the six data sets consists of 50 SN simulations. Mean values and the standard deviation are shown in red. The mean ambient density (blue line; top panel) is well sampled and the momentum injection converges to  $29.4 p_0$  (blue line; bottom panel).

momentum of the homogeneous runs ( $18.8 p_0$ ) compares with the input from structured media at later phases of  $17.7 p_0$  ( $n_{0,\text{turb}} = 1 \text{ cm}^{-3}$ ).

To summarize, we find that momentum input from low- $\mathcal{M}$ -turbulent structures is comparable to SNR in homogeneous media. We find similar values compared to different three-dimensional numerical simulations, under the assumption of an atomic medium. We show that high- $\mathcal{M}$ -turbulent structures boost the radial momentum input. We conclude that turbulence could be important for the momentum input. However, more three-dimensional models with very high resolution will be required to address the impact of a highly turbulent substructure.

### 6.4 Velocity–mass distribution in turbulent media

The SN model assumes that the swept-up ambient material is condensed into a small volume at the shock front (Klein et al. 1994). The density profile inside the SNR can be neglected as the mass is only a small fraction of the total mass. We show the distribution of the shock velocity and the swept-up mass to mean densities  $n_{0,\text{turb}}$  of  $1 \text{ cm}^{-3}$  (Fig. 13, top panel) and  $100 \text{ cm}^{-3}$  (Fig. 13, bottom panel) with turbulent Mach numbers of 1 and 10 both with  $N_{\text{cones}} = 384$ .



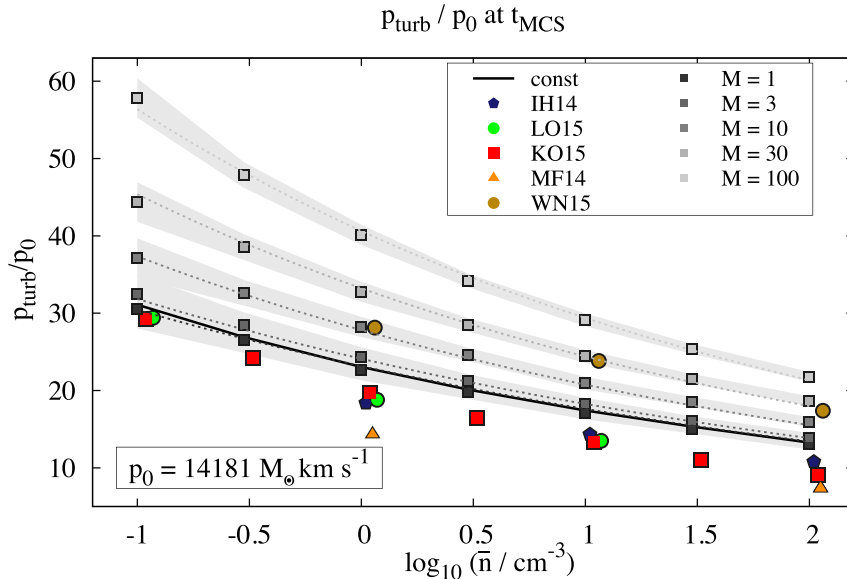


**Figure 12.** Final (at  $t_{\text{MCS}}$ ) radial momentum input  $p_{\text{turb}}$  to turbulent media with mean densities in the range of  $n_{0,\text{turb}} = 0.1\text{--}100\text{ cm}^{-3}$  and Mach numbers increasing from  $\mathcal{M} = 1\text{--}100$  (different grey squares). The environment of each SN is separated into 195 cones. Each data point corresponds to the mean of 20 realizations and a standard deviation (grey shaded areas). We add recent numerical simulations from Iffrig & Hennebelle (2015, here IH14, blue pentagons), Kim & Ostriker (2015, here KO15, red squares), Martizzi et al. (2015, here MF14, orange triangles), Walch & Naab (2015, here WN15, dark yellow circles), and Li et al. (2015, here LO15, green circles). For better visibility these symbols are shifted to the right of the corresponding number density.

The distributions are evaluated at fixed times between  $t = 10^{2.5}$  and  $10^{4.5}$  yr. In dense environments ( $n_{0,\text{turb}} = 100\text{ cm}^{-3}$ ) the simulations terminate earlier, explaining why in Fig. 13 (bottom panel) the distributions at  $t = 10^{4.5}$  yr are missing.

As expected, the swept-up mass continuously increases during the decelerating expansion of the SNR. At  $10^{2.5}$  yr the swept-up mass in a low-density and low- $\mathcal{M}$ -turbulence environment ( $\mathcal{M} = 1$ ,  $n_{0,\text{turb}} = 1\text{ cm}^{-3}$ ) is  $6.5\text{ M}_{\odot}$ . For the case of  $n_{0,\text{turb}} = 100\text{ cm}^{-3}$  the swept-up mass is  $29.8\text{ M}_{\odot}$ . In general higher- $\mathcal{M}$ -turbulence results in lower swept-up masses, by 12 per cent in low-density and 24 per cent in high-density environments. At  $10^4$  yr the swept-up masses have increased to  $280\text{ M}_{\odot}$  and  $1279\text{ M}_{\odot}$  in the low- and high-density ambient medium. At this time the SNR evolution in the latter case has almost reached the end of the PDS, whereas in the first medium the PDS lasts longer, until  $\sim 10^5$  yr.

The mean velocity at  $t = 10^{2.5}$  yr is  $2569\text{ km s}^{-1}$  in the low-density environment. High- $\mathcal{M}$ -turbulence increases the value to  $3096\text{ km s}^{-1}$ . The SNR slows down by  $\sim 50$  per cent in high-density structures with  $n_{0,\text{turb}} = 100\text{ cm}^{-3}$ . Typically, at each plotted time the mean velocity decreases by  $\sim 50$  per cent compared with the previous time. At  $t = 10^4$ , the velocities have dropped to  $323\text{ km s}^{-1}$  in low-density structures with  $n_{0,\text{turb}} = 1\text{ cm}^{-3}$  and trans-sonic turbulence. In high-density environment the mean velocity is  $151\text{ km s}^{-1}$ .

At the end of the simulations, the distributions within an environment with trans-sonic turbulence cover a small velocity range. High- $\mathcal{M}$ -turbulence broadens the mass-(shock-) velocity distribution and therefore, a small fraction of the swept-up mass remains at high velocities.

Similar behaviour is found in numerical simulations by Walch & Naab (2015). At  $0.2\text{ Myr}$  the velocity distribution in a dense ( $n_{0,\text{turb}} = 100\text{ cm}^{-3}$ ) fractal environment shows that about 2 per cent of a cloud mass of  $10^5\text{ M}_{\odot}$  are accelerated to velocities larger than  $\sim 20\text{ km s}^{-1}$ .

## 7 SUMMARY AND DISCUSSION

We present a fast model to follow the evolution of SN blast waves in their momentum generating phases (ST, TR, and PDS phase). We test the model for homogeneous and power-law density distributions and extend it to the evolution of SNR in wind-blown bubbles and a turbulent ISM. Previous analytic work is combined in our SN model and extended by the inclusion of a cooling function, a detailed treatment of the thermal energy, and a TR phase between the adiabatic and radiative phase.

The main results are summarized as follows.

- (i) We recover recent numerical results (e.g. Kim & Ostriker 2015; Li et al. 2015; Martizzi et al. 2015) of a single SN in a homogeneous medium as well as the analytic ST solution. The final momentum for a density range between  $1$  and  $100\text{ cm}^{-3}$  is  $\sim 13\text{--}31\text{ p}_0$  ( $p_0 = 14181\text{ M}_{\odot}\text{ km s}^{-1}$ ). We obtain reliable values for the radial momentum, the expansion radius and the thermal energy with small computational effort of a few seconds. The results depend solely on the ambient density.
- (ii) In ambient media with a power-law density distribution and a surrounding density floor, the final momentum clearly exceeds the homogeneous results by at most a factor of 2. This is independent of the central density and is controlled by the density of the density floor. The inner power-law part has minor effect.
- (iii) The momentum input of SNR in wind-blown bubbles depend on the initial ambient medium. Low initial temperatures result in dense shells, where the incoming SN shock cools efficiently. The momentum input is only  $\sim 3\text{ p}_0$ . Higher temperatures of the initial ambient medium delay the radiative cooling in the wind-blown shell. The momentum input increases by a factor up to 10. A high density inside the bubble and a small difference between the swept-up mass and the mass of the wind-blown shell show a behaviour that is comparable to a uniform medium with that bubble density.

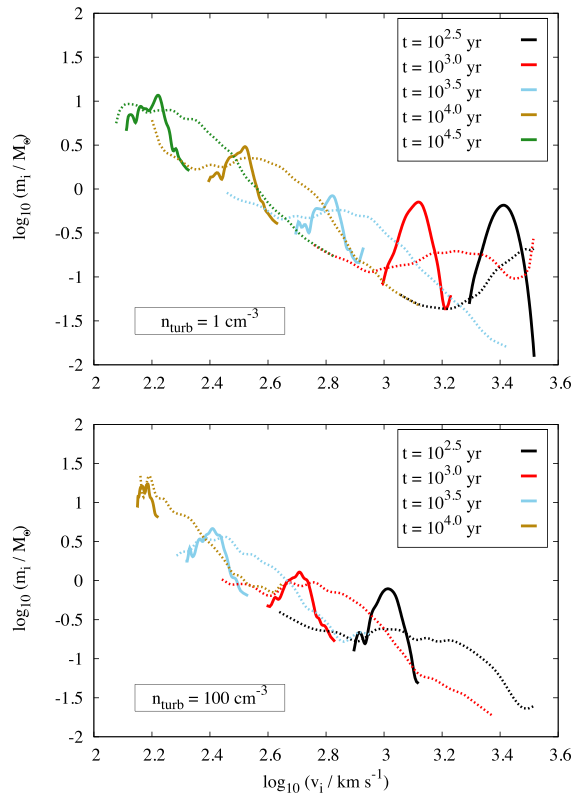


**Figure 13.** Evolution of the mass–velocity distribution at times between  $10^{2.5}$  and  $10^{4.5}$  yr with different turbulent Mach numbers of  $\mathcal{M} = 1$  (solid lines) and  $\mathcal{M} = 100$  (dashed lines). Top panel: low-density environment with a mean ambient density  $n_{0,\text{turb}} = 1 \text{ cm}^{-3}$ . Bottom panel: ambient medium with a density  $n_{0,\text{turb}} = 100 \text{ cm}^{-3}$ .

(iv) We use the SN model to approximate the lower limit of momentum input in turbulent ambient media. To do this, we randomly sample densities from a lognormal density distribution with a given dispersion which is related to the Mach number in the turbulent gas. For low turbulent Mach numbers ( $\mathcal{M} \sim 1$ ) the momentum input is very similar to homogeneous media ( $\sim 13 - 31 p_0$ ). We obtain the largest momentum input in turbulent media with  $\mathcal{M} \sim 100$  by as much as a factor of 2 in a low-density environment ( $n_{0,\text{turb}} = 0.1 \text{ cm}^{-3}$ ). We have parametrized the momentum input as a function of Mach number and average environmental density as follows:

$$p_{\text{turb}}/p_0 = 23.07 (n_{0,\text{turb}}/1 \text{ cm}^{-3})^{-0.12} + 0.82 (\ln(1 + b^2 \mathcal{M}^2))^{1.49} (n_{0,\text{turb}}/1 \text{ cm}^{-3})^{-0.17}. \quad (35)$$

Under the assumption of a neutral ambient medium we find values comparable to recent numerical simulations (e.g. Kim & Ostriker 2015; Martizzi et al. 2015; Walch & Naab 2015).

(v) The model is computationally cheap and can be used for a variety of parameters. This model is an accurate alternative to recent SN subgrid models.

## ACKNOWLEDGEMENTS

We thank J. P. Ostriker for the useful suggestions and discussion, which added significantly to the presented paper. SH, SW, and DS acknowledge the support by the Bonn-Cologne Graduate School for

## Supernova blast waves in ambient media 2977

physics and astronomy as well as the SFB 956 on the ‘Conditions and impact of star formation’. JM acknowledges funding from a Royal Society – Science Foundation Ireland University Research Fellowship. We acknowledge the support by the DFG Priority Program 1573 ‘The physics of the interstellar medium’. We thank Anika Schmiedeke for her help of fitting with MAGIX and Thomas Möller for providing this tool. We thank the anonymous referees for constructive input.

## REFERENCES

- Agertz O., Kravtsov A. V., Leitner S. N., Gnedin N. Y., 2013, *ApJ*, 770, 25  
Aumer M., White S. D. M., Naab T., Scannapieco C., 2013, *MNRAS*, 434, 3142  
Balogh M. L., Pearce F. R., Bower R. G., Kay S. T., 2001, *MNRAS*, 326, 1228  
Band D. L., Liang E. P., 1988, *ApJ*, 334, 266  
Bernst I., Schilke P., Moeller T., Panoglou D., Ossenkopf V., Roellig M., Stutzki J., Muders D., 2011, in Evans I. N., Accomazzi A., Mink D. J., Rots A. H., eds, *ASP Conf. Ser. Vol. 442, Astronomical Data Analysis Software and Systems XX*. Astron. Soc. Pac., San Francisco, p. 505  
Bisnovatyi-Kogan G. S., Silich S. A., 1995, *Rev. Mod. Phys.*, 67, 661  
Blondin J. M., Wright E. B., Borkowski K. J., Reynolds S. P., 1998, *ApJ*, 500, 342  
Breitschwerdt D., de Avillez M. A., Feige J., Dettbarn C., 2012, *Astron. Nachr.*, 333, 486  
Brook C. B., Stinson G., Gibson B. K., Roškar R., Wadsley J., Quinn T., 2012, *MNRAS*, 419, 771  
Brunt C. M., 2010, *A&A*, 513, A67  
Brunt C. M., Federrath C., Price D. J., 2010a, *MNRAS*, 403, 1507  
Brunt C. M., Federrath C., Price D. J., 2010b, *MNRAS*, 405, L56  
Butcher J. C., 1996, *Appl. Numer. Math.*, 20, 247  
Cavaliere A., Messina A., 1976, *ApJ*, 209, 424  
Chevalier R. A., 1976, *ApJ*, 207, 872  
Chevalier R. A., 1982, *ApJ*, 258, 790  
Cioffi D. F., McKee C. F., Bertschinger E., 1988, *ApJ*, 334, 252  
Cohen E., Piran T., Sari R., 1998, *ApJ*, 509, 717  
Cowie L. L., McKee C. F., Ostriker J. P., 1981, *ApJ*, 247, 908  
Cox D. P., 1972, *ApJ*, 178, 159  
Cox D. P., Franco J., 1981, *ApJ*, 251, 687  
Creasey P., Theuns T., Bower R. G., Lacey C. G., 2011, *MNRAS*, 415, 3706  
Creasey P., Theuns T., Bower R. G., 2013, *MNRAS*, 429, 1922  
Dale J. E., Bonnell I. A., Clarke C. J., Bate M. R., 2005, *MNRAS*, 358, 291  
Dalla Vecchia C., Schaye J., 2012, *MNRAS*, 426, 140  
Dawson J. R., Mizuno N., Onishi T., McClure-Griffiths N. M., Fukui Y., 2008, *MNRAS*, 387, 31  
Dawson J. R., McClure-Griffiths N. M., Dickey J. M., Fukui Y., 2011, *ApJ*, 741, 85  
de Avillez M. A., Breitschwerdt D., 2004, in Alfaro E. J., Pérez E., Franco J., eds, *Astrophysics and Space Science Library*, Vol. 315, *How Does the Galaxy Work? A Galactic Tertulia with Don Cox and Ron Reynolds*. Kluwer, Dordrecht, p. 331  
Dekel A., Silk J., 1986, *ApJ*, 303, 39  
Dib S., Bell E., Burkert A., 2006, *ApJ*, 638, 797  
Draine B. T., 2011, *Physics of the Interstellar and Intergalactic Medium*. Princeton Univ. Press, Princeton, NJ  
Dwarkadas V. V., 2007, *ApJ*, 667, 226  
Dyson J. E., 1973, *A&A*, 23, 381  
Elmegreen B. G., Lada C. J., 1977, *ApJ*, 214, 725  
Falle S. A. E. G., 1975, *MNRAS*, 172, 55  
Federrath C., 2013, *MNRAS*, 436, 1245  
Federrath C., Klessen R. S., Schmidt W., 2008, *ApJ*, 688, L79  
Fierlinger K. M., Burkert A., Ntormousi E., Fierlinger P., Schartmann M., Ballone A., Krause M. G. H., Diehl R., 2016, *MNRAS*, 456, 710  
Franco J., Miller W. W., III, Arthur S. J., Tenorio-Tagle G., Terlevich R., 1994, *ApJ*, 435, 805  
Gaffet B., 1983, *ApJ*, 273, 267

- García-Segura G., Mac Low M.-M., 1995, *ApJ*, 455, 145
- Gatto A. et al., 2015, *MNRAS*, 449, 1057
- Geen S., Rosdahl J., Blaizot J., Devriendt J., Slyz A., 2015, *MNRAS*, 448, 3248
- Gent F. A., Shukurov A., Fletcher A., Sarson G. R., Mantere M. J., 2013, *MNRAS*, 432, 1396
- Girichidis P. et al., 2016, *MNRAS*, 456, 3432
- Goldbaum N. J., Krumholz M. R., Matzner C. D., McKee C. F., 2011, *ApJ*, 738, 101
- Górski K. M., Hivon E., Banday A. J., Wandelt B. D., Hansen F. K., Reinecke M., Bartelmann M., 2005, *ApJ*, 622, 759
- Greif T. H., Springel V., White S. D. M., Glover S. C. O., Clark P. C., Smith R. J., Klessen R. S., Bromm V., 2011, *ApJ*, 737, 75
- Gritschneider M., Naab T., Walch S., Burkert A., Heitsch F., 2009, *ApJ*, 694, L26
- Hennebelle P., Falgarone E., 2012, *A&AR*, 20, 55
- Hennebelle P., Iffrig O., 2014, *A&A*, 570, A81
- Hill A. S., Joung M. R., Mac Low M.-M., Benjamin R. A., Haffner L. M., Klingenberg C., Waagan K., 2012, *ApJ*, 750, 104
- Hopkins P. F., Kereš D., Oñorbe J., Faucher-Giguère C.-A., Quataert E., Murray N., Bullock J. S., 2014, *MNRAS*, 445, 581
- Hu C.-Y., Naab T., Walch S., Glover S. C. O., Clark P. C., 2016, *MNRAS*, 458, 3528
- Iffrig O., Hennebelle P., 2015, *A&A*, 576, A95
- Janka H.-T. et al., 2012, *Prog. Theor. Exp. Phys.*, 2012, 010000
- Joung M. K. R., Mac Low M.-M., 2006, *ApJ*, 653, 1266
- Kainulainen J., Beuther H., Henning T., Plume R., 2009, *A&A*, 508, L35
- Keller B. W., Wadsley J., Couchman H. M. P., 2015, *MNRAS*, 453, 3499
- Kessel-Deynet O., Burkert A., 2003, *MNRAS*, 338, 545
- Kim C.-G., Ostriker E. C., 2015, *ApJ*, 802, 99
- Kim C.-G., Ostriker E. C., Kim W.-T., 2013, *ApJ*, 776, 1
- Klein R. I., McKee C. F., Colella P., 1994, *ApJ*, 420, 213
- Klessen R. S., Burkert A., Bate M. R., 1998, *ApJ*, 501, L205
- Klessen R. S., Heitsch F., Mac Low M.-M., 2000, *ApJ*, 535, 887
- Koyama H., Inutsuka S.-I., 2000, *ApJ*, 532, 980
- Koyama H., Inutsuka S.-I., 2002, *ApJ*, 564, L97
- Kritsuk A. G., Wagner R., Norman M. L., Padoan P., 2006, in Zank G. P., Pogorelov N. V., eds, *ASP Conf. Ser. Vol. 359, Numerical Modeling of Space Plasma Flows*. Astron. Soc. Pac., San Francisco, p. 84
- Krumholz M. R., 2014, *Phys. Rep.*, 539, 49
- Kushnir D., Waxman E., 2010, *ApJ*, 723, 10
- Larson R. B., 1974, *MNRAS*, 169, 229
- Lemaster M. N., Stone J. M., 2009, *Rev. Mex. Astron. Astrofis. Ser. Conf.*, 36, 243
- Li M., Ostriker J. P., Cen R., Bryan G. L., Naab T., 2015, *ApJ*, 814, 4
- McCrack R., Kafatos M., 1987, *ApJ*, 317, 190
- McKee C. F., 1995, in Ferrara A., McKee C. F., Heiles C., Shapiro P. R., eds, *ASP Conf. Ser. Vol. 80, The Physics of the Interstellar Medium and Intergalactic Medium*. Astron. Soc. Pac., San Francisco, p. 292
- McKee C. F., Ostriker J. P., 1977, *ApJ*, 218, 148
- Mac Low M.-M., Ferrara A., 1999, *ApJ*, 513, 142
- Mac Low M.-M., Klessen R. S., 2004, *Rev. Mod. Phys.*, 76, 125
- Mac Low M.-M., McCray R., 1988, *ApJ*, 324, 776
- Marinacci F., Pakmor R., Springel V., 2014, *MNRAS*, 437, 1750
- Martizzi D., Faucher-Giguère C.-A., Quataert E., 2015, *MNRAS*, 450, 504
- Möller T., Bernst I., Panoglou D., Muders D., Ossenkopf V., Röllig M., Schilke P., 2013, *Astrophysics Source Code Library*, record ascl:1303.009
- Newman W. I., 1980, *ApJ*, 236, 880
- Nordlund A., Spruit H. C., Ludwig H.-G., Trampedach R., 1997, *A&A*, 328, 229
- Ntormousi E., Burkert A., Fierlinger K., Heitsch F., 2011, *ApJ*, 731, 13
- Ostriker J. P., McKee C. F., 1988, *Rev. Mod. Phys.*, 60, 1
- Ostriker E. C., Stone J. M., Gammie C. F., 2001, *ApJ*, 546, 980
- Ostriker E. C., McKee C. F., Leroy A. K., 2010, *ApJ*, 721, 975
- Padoan P., Nordlund P., Jones B. J. T., 1997a, *Commun. Konkoly Obs. Hungary*, 100, 341
- Padoan P., Nordlund A., Jones B. J. T., 1997b, *MNRAS*, 288, 145
- Palouš J., Wünsch R., Tenorio-Tagle G., Silich S., 2009, *Ap&SS*, 324, 195
- Petrak O., 2006, preprint ([arXiv:astro-ph/0604057](https://arxiv.org/abs/0604057))
- Pittard J. M., 2013, *MNRAS*, 435, 3600
- Plewa T., 1995, *MNRAS*, 275, 143
- Puls J., Sundqvist J. O., Najarro F., Hanson M. M., 2009, in Hubeny I., Stone J. M., MacGregor K., Werner K., eds, *AIP Conf. Proc. Vol. 1171, Recent Directions in Astrophysical Quantitative Spectroscopy and Radiation Hydrodynamics*. Am. Inst. Phys., New York, p. 123
- Rogers H., Pittard J. M., 2013, *MNRAS*, 431, 1337
- Salpeter E. E., 1955, *ApJ*, 121, 161
- Schaye J. et al., 2015, *MNRAS*, 446, 521
- Schneider N. et al., 2011, *A&A*, 529, A1
- Sedov L. I., 1946, *J. Appl. Math. Mech.*, 10, 241
- Sedov L. I., 1958, *Rev. Mod. Phys.*, 30, 1077
- Sharma P., Roy A., Nath B. B., Shchekinov Y., 2014, *MNRAS*, 443, 3463
- Shetty R., Ostriker E. C., 2012, *ApJ*, 754, 2
- Stinson G., Seth A., Katz N., Wadsley J., Governato F., Quinn T., 2006, *MNRAS*, 373, 1074
- Sutherland R. S., Bicknell G. V., Dopita M. A., 1993, *ApJ*, 414, 510
- Taylor G., 1950, *Proc. R. Soc. A*, 201, 159
- Tenorio-Tagle G., Bodenheimer P., 1988, *ARA&A*, 26, 145
- Thompson T. A., Krumholz M. R., 2016, *MNRAS*, 455, 334
- Tomassetti M., Porciani C., Romano-Díaz E., Ludlow A. D., 2015, *MNRAS*, 446, 3330
- Truelove J. K., McKee C. F., 1999, *ApJS*, 120, 299
- Übler H., Naab T., Oser L. et al., 2014, *MNRAS*, 443, 2092
- Vazquez-Semadeni E., 1994, *ApJ*, 423, 681
- Vazquez-Semadeni E. C., Passot T., Pouquet A., 1993, *BAAS*, 25, 1462
- Vink J., 2012, *A&AR*, 20, 49
- Walch S., Naab T., 2015, *MNRAS*, 451, 2757
- Walch S., Whitworth A., Bisbas T., Hubber D. A., Wuensch R., 2011, preprint ([arXiv:1109.3478](https://arxiv.org/abs/1109.3478))
- Walch S. K., Whitworth A. P., Bisbas T., Wünsch R., Hubber D., 2012, *MNRAS*, 427, 625
- Walch S. et al., 2015, *MNRAS*, 454, 238
- Ward R. L., Wadsley J., Sills A., 2014, *MNRAS*, 445, 1575
- Weaver R., McCray R., Castor J., Shapiro P., Moore R., 1977, *ApJ*, 218, 377
- Wünsch R., Dale J. E., Palouš J., Whitworth A. P., 2010, *MNRAS*, 407, 1963

This paper has been typeset from a  $\text{\LaTeX}$  file prepared by the author.

## SUMMARY AND CONCLUSION

## 7.1

## SUMMARY

In *Paper I*, I discuss the relative impact of stellar winds and ionizing radiation in different, homogeneous ambient media. Initially, the new implementation of ionizing radiation is tested against the Monte-Carlo photoionization code MOCASSIN. The simulations show that the differential (individually evaluated) impact of stellar winds and ionizing radiation is highly dependent on the properties of the ambient medium. In the CNM, ionizing radiation dominates the momentum input over the impact of stellar winds. In combination, stellar winds are confined inside the HII region, where it causes a small but hot bubble to expand with only small contributions to the total momentum. A comparison between a single SN and the radiative feedback from massive stars with masses above  $23 M_{\odot}$  reveals that the momentum input from radiative bubbles is equal or even higher than the SN impact.

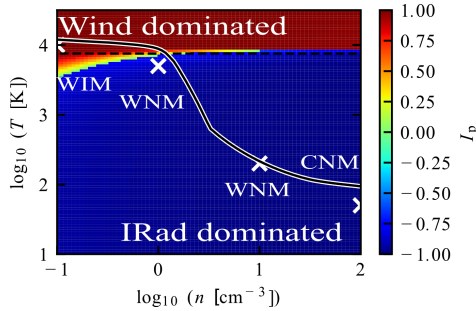


Figure 4: Time averaged relative impact  $I_p$  (color) between stellar winds and ionizing radiation as a function of a constant ambient density and temperature around a star with a mass of  $20 M_{\odot}$ . The wind dominated ( $I_p > 0$ ) and radiation dominated ( $I_p < 0$ ) regime is indicated. The black solid line corresponds to equilibrium conditions where heating and cooling balances ( $\dot{u}_{\text{heat}} = 0$ ). The white crosses indicate four specific environments used in this work with the WIM (right) and CNM (left). The original picture is found in *Paper I*.

the wind-dominated and radiation dominated regimes are indicated. The thermal equi-

In the WIM, stellar winds are the predominant form of feedback, which provides the same momentum input as in the CNM. Radiation does not couple to the warm, tenuous medium and the impact falls short. Energetically, stellar winds couple more efficiently to the ISM than ionizing radiation. In the WIM, the low coupling efficiency of ionizing radiation results from the insufficient coupling of photons to the medium. In combination, ionization always supports the wind-driven expansion by preventing the rarefied medium from cooling and recombining.

To estimate the global impact from massive stars on different, homogeneous media, a ratio between the impact of wind and radiation is used. It underlines the media-dependency. The mass of the source is equally important because it determines the ratio of emitted wind and radiative energy, hence also influences the impact. This is shown in Fig. 4 for a star with  $23 M_{\odot}$  where the ambient medium is represented by the temperature and the density. The

librium curve (black) is included and the presented ambient media for which we carried out simulations are indicated with crosses. The WNM is a transition regime from ionization dominated momentum injection in the CNM to wind dominated injection in the WIM.

In summary, this study shows that the relative impact of stellar winds and ionizing radiation depends on the stellar mass considered but even more strongly on the properties of the ambient medium. This is important to understand because it is likely that a massive star interacts with vastly different environments during its lifetime due to the short dispersal time scales of the gas in young star clusters and the significant fraction of runaway massive stars.

In *Paper II*, the early radiative impact from massive stars on MCs is investigated, which self-consistently form out of a SN-driven, multiphase ISM. We compare two MCs in the reference simulation without feedback to the run where massive stars are emitting photoionizing radiation. The initial properties of the two MCs are similar, i.e. the mass, the volume, or the virial state are comparable. However, during the evolution, the cloud morphologies under the influence of ionizing radiation appear to be different.

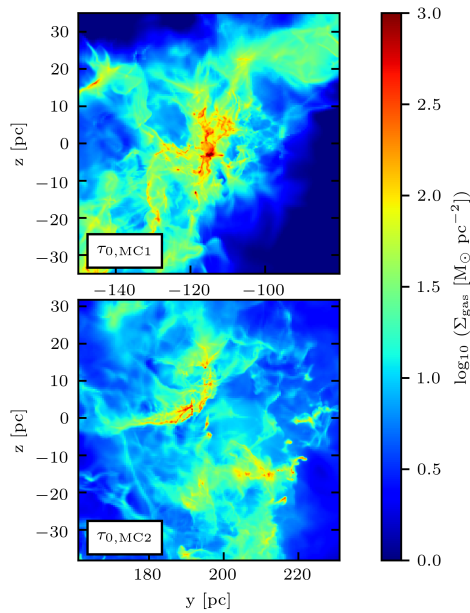


Figure 5: Gas column density  $\Sigma_{\text{gas}}$  in the  $y$ - $z$ -plane for the total volume of the two clouds MC<sub>1</sub> (top) and MC<sub>2</sub> (bottom) at  $\tau = 3$  Myr. The figures are taken from simulations shown in *Paper II*.

rate is increased with the result of dispersing gas, hence lowering the efficiency on the longer turn, and vice versa. We find  $\text{SFE}_{\text{ff}}$  of  $\sim 9 - 20$  percent, depending on the chosen cloud selection criterion and hence free-fall time.

This paper shows that the cloud evolution is dominated by well-shielded, dense substructures. Subtle differences in the density substructures of the two investig-

Fig. 5 shows the gas column densities in the  $y$ - $z$ -plane of the two clouds affected by 3 Myr of radiative feedback. This difference is not related to an imbalance of massive stars but seems to be linked to the dense and well-shielded substructures in the clouds. These substructures embed massive stars, radiation is locked inside bubbles and the radiative impact is delayed until the bubble opens into the ambient medium. The mass of well-shielded gas, i.e. gas with an effective column density that is correlated to a visual extinction above 1 mag, describes this behaviour. These substructures are already imprinted during the formation of the clouds. Star formation can be regulated by radiative feedback. A comparison to the reference simulation shows that photoionization reduces the star formation efficiency per free-fall time  $\text{SFE}_{\text{ff}}$  by a factor of  $\sim 3 - 4$ . The clouds show similar star formation rates, despite the diverging morphologies. It seems that radiation regulates star formation, which means that in dense clouds the



ated clouds affect the impact of radiative feedback which appears to regulate star formation. This is in contrast to simulations of isolated MCs where radiative feedback is unable to efficiently regulate the star formation rate.

In *Paper III*, a new, one-dimensional program is introduced that follows the evolution of a SN remnant from the adiabatic Sedov-Taylor phase until the end of the radiative, pressure-driven snowplough phase to obtain the radial momentum transferred to the ambient gas. The code is tested in homogeneous media and the results reflect those from three-dimensional numerical simulations. The ambient structure is extended to a power-law density distribution, where the final momentum clearly exceeds the homogeneous values. A high central density is not influencing the evolution, which is rather controlled by the density of the density floor far from the explosion site.

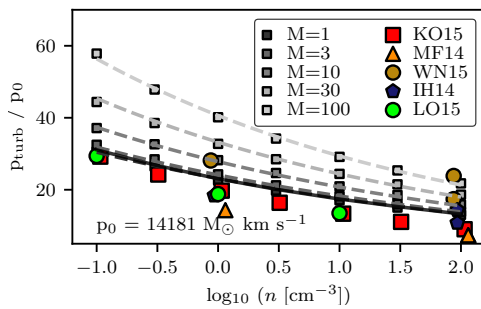


Figure 6: Radial SN momentum input  $p_{\text{turb}}$  at the beginning of the momentum-conserving phase in turbulent ambient media with mean number densities in the range  $\bar{n} = 0.1\text{--}100\text{ cm}^{-3}$  and Mach numbers  $M$  increasing from  $M=1\text{--}100$ . The environment is separated into 195 cones. Each data point corresponds to the mean of 20 realizations. Recent numerical simulation are added from [Iffrig & Hennebelle \(2015\)](#), [Kim & Ostriker \(2015\)](#), [Martizzi et al. \(2015\)](#), [Walch et al. \(2015\)](#), and [Li et al. \(2015\)](#). For better visibility these symbols are shifted around the corresponding number density. The original figure is found in *Paper III*.

As seen in Fig. 6, this idealized setup reproduces the results from comparable numerical simulations. The impact of SNe increases with lower densities and higher Mach numbers, which can boost the momentum by a factor up to 2. The results are condensed into a simple formula for the SN impact in turbulent media dependent on the average density and the Mach number (see Fig. 6).

This work shows that the adiabatic and the radiative phases are essential for the momentum input by SNe. A SN remnant is strongly influenced by the ambient density, which determines the cooling, hence the amount of created momentum.

Stellar winds and ionizing radiation shape the ambient medium before the SN explosion. Taking this into account, the blast wave expands into a low-density bubble which is surrounded by a shock shell. The density and temperature of this shell determine the final momentum of the SN. Low initial temperatures result in high shell densities and an efficient cooling of the incoming SN blast wave. The final SN impact is small. In case of higher initial densities, on the other hand, radiative cooling is delayed and the momentum input increases by a factor up to 10. As soon as the mass swept-up by the SN shock and the mass in the existing shock shell becomes comparable, the homogeneous result is recovered.

The one-dimensional, radial behaviour of the model is utilized to treat a turbulent quasi-three-dimensional environment. A lognormal density distribution with a mean density and dispersion that is related to the Mach number of the turbulent medium is used to sample densities for multiple ambient media. In combination, the impact of SNe in turbulent media is obtained. As



Pre-existing shocks, i.e. wind or radiative driven, obstruct the expansion of SN shocks. In turbulent media, the SN momentum can be boosted.

## 7.2

### CONCLUSION

This work presents three manuscripts that investigate the impact of stellar feedback from massive stars in the ISM. Considering the net energetics, stellar winds, ionizing radiation, and SNe are the most important feedback processes in MCs. The individual impacts are determined by the efficiency of the processes to couple the net emitted energy to the ambient medium. However, the relative impact and the resulting importance of stellar feedback is still unclear. Stellar feedback is debated to shape dense filaments, redistribute gas, induce turbulence to support clouds against gravitational collapse, change the chemical state of the gas, disperse MCs, set the properties of the multiphase ISM, drive galactic-scale motions, and even expel gas from the galactic disc. In discussions about the cycle of star formation, feedback is considered as regulator between gas condensation, accretion onto stars and star formation.

This work shows that the impact from stellar feedback is dependent on the ambient medium. The momentum-driven wind is efficiently processing the provided energy and the effective impact is almost constant. The pressure-driven impact from ionizing radiation is highly media dependent. The process is inefficiently coupling the energy to the surroundings because of the high cooling rate associated with radiative combination and free-free emission. SNe, especially the adiabatic Sedov-Taylor and the pressure-driven phase are prone to cooling processes, which scale with the ambient density and determine the final momentum input.

In homogeneous media, the cold and dense gas is dominated by radiative impact with a final momentum that can be equally or even larger than the SN impact. The contribution from stellar winds is minor. In warm and rarefied media, the radiative energy is not coupling to the medium and by this the pressure-driven impact vanishes. Stellar winds increase in importance, however the impact from SNe is dominant. In environments with supersonic, isothermal turbulence, which is described by a lognormal density distribution around a mean ambient density with a dispersion that is related to the Mach number, the momentum input from SNe is boosted up to a factor of 2. In MCs, that form out of a SN-driven, multiphase ISM, ionizing radiation is the main source of feedback at least in the early stage, where the massive stars are too embedded in dense structures, hence stellar winds are negligible.

## 7.3

### OUTLOOK

This thesis helps to understand stellar feedback in an ISM framework. However, this is only one aspect in the cycle of star formation. Computational progress will help to pursue research with increasing detail and in many more facets.

Together with this work, numerical implementations of feedback processes evolved in the FLASH code. These well-tested modules treat stellar winds, ionizing radiation, and SNe. For the near futures, simulations with all feedback processes in the complex MC setup are scheduled. The presented simulations are repeated with magnetic fields. The required computational power is inquired by proposals at the

high performance computing center SUPERMUC at the Leibnitz-Rechenzentrum in Garching.

However, other physical processes are scientifically interesting and might be considered in the future. Radiation pressure on gas and dust is a widely discussed agent of radiation. The impact was found to be negligible in low density regions however in MC this process might contribute significantly ([Krumholz & Matzner 2009](#); [Draine 2011a](#); [Rahner et al. 2017](#)). Likewise, massive stars do not exclusively emit Lyman-continuum photons but also contribute to the FUV field. The resulting photoelectric heating affects intermediate dense regions in MCs ([Habing 1968](#); [Draine 1978](#)). In a future implementation the field is not assumed to be constant but treated self-consistently via radiative transfer. The primary scientific goal is to understand feedback processes and the mutual interaction with the ambient medium in far higher, physical detail.

## BIBLIOGRAPHY

---

- Adams, S. M., Kochanek, C. S., Beacom, J. F., Vagins, M. R., & Stanek, K. Z., Observing the Next Galactic Supernova. 2013, *ApJ*, 778, 164
- Agertz, O. & Kravtsov, A. V., On the Interplay between Star Formation and Feedback in Galaxy Formation Simulations. 2015, *ApJ*, 804, 18
- Andersson, B.-G., Lazarian, A., & Vaillancourt, J. E., Interstellar Dust Grain Alignment. 2015, *ARA&A*, 53, 501
- Arthur, S. J., Kurtz, S. E., Franco, J., & Albarrán, M. Y., The Effects of Dust on Compact and Ultracompact H II Regions. 2004, *ApJ*, 608, 282
- Ballesteros-Paredes, J., Gómez, G. C., Loinard, L., Torres, R. M., & Pichardo, B., Tidal forces as a regulator of star formation in Taurus. 2009a, *MNRAS*, 395, L81
- Ballesteros-Paredes, J., Gómez, G. C., Pichardo, B., & Vázquez-Semadeni, E., On the gravitational content of molecular clouds and their cores. 2009b, *MNRAS*, 393, 1563
- Ballesteros-Paredes, J., Klessen, R. S., Mac Low, M.-M., & Vazquez-Semadeni, E., Molecular Cloud Turbulence and Star Formation. 2007, *Protostars and Planets V*, 63
- Barnes, J. & Hut, P., A hierarchical  $O(N \log N)$  force-calculation algorithm. 1986, *Nature*, 324, 446
- Bastian, N., Covey, K. R., & Meyer, M. R., A Universal Stellar Initial Mass Function? A Critical Look at Variations. 2010, *ARA&A*, 48, 339
- Bigiel, F., Leroy, A., Walter, F., et al., The Star Formation Law in Nearby Galaxies on Sub-Kpc Scales. 2008, *AJ*, 136, 2846
- Bisbas, T. G., Haworth, T. J., Williams, R. J. R., et al., STARBENCH: the D-type expansion of an H II region. 2015, *MNRAS*, 453, 1324
- Black, J. H. 1994, in *Astronomical Society of the Pacific Conference Series*, Vol. 58, The First Symposium on the Infrared Cirrus and Diffuse Interstellar Clouds, ed. R. M. Cutri & W. B. Latter, 355
- Black, J. H. & Dalgarno, A., Models of interstellar clouds. I - The Zeta Ophiuchi cloud. 1977, *ApJS*, 34, 405
- Blasi, P., Recent Results in Cosmic Ray Physics and Their Interpretation. 2014, *Brazilian Journal of Physics*, 44, 426
- Bouchut, F., Klingenberg, C., & Waagan, K., A multiwave approximate Riemann solver for ideal MHD based on relaxation. I: theoretical framework. 2007, *Numerische Mathematik*, 108, 7, 10.1007/s00211-007-0108-8
- Bouchut, F., Klingenberg, C., & Waagan, K., A multiwave approximate Riemann solver for ideal MHD based on relaxation II: numerical implementation with 3 and 5 waves. 2010, *Numerische Mathematik*, 115, 647, 10.1007/s00211-010-0289-4
- Brunt, C. M., Heyer, M. H., & Mac Low, M.-M., Turbulent driving scales in molecular clouds. 2009, *A&A*, 504, 883
- Carpenter, J. M., Meyer, M. R., Dougados, C., Strom, S. E., & Hillenbrand, L. A., Properties of the Monoceros R2 Stellar Cluster. 1997, *AJ*, 114, 198
- Caselli, P. & Myers, P. C., The Line Width-Size Relation in Massive Cloud Cores. 1995, *ApJ*, 446, 665
- Castor, J., McCray, R., & Weaver, R., Interstellar bubbles. 1975, *ApJ*, 200, L107

- Chabrier, G., The Galactic Disk Mass Budget. I. Stellar Mass Function and Density. 2001, *ApJ*, 554, 1274
- Chabrier, G., The Galactic Disk Mass Function: Reconciliation of the Hubble Space Telescope and Nearby Determinations. 2003, *ApJ*, 586, L133
- Chevalier, R. A. & Clegg, A. W., Wind from a starburst galaxy nucleus. 1985, *Nature*, 317, 44
- Churchwell, E., Babler, B. L., Meade, M. R., et al., The Spitzer/GLIMPSE Surveys: A New View of the Milky Way. 2009, *PASP*, 121, 213
- Cioffi, D. F., McKee, C. F., & Bertschinger, E., Dynamics of radiative supernova remnants. 1988, *ApJ*, 334, 252
- Colombo, D., Hughes, A., Schinnerer, E., et al., The PdBI Arcsecond Whirlpool Survey (PAWS): Environmental Dependence of Giant Molecular Cloud Properties in M51. 2014, *ApJ*, 784, 3
- Congiu, E., Matar, E., Kristensen, L. E., Dulieu, F., & Lemaire, J. L., Laboratory evidence for the non-detection of excited nascent  $H_2$  in dark clouds. 2009, *MNRAS*, 397, L96
- Crutcher, R. M., Magnetic Fields in Molecular Clouds: Observations Confront Theory. 1999, *ApJ*, 520, 706
- Crutcher, R. M., Troland, T. H., Lazareff, B., Paubert, G., & Kazès, I., Detection of the CN Zeeman Effect in Molecular Clouds. 1999, *ApJ*, 514, L121
- Dale, J. E., The modelling of feedback in star formation simulations. 2015, *New A Rev.*, 68, 1
- Dale, J. E., Bonnell, I. A., Clarke, C. J., & Bate, M. R., Photoionizing feedback in star cluster formation. 2005, *MNRAS*, 358, 291
- Dale, J. E., Ercolano, B., & Bonnell, I. A., Ionizing feedback from massive stars in massive clusters - II. Disruption of bound clusters by photoionization. 2012, *MNRAS*, 424, 377
- Dale, J. E., Ngoumou, J., Ercolano, B., & Bonnell, I. A., Before the first supernova: combined effects of H II regions and winds on molecular clouds. 2014, *MNRAS*, 442, 694
- Dalgarno, A., Yan, M., & Liu, W., Electron Energy Deposition in a Gas Mixture of Atomic and Molecular Hydrogen and Helium. 1999, *ApJS*, 125, 237
- Dalla Vecchia, C. & Schaye, J., Simulating galactic outflows with thermal supernova feedback. 2012, *MNRAS*, 426, 140
- Dame, T. M., Ungerechts, H., Cohen, R. S., et al., A composite CO survey of the entire Milky Way. 1987, *ApJ*, 322, 706
- de Avillez, M. A., Disc-halo interaction - I. Three-dimensional evolution of the Galactic disc. 2000, *MNRAS*, 315, 479
- de Avillez, M. A. & Breitschwerdt, D. 2004, in *Astrophysics and Space Science Library*, Vol. 315, *How Does the Galaxy Work?*, ed. E. J. Alfaro, E. Pérez, & J. Franco, 331
- de Avillez, M. A. & Breitschwerdt, D., The Generation and Dissipation of Interstellar Turbulence: Results from Large-Scale High-Resolution Simulations. 2007, *ApJ*, 665, L35
- De Pree, C. G., Peters, T., Mac Low, M.-M., et al., Flickering of 1.3 cm Sources in Sgr B2: Toward a Solution to the Ultracompact H II Region Lifetime Problem. 2014, *ApJ*, 781, L36
- Dib, S., Bell, E., & Burkert, A., The Supernova Rate-Velocity Dispersion Relation in the Interstellar Medium. 2006, *ApJ*, 638, 797
- Dobbs, C. L., Krumholz, M. R., Ballesteros-Paredes, J., et al., Formation of Molecular

- Clouds and Global Conditions for Star Formation. 2014, *Protostars and Planets VI*, 3
- Dobbs, C. L. & Pringle, J. E., The exciting lives of giant molecular clouds. 2013, *MNRAS*, 432, 653
- Draine, B. T., Photoelectric heating of interstellar gas. 1978, *ApJS*, 36, 595
- Draine, B. T., Interstellar Dust Grains. 2003, *ARA&A*, 41, 241
- Draine, B. T., On Radiation Pressure in Static, Dusty H II Regions. 2011a, *ApJ*, 732, 100
- Draine, B. T. 2011b, *Physics of the Interstellar and Intergalactic Medium* (Princeton Series in Astrophysics)
- Draine, B. T. & Bertoldi, F., Structure of Stationary Photodissociation Fronts. 1996, *ApJ*, 468, 269
- Draine, B. T. & Lee, H. M., Optical properties of interstellar graphite and silicate grains. 1984, *ApJ*, 285, 89
- Dubey, A., Fisher, R., Graziani, C., et al. 2008, in *Astronomical Society of the Pacific Conference Series*, Vol. 385, *Numerical Modeling of Space Plasma Flows*, ed. N. V. Pogorelov, E. Audit, & G. P. Zank, 145
- Dupac, X., Bernard, J.-P., Boudet, N., et al., Inverse temperature dependence of the dust submillimeter spectral index. 2003, *A&A*, 404, L11
- Dwek, E. & Arendt, R. G., Dust-gas interactions and the infrared emission from hot astrophysical plasmas. 1992, *ARA&A*, 30, 11
- Ekström, S., Georgy, C., Eggenberger, P., et al., Grids of stellar models with rotation. I. Models from 0.8 to 120  $M_{\odot}$  at solar metallicity ( $Z = 0.014$ ). 2012, *A&A*, 537, A146
- Elmegreen, B. G., Star Formation in a Crossing Time. 2000, *ApJ*, 530, 277
- Elmegreen, B. G. & Falgarone, E., A Fractal Origin for the Mass Spectrum of Interstellar Clouds. 1996, *ApJ*, 471, 816
- Elmegreen, B. G. & Lada, C. J., Sequential formation of subgroups in OB associations. 1977, *ApJ*, 214, 725
- Elmegreen, B. G. & Scalo, J., Interstellar Turbulence I: Observations and Processes. 2004, *ARA&A*, 42, 211
- Evans, II, N. J., Dunham, M. M., Jørgensen, J. K., et al., The Spitzer c2d Legacy Results: Star-Formation Rates and Efficiencies; Evolution and Lifetimes. 2009, *ApJS*, 181, 321
- Falgarone, E., Pety, J., & Hily-Blant, P., Intermittency of interstellar turbulence: extreme velocity-shears and CO emission on milliparsec scale. 2009, *A&A*, 507, 355
- Federrath, C., Banerjee, R., Clark, P. C., & Klessen, R. S., Modeling Collapse and Accretion in Turbulent Gas Clouds: Implementation and Comparison of Sink Particles in AMR and SPH. 2010, *ApJ*, 713, 269
- Federrath, C. & Klessen, R. S., The Star Formation Rate of Turbulent Magnetized Clouds: Comparing Theory, Simulations, and Observations. 2012, *ApJ*, 761, 156
- Federrath, C., Klessen, R. S., & Schmidt, W., The Density Probability Distribution in Compressible Isothermal Turbulence: Solenoidal versus Compressive Forcing. 2008, *ApJ*, 688, L79
- Field, G. B., Goldsmith, D. W., & Habing, H. J., Cosmic-Ray Heating of the Interstellar Gas. 1969, *ApJ*, 155, L149
- Freyer, T., Hensler, G., & Yorke, H. W., Massive Stars and the Energy Balance of the Interstellar Medium. I. The Impact of an Isolated 60  $M_{\text{Solar}}$  Star. 2003, *ApJ*, 594, 888
- Freyer, T., Hensler, G., & Yorke, H. W., Massive Stars and the Energy Balance of the

- Interstellar Medium. II. The 35  $M_{\text{solar}}$  Star and a Solution to the “Missing Wind Problem”. 2006, *ApJ*, 638, 262
- Fryxell, B., Olson, K., Ricker, P., et al., FLASH: An Adaptive Mesh Hydrodynamics Code for Modeling Astrophysical Thermonuclear Flashes. 2000, *ApJS*, 131, 273
- Gaisser, T. K. 2006, in *Journal of Physics Conference Series*, Vol. 47, *Journal of Physics Conference Series*, 15–20
- Gatto, A., Walch, S., Low, M.-M. M., et al., Modelling the supernova-driven ISM in different environments. 2015, *MNRAS*, 449, 1057
- Gatto, A., Walch, S., Naab, T., et al., The SILCC project - III. Regulation of star formation and outflows by stellar winds and supernovae. 2017, *MNRAS*, 466, 1903
- Geen, S., Hennebelle, P., Tremblin, P., & Rosdahl, J., Photoionization feedback in a self-gravitating, magnetized, turbulent cloud. 2015a, *MNRAS*, 454, 4484
- Geen, S., Rosdahl, J., Blaizot, J., Devriendt, J., & Slyz, A., A detailed study of feedback from a massive star. 2015b, *MNRAS*, 448, 3248
- Gent, F. A., Shukurov, A., Fletcher, A., Sarson, G. R., & Mantere, M. J., The supernova-regulated ISM - I. The multiphase structure. 2013, *MNRAS*, 432, 1396
- Genzel, R., Tacconi, L. J., Lutz, D., et al., Combined CO and Dust Scaling Relations of Depletion Time and Molecular Gas Fractions with Cosmic Time, Specific Star-formation Rate, and Stellar Mass. 2015, *ApJ*, 800, 20
- Gies, D. R. & Bolton, C. T., The binary frequency and origin of the OB runaway stars. 1986, *ApJS*, 61, 419
- Girichidis, P., Naab, T., Walch, S., et al., Launching Cosmic-Ray-driven Outflows from the Magnetized Interstellar Medium. 2016a, *ApJ*, 816, L19
- Girichidis, P., Walch, S., Naab, T., et al., The SILCC (Simulating the LifeCycle of molecular Clouds) project - II. Dynamical evolution of the supernova-driven ISM and the launching of outflows. 2016b, *MNRAS*, 456, 3432
- Glassgold, A. E., Galli, D., & Padovani, M., Cosmic-Ray and X-Ray Heating of Interstellar Clouds and Protoplanetary Disks. 2012, *ApJ*, 756, 157
- Glover, S. C. O., Federrath, C., Mac Low, M.-M., & Klessen, R. S., Modelling CO formation in the turbulent interstellar medium. 2010, *MNRAS*, 404, 2
- Glover, S. C. O. & Mac Low, M.-M., Simulating the Formation of Molecular Clouds. I. Slow Formation by Gravitational Collapse from Static Initial Conditions. 2007a, *ApJS*, 169, 239
- Glover, S. C. O. & Mac Low, M.-M., Simulating the Formation of Molecular Clouds. II. Rapid Formation from Turbulent Initial Conditions. 2007b, *ApJ*, 659, 1317
- Gnat, O. & Ferland, G. J., Ion-by-ion Cooling Efficiencies. 2012, *ApJS*, 199, 20
- Goldbaum, N. J., Krumholz, M. R., Matzner, C. D., & McKee, C. F., The Global Evolution of Giant Molecular Clouds. II. The Role of Accretion. 2011, *ApJ*, 738, 101
- Goldsmith, P. F. & Langer, W. D., Molecular cooling and thermal balance of dense interstellar clouds. 1978, *ApJ*, 222, 881
- Górski, K. M., Hivon, E., Banday, A. J., et al., HEALPix: A Framework for High-Resolution Discretization and Fast Analysis of Data Distributed on the Sphere. 2005, *ApJ*, 622, 759
- Gratier, P., Braine, J., Rodriguez-Fernandez, N. J., et al., Giant molecular clouds in the Local Group galaxy M 33\*. 2012, *A&A*, 542, A108
- Gritschneider, M., Naab, T., Walch, S., Burkert, A., & Heitsch, F., Driving Turbulence and Triggering Star Formation by Ionizing Radiation. 2009, *ApJ*, 694, L26
- Habing, H. J., The interstellar radiation density between 912 Å and 2400 Å. 1968,



- Bull. Astron. Inst. Netherlands, 19, 421
- Hartmann, L., Ballesteros-Paredes, J., & Bergin, E. A., Rapid Formation of Molecular Clouds and Stars in the Solar Neighborhood. 2001, *ApJ*, 562, 852
- Heitsch, F., Gravitational Infall onto Molecular Filaments. 2013, *ApJ*, 769, 115
- Heyer, M. & Dame, T., Molecular Clouds in the Milky Way. 2015, *Annual Review of Astronomy and Astrophysics*, 53, 583
- Heyer, M., Krawczyk, C., Duval, J., & Jackson, J. M., Re-Examining Larson's Scaling Relationships in Galactic Molecular Clouds. 2009, *ApJ*, 699, 1092
- Heyer, M. H., Carpenter, J. M., & Snell, R. L., The Equilibrium State of Molecular Regions in the Outer Galaxy. 2001, *ApJ*, 551, 852
- Hildebrand, R. H., The Determination of Cloud Masses and Dust Characteristics from Submillimetre Thermal Emission. 1983, *QJRAS*, 24, 267
- Hill, A. S., Joung, M. R., Mac Low, M.-M., et al., Vertical Structure of a Supernova-driven Turbulent, Magnetized Interstellar Medium. 2012, *ApJ*, 750, 104
- Hopkins, P. F., Kereš, D., Oñorbe, J., et al., Galaxies on FIRE (Feedback In Realistic Environments): stellar feedback explains cosmologically inefficient star formation. 2014, *MNRAS*, 445, 581
- Hosokawa, T. & Inutsuka, S.-i., Dynamical Expansion of Ionization and Dissociation Front around a Massive Star. II. On the Generality of Triggered Star Formation. 2006, *ApJ*, 646, 240
- Howard, C., Pudritz, R., & Klessen, R., Ultraviolet Escape Fractions from Giant Molecular Clouds during Early Cluster Formation. 2017, *ApJ*, 834, 40
- Hughes, A., Meidt, S. E., Colombo, D., et al., A Comparative Study of Giant Molecular Clouds in M51, M33, and the Large Magellanic Cloud. 2013, *ApJ*, 779, 46
- Ibáñez-Mejía, J. C., Mac Low, M.-M., Klessen, R. S., & Baczynski, C., Feeding versus Falling: The Growth and Collapse of Molecular Clouds in a Turbulent Interstellar Medium. 2017, *ApJ*, 850, 62
- Iffrig, O. & Hennebelle, P., Mutual influence of supernovae and molecular clouds. 2015, *A&A*, 576, A95
- Janka, H.-T., Hanke, F., Hudepohl, L., et al., Core-collapse supernovae: Reflections and directions. 2012, *Progress of Theoretical and Experimental Physics*, 2012, 010000
- Joung, M. K. R. & Mac Low, M.-M., Turbulent Structure of a Stratified Supernova-driven Interstellar Medium. 2006, *ApJ*, 653, 1266
- Kalberla, P. M. W. & Dedes, L., Global properties of the H I distribution in the outer Milky Way. Planar and extra-planar gas. 2008, *A&A*, 487, 951
- Kennicutt, R. C. & Evans, N. J., Star Formation in the Milky Way and Nearby Galaxies. 2012, *ARA&A*, 50, 531
- Kennicutt, Jr., R. C., The Global Schmidt Law in Star-forming Galaxies. 1998, *ApJ*, 498, 541
- Kim, C.-G., Kim, W.-T., & Ostriker, E. C., Regulation of Star Formation Rates in Multiphase Galactic Disks: Numerical Tests of the Thermal/Dynamical Equilibrium Model. 2011, *ApJ*, 743, 25
- Kim, C.-G. & Ostriker, E. C., Momentum Injection by Supernovae in the Interstellar Medium. 2015, *ApJ*, 802, 99
- Kim, C.-G., Ostriker, E. C., & Kim, W.-T., Three-dimensional Hydrodynamic Simulations of Multiphase Galactic Disks with Star Formation Feedback. I. Regulation of Star Formation Rates. 2013, *ApJ*, 776, 1
- Klessen, R. S. & Glover, S. C. O., Physical Processes in the Interstellar Medium. 2016,

- Star Formation in Galaxy Evolution: Connecting Numerical Models to Reality, Saas-Fee Advanced Course, Volume 43. ISBN 978-3-662-47889-9. Springer-Verlag Berlin Heidelberg, 2016, p. 85, 43, 85
- Klessen, R. S., Heitsch, F., & Mac Low, M.-M., Gravitational Collapse in Turbulent Molecular Clouds. I. Gasdynamical Turbulence. 2000, *ApJ*, 535, 887
- Kroupa, P., On the variation of the initial mass function. 2001, *MNRAS*, 322, 231
- Krumholz, M. R., Radiation Feedback and Fragmentation in Massive Protostellar Cores. 2006, *ApJ*, 641, L45
- Krumholz, M. R., The big problems in star formation: The star formation rate, stellar clustering, and the initial mass function. 2014, *Phys. Rep.*, 539, 49
- Krumholz, M. R., Notes on Star Formation. 2015, ArXiv e-prints
- Krumholz, M. R., Klein, R. I., McKee, C. F., Offner, S. S. R., & Cunningham, A. J., The Formation of Massive Star Systems by Accretion. 2009, *Science*, 323, 754
- Krumholz, M. R. & Matzner, C. D., The Dynamics of Radiation-pressure-dominated H II Regions. 2009, *ApJ*, 703, 1352
- Kudritzki, R.-P. & Puls, J., Winds from Hot Stars. 2000, *ARA&A*, 38, 613
- Lada, C. J. & Lada, E. A., Embedded Clusters in Molecular Clouds. 2003, *ARA&A*, 41, 57
- Landau, L. & Lifshits, E. 1959, *Fluid Mechanics*, by L.D. Landau and E.M. Lifshitz, *Teoreticheskaya fizika* (Pergamon Press)
- Larson, R. B., Effects of supernovae on the early evolution of galaxies. 1974, *MNRAS*, 169, 229
- Larson, R. B., Turbulence and star formation in molecular clouds. 1981, *MNRAS*, 194, 809
- Le Bourlot, J., Le Petit, F., Pinto, C., Roueff, E., & Roy, F., Surface chemistry in the interstellar medium. I. H<sub>2</sub> formation by Langmuir-Hinshelwood and Eley-Rideal mechanisms. 2012, *A&A*, 541, A76
- Li, M., Ostriker, J. P., Cen, R., Bryan, G. L., & Naab, T., Supernova Feedback and the Hot Gas Filling Fraction of the Interstellar Medium. 2015, *ApJ*, 814, 4
- Mac Low, M.-M., The Energy Dissipation Rate of Supersonic, Magnetohydrodynamic Turbulence in Molecular Clouds. 1999, *ApJ*, 524, 169
- Mac Low, M.-M., de Avillez, M. A., & Korpi, M. J. 2004, in *Astrophysics and Space Science Library*, Vol. 315, *How Does the Galaxy Work?*, ed. E. J. Alfaro, E. Pérez, & J. Franco, 339
- Mac Low, M.-M. & Klessen, R. S., Control of star formation by supersonic turbulence. 2004, *Reviews of Modern Physics*, 76, 125
- Mac Low, M.-M. & McCray, R., Superbubbles in disk galaxies. 1988, *ApJ*, 324, 776
- Markova, N., Puls, J., Repolust, T., & Markov, H., Bright OB stars in the Galaxy. I. Mass-loss and wind-momentum rates of O-type stars: A pure H $\alpha$  analysis accounting for line-blanketing. 2004, *A&A*, 413, 693
- Martizzi, D., Faucher-Giguère, C.-A., & Quataert, E., Supernova feedback in an inhomogeneous interstellar medium. 2015, *MNRAS*, 450, 504
- Massey, P., MASSIVE STARS IN THE LOCAL GROUP: Implications for Stellar Evolution and Star Formation. 2003, *ARA&A*, 41, 15
- Mathis, J. S., Mezger, P. G., & Panagia, N., Interstellar radiation field and dust temperatures in the diffuse interstellar matter and in giant molecular clouds. 1983, *A&A*, 128, 212
- Matzner, C. D., On the Role of Massive Stars in the Support and Destruction of Giant Molecular Clouds. 2002, *ApJ*, 566, 302
- McCray, R. & Kafatos, M., Supershells and propagating star formation. 1987, *ApJ*,

- 317, 190
- McKee, C. F., Photoionization-regulated star formation and the structure of molecular clouds. 1989, *ApJ*, 345, 782
- McKee, C. F. & Ostriker, E. C., Theory of Star Formation. 2007, *ARA&A*, 45, 565
- McKee, C. F. & Ostriker, J. P., A theory of the interstellar medium - Three components regulated by supernova explosions in an inhomogeneous substrate. 1977, *ApJ*, 218, 148
- Meingast, S., Alves, J., Mardones, D., et al., VISION - Vienna survey in Orion. I. VISTA Orion A Survey. 2016, *A&A*, 587, A153
- Molina, F. Z., Glover, S. C. O., Federrath, C., & Klessen, R. S., The density variance-Mach number relation in supersonic turbulence - I. Isothermal, magnetized gas. 2012, *MNRAS*, 423, 2680
- Murray, N., Star Formation Efficiencies and Lifetimes of Giant Molecular Clouds in the Milky Way. 2011, *ApJ*, 729, 133
- Murray, N., Ménard, B., & Thompson, T. A., Radiation Pressure from Massive Star Clusters as a Launching Mechanism for Super-galactic Winds. 2011, *ApJ*, 735, 66
- Murray, N., Quataert, E., & Thompson, T. A., On the Maximum Luminosity of Galaxies and Their Central Black Holes: Feedback from Momentum-driven Winds. 2005, *ApJ*, 618, 569
- Murray, N., Quataert, E., & Thompson, T. A., The Disruption of Giant Molecular Clouds by Radiation Pressure & the Efficiency of Star Formation in Galaxies. 2010, *ApJ*, 709, 191
- Naab, T. & Ostriker, J. P., Theoretical Challenges in Galaxy Formation. 2017, *ARA&A*, 55, 59
- Nelson, R. P. & Langer, W. D., The Dynamics of Low-Mass Molecular Clouds in External Radiation Fields. 1997, *ApJ*, 482, 796
- Ngoumou, J., Hubber, D., Dale, J. E., & Burkert, A., First Investigation of the Combined Impact of Ionizing Radiation and Momentum Winds from a Massive Star on a Self-gravitating Core. 2015, *ApJ*, 798, 32
- Ostriker, E. C., McKee, C. F., & Leroy, A. K., Regulation of Star Formation Rates in Multiphase Galactic Disks: A Thermal/Dynamical Equilibrium Model. 2010, *ApJ*, 721, 975
- Ostriker, E. C. & Shetty, R., Maximally Star-forming Galactic Disks. I. Starburst Regulation Via Feedback-driven Turbulence. 2011, *ApJ*, 731, 41
- Ostriker, J. P. & McKee, C. F., Astrophysical blastwaves. 1988, *Reviews of Modern Physics*, 60, 1
- Padoan, P. & Nordlund, Å., The Star Formation Rate of Supersonic Magnetohydrodynamic Turbulence. 2011, *ApJ*, 730, 40
- Padoan, P., Pan, L., Haugbølle, T., & Nordlund, Å., Supernova Driving. I. The Origin of Molecular Cloud Turbulence. 2016, *ApJ*, 822, 11
- Padovani, M., Galli, D., & Glassgold, A. E., Cosmic-ray ionization of molecular clouds. 2009, *A&A*, 501, 619
- Pan, L. & Padoan, P., The Temperature of Interstellar Clouds from Turbulent Heating. 2009, *ApJ*, 692, 594
- Peters, T., Klessen, R. S., Mac Low, M.-M., & Banerjee, R., Limiting Accretion onto Massive Stars by Fragmentation-induced Starvation. 2010, *ApJ*, 725, 134
- Peters, T., Naab, T., Walch, S., et al., The SILCC project - IV. Impact of dissociating and ionizing radiation on the interstellar medium and  $H\alpha$  emission as a tracer of the star formation rate. 2017, *MNRAS*, 466, 3293
- Petruk, O., On the transition of the adiabatic supernova remnant to the radiative

- stage in a nonuniform interstellar medium. 2006, ArXiv e-prints astro-ph/060405
- Pittard, J. M., Self-sealing shells: blowouts and blisters on the surfaces of leaky wind-blown bubbles and supernova remnants. 2013, *MNRAS*, 435, 3600
- Puls, J., Kudritzki, R.-P., Herrero, A., et al., O-star mass-loss and wind momentum rates in the Galaxy and the Magellanic Clouds Observations and theoretical predictions. 1996, *A&A*, 305, 171
- Puls, J., Vink, J. S., & Najarro, F., Mass loss from hot massive stars. 2008, *A&A Rev.*, 16, 209
- Rahner, D., Pellegrini, E. W., Glover, S. C. O., & Klessen, R. S., Winds and radiation in unison: a new semi-analytic feedback model for cloud dissolution. 2017, *MNRAS*, 470, 4453
- Rey-Raposo, R., Dobbs, C., Agertz, O., & Alig, C., The roles of stellar feedback and galactic environment in star-forming molecular clouds. 2017, *MNRAS*, 464, 3536
- Rogers, H. & Pittard, J. M., Feedback from winds and supernovae in massive stellar clusters - I. Hydrodynamics. 2013, *MNRAS*, 431, 1337
- Röllig, M., Abel, N. P., Bell, T., et al., A photon dominated region code comparison study. 2007, *A&A*, 467, 187
- Roman-Duval, J., Jackson, J. M., Heyer, M., Rathborne, J., & Simon, R., Physical Properties and Galactic Distribution of Molecular Clouds Identified in the Galactic Ring Survey. 2010, *ApJ*, 723, 492
- Rybicki, G. B. & Lightman, A. P. 2004, *Radiative Processes in Astrophysics* (Wiley-Vch Verlag)
- Sales, L. V., Marinacci, F., Springel, V., & Petkova, M., Stellar feedback by radiation pressure and photoionization. 2014, *MNRAS*, 439, 2990
- Salpeter, E. E., The Luminosity Function and Stellar Evolution. 1955, *ApJ*, 121, 161
- Scalo, J. & Elmegreen, B. G., Interstellar Turbulence II: Implications and Effects. 2004, *ARA&A*, 42, 275
- Schmidt, M., The Rate of Star Formation. 1959, *ApJ*, 129, 243
- Schruba, A., Leroy, A. K., Walter, F., et al., A Molecular Star Formation Law in the Atomic-gas-dominated Regime in Nearby Galaxies. 2011, *AJ*, 142, 37
- Scoville, N. Z., Yun, M. S., Sanders, D. B., Clemens, D. P., & Waller, W. H., Molecular clouds and cloud cores in the inner Galaxy. 1987, *ApJS*, 63, 821
- Scuderi, S., Panagia, N., Stanghellini, C., Trigilio, C., & Umana, G., Radio observations of stellar winds from early type stars. 1998, *A&A*, 332, 251
- Seifried, D., Walch, S., Girichidis, P., et al., SILCC-Zoom: the dynamic and chemical evolution of molecular clouds. 2017, *MNRAS*, 472, 4797
- Sembach, K. R., Howk, J. C., Ryans, R. S. I., & Keenan, F. P., Modeling the Warm Ionized Interstellar Medium and Its Impact on Elemental Abundance Studies. 2000, *ApJ*, 528, 310
- Shapiro, P. R. & Field, G. B., Consequences of a New Hot Component of the Interstellar Medium. 1976, *ApJ*, 205, 762
- Sharma, P., Roy, A., Nath, B. B., & Shchekinov, Y., In a hot bubble: why does superbubble feedback work, but isolated supernovae do not? 2014, *MNRAS*, 443, 3463
- Shetty, R., Kauffmann, J., Schnee, S., & Goodman, A. A., The Effect of Noise on the Dust Temperature-Spectral Index Correlation. 2009a, *ApJ*, 696, 676
- Shetty, R., Kauffmann, J., Schnee, S., Goodman, A. A., & Ercolano, B., The Effect of Line-of-Sight Temperature Variation and Noise on Dust Continuum Observations. 2009b, *ApJ*, 696, 2234
- Shetty, R. & Ostriker, E. C., Maximally Star-forming Galactic Disks. II. Vertically

- Resolved Hydrodynamic Simulations of Starburst Regulation. 2012, *ApJ*, 754, 2
- Shu, F. H. 1992, *Physics of Astrophysics*, Vol. II (University Science Books)
- Snowden, S. L., Egger, R., Freyberg, M. J., et al., ROSAT Survey Diffuse X-Ray Background Maps. II. 1997, *ApJ*, 485, 125
- Solomon, P. M., Rivolo, A. R., Barrett, J., & Yahil, A., Mass, luminosity, and line width relations of Galactic molecular clouds. 1987, *ApJ*, 319, 730
- Spitzer, L. 1978, *Physical processes in the interstellar medium* (A Wiley-Interscience Publication)
- Spitzer, Jr., L., The Dynamics of the Interstellar Medium. III. Galactic Distribution. 1942, *ApJ*, 95, 329
- Strömgren, B., The Physical State of Interstellar Hydrogen. 1939, *ApJ*, 89, 526
- Sutherland, R. S., Bicknell, G. V., & Dopita, M. A., Shock excitation of the emission-line filaments in Centaurus A. 1993, *ApJ*, 414, 510
- Tenorio-Tagle, G. & Bodenheimer, P., Large-scale expanding superstructures in galaxies. 1988, *ARA&A*, 26, 145
- Tielens, A. G. G. M. 2005, *The Physics and Chemistry of the Interstellar Medium* (Cambridge, UK: Cambridge University Press)
- Troland, T. H., Crutcher, R. M., Goodman, A. A., et al., The Magnetic Fields in the Ophiuchus and Taurus Molecular Clouds. 1996, *ApJ*, 471, 302
- Troland, T. H. & Heiles, C., The Zeeman effect in 21 centimeter line radiation - Methods and initial results. 1982, *ApJ*, 252, 179
- Truelove, J. K., Klein, R. I., McKee, C. F., et al., The Jeans Condition: A New Constraint on Spatial Resolution in Simulations of Isothermal Self-gravitational Hydrodynamics. 1997, *ApJ*, 489, L179
- van Dishoeck, E. F. & Blake, G. A., Chemical Evolution of Star-Forming Regions. 1998, *ARA&A*, 36, 317
- Vázquez-Semadeni, E., Ryu, D., Passot, T., González, R. F., & Gazol, A., Molecular Cloud Evolution. I. Molecular Cloud and Thin Cold Neutral Medium Sheet Formation. 2006, *ApJ*, 643, 245
- Vink, J. S., The theory of stellar winds. 2011, *Ap&SS*, 336, 163
- Waagan, K., A positive MUSCL-Hancock scheme for ideal magnetohydrodynamics. 2009, *Journal of Computational Physics*, 228, 8609
- Waagan, K., Federrath, C., & Klingenberg, C., A robust numerical scheme for highly compressible magnetohydrodynamics: Nonlinear stability, implementation and tests. 2011, *Journal of Computational Physics*, 230, 3331
- Walch, S., Girichidis, P., Naab, T., et al., The SILCC (SIMulating the LifeCYcle of molecular Clouds) project - I. Chemical evolution of the supernova-driven ISM. 2015, *MNRAS*, 454, 238
- Walch, S. & Naab, T., The energy and momentum input of supernova explosions in structured and ionized molecular clouds. 2015, *MNRAS*, 451, 2757
- Walch, S., Whitworth, A. P., Bisbas, T. G., Wünsch, R., & Hubber, D. A., Clumps and triggered star formation in ionized molecular clouds. 2013, *MNRAS*, 435, 917
- Walch, S. K., Whitworth, A. P., Bisbas, T., Wünsch, R., & Hubber, D., Dispersal of molecular clouds by ionizing radiation. 2012, *MNRAS*, 427, 625
- Wareing, C. J., Pittard, J. M., & Falle, S. A. E. G., Hydrodynamic simulations of mechanical stellar feedback in a molecular cloud formed by thermal instability. 2017, *MNRAS*, 470, 2283
- Weaver, R., McCray, R., Castor, J., Shapiro, P., & Moore, R., Interstellar bubbles. II - Structure and evolution. 1977, *ApJ*, 218, 377
- Weiler, K. W. & Sramek, R. A., Supernovae and supernova remnants. 1988, *ARA&A*,

- 26, 295
- Weingartner, J. C. & Draine, B. T., Dust Grain-Size Distributions and Extinction in the Milky Way, Large Magellanic Cloud, and Small Magellanic Cloud. 2001, *ApJ*, 548, 296
- Whitworth, A., The erosion and dispersal of massive molecular clouds by young stars. 1979, *MNRAS*, 186, 59
- Williams, J. P., Blitz, L., & McKee, C. F., The Structure and Evolution of Molecular Clouds: from Clumps to Cores to the IMF. 2000, *Protostars and Planets IV*, 97
- Wolfire, M. G., Hollenbach, D., McKee, C. F., Tielens, A. G. G. M., & Bakes, E. L. O., The neutral atomic phases of the interstellar medium. 1995, *ApJ*, 443, 152
- Wünsch, R., Silich, S., Palouš, J., Tenorio-Tagle, G., & Muñoz-Tuñón, C., Evolution of Super Star Cluster Winds with Strong Cooling. 2011, *ApJ*, 740, 75
- Wünsch, R., Walch, S., Dinnbier, F., & Whitworth, A., Tree-based solvers for adaptive mesh refinement code FLASH - I: gravity and optical depths. 2018, *MNRAS*
- Zuckerman, B. & Evans, II, N. J., Models of massive molecular clouds. 1974, *ApJ*, 192, L149



## ACKNOWLEDGEMENTS

Mein größter Dank gilt meiner Betreuerin Stefanie Walch-Gassner, die mich mit ihrer außerordentlichen fachlichen Kompetenz, ihrer persönlichen Motivation und ihrer schier unendlichen Geduld während meiner Zeit als Doktorand nicht nur fortwährend unterstützt sondern auch gefördert (gefordert) hat.

Ein großer Dank geht an Daniel Seifried, dem Zappel-Philipp der Bürokollegen, für seinen freundschaftlichen Rat, seine wissenschaftliche Hilfe, und das abwechslungsreiche Unterhaltungsprogramm nach getaner Arbeit. Weiterer Dank geht an alle meine Kollegen der Theoretischen Astrophysik Gruppe und des I. Physikalischen Instituts. Ich möchte Jonathan Mackey, Richard Wunsch und Thorsten Naab für Ihre wissenschaftliche Unterstützung und die Zusammenarbeit danken. Dank gebührt Seamus, Sü, Anika sowie Franta für die schwierige Korrektur dieser Arbeit sowie der darin enthaltenen wissenschaftlichen Publikationen.

Ein ganz besonderer Dank geht an die "The Core" Gruppe und im speziellen sei Sümeyye genannt, für deren Unnachgiebigkeit und ihre bedingungslose Freundschaft. Den Dank von Andrea Gatto für das eine oder andere Bier möchte ich erwidern. Die drei Grazer und zwei Stuttgarter, die wissen es ja eh. Bei Stophl und Axel möchte ich mich für die tiefe Freundschaft und Unterstützung bedanken. Ich danke meiner restlichen Familie und speziell meinem Großvater für das Interesse an der Wissenschaft.

Am meisten möchte ich mich schließlich bei meinen Eltern und meinem Bruder für die Begleitung, Unterstützung, und Liebe in jeder Phase meines Lebens bedanken. Ohne euch Drei wäre nichts in dieser Form möglich gewesen.

## SELBSTSTÄNDIGKEITSERKLÄRUNG

Ich versichere, dass ich die von mir vorgelegte Dissertation selbständig angefertigt, die benutzten Quellen und Hilfsmittel vollständig angegeben und die Stellen der Arbeit -einschließlich Tabellen, Karten und Abbildungen-, die anderen Werken im Wortlaut oder dem Sinn nach entnommen sind, in jedem Einzelfall als Entlehnung kenntlich gemacht habe; dass diese Dissertation noch keiner anderen Fakultät oder Universität zur Prüfung vorgelegen hat; dass sie -abgesehen von den angegebenen Teilpublikationen- noch nicht veröffentlicht worden ist, sowie, dass ich eine solche Veröffentlichung vor Abschluss des Promotionsverfahrens nicht vornehmen werde. Die Bestimmungen der Promotionsordnung sind mir bekannt. Die von mir vorgelegte Dissertation ist von Prof. Dr. Stefanie Walch-Gassner betreut worden.

Köln, den 07.12.2018

(Sebastian Haid)

## TEILPUBLIKATIONEN

Es folgt eine Auflistung der Publikationen, die dieser kumulativen Arbeit zugrunde liegen. In Kürze wird hier auf die Beiträge der jeweiligen Koautoren/Koautorinnen, mit dem Fokus auf den Beiträgen des Promovenden S. Haid, eingegangen. Im Allgemeinen gelten für alle drei Beiträge die folgenden Punkte

- Sowohl die zugrundeliegende Forschungsarbeit als auch die Manuskripte der Veröffentlichungen wurden maßgeblich vom Erstautor S. Haid erstellt.
- S. Walch und D. Seifried sind die wissenschaftlichen Betreuer von S. Haid und waren daher von Beginn an in die wissenschaftliche Diskussion eingebunden.
- Jeder/jede Koautor/Koautorin hat hilfreiche Kommentare zu einer fortgeschrittenen Version des Manuskripts beigesteuert.
- Bei den Beiträgen handelt es sich um peer-reviewed Veröffentlichungen. Die anonymen Referees haben jeweils einige Hinweise zum Manuskript gegeben, die in die endgültige Version mit eingeflossen sind.

Spezielle Beiträge der einzelner Koautoren/Koautorinnen seien im Rahmen der folgenden Aufzählung genannt.

- **Haid S.**, Walch S., Seifried D., Wunsch R., Dinnbier F. and Naab T., *The relative impact of photoionizing radiation and stellar winds on different environments*. 2018, MNRAS 478

Das verwendete numerische Programm FLASH wurde vom FLASH Center for Computation Science der Universität Chicago entwickelt. Erweiterungen wurden im Rahmen der SILCC-Kollaboration hinzugefügt und sind in dieser Publikation ausführlich beschrieben. Das für dieses Manuskript essentielle FEEDBACK-SINK Modul und die Kopplung der ionisierender Strahlung mit dem

CHEMISTRY Modul wurden vom Erstautor S. Haid entwickelt, getestet bzw. erweitert. Mehrere Verbesserungen wurden von F. Dinnbier initialisiert. Die gezeigten Simulationen wurden von S. Haid durchgeführt. Das Kapitel 2.2.2 über das Modul TREERAY wurde auf Grund der hohen Komplexität maßgeblich von dessen Entwickler R. Wünsch verfasst. Die Rechenkapazität wurde aus dem Gauss-Projekt *SILCC-Zoom: The formation and dispersal of filamentary molecular clouds* am Leibniz-Rechenzentrum der Bayerischen Akademie der Wissenschaften bereitgestellt.

- **Haid S.**, Walch S., Seifried D., Wünsch R., Dinnbier F. and Naab T., *SILCC-Zoom: The early impact of ionizing radiation on forming molecular clouds*. 2019, MNRAS 482

Das verwendete numerische Programm FLASH 4 wurde vom FLASH Center for Computation Science der Universität Chicago entwickelt. Erweiterungen wurden im Rahmen der SILCC-Kooperation hinzugefügt und sind in dieser Publikation ausführlich beschrieben. Das für dieses Manuskript essentielle FEEDBACK-SINK Modul und die Kopplung der ionisierender Strahlung mit dem CHEMISTRY Modul wurden vom Erstautor S. Haid entwickelt, getestet bzw. erweitert. Mehrere Verbesserungen wurden von F. Dinnbier initialisiert. Die gezeigten Simulationen basieren auf dem numerischen Setup von S. Walch, D. Seifried, sowie der SILCC-Kollaboration und wurden von S. Haid durchgeführt. Die Rechenkapazität wurde aus dem Gauss-Projekt *SILCC-Zoom: The formation and dispersal of filamentary molecular clouds* am Leibniz-Rechenzentrum der Bayerischen Akademie der Wissenschaften bereitgestellt.

- **Haid S.**, Walch S., Naab T., Seifried D., Mackey J. and Gatto A., *Supernova blast waves in wind-blown bubbles, turbulent, and power-law ambient media*. 2016, MNRAS 460

Das verwendete Programm zur Berechnung der Supernova Evolution wurde von S. Haid von Grund auf neu entwickelt. Hierbei haben alle Koautoren/Koautorinnen wichtige wissenschaftliche Verbesserungen vorgeschlagen.

## CURICULUM VITAE

Sebastian Haid  
MSc., BSc.

## PERSONAL DETAILS

Date of Birth	2 March 1985
Place of Birth	Graz, Austria
Nationality	Austrian



## CONTACT ADDRESS

I. Physikalisches Institut University of Cologne Zùlpicher Strasse 77 50937 Cologne	Email: haid@ph1.uni-koeln.de Phone: (+221) 470 - 6147
--	--

## EDUCATIONAL QUALIFICATION

8 April 2018	PhD Defense: <i>The impact of stellar feedback processes from massive stars in the ISM</i> , Supervisor: Prof. Dr. Stefanie Walch-Gassner
1 Mar 2014 - April 2018	PhD, I. Physikalisches Institut, University of Cologne
Apr 2011 - 12 June 2013	Graduation Master of Technical Physics, TU Graz
Aug 2011 - Apr 2012	Master's Thesis, University Stuttgart, Institute of Space Systems
Oct 2004 - 27 Apr 2011	Bachelor of Technical Physics, TU Graz
Jan 2004 - Aug 2004	Obligatory military service
Sep 1995 - June 2003	Secondary School, Akademisches Gymnasium Graz, Graduation June 2003

## PUBLICATIONS AND THESIS

Haid S., Walch S., Seifried D., Wùnsch R., Dinnbier F. and Naab T., *SILCC-Zoom: The early impact of ionizing radiation on forming molecular clouds*. 2019, MNRAS 482, 4062

Haid S., Walch S., Seifried D., Wùnsch R., Dinnbier F. and Naab T., *The relative impact of photoionizing radiation and stellar winds on different environments*. 2018, MNRAS, 478, 4799

Seifried D., Walch S., Haid S., Girichidis P. and Naab T., *Is molecular cloud turbulence driven by external supernova explosions?*. 2018, ApJ 855, 81

Haid S., Walch S., Naab T., Seifried D., Mackey J. and Gatto A., *Supernova blast waves in wind-blown bubbles, turbulent, and power-law ambient media*. 2016, MNRAS 460, 2962

Gatto A., Walch S., Mac Low M.-M., Naab P., Girichidis P., Glover S.C.O., Wùnsch R., Clark P.C., Baczynski C., Peters T., Ostriker J.P., Ibanez-Mejia J.C. and Haid S., *Modelling the supernova-driven ISM in different environments*. 2015, MNRAS 449, 1057

Master (Diploma) Thesis: *System Study of Side Reactions in a Magnetically Confined Fusion Plasma for Space Propulsion Units*, Graz, Stuttgart, 2012; Supervisor: Prof. Dr. Martin Heyn, Dr. Georg Herdrich

